Università di Brescia

DIPARTIMENTO DI INGEGNERIA MECCANICA E INDUSTRIALE

DOTTORATO DI RICERCA IN TRANSIZIONE ENERGETICA E SISTEMI PRODUTTIVI SOSTENIBILI

---

settore scientifico disciplinare ING-IND/09 SISTEMI PER L'ENERGIA E L'AMBIENTE

CICLO XXXVIII

SUPERCRITICAL CO_2 CYCLES FOR THE NEXT GENERATION OF CONCENTRATED SOLAR POWER PLANTS

Dottorando:
Vladimir Naumov

Supervisore:
Prof. Paolo Giulio Iora, PhD
Prof. Gioele Di Marcoberardino, PhD

Abstract

Renewable energy plays a central role in the net-zero economy transition, with solar energy being one of the most promising resources. The concentrated solar power (CSP) plants can integrate relatively low-cost thermal energy storage, which makes them flexible and enables dispatchable electricity generation up to 24 hours. This is increasingly important as the share of non-dispatchable renewable generation (such as photovoltaic plants with no or only short-term energy storage) in the power grid continues to grow.

The competitiveness of the next-generation CSP plants can be enhanced through the adoption of advanced CO_2 power cycles operating at higher turbine inlet temperatures. Considering the operation of CSP plants in hot and arid climates, power cycle operation in a supercritical state (sCO_2) is expected. Further performance improvement can be achieved by utilizing CO_2-based mixtures using dopants with high critical temperatures. This enables a transition from supercritical to transcritical cycles with compression in the liquid phase, allowing for both improved efficiency and lower cost of the power cycle and CSP plant.

The thesis is structured as a collection of scientific papers organized into four parts. Part one focuses on the design and experimental characterization of equipment for sCO_2 and CO_2 mixture power cycles. The comparison of different commercial technologies available today for recuperators and primary heat exchangers is carried out. Then the similarity between water and solar salt is explored to experimentally characterize the thermo-hydraulic performance of innovative heat exchanger design for primary heat exchanger applications. Finally, the equipment for sCO_2, CO_2 mixture, and steam Rankine power cycles is designed with mass, cost, and flexibility estimations performed.

Part two investigates the novel dopants proposed in this work. New CO_2 mixtures for CSP plants are proposed and evaluated through preliminary thermodynamic optimization of power cycle performance and techno-economic optimization of CSP plants. Thermal stability tests of C_3F_6 and $GeCl_4$ were carried out, showing low thermal stability limits of both fluids.

Part three evaluates the techno-economic performance of sCO_2 and CO_2 mixture power cycles in CSP plants. The use of sCO_2 and $CO_2 + SiCl_4$ mixture power cycles in Gen2 and Gen3 CSP plants is assessed for different cycle layouts, solar multiples, and thermal energy storage capacities. Additionally, off-design modeling of supercritical and transcritical simple recuperated cycles is conducted to assess the influence of air-cooled heat rejection unit design on the overall techno-economic performance of CSP plants.

Part four presents a high-temperature combined cycle configuration for CSP applications. The combined cycle consisting of the topping alkali metal cycle and bottoming sCO_2 recompression power cycle is proposed and compared with a standalone sCO_2 recompression cycle.

In summary, this thesis presents theoretical and experimental investigations of equipment, novel dopants, and the techno-economic performance of CSP plants using sCO_2 and CO_2 mixture power cycles, as well as high-temperature combined cycle configuration for CSP. The findings contribute to both industry and academia by providing a valuable basis for the design of next-generation CSP plants with sCO_2 and CO_2 mixture power cycles.

Sommario

Le energie rinnovabili hanno un ruolo centrale nella transizione verso una produzione dell'energia ad impatto zero, e l'energia solare rappresenta una delle risorse più promettenti. Gli impianti concentrazione solare (CSP) possono integrare sistemi di accumulo di energia termica a costi relativamente bassi, risultando così flessibili e consentendo una produzione di energia elettrica programmabile fino a 24 ore. Un aspetto sempre più importante dato che la quota di generazione rinnovabile non programmabile (come i sistemi fotovoltaici, che non hanno accumulo di energia o ne hanno solo a breve termine) nella rete elettrica continua a crescere.

La competitività degli impianti CSP di futura generazione può essere migliorata attraverso l'adozione di cicli di potenza a CO_2 avanzati che operano a temperature di ingresso della turbina più elevate. Considerando il funzionamento degli impianti CSP in climi caldi e aridi, è previsto che il ciclo di potenza operi in uno stato supercritico (sCO_2). Ulteriori miglioramenti delle prestazioni possono essere ottenuti utilizzando miscele a base di CO_2 con dopanti ad alta temperatura critica. Ciò consente una transizione dai cicli supercritici a quelli transcritici con compressione in fase liquida, permettendo sia una maggiore efficienza che un costo inferiore del ciclo di potenza e dell'intero impianto CSP.

La tesi è strutturata come una raccolta di articoli scientifici organizzati in quattro parti. La prima parte si concentra sulla progettazione e sulla caratterizzazione sperimentale dei componenti dei cicli di potenza a sCO_2 e a miscela di CO_2. Viene effettuato un confronto tra le diverse tecnologie commerciali attualmente disponibili per i recuperatori e gli scambiatori di calore primari. Successivamente, viene esplorata la similitudine tra acqua e sali fusi per caratterizzare sperimentalmente le prestazioni termoidrauliche di un design innovativo di scambiatore di calore per applicazioni di scambio termico ad alta temperatura. Infine, vengono progettate le apparecchiature per i cicli di potenza a sCO_2, a miscela di CO_2 e a vapore, con stime di massa, costi e flessibilità.

La seconda parte indaga i nuovi dopanti proposti in questo lavoro. Nuove miscele di CO_2 per impianti CSP vengono proposte e valutate attraverso un'ottimizzazione termodinamica preliminare delle prestazioni del ciclo di potenza e un'ottimizzazione tecnico-economica degli impianti CSP. Sono stati effettuati inoltre test di stabilità termica su C_3F_6 e $GeCl_4$, che hanno evidenziato bassi limiti di stabilità termica per entrambi i fluidi.

La terza parte valuta le prestazioni tecnico-economiche dei cicli di potenza a sCO_2 e a miscela di CO_2 negli impianti CSP. L'utilizzo di cicli di potenza a sCO_2 e a miscela di CO_2 + $SiCl_4$ negli impianti CSP di seconda e terza generazione viene valutato per diverse configurazioni di ciclo, multipli solari e capacità di accumulo di energia termica. Inoltre, viene condotta una modellazione fuori progetto di cicli a recupero semplice supercritici e transcritici per valutare l'influenza della progettazione dell'unità di dissipazione del calore raffreddata ad aria sulle prestazioni tecnico-economiche complessive degli impianti CSP.

La quarta parte presenta una configurazione di ciclo combinato ad alta temperatura per applicazioni CSP. Il ciclo combinato, costituito da un ciclo a metalli alcalini e un secondo ciclo ricompresso a sCO_2, viene proposto e confrontato con un ciclo ricompresso a sCO_2.

In sintesi, questa tesi presenta indagini teoriche e sperimentali su apparecchiature, nuovi dopanti, prestazioni tecnico-economiche di impianti CSP che utilizzano cicli di potenza a sCO_2 e a miscela di CO_2, nonché un ciclo combinato ad alta temperatura per CSP. I risultati contribuiscono sia al settore industriale che a quello accademico, fornendo una base preziosa per la progettazione di impianti CSP di prossima generazione con cicli di potenza a sCO_2 e a miscela di CO_2.

Acknowledgments

I would like to express my sincere gratitude to Professors Paolo Giulia Iora, Gioele Di Marcoberardino, and Costante Invernizzi for providing me with this opportunity, their guidance, and for their support both in research and beyond academic matters. I am also grateful to my colleagues from the ERGO research group for their assistance in research and laboratory activities, as well as outside of work.

I would like to thank the staff at Brembana&Rolle S.p.A., especially Marta Mantegazza and Marcello Garavaglia, for their valuable support and technical insights during the design and experimental investigation of heat exchangers.

My sincere thanks also go to my colleagues at the Institute of Power Plant Technology, Steam and Gas Turbines, at RWTH Aachen University, including Eylül Gedik, Nils Petersen, and Manfred Wirsum, for their collaboration and support.

Finally, I am deeply thankful to my wife, Valeriia, for her unwavering support and patience throughout these years, and to my parents, Elena and Yurii, for always believing in me.

This work was made possible thanks to the funding from the European Union under the HORIZON MSCA Doctoral Network project TOPCSP (Project number 101072537).

Contents

List of tables

List of figures

1. Introduction

Global energy consumption has increased consistently over the past decades, driven by population growth, industrialization, and rapid technological expansion. Developing countries now account for more than half of global energy use and represent the primary source of additional demand growth, reflecting both their large populations and rapid economic development trajectories [1]. Consequently, ensuring access to affordable, reliable, sustainable, and modern energy has become one of the sustainable development goals [2]. Among all energy carriers, electricity occupies a special position because it supports both essential services and advanced technologies. Specific electricity consumption is strongly correlated with GDP per capita, as shown in Figure 1.1 [3]. Therefore, access to secure, affordable, and sustainable electricity is widely considered a prerequisite for socio-economic development in the twenty-first century. As development continues, electricity demand is expected to grow disproportionately. The electrification of transport, heating, and industrial processes, together with ongoing digitalization, will continue to increase the central role of electricity in energy systems worldwide. This highlights the need for robust, efficient, and sustainable energy infrastructure, particularly in regions where access to electricity remains inconsistent or insufficient.

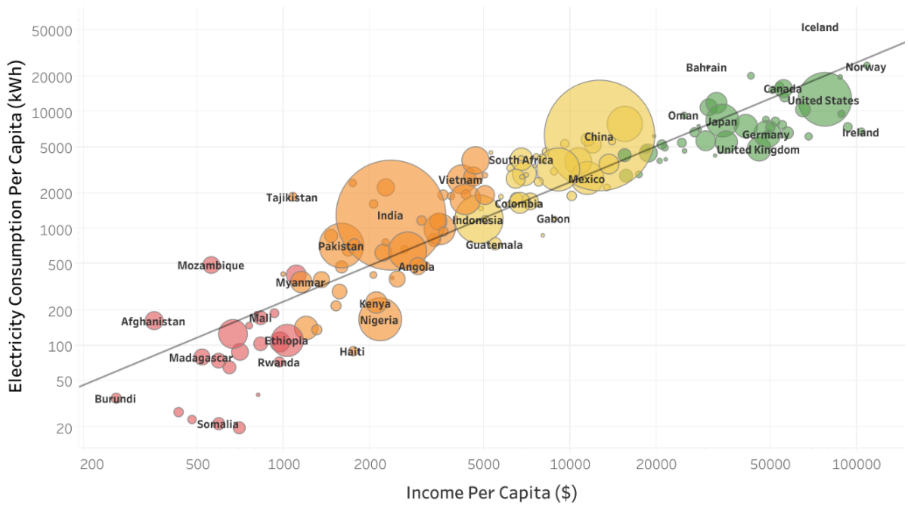

Figure 1.1. Electric energy consumption per capita vs GDP per capita in 2022 [3]. Colors correspond to income groups, while the size of each circle represents the total population.

Ensuring the affordable and sustainable electricity production means the long-term socio-economic development of societies. The EU, according to the 2050 long-term strategy [4], aims to be climate-neutral by 2050, an economy with net-zero greenhouse gas emissions [5]. As a part of this, the European Green Deal aims to cut EU emissions by at least 55% by 2030 and 90% by 2040 through different mechanisms, including but not limited to NextGenerationEU, REPowerEU, the Net-Zero Industry Act, and the EU Emissions Trading System [6]. In 2023, 44% of all EU power was generated from renewable sources, with 18% coming from wind turbines, 12% from hydropower plants, 9% from solar power, and 5% from biofuels [7]. Europe is expected to add over 630 GW of renewable energy capacity between 2025 and 2030 (67% increase), with 70% of it made up equally by utility and distributed photovoltaic solar systems (PV) [8]. Therefore, solar power is projected to be a significant source of electricity in the following decades.

Solar power plants are represented by two main technologies: photovoltaic (PV) and concentrated solar power (CSP). Both technologies could be used to produce electricity and heat. The PV solar plants are based on the photovoltaic effect, where solar energy is directly converted into electricity using semiconducting material. The CSP plants use mirrors to concentrate solar light and achieve high temperatures, which are then used by thermodynamic power cycles to generate electricity. Since they rely on mirrors, the main parameter describing resource availability for CSP plants is the solar radiation received by a surface perpendicular to the sun rays, known as direct normal irradiance (DNI). Figure 1.2 illustrates its global distribution [9]. One can see that Spain, the south of France, Italy, and Greece have the most irradiation in Europe, with higher values to be found on the west coast of the USA, Chile, the Arabian Peninsula, the north and south of Africa, and in Australia.

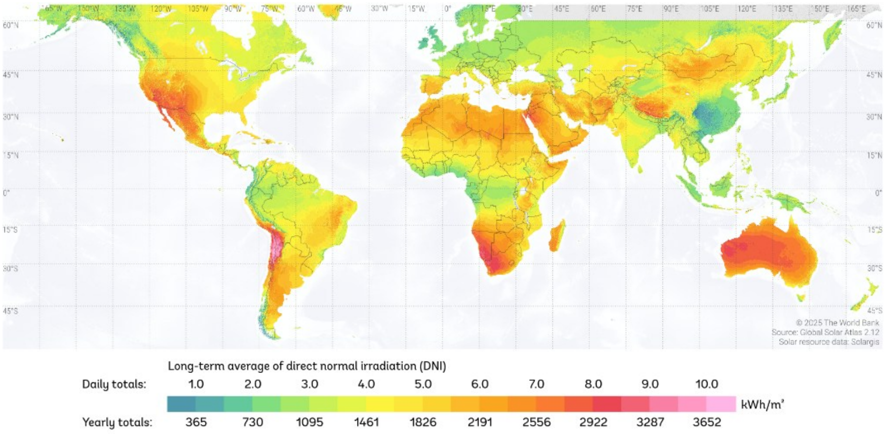

Figure 1.2. Direct normal irradiation in the world [9]

The levelized cost of electricity (LCOE) from CSP plants is steadily decreasing, as can be seen in Figure 1.3; however, it is still one of the most expensive renewable electricity sources. The vast majority of the new 582 GW of renewable capacity added in 2024 in the world is represented by PV (77.8%) and wind plants (19.6%), which have an LCOE of around 30-50 USD/MWh [10]. But in the same year, battery energy storage systems (BESS) installed capacity increased only by 169 GWh, leaving most of the PV plants without storage. This limits their electricity production to daytime and makes their output highly dependent on the radiation available. The LCOE of solar PV plants with up to 4 hours of BESS is higher and varies between 50 USD/MWh and 150 USD/MWh [10]. On the other hand, CSP plants, equipped with 8-16 hours of low-cost thermal energy storage (TES) [10], have LCOE in the same range, and could be used for energy grid balancing and frequency control using the inertia of rotating turbomachinery [11].

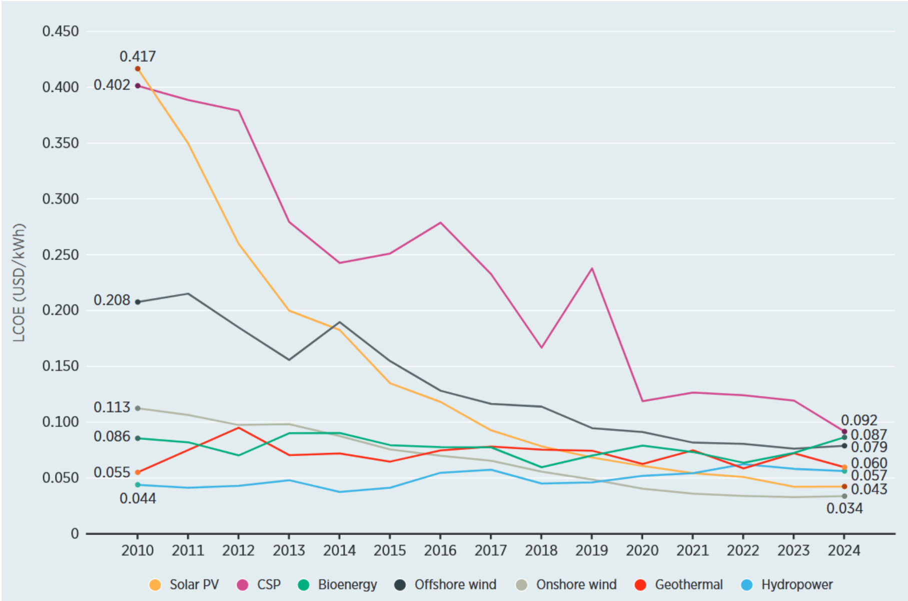

Figure 1.3. Renewable energy LCOE decline, 2010-2024 [10]

The increasing amount of PV installations with short-duration or no battery storage at all leads to the drastic change in the energy grid demand profile, which was nicknamed the "duck curve" [12]. Such a curve for California is shown in Figure 1.4 [13], with similar curves already present in Australia and in Europe in Greece, Germany, Spain, and Serbia [14]. With the curve being more pronounced as time goes on and solar PV penetration grows, the amount of curtailment in PV plants will continue to increase. This raises the need for additional sources of power system flexibility to accommodate fast ramp-down and ramp-up rates by having more flexible fossil fuel plants and energy storage. Therefore, the applicability of LCOE for comparison of renewable energy generation technologies in real-world operation is limited. For example, the net present value of PV with BESS and CSP plants can be comparable, even though the LCOE is significantly lower for PV [15].

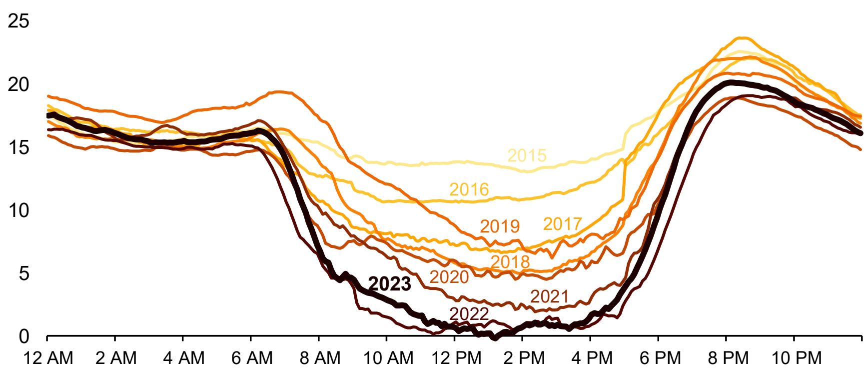

Figure 1.4. California's lowest net load day each spring [13]

Another option is to adjust the levelized cost of electricity, considering the variability of renewable energy resources. In 2013 the US Energy Information Administration (EIA) introduced the levelized avoided cost of electricity (LACE), which shows "potential revenue available to the project owner from the sale of energy and generating capacity" [16,17]. The ratio of LACE and LCOE above one means the project is considered economically feasible. Another prominent indicator is value-adjusted LCOE (VALCOE), proposed in 2018 by the International Energy Agency (IEA) [18]. It is equal to LCOE adjusted for energy, capacity, and flexibility values of technology compared to the average system values in the region. It is closely similar to System LCOE [19], which includes the costs on a system level due to the technology variability. Another indicator is the actual cost of electricity (ACOE) proposed by Manzolini et al. [20], which takes into account the renewable energy source penetration into the grid. Based on their research, with higher solar penetration, PV plants with bigger BESS become more attractive, reaching 2 hours of storage at penetration above 50%. At the same time, CSP plants have lower ACOE at penetration above 40%.

1.1. CSP plants

The main types of CSP technologies are parabolic troughs, linear Fresnel reflectors, parabolic dishes, and solar towers (Figure 1.5) [21]. Parabolic trough systems are made of curved rows of mirrors more than 100 m long with evacuated glass stainless steel pipes and a special light-absorbing coating. Synthetic oil is used to transfer heat from steel tubes to the superheated steam cycle to produce electricity. It is the most mature and widespread technology (73% of all operating CSP plants capacity). However, there is little or no use of thermal storage currently, and they often use combustible fuel as a backup to firm capacity [21]. New parabolic trough plants are usually built with thermal energy storage using molten salts [10]. Linear Fresnel reflectors are similar to parabolic in principle but use rows of flat mirrors to approximate a parabolic shape. They can be used for direct generation of steam but are less efficient and harder to use with energy storage.

Solar towers use hundreds and thousands of heliostats (sun-tracking mirrors) to concentrate light on the central receiver in the tower. In the receiver, water or heat transfer fluid (HTF) is heated with heat used in the power cycle. Beam-down tower technology is similar in working principle, but instead of putting the receiver on the tower, a hyperbolic mirror focuses all light on the concentrator with the receiver located on the ground. Due to higher solar concentration, both high temperatures in the receiver and higher electric efficiencies can be achieved. The technology is very flexible since one can choose from different types of heliostats, receivers, HTFs, heat storage systems, and power cycles. Solar towers make up 22% of the operational installed capacity of CSP systems [22].

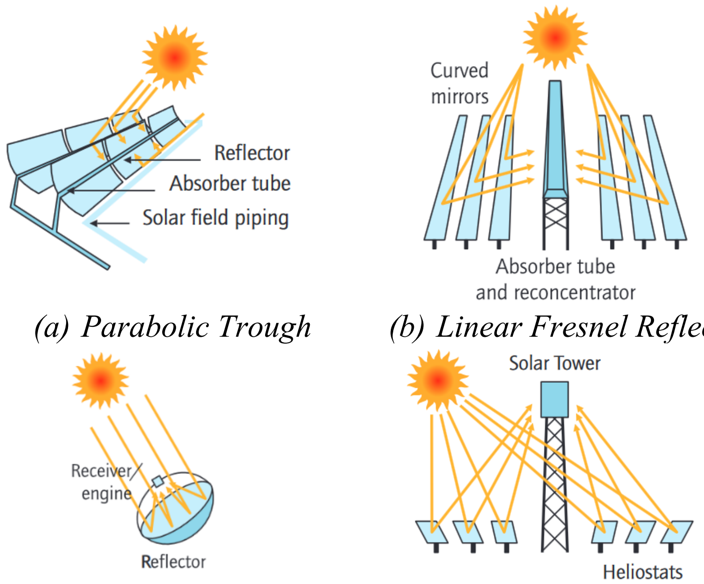

(a) Parabolic Trough *(b) Linear Fresnel Reflectors*

(c) Parabolic dishes *(d) Solar towers*

Figure 1.5. Concentrated solar power technologies [21]

Around 30% of installed CSP plants capacity has above 7 hours of storage [22]. One can see that the capacity factor is more influenced by storage than by DNI (Figure 1.6), and newer plants usually have a bigger capacity and storage [10]. This allows to improve not only the flexibility of power production but also the economics by increasing the capacity factor and bringing down the LCOE [23]. In the 10+ hours storage category, most of the CSP plants are of the solar tower type.

Figure 1.6. Capacity factor trends for CSP plants, 2010-2024 [10]

Most CSP plants under construction by 2023 were equipped with at least 6 hours of TES (Table 1.1) [22]. Most new large-scale CSP projects use a central receiver tower with molten salt storage (Figure 1.7a) [24]. For new tower designs, the standard installed capacity is 100 MW, while heat storage is 8-16 hours, making them very flexible throughout the day. The state-of-the-art second generation (Gen2) solar tower CSP plants (Figure 1.7a) use solar salt (60 wt% $NaNO_3$ + 40%wt KNO_3) as a HTF and for TES. The Gen2 CSP plants have receiver outlet temperatures up to 565°C and use subcritical steam Rankine power cycles with reheat for electricity generation.

The next third generation (Gen3) of CSP plants is planned to reach temperatures above 700°C and generate electricity using CO_2 Brayton cycles [25]. One of the ways to classify the Gen CSP plants is by the type of HTF used: liquid, particle, and gas [26]. The Gen3 CSP plants with molten salt, sodium, and particle heat transfer fluids are shown in Figure 1.7b, Figure 1.7c, and Figure 1.7d respectively.

Liquid Gen3 CSP plants consider using advanced high-temperature chloride or carbonate salts for TES and either salt (Figure 1.7b) or liquid metal as HTF in the receiver [27]. The sodium receiver coupled with the chloride salt storage (Figure 1.7c) was chosen as more efficient and having a lower LCOE with only slightly higher risk in the US Department of Energy (DOE) SunShot program by NREL, EPRI, and ANU [28]. Sodium receiver development began in the 1970s and continued throughout the 80s, with the main testing grounds being the "Plataforma Solar" in Almeria, Spain, and the Sandia Central Receiver Test Facility (CRTF) in Albuquerque, New Mexico [29]. At the first facility, a receiver designed by Interatom (Germany) and manufactured by Sulzer (Switzerland), as well as a receiver developed by Franco Tosi Industriale and AGIP SpA (Italy), were tested. At the CRTF at Sandia, a receiver manufactured by Rockwell International (USA) was tested. Research on sodium receivers has continued in the USA [30,31] and Australia [32,33], with the Vast Renewables Limited receiver tower being close to commercial application [34].

Another advanced solution is the adoption of particle based receivers (Figure 1.7d), among which the most developed are free-falling, rotating kiln, and fluidized bed particle receivers [35]. These designs are actively being developed and tested in the USA (G3P3) [36], Germany [37], France [38], and Australia [39], where a spin-off company, FPR Energy, has also been established to further develop and implement falling particle receiver technology [40].

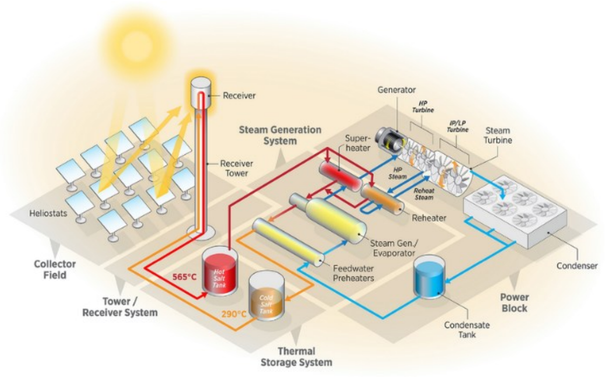

(e)

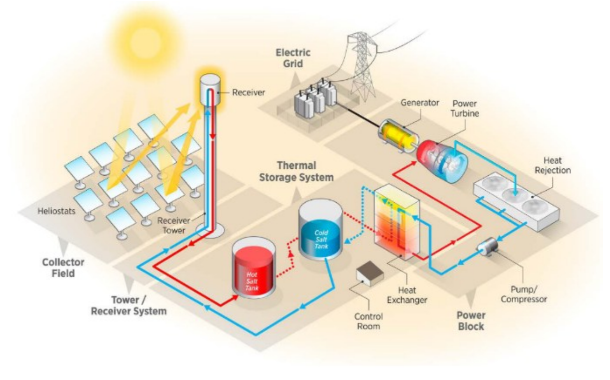

(f)

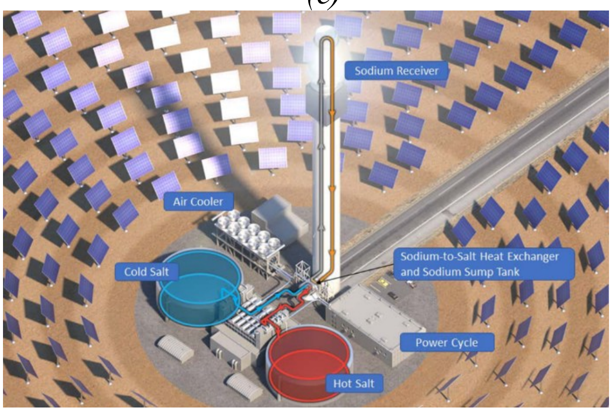

(g)

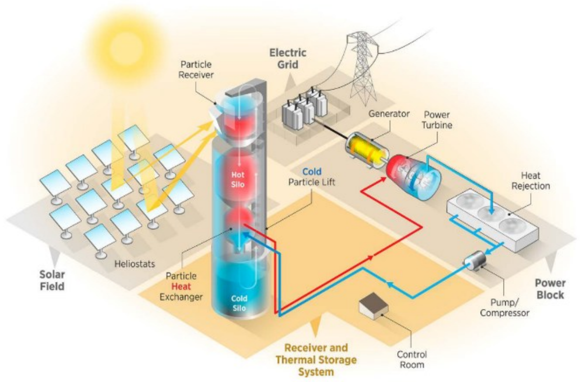

(h)

Figure 1.7. CSP tower plants designs: molten salt used as HTF and heat storage and steam Rankine cycle (a), high temperature salt with sCO_2 cycle (b), sodium as HTF with salt TES and sCO_2 cycle (c), and particles as HTF and TES and sCO_2 cycle (d) [26,30].

Table 1.1. CSP plants under construction in 2023 [22]

Power station	**Capacity, MWe**	**Type**	**DNI, kWh/m²/year**	**HTF and TES**	**Storage, hours**	**Power cycle**	**Country**	**Construction - operation**
ISCC Green Duba 1	43	Trough	2469	Thermal Oil	-	Steam Rankine	Saudi Arabia	2016 - 2023
Noor Energy 1 / DEWA IV	600	Trough	1967	HTF: Biphenyl/Diphenyl oxide (Dowtherm A) TES: Molten salt	11	Steam Rankine	UAE	2018 - 2023
CSP-PV hybrid project Noor Energy 1 / DEWA IV	-	Trough, Tower	1967	-	-	-	UAE	2018 - 2023
Jinta Zhongguang Solar	100	Tower	1550	Molten Salt	9	Steam Rankine	China	2022 - 2023
Redstone	100	Tower	-	Molten Salt	12	-	South Africa	2021 - 2023
CEIC Dunhuang	100	Fresnel	1649	Molten Salt	-	-	China	2021 - 2024
Huidong New Energy Akesai	110	Tower	-	Molten Salt	8	Steam Rankine	China	2022 - 2023
CSP2 SOLINPAR Sicily Stromboli MS-LFR	4	Fresnel	1800	Molten Salt	16	-	Italy	2020 - 2021
Three Gorges CTGR Henderson Energy Guazhou	100	Tower	1683	Molten Salt	-	Steam Rankine	China	2022 - 2024
CNNC Yumen	100	Fresnel	1641	Molten Salt	8	-	China	2022 - 2023
Power China Toksun	100	Tower	-	Molten Salt	12	-	China	2023 - 2025
Power China Ruoqiang	100	Tower	1767	Molten Salt	8	-	China	2022 - 2024
SIDC Ruoqiang	100	Tower	1767	Molten Salt	8	-	China	2023 - 2025
CTGR Qinghai Golmud	100	Tower	1713	Molten Salt	-	-	China	2023 - 2024
CSP3 BILANCIA Sicily MS-LFR	4	Fresnel	1737	Molten Salt	16	-	Italy	2022 -
CTGR Qinghai Quingyu DC	100	Tower	1723	Molten Salt	-	-	China	2023 - 2024
Generation 3 Particle Pilot Plant Sandia (G3P3)	1	Tower	-	Particle	6	sCO_2 Brayton	USA	2022 - 2025
Generation 3 Particle Pilot Plant Saudi	2	Tower	2592	White Sand	6	Air Brayton	Saudi Arabia	2023 - 2026

1.2. Power cycles

The main pathway to further improve the efficiency of CSP plants is to increase the maximum temperature in the receiver, raising the power cycle turbine inlet temperatures (TIT) and cycle thermal efficiency. Currently, most systems use solar salt as a HTF and a steam Rankine cycle for power generation, with TIT up to 560°C. Nevertheless, significantly higher temperatures are achievable, reaching more than 1000°C for falling particle receiver [35] and 1300°C in the graphite receiver using tin as the HTF [41]. This means that power cycles can utilize significantly higher TIT. Such high temperatures are currently present only in open gas turbine combustion cycles that use air as a working fluid. The indirect heating in combined cycles with an open air Brayton topping cycle and a bottoming Rankine cycle leads to efficiencies of around 45% for a 700°C maximum temperature [42], 46% at 1050°C, and up to 50.7% at 1250°C TIT [43]. Closed gas cycles, such as the helium Brayton one, have around 40% efficiency at 800°C maximum temperature [43]. However, those efficiencies are close to the existing state-of-the-art steam Rankine cycles with the TIT of only 600°C. The expensive materials needed to withstand high-temperature corrosion and creep limit the further increase in maximum temperature using the steam Rankine cycles [44,45].

One of the approaches is to go toward alternative working fluids, which could allow an increase in turbine inlet temperature or higher efficiencies at similar temperatures by having lower pressures and less corrosion activity. Combined cycles using gas or metal in the topping high-temperature cycle with the more traditional low-temperature bottoming cycle have been widely investigated in the literature [43,46]. A solution using alkali metals in the topping and CO_2 in the bottoming recompression cycle is proposed in Chapter 9 with layout shown in Figure 1.8a and T-s diagram in Figure 1.8c.

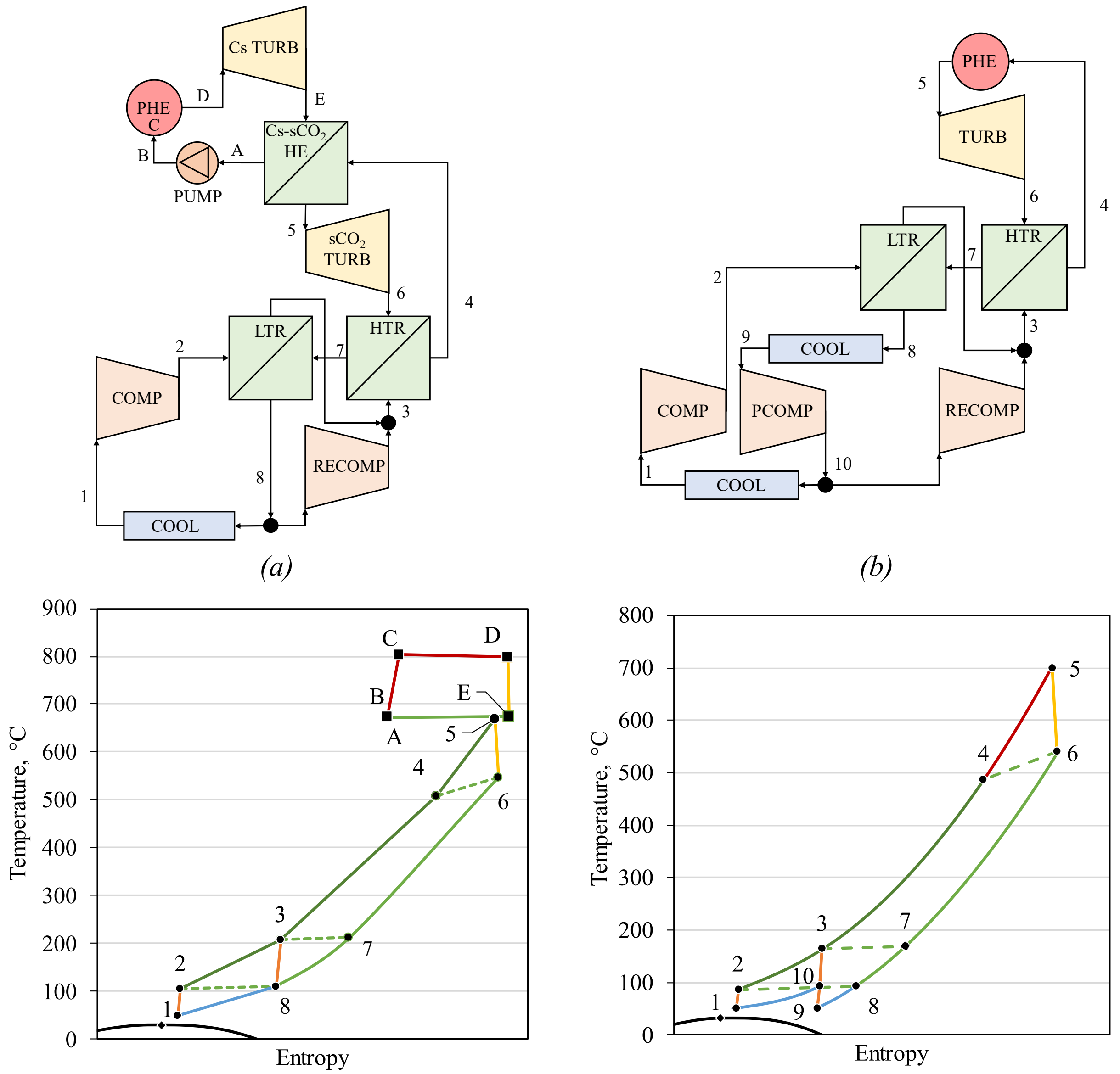

(c) *(d)*

Figure 1.8. Layout and T-s diagram of combined (a, c) and partial cooling (b, d), cycles, with the CO_2 saturation dome shown by a black line and the critical point indicated by a diamond marker. PHE – primary heat exchanger; TURB – turbine; HE – heat exchanger; HTR – high-temperature recuperator; LTR – low-temperature recuperator; COMP – compressor; RECOMP – recompressing compressor; PCOMP – partial cooling compressor; COOL – air-cooled cooler.

Alternative way forward are closed supercritical CO_2 cycles, which offer the efficiency advantage over both the steam Rankine and helium cycles at TIT above 600°C and can reach more than 50% efficiency at 700°C TIT [47]. Different CO_2 cycle layouts have been extensively studied since the 60s, including simple recuperated, recompression, partial cooling, partial cooling with improved regeneration, precompression, and others [48–51]. Most of the Gen3 CSP projects consider using a simple recuperated, recompression, or partial cooling layout. The simple recuperated cycle is the least expensive and efficient one, whereas the recompression cycle shown is the most efficient and costly, with partial cooling cycle (layout shown in Figure 1.8b with T-s diagram in Figure 1.8d) balancing the two aspects [30,36,52,53].

The sCO_2 cycles have been widely experimentally investigated, with commercial plants available up to 7.5 MWe at 450°C TIT [54] from Echogen Power Systems [55] and a new experimental loops focusing on higher power and TIT. The most advanced experimental sCO_2 cycle realized to date is the 10 MWe Supercritical Transformational Electric Power (STEP) Demo pilot plant. It was completed in 2023 at the Southwest Research Institute in San Antonio, Texas, USA [56]. In 2024 it operated in the simple layout at 500°C TIT with 4 MWe synchronized power and is planned to reach 715°C TIT and 10 MWe in recompression mode in the near future [57].

The efficiency of closed sCO_2 cycles can be further improved by using dopants. One can adjust the critical temperature of the CO_2 mixture by changing the amount of dopant to reach the desired value. That way, for low minimum cycle temperatures, the compressor inlet can be kept close to the critical point to reduce the compression work required. Alternatively, by using dopants with high critical parameters, the cycle minimum temperature can be shifted to subcritical conditions. This enables transition from supercritical to transcritical cycle, with compression happening in the liquid phase. As a result, the required compression work is significantly reduced, as shown in Figure 1.9, leading to an increase in cycle efficiency. Other advantages include lower power cycle cost and HTF minimum temperature, reducing the cost of TES.

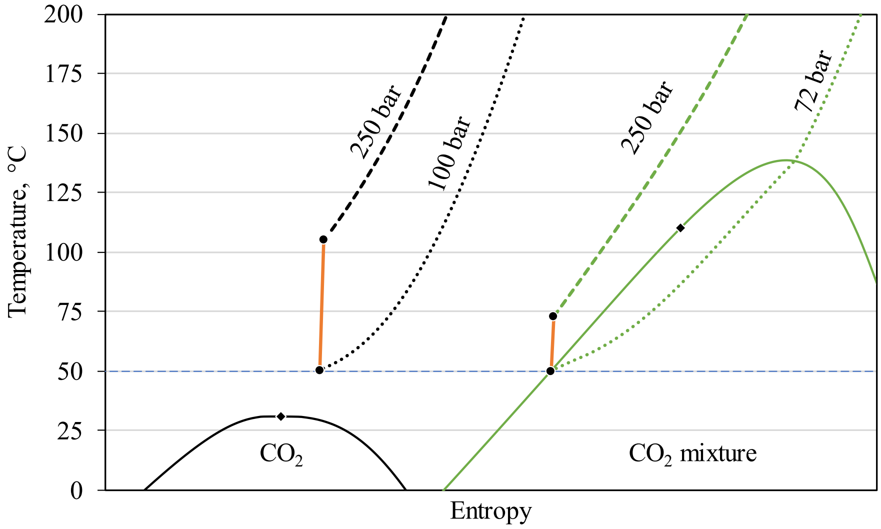

Figure 1.9. The comparison of compression in sCO_2 and CO_2 mixture cycles

1.3. Working fluids

The selection of a dopant is a crucial step, as it defines not only the thermophysical properties of the resulting CO_2 mixture, but also its maximum operating temperature, compatibility with equipment materials, and environmental characteristics, among other factors. Therefore, the ideal dopant for application in tower CPS plants should satisfy a set of key requirements:

1. It must have a high critical temperature (preferably above 100°C) and low melting point to ensure reliable operation at all ambient temperatures in the location.
2. It must have high thermal stability.
3. It must be soluble in CO_2.
4. It must exhibit low chemical reactivity and high compatibility with materials used in power cycle equipment.
5. It must have low toxicity and flammability.
6. It should have low global warming potential (GWP), and ozone depletion potential (ODP).
7. It should have high molecular complexity in order to reduce heat capacity differences in the recuperators.

Various dopants have been extensively investigated in the literature for application in CO_2 mixture transcritical cycles. The CO_2 mixture cycles efficiency gains compared to pure sCO_2 cycles have been widely reported. For example, a simple recuperated cycle can achieve 46.7% thermal efficiency with N_2O_4 and 51% with $TiCl_4$ dopant, a precompression cycle using C_6F_6 can reach 50.3%, and recompression can attain 50.1% with $SiCl_4$ and 50.8% with SO_2 at 700°C TIT (recompression sCO_2 cycle has 48.7-48.8% thermal efficiency) [58–62]. However, the number of dopants that have proven to be thermally stable even up to 550°C is very limited: C_6F_6, $TiCl_4$, SO_2, and $SiCl_4$. The N_2O_4 reversibly decomposes at high temperatures and is strongly corrosive and toxic. The previously investigated NH_3 and COS [63] decompose at high temperatures and are toxic [64–68], while potentially thermally stable H_2S [63] is too corrosive and toxic. The C_6F_6 proved to be stable only up to 600°C, making it useful only for Gen2 CSP plants. Another downside is that fluorocarbon dopants and fluorinated compounds react with stainless steel in the CO_2 mixture already at 500°C [69] and even form long cracks along the welding heat-affected zone when Inconel alloys are used [70]. The pure dopant fluid is expected to be even more reactive, with titanium and silicon being the catalysts [71]. In the case of SO_2, there are material compatibility issues due to high corrosion activity, which will require specific alloys development, while thermal stability is expected to be high but has not been proven yet. The $TiCl_4$ has proven to be thermally stable up to at least 500°C [72], but is highly reactive, easily hydrolyzes with water, and has a history of failed tests because of that [73]. The $SiCl_4$ dopant was tested at 650°C with no degradation after prolonged contact with common stainless steel AISI 316L [74] and could be thermally stable up to 900°C [75]. It is much less reactive than $TiCl_4$ and has CO_2+$SiCl_4$ mixture vapor-liquid equilibrium (VLE) data available for the power cycle characterization [62]. The parameters of dopants considered in literature are shown in Table 1.2, thermodynamic parameters were obtained from NIST TDE (version 104.3 with database version 10.17) [76] in Aspen V14 [77], while the remaining parameters were collected from the references cited in this section (all dopants have CO_2 mixture data).

Table 1.2. Dopants for CO_2 mixture power cycles considered in literature

Formula	CAS	T_{melt}, °C	T_{boil}, °C	T_{cr}, °C	P_{cr}, bar	Safety data (NFPA 704)			GWP	ODP	T_{limit}, °C
						Health	Flammability	Reactivity			
$SiCl_4$	10026-04-7	-69	58	234	35.9	3	0	2-w	0	0	>650
$TiCl_4$	7550-45-0	-23	136	366	39.3	3	0	2-w	0	0	>500
C_6F_6	3922-56-3	5	80	243	32.8	0	3	0	7	0	<600
SO_2	7446-09-5	-75	-10	157	78.2	3	0	0	-40	0	-
N_2O_4	10544-72-6	-11	-	158	105	3	0	0	273	0	130
NH_3	7664-41-7	-78	167	132	113.6	3	1	0	0	0	450-500
COS	463-58-1	-139	-50	106	63.5	3	4	0	27	0	<500
H_2S	7783-06-4	-86	-60	100	85.0	4	4	0	0	0	-

T_{melt} – melting point; T_{boil} – normal boiling point; T_{cr} – critical temperature; P_{cr} – critical pressure, bar, T_{limit} – maximum operating temperature.

Based on literature data, promising candidates can be found in the groups of perfluorocarbons, sulfur compounds, and metal halides. A review of CO_2 dopants was carried out based on critical parameters, health, flammability and reactivity characteristics, GWP, and ODP, identifying the most promising ones for CSP application: C_3F_6, $SiCl_4$, $GeCl_4$, Cl_3FSi, and $SiBr_4$. The parameters of selected dopants obtained from NIST TDE are shown in Table 1.3. The $SiCl_4$ dopant has a lot of experimental data available, including thermal stability, thermodynamic properties in CO_2 mixture, and transport properties [62,74]. Therefore, $SiCl_4$+CO_2 mixture cycles were investigated in Chapters 2, 4, 7, and 8 for application in CSP plants. The $GeCl_4$ and Cl_3FSi mixture power cycles preliminary performances in CSP plants were investigated in Chapter 5. The $SiBr_4$ and Cl_3FSi have been considered to be too harmful for experimental characterization, while C_3F_6 and $GeCl_4$ have been ordered and experimentally tested in the laboratory. The results of C_3F_6 and $GeCl_4$ thermal stability testing are presented in Chapter 6, with the corresponding thermal stability limits obtained summarized in Table 1.3.

Table 1.3. Promising dopants for CSP plants CO_2 mixture power cycles

Formula	CAS	T_{melt}, °C	T_{boil}, °C	T_{cr}, °C	P_{cr}, bar	Safety data			GWP	ODP	CO_2 mixture data	T_{limit}, °C
						H	F	R				
$SiBr_4$	7789-66-4	5	153	383	-	3	0	2-w	0	0	no	-
C_3F_6	116-15-4	49	56	95	29	2	0	0	17340	0	yes	<400
$SiCl_4$	10026-04-7	-69	58	234	35.9	3	0	2-w	0	0	yes	>650 in 316L
$GeCl_4$	10038-98-9	-51	83	280	38.6	3	0	2-w	-	-	no	<450
Cl_3FSi	14965-52-7	-	10	165	35.7	3	0	2	-	-	no	-

NFPA 704: H – health hazard; F – flammability hazard; R – instability/reactivity hazard.

To model both pure fluids and mixtures thermodynamic properties, various equations of state (EoS) can be used. Four main types of EoS commonly used for thermodynamic calculations are:

- Cubic EoS based on the van der Waals EoS.
- Virial EoS.
- EoS based on statistical association fluid theory (SAFT).
- Multiparameter EoS based on Helmholtz free energy.

Cubic equations are simple models with limited parameters determined mainly by critical point and vapor pressure curve with limited accuracy and applicability for the liquid state. They include Riedlich-Kwong (RK) [78], Soave-Riedlich-Kwong (SRK) [79], Peng-Robinson (PR) [80], and many others with different alpha functions, volume corrections, mixing rules, etc. Virial EoS models are more complex and can better predict both gas and liquid properties but require fitting of multiple parameters and are represented by Lee-Kesler-Plöcker [81] and Benedict-Webb-Rubin [82], among others. Equations of state based on the SAFT can account for different interactions (hard chain, dispersion, association, polar interactions, and ions) and use parameters with physical meaning. These EoS usually have better accuracy than cubic EoS, but have to be fitted to experimental data. Many variations of SAFT EoS exist based on the included intermolecular interactions and the way they are described, with the most prominent being the Perturbed-Chain SAFT (PC-SAFT) [83]. At the same time, cubic EoS can be combined with SAFT, with one of the examples being the cubic-plus-association (CPA) EoS [84]. The multiparameter EoS expressed in Helmholtz free energy are complex models with tens of parameters fitted to experimental data and can predict very accurately both gas and liquid properties, but they require much more computational power than the rest of the EoS. The examples are Span&Wagner EoS for CO_2 [85], GERG-2008 by Kunz and Wagner for natural gas mixtures [86], IAPWS-95 [87], and the computationally much lighter and slightly less accurate IAPWS-97 [88] for water thermodynamic properties. The application of PR EoS for modelling a CO_2 mixture is presented in Chapter 6, while Chapter 9 provides a comparison of SRK and PC-SAFT EoS for modelling the thermodynamic properties pure alkali metals.

1.4. Research methodology

Current research on the use of CO_2 mixtures in CSP plants has often been limited to dopants with low thermal stability, high toxicity or corrosivity. Moreover, most studies have focused primarily on optimizing power cycle efficiency. However, the literature [53,61,89] indicates a trade-off between cycle efficiency and the costs of both the power cycle and the overall CSP plant. Only limited work has addressed the design of air-cooled heat rejection unit and its influence on sCO_2 cycle CSP plant techno-economic performance , and no comparable analysis has been reported for CO_2 mixtures. Another important gap is the limited research comparing the steam Rankine, sCO_2 and CO_2 mixture cycles costs and equipment characteristics. This is particularly important for heat exchangers, which account for a significant share of sCO_2 and CO_2 mixture power cycle costs.

The main objective of this thesis is to assess both efficiency and the cost of CO_2 mixture power cycles and whole CSP plants employing them. The second objective is to investigate, experimentally and numerically, novel CO_2 dopants suitable for CSP plant application. The overarching research framework, shown in Figure 1.10, combines both theoretical and experimental activities. First, promising dopants (either novel or already investigated in literature) are identified, followed by preliminary modeling of the power cycle and identification of optimum molar fraction. Next, for each dopant thermal stability limit and CO_2 mixture properties are assessed to ensure stable operation at the maximum temperature of the power cycle and enable accurate thermodynamic modeling, respectively. Dopants lacking thermal stability data are experimentally tested in the Fluid Testing Laboratory of the University of Brescia to determine their thermal stability limit. For dopants with limited data on CO_2 mixture behaviour but with sufficient thermal stability the vapor-liquid equilibrium tests are carried out at the composition of interest. The resulting binary VLE data is then used together with literature data to calibrate the EoS. The calibrated EoS is utilized to accurately model the power cycle and calculate its techno-economic parameters. At this stage, power cycle equipment is designed to assess the mass and cost of individual components, as presented in Chapters 2 and 4. This work is further supported by the experimental characterization of novel primary heat exchanger design, described in Chapter 3. The power cycle parameters then are supplied to the CSP plant model to calculate the plant techno-economic parameters, such as the electricity output, total plant cost, and LCOE. The EoS calibration was carried out in Aspen Plus [77], while power cycle modeling was done in Aspen Plus and MATLAB [90].

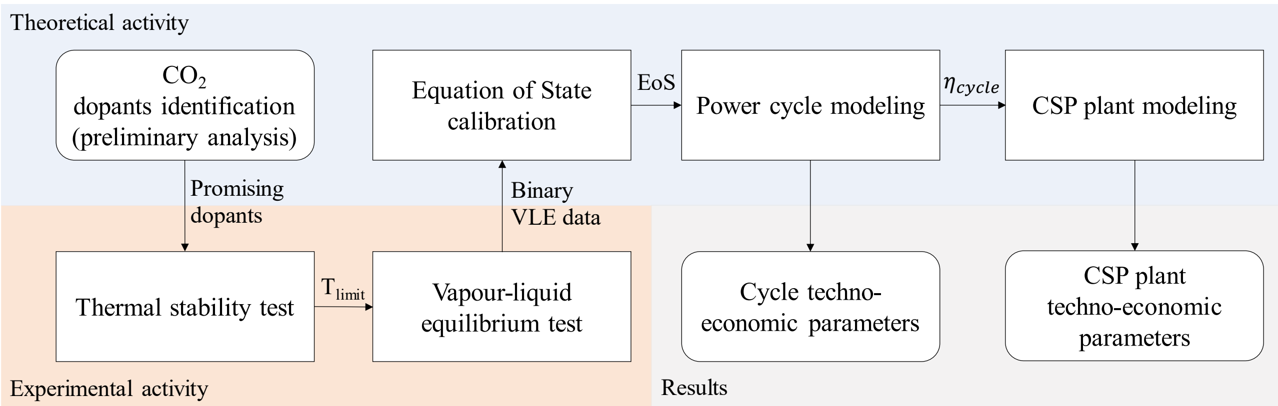

Figure 1.10. The overall research framework

The CSP plant model was implemented in Python with multiple models employed for different parts of the plant. The solar field was modeled using the SolarPILOT [91] through the Python-based CoPylot API [92]. The cylindrical external receiver model from Open_CSPERB [32,93] was used and supplemented with pressure drop calculation. Additionally, a thermal energy storage model with a control strategy and a power cycle model were implemented. The CSP plant model and its components are discussed in greater detail in Chapters 5, 7, and 8. The general CSP plant calculation process is shown in Figure 1.11 and consists of the following steps:

1. Treatment of typical meteorological year data specific to location to determine DNI and temperature profiles for design point calculation and hourly sun azimuth and elevation angles for annual modeling.
2. Solar field design, followed by the calculation of the receiver flux map and solar field optical efficiency map.
3. Receiver design with calculation of the off-design receiver efficiency and HTF pump maps.
4. Thermal energy storage design.
5. Power cycle design and off-design efficiency calculation.

6. Annual off-design hourly calculation of the solar field, receiver, TES using the simple control strategy, and power cycle performance to determine the annual amount of electricity produced and capacity factor.
7. Economic evaluation to determine the total capital cost and LCOE.

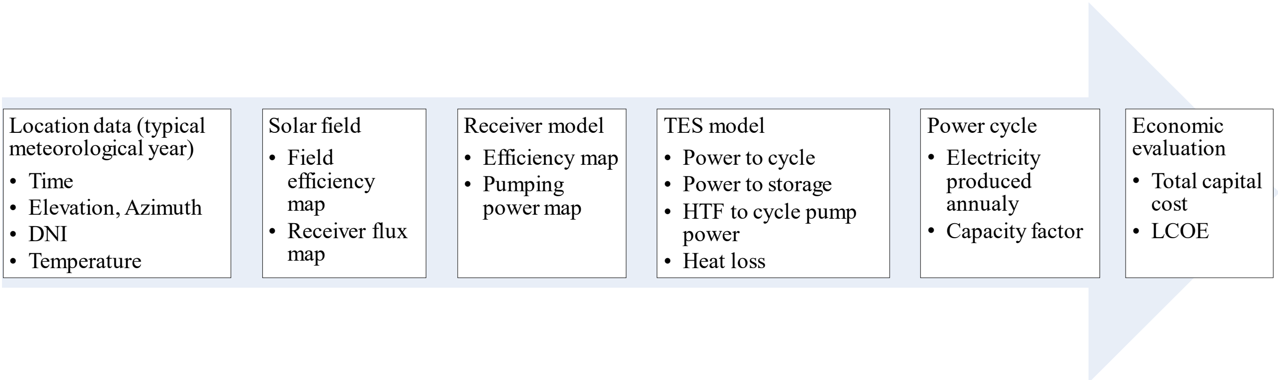

Figure 1.11. The CSP plant model calculation process

The limitations of this approach stem from the uncertainties associated with each step. Starting from the uncertainty related to the experimental activities focused on the identification of thermodynamic and transport properties from a limited amount of available information and finishing with the uncertainties in components efficiencies, cost correlations, and typical meteorological year data. However, reducing each of these uncertainties would require a dedicated capital-intensive study. Therefore, this thesis attempts to characterize the cost of the primary heat exchanger in these cycles, while the remaining uncertainties are considered outside the scope of this thesis.

1.5. Bibliography

[1] Developing countries to use 25% more energy. ExxonMobil n.d. https://corporate.exxonmobil.com/publications/global-outlook/developing-countries-use-25-percent-more-energy (accessed February 26, 2026).
[2] Goal 7 | Department of Economic and Social Affairs n.d. https://sdgs.un.org/goals/goal7 (accessed December 3, 2025).
[3] Consumption vs GDP (Updated Sept 2024) | Tableau Public n.d. https://public.tableau.com/app/profile/energyforgrowthhub/viz/final_ConsumptionvsGDP/Sheet1 (accessed December 3, 2025).
[4] 2050 long-term strategy - Climate Action - European Commission n.d. https://climate.ec.europa.eu/eu-action/climate-strategies-targets/2050-long-term-strategy_en (accessed December 3, 2025).
[5] European Commission. Directorate General for Climate Action. Going climate-neutral by 2050: a strategic long term vision for a prosperous, modern, competitive and climate neutral EU economy. LU: Publications Office; 2019.
[6] The European Green Deal - European Commission n.d. https://commission.europa.eu/strategy-and-policy/priorities-2019-2024/european-green-deal_en (accessed December 3, 2025).
[7] European Commission. Eurostat. Shedding light on energy in Europe. LU: Publications Office; 2025.
[8] IEA. Renewables 2025. Paris, France: International Energy Agency; 2025.
[9] Global Solar Atlas n.d. https://globalsolaratlas.info/download/world (accessed December 3, 2025).
[10] IRENA. Renewable power generation costs in 2024. Abu Dhabi, United Arab Emirates: International Renewable Energy Agency; 2025.
[11] Denholm P, Mai T, Kenyon R, Kroposki B, O'Malley M. Inertia and the Power Grid: A Guide Without the Spin. 2020. https://doi.org/10.2172/1659820.
[12] Denholm P, O'Connell M, Brinkman G, Jorgenson J. Overgeneration from Solar Energy in California. A Field Guide to the Duck Chart. 2015. https://doi.org/10.2172/1226167.
[13] As solar capacity grows, duck curves are getting deeper in California - U.S. Energy Information Administration (EIA) n.d. https://www.eia.gov/todayinenergy/detail.php?id=56880 (accessed December 3, 2025).

[14] Jomaux J. The Emergence of Duck Curves in Europe. GEM Energy Analytics 2024. https://gemenergyanalytics.substack.com/p/the-emergence-of-duck-curves-in-europe (accessed December 3, 2025).
[15] Manzolini G, Gentile G, Pilotti L, Martelli E, Picotti G, Binotti M, et al. Limitations of using LCOE as economic indicator for solar power plants. Renewable and Sustainable Energy Reviews 2025;209:115087. https://doi.org/10.1016/j.rser.2024.115087.
[16] Levelized Cost of Electricity and Levelized Avoided Cost of Electricity Methodology Supplement. EIA; 2013.
[17] EIA. Assessing the Economic Value of New Utility - Scale Electricity Generation Projects. EIA; 2013.
[18] IEA. World Energy Outlook 2018. Paris, France: International Energy Agency; 2018.
[19] Ueckerdt F, Hirth L, Luderer G, Edenhofer O. System LCOE: What are the costs of variable renewables? Energy 2013;63:61–75. https://doi.org/10.1016/j.energy.2013.10.072.
[20] Manzolini G, Binotti M, Gentile G, Picotti G, Pilotti L, Cholette ME. Actual cost of electricity: An economic index to overcome levelized cost of electricity limits. iScience 2024;27:109897. https://doi.org/10.1016/j.isci.2024.109897.
[21] IEA. Technology Roadmap - Solar Thermal Electricity 2014. Paris, France: International Energy Agency; 2014.
[22] Thonig R, Gilmanova A, Lilliestam J. CSP.guru 2023-07-01 2023. https://doi.org/10.5281/zenodo.8191855.
[23] Murphy C, Sun Y, Cole WJ, Maclaurin GJ, Mehos MS, Turchi CS. The Potential Role of Concentrating Solar Power within the Context of DOE's 2030 Solar Cost Targets. Golden, USA: NREL; 2019. https://doi.org/10.2172/1491726.
[24] Renewables 2020. Paris, France: IEA; 2020.
[25] He Y-L, Qiu Y, Wang K, Yuan F, Wang W-Q, Li M-J, et al. Perspective of concentrating solar power. Energy 2020;198:117373. https://doi.org/10.1016/j.energy.2020.117373.
[26] Mehos M, Turchi C, Vidal J, Wagner M, Ma Z, Ho C, et al. Concentrating Solar Power Gen3 Demonstration Roadmap. NREL, SNL; 2017. https://doi.org/10.2172/1338899.
[27] Manzolini G, Lucca G, Binotti M, Lozza G. A two-step procedure for the selection of innovative high temperature heat transfer fluids in solar tower power plants. Renewable Energy 2021;177:807–22. https://doi.org/10.1016/j.renene.2021.05.153.
[28] Turchi CS, Libby C, Pye J, Coventry J. Molten salt vs. liquid sodium receiver selection using the analytic hierarchy process, Freiburg, Germany: 2022, p. 110016. https://doi.org/10.1063/5.0087043.
[29] Coventry J, Andraka C, Pye J, Blanco M, Fisher J. A review of sodium receiver technologies for central receiver solar power plants. Solar Energy 2015;122:749–62.
[30] Turchi C, Gage S, Martinek J, Jape S, Armijo K, Coventry J, et al. CSP Gen3: Liquid-Phase Pathway to SunShot. 2021. https://doi.org/10.2172/1807668.
[31] Armijol KM, Carlson' MD, Dorsey DS, Ortega' JD, Madden' D, Turchi CS. Operational Modes and System Design of a 2.0 MWth Sodium-Molten Salt Pilot System n.d.
[32] Asselineau C-A, Pye J, Coventry J. Exploring efficiency limits for molten-salt and sodium external cylindrical receivers for third-generation concentrating solar power. Solar Energy 2022;240:354–75. https://doi.org/10.1016/j.solener.2022.05.001.
[33] Asselineau C-A, Fontalvo A, Wang S, Venn F, Pye J, Coventry J. Techno-economic assessment of a numbering-up approach for a 100 MWe third generation sodium-salt CSP system. Solar Energy 2023;263:111935. https://doi.org/10.1016/j.solener.2023.111935.
[34] Kraemer S. Vast's Cutting-Edge Clean Energy Solution Nears Market Launch After Final Testing. SolarPACES 2025. https://www.solarpaces.org/vasts-cutting-edge-clean-energy-solution-nears-market-launch-after-final-testing/ (accessed January 21, 2026).
[35] Ho CK. A review of high-temperature particle receivers for concentrating solar power. Applied Thermal Engineering 2016;109:958–69. https://doi.org/10.1016/j.applthermaleng.2016.04.103.
[36] University of Adelaide, PROMES-CNRS, DLR, Bridgers & Paxton, Bohannan Huston, Solar Dynamics, et al. Gen 3 Particle Pilot Plant (G3P3) -- High-Temperature Particle System for Concentrating Solar Power (Phases 1 and 2). 2021. https://doi.org/10.2172/1832285.
[37] Buck R, Giuliano S. Impact of solar tower design parameters on sCO2-based solar tower plants 2018. https://doi.org/10.17185/DUEPUBLICO/46098.
[38] Gueguen R, Sahuquet G, Tessoneaud M, Sans J-L, Guillot E, Le Gal A, et al. Heat transfer in a fluidized bed tubular solar receiver. On-sun experimental investigation. Solar Energy 2023;265:112118. https://doi.org/10.1016/j.solener.2023.112118.
[39] Could falling particles of solar energy help us reach net zero? - CSIRO n.d. https://www.csiro.au/en/news/all/articles/2023/october/concentrated-solar-thermal-power (accessed December 4, 2025).
[40] FPR Energy n.d. https://www.fprenergy.com.au/ (accessed December 4, 2025).
[41] Zhang Y, Qiu Y, Li Q, Henry A. Optical-thermal-mechanical characteristics of an ultra-high-temperature graphite receiver designed for concentrating solar power. Applied Energy 2022;307:118228. https://doi.org/10.1016/j.apenergy.2021.118228.
[42] Zohuri B. Innovative open air Brayton combined cycle systems for the next generation nuclear power plants. The University of New Mexico, 2014.
[43] Angelino G, Invernizzi C. Binary conversion cycles for concentrating solar power technology. Solar Energy 2008;82:637–47. https://doi.org/10.1016/j.solener.2008.01.003.
[44] Nicol K. Status of advanced ultra-supercritical pulverised coal technology. IEA Clean Coal Centre; 2013.

[45] Di Gianfrancesco A, Blum R. A-USC programs in the European Union. Materials for Ultra-Supercritical and Advanced Ultra-Supercritical Power Plants, Elsevier; 2017, p. 773–846. https://doi.org/10.1016/B978-0-08-100552-1.00024-5.
[46] Li Q, E E, Qiu Y, Wang J, Zhang Y. Conceptual design of novel He-SCO2 Brayton cycles for ultra-high-temperature concentrating solar power. Energy Conversion and Management 2022;260:115618. https://doi.org/10.1016/j.enconman.2022.115618.
[47] Dostal V, Driscoll MJ, Hejzlar P, Wang Y. Supercritical CO2 Cycle for Fast Gas-Cooled Reactors. Volume 7: Turbo Expo 2004, Vienna, Austria: ASMEDC; 2004, p. 683–92. https://doi.org/10.1115/GT2004-54242.
[48] Dekhtyarev V. On the creation of a carbon dioxide power plant with high power and high efficiency. Electric stations 1962:2–6. https://doi.org/10.5281/zenodo.12191690.
[49] Feher EG. The supercritical thermodynamic power cycle. Energy Conversion 1968;8:85–90.
[50] Angelino G. Real Gas Effects in Carbon Dioxide Cycles. ASME 1969 Gas Turbine Conference and Products Show, Cleveland, Ohio, USA: American Society of Mechanical Engineers; 1969, p. V001T01A071. https://doi.org/10.1115/69-GT-102.
[51] Dostal V, Driscoll MJ, Hejzlar P. A Supercritical Carbon Dioxide Cycle for Next Generation Nuclear Reactors. MIT; 2004.
[52] Heller L, Glos S, Buck R. Cost benefit analysis of supercritical CO2 cycles in next-generation solar thermal power plants. Renewable Energy 2026;256:123613. https://doi.org/10.1016/j.renene.2025.123613.
[53] Neises T, Turchi C. Supercritical carbon dioxide power cycle design and configuration optimization to minimize levelized cost of energy of molten salt power towers operating at 650 °C. Solar Energy 2019;181:27–36. https://doi.org/10.1016/j.solener.2019.01.078.
[54] Held T, Avadhanula V, Buckmaster D, Sjunnesson A, Bacalao N. Integrated Optimization and Control of a Hybrid Gas Turbine/sCO_2 Power System. 2022. https://doi.org/10.2172/1670695.
[55] Heat To Power | Echogen Power n.d. https://www.echogen.com/technology/heat-to-power (accessed December 18, 2025).
[56] Follett IV WW, Moore J, Wade J, Pierre S. The STEP 10 MWe sCO2 pilot installation and commissioning status update. Proceedings of the 8th International sCO2 Power Cycles Symposium 2024;2.
[57] STEP Demo Pilot Achieves Phase 1 Testing Milestone, Paving the Way for Next-Generation Supercritical CO2 Power Production. GTI Energy n.d. https://www.gti.energy/step-demo/achieves-phase-1-testing-milestone/ (accessed December 18, 2025).
[58] Binotti M, Invernizzi CM, Iora P, Manzolini G. Dinitrogen tetroxide and carbon dioxide mixtures as working fluids in solar tower plants. Solar Energy 2019;181:203–13. https://doi.org/10.1016/j.solener.2019.01.079.
[59] Crespi F, Rodríguez De Arriba P, Sánchez D, Ayub A, Di Marcoberardino G, Invernizzi CM, et al. Thermal efficiency gains enabled by using CO2 mixtures in supercritical power cycles. Energy 2022;238:121899. https://doi.org/10.1016/j.energy.2021.121899.
[60] Manzolini G, Binotti M, Bonalumi D, Invernizzi C, Iora P. CO2 mixtures as innovative working fluid in power cycles applied to solar plants. Techno-economic assessment. Solar Energy 2019;181:530–44. https://doi.org/10.1016/j.solener.2019.01.015.
[61] Morosini E, Villa E, Quadrio G, Binotti M, Manzolini G. Solar tower CSP plants with transcritical cycles based on CO2 mixtures: A sensitivity on storage and power block layouts. Solar Energy 2023;262:111777. https://doi.org/10.1016/j.solener.2023.05.054.
[62] Doninelli M, Morosini E, Di Marcoberardino G, Invernizzi CM, Iora P, Riva M, et al. Experimental investigation of the CO2+SiCl4 mixture as innovative working fluid for power cycles: Bubble points and liquid density measurements. Energy 2024:131197. https://doi.org/10.1016/j.energy.2024.131197.
[63] Tafur-Escanta P, López-Paniagua I, Muñoz-Antón J. Thermodynamics analysis of the supercritical CO2 binary mixtures for Brayton power cycles. Energy 2023;270:126838. https://doi.org/10.1016/j.energy.2023.126838.
[64] Chengelis CP, Neal RA. Studies of carbonyl sulfide toxicity: Metabolism by carbonic anhydrase. Toxicology and Applied Pharmacology 1980;55:198–202. https://doi.org/10.1016/0041-008X(80)90236-7.
[65] Huang H-M, Govind R. Studies on power plants using dissociating gases as working fluids. Chemical Engineering Communications 1988;72:95–119. https://doi.org/10.1080/00986448808940011.
[66] Taichman O, Kaplan V, Wachtel E, Lubomirsky I. Thermal Decomposition of COS to CO and Sulfur: Byproducts of Flue Gas Scrubbing. Solid Fuel Chem 2022;56:21–8. https://doi.org/10.3103/S0361521922010074.
[67] Malenkov AS, Naumov VYu, Shabalova SI, Kharlamova DM. Development of an Ammonia Decomposition Unit. In: Solovev DB, Kyriakopoulos GL, Venelin T, editors. SMART Automatics and Energy, vol. 272, Singapore: Springer Nature Singapore; 2022, p. 205–16. https://doi.org/10.1007/978-981-16-8759-4_22.
[68] Deka DJ, Boruah B, Lee G, Rappé KG. Recent Advances in Ammonia Decomposition Technologies for Hydrogen Production. Energy Fuels 2025;39:10802–52. https://doi.org/10.1021/acs.energyfuels.5c01100.
[69] Di Marcoberardino G, Morosini E, Di Bona D, Chiesa P, Invernizzi C, Iora P, et al. Experimental characterisation of CO2 + C6F6 mixture: Thermal stability and vapour liquid equilibrium test for its application in transcritical power cycle. Applied Thermal Engineering 2022;212:118520. https://doi.org/10.1016/j.applthermaleng.2022.118520.
[70] Putelli L, Di Marcoberardino G, Gelfi M, Invernizzi CM, Iora PG, Manzolini G. Preliminary Analysis of High-Temperature Corrosion of Metallic Alloys With CO2 and CO2-Based Working Mixtures for Power Plants Applications, American Society of Mechanical Engineers Digital Collection; 2022. https://doi.org/10.1115/GT2022-84197.

[71] Gerasimov RL, Mazurin IM. Thermal stability of R218 (C3F8) and R31-10 (C4F10) under heat exposure. High Temp 2015;53:924–7. https://doi.org/10.1134/S0018151X15060085.
[72] Invernizzi CM, Iora P, Bonalumi D, Macchi E, Roberto R, Caldera M. Titanium tetrachloride as novel working fluid for high temperature Rankine Cycles: Thermodynamic analysis and experimental assessment of the thermal stability. Applied Thermal Engineering 2016;107:21–7. https://doi.org/10.1016/j.applthermaleng.2016.06.136.
[73] Thermophysical characterisation of innovative working fluids for closed thermodynamic cycles. Università degli studi di Brescia, 2025.
[74] Doninelli M, Di Marcoberardino G, Iora P, Gelfi M, Invernizzi CM, Manzolini G. Silicon Tetrachloride as innovative working fluid for high temperature Rankine cycles: Thermal Stability, material compatibility, and energy analysis. Applied Thermal Engineering 2024;249:123239. https://doi.org/10.1016/j.applthermaleng.2024.123239.
[75] Nakayama M, Miyamoto S, Ogawa T, Osae S, Tomono K, Sumimoto M, et al. Thermal decomposition of tetrabromosilane and deposition of crystalline silicon. Materials Science in Semiconductor Processing 2014;23:93–7. https://doi.org/10.1016/j.mssp.2014.02.045.
[76] NIST. NIST Standard Reference Database 103b. NIST 2010.
[77] Aspen. Aspen Plus | Leading Process Simulation Software | AspenTech n.d. https://www.aspentech.com/en/products/engineering/aspen-plus (accessed June 28, 2023).
[78] Redlich Otto, Kwong JNS. On the Thermodynamics of Solutions. V. An Equation of State. Fugacities of Gaseous Solutions. Chem Rev 1949;44:233–44. https://doi.org/10.1021/cr60137a013.
[79] Soave G. Equilibrium constants from a modified Redlich-Kwong equation of state. Chemical Engineering Science 1972;27:1197–203.
[80] Peng D-Y, Robinson DB. A New Two-Constant Equation of State. Ind Eng Chem Fund 1976;15:59–64. https://doi.org/10.1021/i160057a011.
[81] Plocker U, Knapp H, Prausnitz J. Calculation of High-Pressure Vapor-Liquid Equilibria from a Corresponding-States Correlation with Emphasis on Asymmetric Mixtures. Ind Eng Chem Proc Des Dev 1978;17:324–32. https://doi.org/10.1021/i260067a020.
[82] Benedict M, Webb GB, Rubin LC. An Empirical Equation for Thermodynamic Properties of Light Hydrocarbons and Their Mixtures I. Methane, Ethane, Propane and *n* -Butane. The Journal of Chemical Physics 1940;8:334–45. https://doi.org/10.1063/1.1750658.
[83] Gross J, Sadowski G. Perturbed-Chain SAFT: An Equation of State Based on a Perturbation Theory for Chain Molecules. Ind Eng Chem Res 2001;40:1244–60. https://doi.org/10.1021/ie0003887.
[84] Kontogeorgis GM, Voutsas EC, Yakoumis IV, Tassios DP. An Equation of State for Associating Fluids. Ind Eng Chem Res 1996;35:4310–8. https://doi.org/10.1021/ie9600203.
[85] Span R, Wagner W. A New Equation of State for Carbon Dioxide Covering the Fluid Region from the Triple-Point Temperature to 1100 K at Pressures up to 800 MPa. J Phys Chem Ref Data 1996;25:1509–96. https://doi.org/10.1063/1.555991.
[86] Kunz O, Wagner W. The GERG-2008 Wide-Range Equation of State for Natural Gases and Other Mixtures: An Expansion of GERG-2004. J Chem Eng Data 2012;57:3032–91. https://doi.org/10.1021/je300655b.
[87] Wagner W, Pruß A. The IAPWS Formulation 1995 for the Thermodynamic Properties of Ordinary Water Substance for General and Scientific Use. Journal of Physical and Chemical Reference Data 2002;31:387–535. https://doi.org/10.1063/1.1461829.
[88] Wagner W, Cooper JR, Dittmann A, Kijima J, Kretzschmar H-J, Kruse A, et al. The IAPWS Industrial Formulation 1997 for the Thermodynamic Properties of Water and Steam. Journal of Engineering for Gas Turbines and Power 2000;122:150–84. https://doi.org/10.1115/1.483186.
[89] Alfani D, Neises T, Astolfi M, Binotti M, Silva P. Techno-economic analysis of CSP incorporating sCO2 brayton power cycles: Trade-off between cost and performance, Freiburg, Germany: 2022, p. 090001. https://doi.org/10.1063/5.0086353.
[90] Inc TM. MATLAB version: R2023b 2023.
[91] Wagner MJ, Wendelin T. SolarPILOT: A power tower solar field layout and characterization tool. Solar Energy 2018;171:185–96. https://doi.org/10.1016/j.solener.2018.06.063.
[92] Hamilton WT, Wagner MJ, Zolan AJ. Demonstrating SolarPILOT's Python API Through Heliostat Optimal Aimpoint Strategy Use Case. vol. ASME 2021 15th International Conference on Energy Sustainability, 2021, p. 6. https://doi.org/10.1115/ES2021-60502.
[93] Wang S, Asselineau C-A, Fontalvo A, Wang Y, Logie W, Pye J, et al. Co-optimisation of the heliostat field and receiver for concentrated solar power plants. Applied Energy 2023;348:121513. https://doi.org/10.1016/j.apenergy.2023.121513.

Part 1: Equipment for sCO_2 and CO_2 mixture cycles in CSP

The analysis of the equipment used for sCO_2 and CO_2 mixture power cycles in CSP plants is the focus of Part 1.

In Chapter 2, the thermohydraulic and mechanical design of shell-and-tube primary and recuperative heat exchangers is carried out in collaboration with the Brembana&Rolle S.p.A. using both conventional and EMbaffle® technology for both sCO_2 and CO_2 mixtures cycles. The influence of technology and working fluid on the design and masses of heat exchangers is discussed.

In Chapter 3, the results of an experimental campaign at Brembana&Rolle S.p.A. are presented. The analysis of low-finned tubes in the EMbaffle® heat exchanger with two different baffle spacings is carried out. The use of water to model solar salt heat transfer is proposed. The thermohydraulic performance is described using the Fanning friction factor and Nusselt number correlation and compared with literature data.

In Chapter 4, turbines, primary and recuperative heat exchangers, and condensers with coolers were sized for conventional steam Rankine cycle, sCO_2 and CO_2 mixture power cycles. The mass and cost of components were obtained, analyzed, and compared with the literature values. This chapter was done during the visiting PhD period at RWTH Aachen University in collaboration with the researchers from the Institute of Power Plant Technology, Steam and Gas Turbines (IKDG).

2. Shell and Tube Heat Exchangers designs for sCO_2 and CO_2 mixtures cycles for CSP

This chapter is based on the article: *"Comparison of Shell and Tube Heat Exchangers for CO_2 and CO_2+ $SiCl_4$ Mixtures Transcritical Cycles", published in SolarPACES Conference Proceedings Vol. 3: SolarPACES 2024, 30th International Conference on Concentrating Solar Power, Thermal, and Chemical Energy Systems, https://doi.org/10.52825/solarpaces.v3i.2331.*

Abstract

Concentrated solar power (CSP) plants have great potential for clean energy production, but their electricity cost is higher than that of noncontrollable renewable energy sources. The main ways to lower the electricity cost are equipment cost reduction and plant efficiency increase. Looking at the power unit, the closed supercritical CO_2 (sCO_2) cycles offer the efficiency advantage over both the steam Rankine and helium Brayton cycles at high turbine inlet temperatures. Further improvement could be achieved by increasing the critical temperatures using mixtures, allowing condensation at temperatures typical for air-cooled condensers. The sCO_2 and CO_2 mixture cycles are significantly affected by the performance of the recuperative system and require high pressures (comparable to steam cycles). An increase in efficiency compensates for higher complexity in the design and construction of the plant, according to the authors. High thermal power together with high pressures and temperatures demand customized CO_2 heat exchanger designs, which makes them a major part of power cycle specific cost. This paper provides a robust technological solution for the implementation of the above cycles in an industrial setup based on shell-and-tube heat exchangers. Based on the thermohydraulic and mechanical design of EMbaffle® Technology, heat exchangers weight reduction can be quantified in the range of 30 to 60% depending on the application, with additional advantages in terms of logistics and installation (footprint, foundations, etc…). Using the CO_2+$SiCl_4$ mixture instead of pure sCO_2 leads to a lower weight of primary and high-temperature heat exchangers, while the weight of low-temperature heat exchanger increases.

2.1. Introduction

Concentrated solar power (CSP) plants generate thermal power as an intermediate step between solar radiation and electricity and therefore can use cheap thermal energy storage. This makes them a flexible dispatchable source of renewable energy. However, the actual cost of electricity from CSP plants is higher than from photovoltaic or wind power plants [1], but their power generation depends on weather conditions and is uncontrollable. The CSP electricity cost reduction can be pursued by reducing the cost of equipment and increasing the generation efficiency. The closed supercritical CO_2 (sCO_2) cycles offer an efficiency advantage over both the steam Rankine and helium Brayton cycles at turbine inlet temperature (TIT) > 600°C [2]. One of the ways to improve their efficiency is to move towards the CO_2 mixture cycles, which have higher critical temperatures and allow condensation even at 50°C [3]. To improve the sCO_2 cycle performance, a $SiCl_4$ dopant, which could be stable up to 900°C [4], has been considered. Bubble points and liquid density of the CO_2+$SiCl_4$ mixture have recently been measured by Doninelli et al. [5] allowing for the calculation of cycle performance: the use of a CO_2+$SiCl_4$ mixture instead of sCO_2 increased the efficiency of the recompression cycle at 700°C TIT by 1.3%. Pure $SiCl_4$ thermal conductivity and viscosity have been accurately modeled using the friction theory [6,7] therefore allowing for the characterization of the heat exchangers performance. The sCO_2-based cycles are significantly affected by the recuperative system and require high pressures (comparable to supercritical steam cycles). High thermal power together with high pressures and temperatures leads to sCO_2 heat exchangers' complex designs. They can account for up to 70% of CSP power cycle specific cost [8], which makes them a critical piece of equipment for sCO_2 and CO_2 mixture cycles. For recuperative heat exchangers of sCO_2 cycles printed circuit heat exchangers (PCHE) are usually considered in the literature. However, the cost difference between PCHE and non-PCHE is little [9] and the maximum thermal power of existing PCHE does not exceed 50 MWth with significant challenges in scale-up [10]. Therefore, shell and tube heat exchangers were considered for current high-power application (multiple hundred MWth range). This paper aims to identify a robust technological solution for the implementation of the above cycles in an industrial setup. This work is part of the EU-funded TOPCSP project, which aims to improve the design of the different systems of a CSP plant [11]. Estimation of performance of alternative equipment technologies upon heat transfer surface and material mass basis may provide additional insight to users and plant designers aimed at maximizing exchangers' cost reduction.

2.2. Methodology

The duty of heat exchangers was calculated to achieve the power cycle electric output of around 100 MWe based on a CSP with solar multiple of 2.4 and design power to the receiver of 670 MWth similar to Crescent Dunes plant according to SAM default solar tower CSP plant [12]. Both sCO_2 and CO_2+$SiCl_4$ mixture cycles were considered in recompression layout (RC) with the CO_2+$SiCl_4$ mixture also considered in the simple recuperated cycle (SC) at 550°C TIT and 250 bar maximum pressure. The mixture cycles parameters were optimized based on electrical efficiency with a minimum cycle temperature equal to 50°C [3]. For recompression and simple mixture cycles the working fluid molar composition (CO_2/$SiCl_4$) was chosen to be 91/9 and 80/20 respectively based on electrical efficiency optimization as can be seen in Figure 2.1. For the sCO_2 recompression cycle, the optimized minimum pressure was 110 bar with the recompression fraction equal to 0.286.

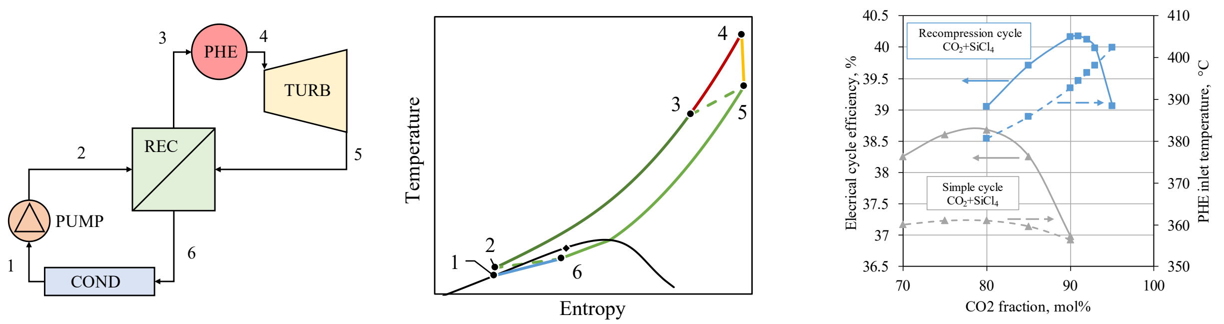

(a) *(b)* *(c)*

Figure 2.1. Layout (a) and T-s diagram (b) of recuperated CO_2+$SiCl_4$ mixture simple cycle, (c) cycles electrical efficiency and PHE inlet temperature vs CO_2 molar fraction at 550°C TIT

The properties of solar salt were calculated according to [13], while for calculating sCO_2 properties Span-Wagner EoS was used [14]. The CO_2+$SiCl_4$ mixture properties were calculated using Peng-Robinson EoS [15] and friction theory models [6,7] with binary interaction parameter equal to 0.06098 [5]. The resulting properties tables were transferred to HTRI with 30 maximum allowable temperature steps and 5 bar pressure steps.

The primary heat exchanger (PHE) and recuperators, including high and low-temperature recuperators (HTR and LTR), have been designed in detail using the shell-and-tube heat exchanger (STHE) in conventional configuration and using the EMbaffle® technology [16]. The main advantages of EMbaffle® technology are due to the pure countercurrent flow, low shellside pressure drops, and no flow-induced vibrations. This leads to a more compact size of EMbaffle® technology under a wide range of process design conditions. The input parameters for heat exchanger designs are shown in Table 2.1. Pressure drops were assumed according to literature [5].

Table 2.1. Heat exchangers design parameters

	Power cycle	**sCO_2 RC**			**CO_2+$SiCl_4$ SC**		**CO_2+$SiCl_4$ RC**		
	Heat exchanger	**PHE**	**HTR**	**LTR**	**PHE**	**Rec.**	**PHE**	**HTR**	**LTR**
	Duty, MWth	283	582	194	285	533	284	411	195
Hot side	Fluid	Salt	sCO_2		Salt	CO_2+$SiCl_4$	Salt	CO_2+$SiCl_4$	
	Flow, kg/s	1429	1748		989	1485	1197	1636	
	T_{in}/T_{out}, °C	570/441	457/175	175/112	570/381	426/93	570/414	435/193	193/94
	$P_{in}/\Delta P$, bar/%	5/10	116/1.5	114/1.5	5/10	75/1.5	5/10	88/1.5	87/1.5
Cold side	Fluid	sCO_2			CO_2+$SiCl_4$				
	Flow, kg/s	1748		1249	1485		1636		1187
	T_{in}/T_{out}, °C	421/550	170/421	90/170	361/550	74/361	394/550	188/394	87/188
	$P_{in}/\Delta P$, bar/%	249/2	249/0.3	250/0.3	249/2	250/0.3	249/2	249/0.3	250/0.3

All STHEs were designed according to TEMA standards [17] using HTRI v.9.1 [18]. The maximum weight of the bundle was assumed to be within 160 tons with a shell outer maximum diameter of 4 m due to transport limitations. The flow with the highest pressure was located on the tube side. The fouling resistance was assumed to be 1.76×10^{-4} m2K/W on the solar salt side and 8.81×10^{-5} m2K/W for the sCO_2 and CO_2 mixture side [19]. The tubes outside diameters were assumed to be equal to 15.875 mm or 5/8" for all cases. The mechanical design was performed according to Section VIII ASME Div.1 with PV Elite [20]. Adequate materials have been identified for the considered fluids. For PHE Alloy 625 was chosen for channels and tubesheets, SS347H for tubes and shell, while for HTR and LTR 9Cr and carbon steel (CS) were used respectively [21–23].

2.3. Results

The main criteria for heat exchanger comparison is usually heat transfer surface, which for many applications allows for accurate cost prediction [24]. However, in the case of CO_2 cycles high pressures and temperatures are present, which makes weight a better indicator of the final cost. Due to high pressures throughout the cycle heat exchanger parts, like channels, covers, and tubesheets, make a significant portion of the final heat exchanger weight. The weight of these elements depends among other parameters on the diameter of shells, which is determined by throughput area and therefore by the maximum accommodating volume flow, governed by the allowable pressure drop, the material availability and the fabrication technology constraints. The solar salt volume flow is below 1 m^3/s and is much smaller compared to the sCO_2 and CO_2+$SiCl_4$ mixture flows as can be seen in Figure 2.2. This is due to the similar heat capacity and the tenfold difference in density of cold and hot fluids which leads to the small pressure drop in the salt side.

The cold fluid mass flow in PHE is smaller in the case of mixture power cycles due to the lower temperature of the cold fluid at the PHE inlet (Table 2.1). The mixture of CO_2+$SiCl_4$ also has a higher density than sCO_2 in PHE conditions. These two effects lead to around 50 and 25% smaller volume flow in the case of mixture simple and recompression power cycles PHE and to smaller shell and channel diameters. The HTR and LTR heat exchangers hot side volume flows are not so sensitive to the fluid chemical composition because of the mixture lower pressure. However, HTR and LTR cold side volume flows are around 20-25% smaller for the CO_2+$SiCl_4$ recompression cycle compared to the sCO_2 one.

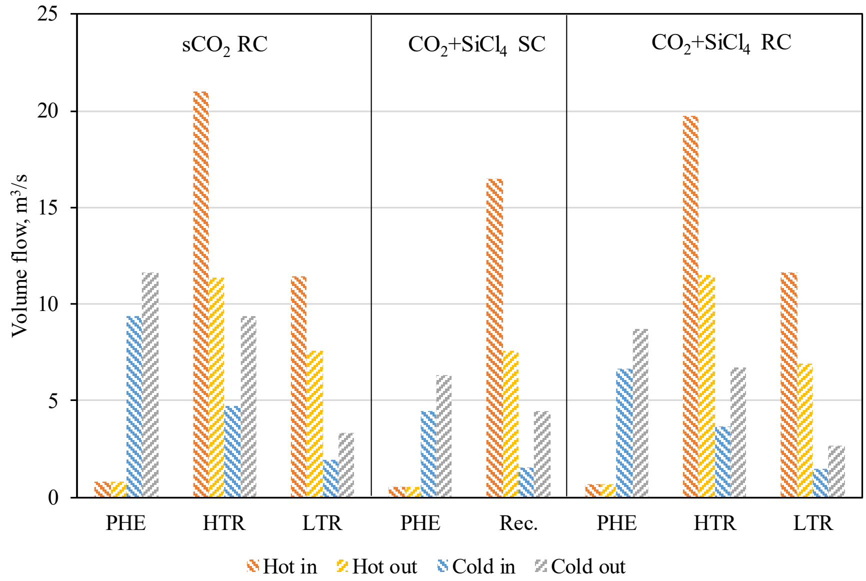

Figure 2.2. Volume flows in heat exchangers

The heat exchangers duty was calculated within 0.4% of the design value, while all pressure drops were within the allowed limits. In the case of conventional STHE, a No Tubes In Window (NTIW) baffle design with supports was adopted to prevent vibrations and reduce shell side pressure drop. The results of the STHE design are shown in Table 2.2.

Table 2.2. Heat exchangers design results

	Power cycle		**sCO$_2$ RC**			**CO$_2$+SiCl$_4$ SC**		**CO$_2$+SiCl$_4$ RC**		
	Heat exchanger		**PHE**	**HTR**	**LTR**	**PHE**	**Rec.**	**PHE**	**HTR**	**LTR**
Conventional	ΔP calc./ allow., bar	Hot	0.48/0.5	1.44/1.74	1.56/1.71	0.44/0.5	0.78/1.12	0.44/0.5	0.78/1.32	0.93/1.3
		Cold	4.17/4.97	0.55/0.75	0.46/0.75	4.28/4.97	0.53/0.75	4.87/4.97	0.64/0.75	0.67/0.75
	Parallel/series/(total)		2/2 (4)	5/3 (15)	4/3 (12)	2/3 (6)	5/4 (20)	2/3 (6)	6/3 (18)	5/4 (20)
	Shell ID, mm		2400	2550	2600	1900	2200	2150	2200	2550
	Eff. length, mm		14292	13950	14950	14049	15450	11532	12950	15800
	Total area, 10^3 m^2		18.07	75.20	97.70	16.97	82.68	17.57	53.78	113.88
Embaffle®	ΔP calc./ allow., bar	Hot	0.44/0.5	1.7/1.74	1.62/1.71	0.44/0.5	1.11/1.12	0.47/0.5	1.24/1.32	1.27/1.3
		Cold	4.75/4.97	0.55/0.75	0.57/0.75	4.87/4.97	0.73/0.75	4.67/4.97	0.7/0.75	0.73/0.75
	Parallel/series/(total)		2/2 (4)	4/3 (12)	3/4 (12)	1/3 (3)	2/4 (8)	1/2 (2)	2/3 (6)	3/4 (12)
	Shell ID, mm		1730	2100	2100	2150	2600	2200	2500	2200
	Eff. length, mm		14409	11250	12142	12674	11268	17542	9950	14580
	Total area, 10^3 m^2		16.64	58.16	62.77	17.18	60.33	16.63	36.86	82.91

As can be seen from Figure 2.3 in the case of PHE due to the use of solar salt on the shell side relatively high heat transfer coefficients are seen in all cases which leads to similar heat exchange areas. In the case of recuperators, there is a significant increase in the shell side heat transfer coefficient due to the use of EMbaffle® technology.

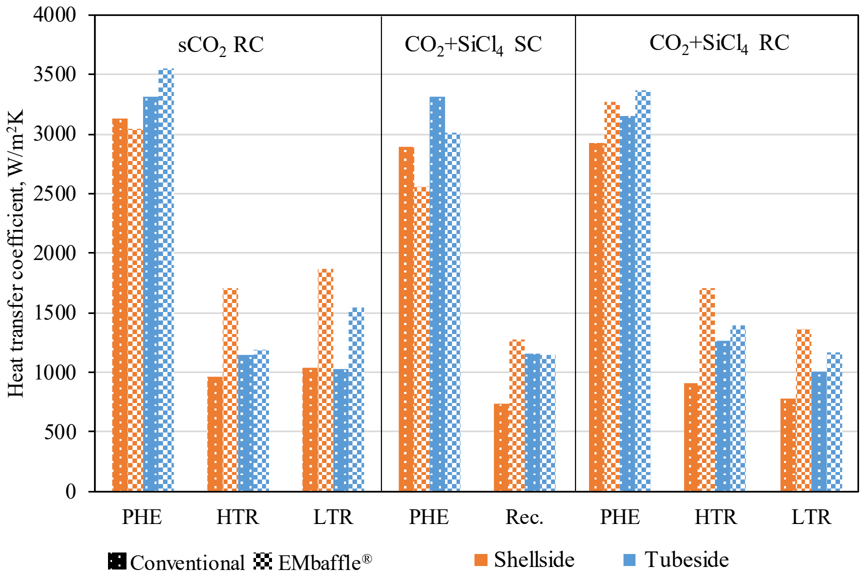

Figure 2.3. The heat transfer coefficient of heat exchangers

The product of effective area and heat transfer coefficient (UA) is used for cost estimation in multiple models for sCO_2 heat exchangers [9], therefore it was used in this study too. Notably, the dependence between the area and UA for EMbaffle® technology has a much lower slope compared to the conventional design as seen in Figure 2.4. In the case of recuperators, EMbaffle® technology has a clear advantage and consistently lower heat exchange area for the same UA. For PHE the area is very similar in all considered cases due to similar heat transfer coefficients. However, adopting the same number of shells in PHE, the EMbaffle® solution would allow for the reduction of the shell's internal diameter, which is important for the selected material use and transportation costs. Moreover, EMbaffle® versus NTIW optimized designs require fewer shells in most cases (Figure 2.5).

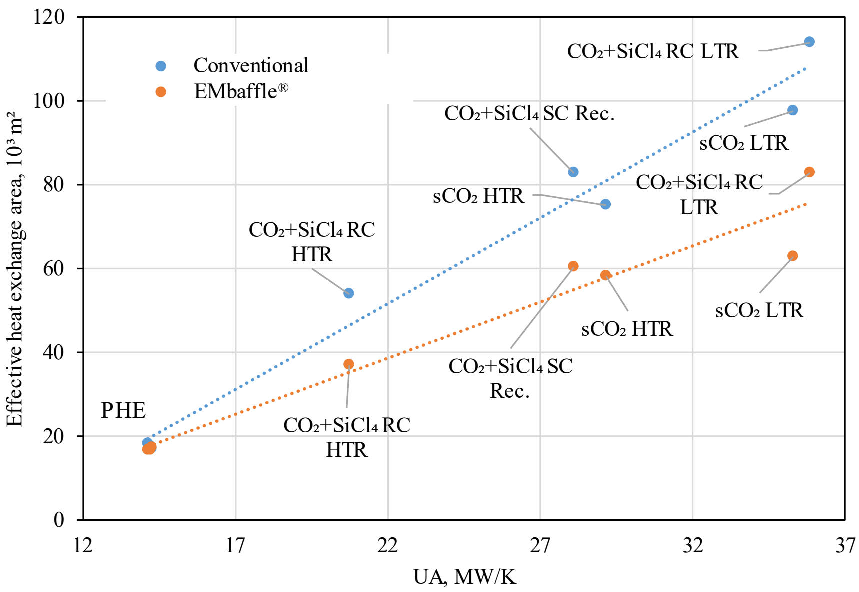

Figure 2.4. The heat exchangers area vs UA

The transition from sCO_2 to CO_2+$SiCl_4$ mixture cycles does not significantly change the PHE and recuperative system area. As can be seen from Figure 2.5 in the case of a mixture recompression cycle the bigger part of the recuperative STHE area is represented by LTR, which is made from cheaper material. It is also important to mention the big deviation in the number of shells between conventional and EMbaffle® designs in the case of the recuperator and HTR for CO_2+$SiCl_4$ mixture cycles. Due to the vibrations occurring in the shell side, the flow speed is limited, which leads to underutilization of hot stream pressure drop and higher than expected heat exchange area.

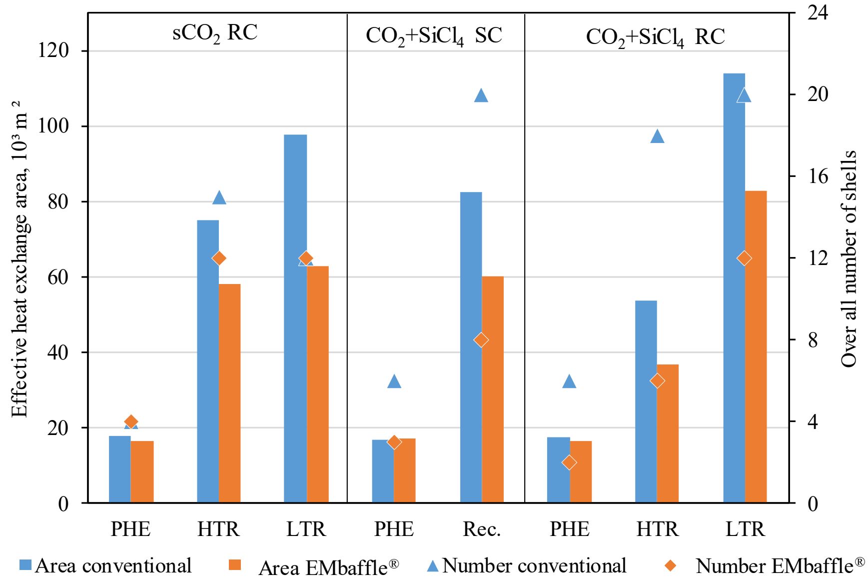

Figure 2.5. The area and number of shells of heat exchangers

The results of the mechanical design for a single shell are shown in Figure 2.6. In the case of sCO_2, as the number of shells is similar in both designs, the weight of the EMbaffle® single shell is lower. Moving to mixtures, although the single shell with conventional design becomes lighter, the total number of shells significantly increases compared to EMbaffle®. The higher heat transfer rate and the larger accommodated surface per shell diameter of the EMbaffle® technology lead to the higher contribution of tubes in the single shell weight in all considered cases. This means that a bigger percentage of materials is spent on heat exchange surfaces, which leads to significant savings in high-temperature applications such as PHE.

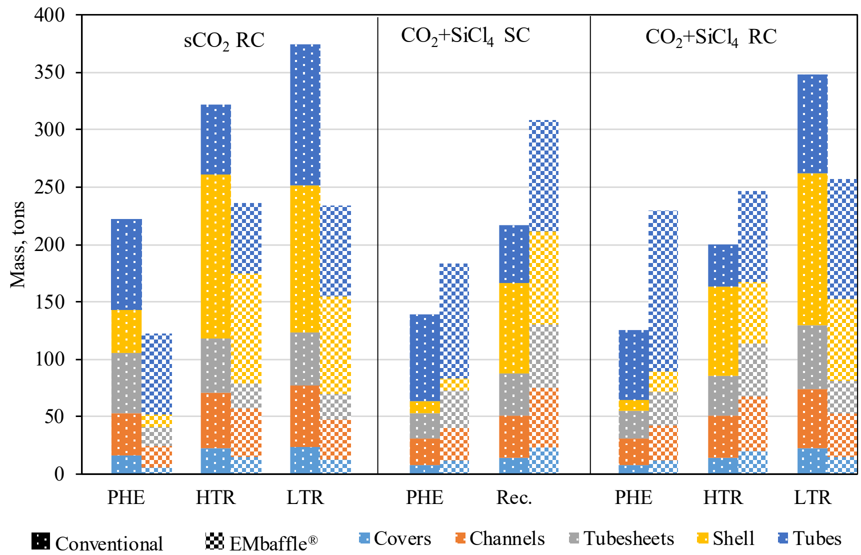

Figure 2.6. The weight distribution of one shell components

The total weights of the heat exchangers considered are shown in Figure 2.7. One can see a significant weight reduction using EMbaffle® technology, especially for recuperative systems. The difference between the technologies increases with the UA as it was in the case of the area dependence on the UA shown in Figure 2.4. This will lead to the overestimation of cost correlations based on conventional STHE UA. However, the weight savings moving to EMbaffle® grow faster than area savings, which is determined by the higher material percentage being spent on tubes, meaning heat exchange surface (as shown in Figure 2.6).

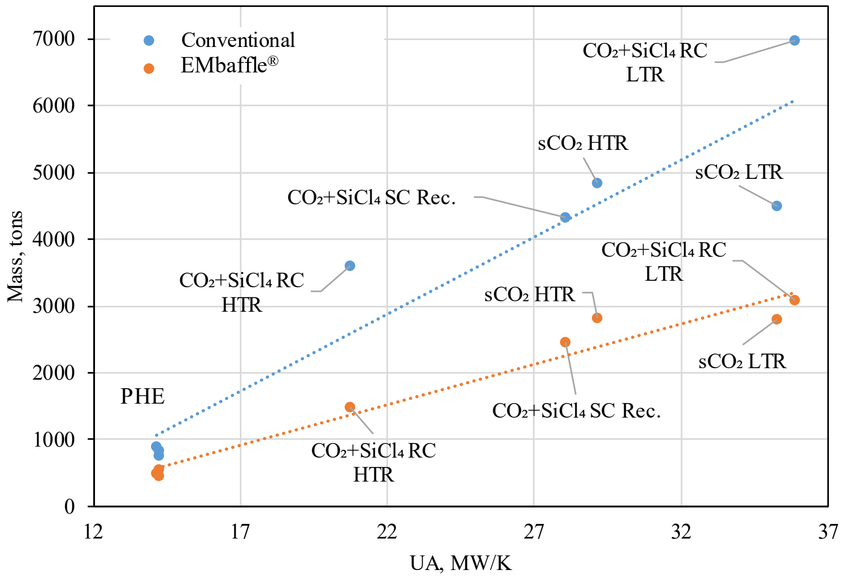

Figure 2.7. Heat exchangers mass vs UA

The material saving is especially important in the case of PHE since it uses an expensive nickel-based alloy 625. Using the EMbaffle® leads to the reduction of Alloy 625 and 347H use by 61 and 28% in the case of sCO_2 PHE, 31 and 36% for CO_2+SiCl_4 simple cycle PHE, 56 and 27% for CO_2+SiCl_4 recompression cycle PHE (Figure 7). For the recuperative system, the weight reduction is 37 and 41% for sCO_2 low and high temperature parts respectively, 44% for the recuperator, 56 and 59% for CO_2+SiCl_4 LTR and HTR.

There is a 15% and 6% reduction in PHE weight mass using conventional and EMbaffle® design, with 24 and 14% reduction in Alloy 625 weight moving from sCO_2 to CO_2+SiCl_4 mixture in the recompression cycle. This is due to the mixture's lower volume flow as shown in Figure 2.2, which leads to a lower throughput area, meaning fewer shells in parallel or smaller shell diameters. For HTR the mass reduction is 24 and 47% for conventional and EMbaffle® designs and is due to the heat exchange area reduction of 28 and 36% respectively. In the case of LTR, the use of a mixture leads to the increase of weight by 56 and 10% for conventional and EMbaffle® designs, while the area increases by 16 and 32% respectively. Since 9Cr-1Mo steel used in HTR is more expensive than carbon steel in LTR, the final cost of the recuperative system could be similar or lower in the case of the CO_2+SiCl_4 mixture recompression cycle.

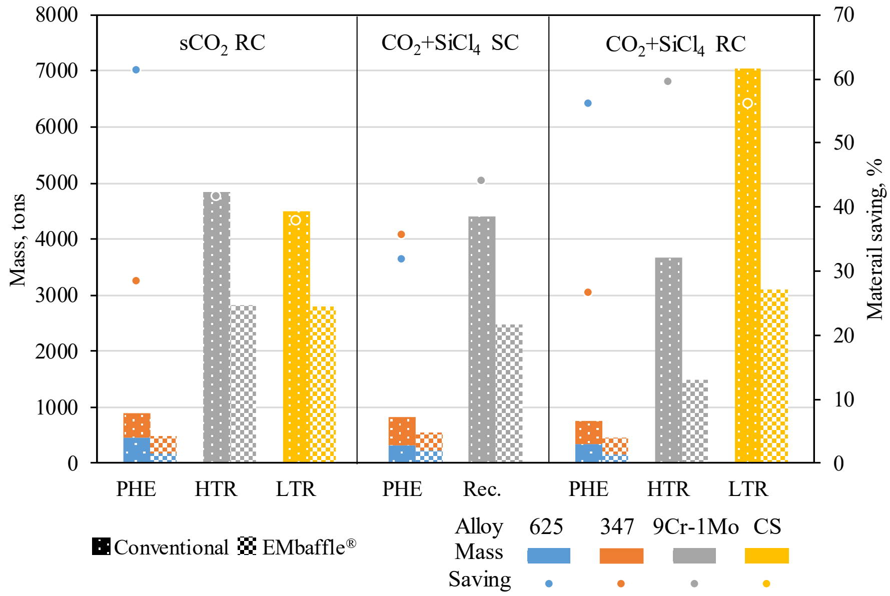

Figure 2.8. The material mass distribution of heat exchangers

2.4. Conclusions

In this paper shell and tube heat exchanger implementation for sCO_2 and CO_2+SiCl_4 cycles was investigated. Materials were chosen and thermal design followed by mechanical design was carried out to determine the heat exchange area, number of shells, weight of components, and materials used.

In the case of primary heat exchangers, the effective heat exchange area is almost the same for all considered technologies and cycles; however, by using EMbaffle® one can get smaller diameter shells maintaining the same pressure drop and lack of vibrations. For recuperators, the use of EMbaffle® allows for a smaller effective heat exchange area and smaller throughput area which translates to smaller shell diameters or fewer shells used. Therefore, in all cases, the use of EMbaffle® technology leads to lower weight in expensive alloys.

All considered primary heat exchangers have a similar UA and area. However, due to the lower mass flow and higher density of the CO_2+SiCl_4 mixture compared to sCO_2 the throughput area and therefore number of shells in parallel or shell diameter are smaller in mixture cycles. This leads to the reduction of recompression cycle primary heat exchanger weight by 15 and 6% using conventional and EMbaffle® technology, with 24 and 14% reduction in Alloy 625. The transition from sCO_2 to CO_2+SiCl_4 in the recompression cycle leads to the redistribution of UA, area, and weight from the high-temperature recuperator to the low-temperature recuperator, which will lead to a similar or smaller overall cost or recuperative system.

Additional experimental investigation of enhanced-tubes geometries in EMbaffle® heat exchangers is ongoing at the B&R industrial site to validate performance over pressure drops improvement for next deployments.

2.5. Bibliography

[1] Renewable power generation costs in 2021. Abu Dhabi: IRENA; 2022.

[2] Dostal V, Driscoll MJ, Hejzlar P, Wang Y. Supercritical CO2 Cycle for Fast Gas-Cooled Reactors. Volume 7: Turbo Expo 2004, Vienna, Austria: ASMEDC; 2004, p. 683–92. https://doi.org/10.1115/GT2004-54242.

[3] Crespi F, Rodríguez De Arriba P, Sánchez D, Ayub A, Di Marcoberardino G, Invernizzi CM, et al. Thermal efficiency gains enabled by using CO2 mixtures in supercritical power cycles. Energy 2022;238:121899. https://doi.org/10.1016/j.energy.2021.121899.

[4] Nakayama M, Miyamoto S, Ogawa T, Osae S, Tomono K, Sumimoto M, et al. Thermal decomposition of tetrabromosilane and deposition of crystalline silicon. Materials Science in Semiconductor Processing 2014;23:93–7. https://doi.org/10.1016/j.mssp.2014.02.045.

[5] Doninelli M, Morosini E, Di Marcoberardino G, Invernizzi CM, Iora P, Riva M, et al. Experimental investigation of the CO2+SiCl4 mixture as innovative working fluid for power cycles: Bubble points and liquid density measurements. Energy 2024:131197. https://doi.org/10.1016/j.energy.2024.131197.

[6] Quiñones-Cisneros SE, Zéberg-Mikkelsen CK, Stenby EH. One parameter friction theory models for viscosity. Fluid Ph Equilib 2001;178:1–16. https://doi.org/10.1016/S0378-3812(00)00474-X.

[7] Quiñones-Cisneros SE, Pollak S, Schmidt KAG. Friction Theory Model for Thermal Conductivity. J Chem Eng Data 2021;66:4215–27. https://doi.org/10.1021/acs.jced.1c00400.

[8] Manzolini G, Binotti M, Morosini E, Sanchez D, Crespi F, Marcoberdino GD, et al. Adoption of CO2 blended with C6F6 as working fluid in CSP plants, Freiburg, Germany: 2022, p. 090005. https://doi.org/10.1063/5.0086520.

[9] Weiland NT, Lance BW, Pidaparti SR. sCO2 Power Cycle Component Cost Correlations From DOE Data Spanning Multiple Scales and Applications. Volume 9: Oil and Gas Applications; Supercritical CO2 Power Cycles; Wind Energy, Phoenix, Arizona, USA: American Society of Mechanical Engineers; 2019, p. V009T38A008. https://doi.org/10.1115/GT2019-90493.

[10] Lariviere B, Marion J, Macadam S, McDowell M, Lesemann M, McClung A, et al. sCO2 power cycle development and STEP Demo pilot project. Conference Proceedings of the European sCO2 Conference4th European sCO2 Conference for Energy Systems: March 23-24 2021;2021:352. https://doi.org/10.17185/DUEPUBLICO/73979.

[11] Doctoral Network | TOPCSP 2022. https://topcsp.eu/ (accessed April 24, 2024).

[12] System advisor model (SAM) case study: Gemasolar. NREL 2013:6.

[13] Benoit H, Spreafico L, Gauthier D, Flamant G. Review of heat transfer fluids in tube-receivers used in concentrating solar thermal systems: Properties and heat transfer coefficients. Renewable and Sustainable Energy Reviews 2016;55:298–315. https://doi.org/10.1016/j.rser.2015.10.059.

[14] Span R, Wagner W. A New Equation of State for Carbon Dioxide Covering the Fluid Region from the Triple-Point Temperature to 1100 K at Pressures up to 800 MPa. J Phys Chem Ref Data 1996;25:1509–96. https://doi.org/10.1063/1.555991.

[15] Peng D-Y, Robinson DB. A New Two-Constant Equation of State. Ind Eng Chem Fund 1976;15:59–64. https://doi.org/10.1021/i160057a011.

[16] Rottoli M, Odry T, Agazzi D, Notarbartolo E. EMbaffle® Heat Exchange Technology. Innovative Heat Exchangers 2018:341–61.

[17] Byrne RC. Standards of the Tubular Exchanger Manufacturers Association, Tenth Edition. TEMA; n.d.

[18] Xist n.d. https://www.htri.net/xist (accessed March 21, 2024).

[19] Investigation of thermal storage and steam generator issues. 1993. https://doi.org/10.2172/10189397.

[20] PV Elite®. Hexagon n.d. https://hexagon.com/it/products/pv-elite (accessed April 5, 2024).

[21] Pint BA, Pillai R, Keiser JR. Defining Temperature Limitations for Steels in sCO2 Applications. vol. 38, San Antonio, Texas: 2022, p. 8.

[22] Li K, Zhu Z, Xiao B, Luo J-L, Zhang N. State of the art overview material degradation in high-temperature supercritical CO2 environments. Progress in Materials Science 2023;136:101107. https://doi.org/10.1016/j.pmatsci.2023.101107.

[23] Moore R, Siegel N, Kolb G, Vernon M, Ho C. Design considerations for concentrating solar power tower systems employing molten salt. 2010. https://doi.org/10.2172/1008140.

[24] Taal M. Cost estimation and energy price forecasts for economic evaluation of retrofit projects. Applied Thermal Engineering 2003;23:1819–35. https://doi.org/10.1016/S1359-4311(03)00136-4.

3. Heat exchanger experimental characterization

3.1. Introduction

Heat exchangers represent a significant part of the CSP plant power cycle cost. Especially critical is the primary heat exchanger, which is in contact with both the HTF (solar salt in state-of-the-art power plants) and the power cycle working fluid.

The aim of the experimental campaign is the characterization of the performance of the low finned tubes together with the EMbaffle® heat exchanger in terms of pressure friction factor and heat transfer coefficient under specified process conditions. The core of the experimental test rig (i.e., the proprietary EMbaffle® heat exchanger) for the present measuring campaign has been designed, engineered, and realized at Brembana&Rolle's Valbrembo workshop in the period from April to September 2015. Under a specified temperature level based on the Reynolds and Nusselt numbers analogy, the obtained performance is verified through comparison between the experimental outcomes and the literature correlations.

The further aim is to assess the applicability of water to model molten salts commonly utilized in concentrated solar power plants. This would allow to analyze the heat transfer characteristics of the heat exchanger without having to use molten salts directly.

The two main goals of the present research activity are therefore:

1. To investigate the performance of the novel technology.
2. To evaluate the use of water as a substitute for molten salts in the test heat exchanger.

3.2. Experimental setup description

The EMbaffle® test heat exchanger is a fixed tube-sheet exchanger with one pass tube side and one pass shell side in counterflow configuration as shown in the layout schematic in Figure 3.1a. Shell inlet and outlet are made with vapor belts, as can be seen in the heat exchanger view in Figure 3.1b. EMbaffle® technology allows for longitudinal flow at the shell side and pure counter-current heat transfer. The main features of the test exchanger are reported in Table 3.3. Two baffle spacings were tested: 200 and 343 mm.

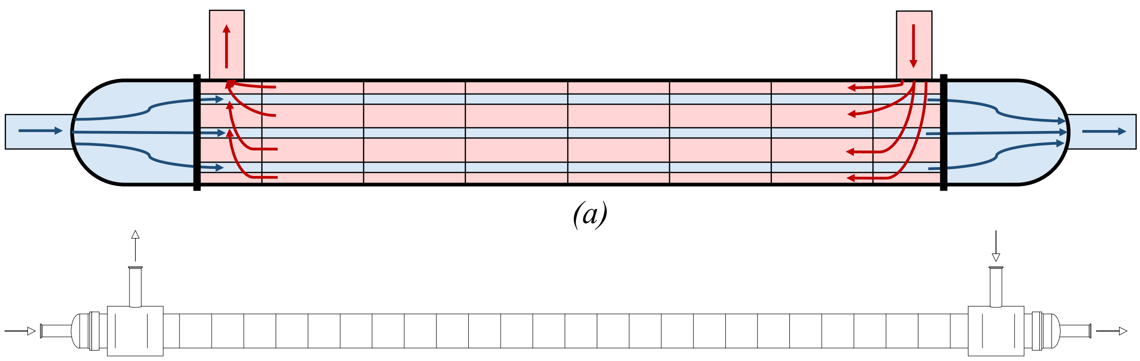

(a)

(b)

Figure 3.1. The heat exchanger schematic layout (a) and view (b)

Table 3.3. The main features of the test heat exchanger

Parameter	Units	Value
Shell internal diameter	mm	211.58
Tube number	-	62
Outside tube diameter	mm	15.875
Tube thickness	mm	1.65
Effective tube length	mm	5820
Tube material	-	SA-789 S31803
EMbaffle® grid baffle type	-	5/8" – B
Baffle spacings	mm	200 and 343

The experimental setup is made of a fully instrumented EMbaffle® test counterflow exchanger with water at both the shell and the tube sides, as can be seen in Figure 3.2. Hot water is supplied to the shell from the hot water tank by a pump. After being cooled in the heat exchanger, hot water, routed at the shell side, passes through the three-way thermostatic valve. This valve controls the amount of water to be sent to the boiler to increase its temperature before mixing it with the rest of the flow; then water is released to the hot water tank. By setting the target temperature in a three-way valve, the hot water tank inlet temperature and, consequently, the heat exchanger hot side inlet temperature can be controlled. Cold water is supplied by the pump from the cold water tank to the tube side of the heat exchanger, warmed up, and sent back to the same tank.

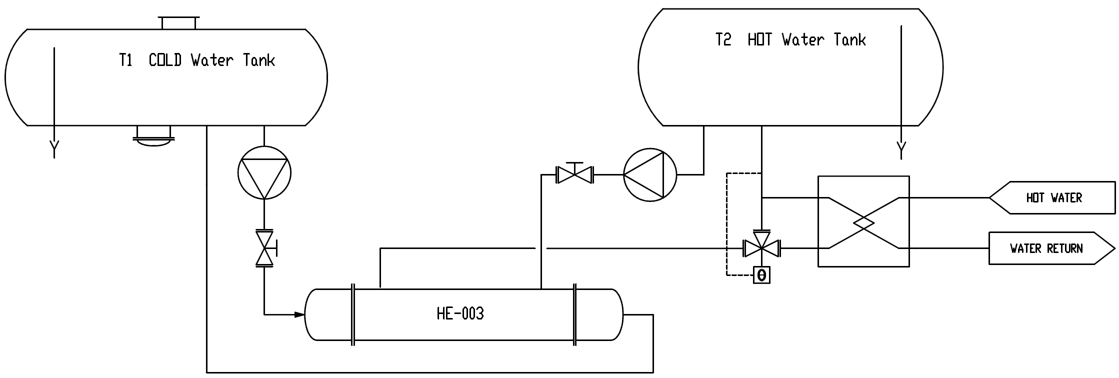

Figure 3.2. Experimental setup layout

The measurement probes locations in the heat exchanger are shown in Figure 3.3 and described in Table 3.4. Both hot and cold water flow rates are controlled by valves positioned after the pumps, as shown in Figure 3.3. The volumetric flow rate is measured by flowmeter FT01 at the shell inlet. To measure the cold flow, a bridge with a valve between the pumps outlets was added. At the tube side, temperature is measured at the inlet (TT20) and outlet (TT21). At the shell side inlet, the temperature (TT30) is being measured, while at the outlet, the temperature (TT38) and pressure (PIT36) are measured.

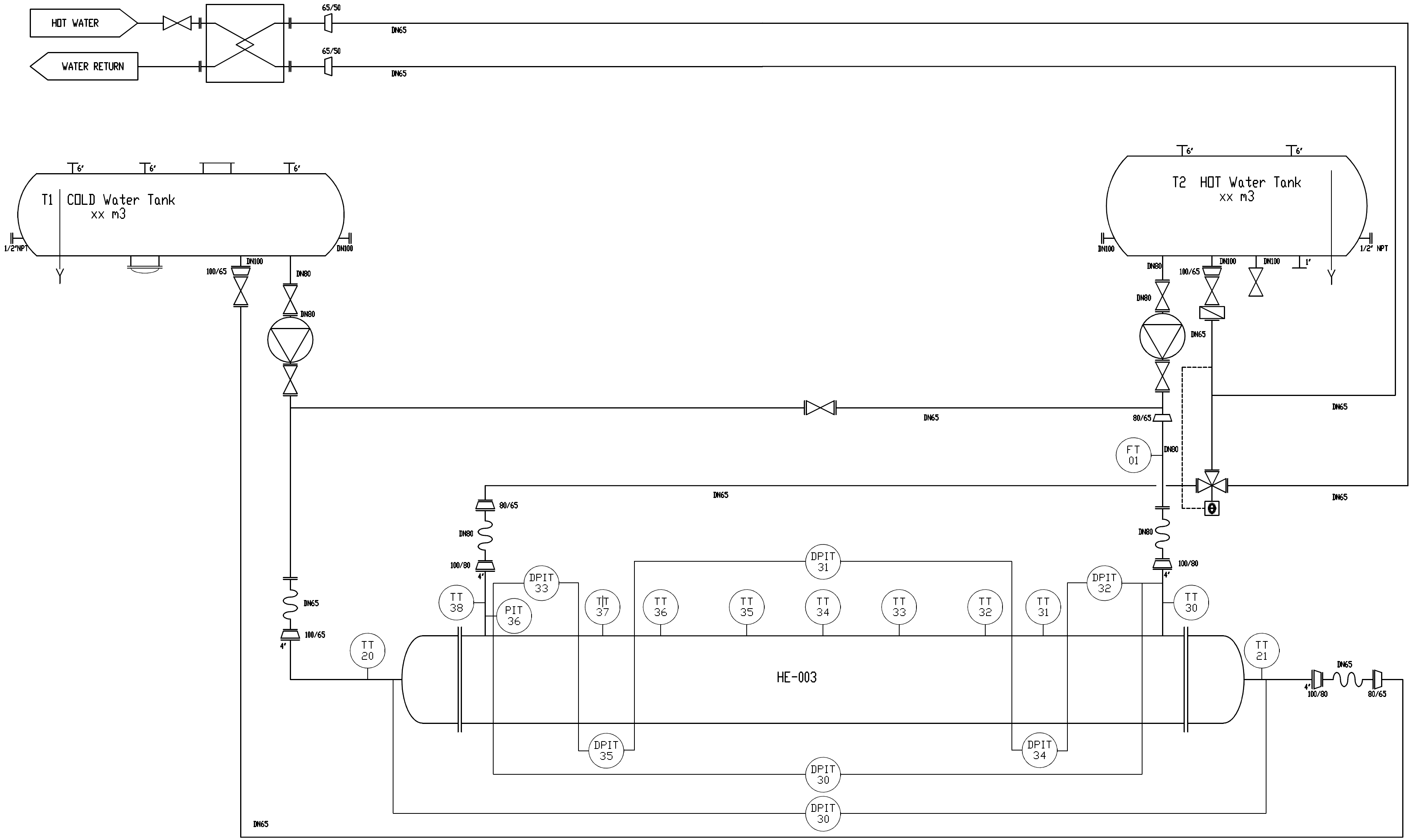

Figure 3.3. Experimental setup piping and instrumentation diagram

Along the shell, seven temperature probes are installed (TT31-37) along with six pressure difference measurements (DPIT31-35):

- Vapor belts inlet (DPIT32) and outlet (DPIT33) regions.
- Flow transition zone at inlet (DPIT34) and outlet (DPIT35).
- Heat exchanger central zone where the flow is longitudinal and stabilized (DPIT31) and the whole heat exchanger (DPIT30).

Inlet pressure can be calculated from the pressure difference measurements between the inlet and outlet (DPIT30).

Table 3.4. Heat exchanger measurements locations list

Description	Distance from tube inlet, m
T shell side inlet	-
T1 shell side	5.257
T2 shell side	4.662
T3 shell side	3.982
T4 shell side	3.062
T5 shell side	1.862
T6 shell side	1.147
T7 shell side	0.560
T shell side outlet	-
T tube side inlet	-
T tube side outlet	-
P shell side inlet	5.820
P after vapor belt inlet	5.337
P after flow transition inlet	4.837
P after central zone and before flow transition outlet	0.982
P before vapor belt outlet	0.475
P shell side outlet	-
P tube side inlet	
P tube side outlet	

The list of measuring devices used is shown in Table 3.5 together with the value being measured, tag, precision class, signal, and ranges. In summary, it is possible to measure temperatures and pressures at the inlet and outlet for both sides of the heat exchanger, while an additional four pressures and seven temperatures are measured on the shell side to better characterize the EMbaffle® performance along the length of the heat exchanger.

Table 3.5. Measuring instruments list

Description	Model	Precision class	Tag	Value range	Value units	Notes
T shell side inlet	PT100	1/3 DIN	TT30	0.0-150.0	°C	
T1 shell side	PT100	1/3 DIN	TT31	0.0-150.0	°C	TE isolated
T2 shell side	PT100	1/3 DIN	TT32	0.0-150.0	°C	TE isolated
T3 shell side	PT100	1/3 DIN	TT33	0.0-150.0	°C	TE isolated
T4 shell side	PT100	1/3 DIN	TT34	0.0-150.0	°C	TE isolated
T5 shell side	PT100	1/3 DIN	TT35	0.0-150.0	°C	TE isolated
T6 shell side	PT100	1/3 DIN	TT36	0.0-150.0	°C	TE isolated
T7 shell side	PT100	1/3 DIN	TT37	0.0-150.0	°C	TE isolated
T shell side outlet	PT100	1/3 DIN	TT38	0.0-100.0	°C	
T tube side inlet	PT100	1/3 DIN	TT20	0.0-100.0	°C	
T tube side outlet	PT100	1/3 DIN	TT21	0.0-100.0	°C	
External DP total shell side	PMD55	0.1%	DPIT30	0.0-150.0	kPa	differential

Description	Model	Precision class	Tag	Value range	Value units	Notes
DP total central shell side	PMD55	0.1%	DPIT31	0.0-50.0	kPa	differential
DP vapor belt inlet	PMD55	0.1%	DPIT32	0.0-50.0	kPa	differential
DP vapor belt outlet	PMD55	0.1%	DPIT33	0.0-50.0	kPa	differential
DP flow transition inlet	PMD55	0.1%	DPIT34	0.0-50.0	kPa	differential
DP flow transition outlet	PMD55	0.1%	DPIT35	0.0-50.0	kPa	differential
P outlet shell side	PMC51	0.1%	PIT36	0.0-250.0	kPa	absolute
Circuit water flow rate	Promag P 10 DN80 / 3"	0.5%	FIT21	0.0-7500.0	l/h	

All the temperatures were measured with PT100 temperature probes using a 4-20 mA transmitter. The flowmeter is a Promag P 10 DN80 / 3" produced by Endress+Hauser with characteristics shown in Table 3.6. The minimum flow rate is 0.72 m^3/h, while the maximum is 180 m^3/h (0.01 to 10 m/s) [1]. The measurement principle is based on Faraday's law in electrically conductive fluids. A magnetic field is created in the flow tube by the coils placed on either side of it. The value of potential difference created is linearly proportional to the flow velocity perpendicular to the magnetic flux lines. The voltage induced in the fluid is measured by two electrodes constructed from non-reacting material inserted into opposite sides of the flow tube.

Table 3.6. Flowmeter specification

Parameter	Units	Minimum	Nominal	Maximum
Flow rate	m^3/h	5	40	65
Velocity	m/s	0.283	2.267	3.684
Volumetric flow rate measurement error	%	0.85	0.54	0.53

For absolute pressure measurements, capacitive pressure transmitters produced by Endress+Hauser were used. Their specification is shown in Table 3.7. Fluid pressure pushes the process isolating diaphragm (Ceraphire 99.9% Al_2O_3) with displacement determined by measuring the capacitance change between the electrode plate installed on the diaphragm and an electrode metal plate installed in the body of the sensor.

Table 3.7. Pressure transmitter PMC51 specification

Parameter	Units	Minimum	Nominal	Maximum
Ambient temperature	°C	0	5	10
Process temperature	°C	0	40	60
Range	kPa		250	
Pressure measurement error	%		0.85	

For differential pressure measurements, transmitters with piezoresistive sensors produced by Endress+Hauser were used. Their performance is shown in Table 3.8. During measurement, welded metallic process membranes are deflected on both sides by the pressures present, after which a fill fluid transfers the pressures to a resistance circuit bridge with a piezoresistive sensor.

Table 3.8. Pressure transmitter PMD55 specification

Parameter	Units	Minimum	Nominal	Maximum
Ambient temperature	°C	0	5	10
Process temperature	°C	0	40	60
Range	kPa	50		150
Pressure measurement error	%	0.39		0.52

The total error of pressure transmitters is based on the measurement point and years of service. The total error shown was calculated for standard and operational conditions presented in the tables using Endress+Hauser Applicator [2] for 1 year.

The pumps used are produced by KSB model ETB 80-65-315/00226 with characteristics shown in Table 3.9.

Table 3.9. Pump specification

Parameter	**Units**	**Value**
Impeller diameter	mm	305
Design point efficiency	%	72.04
Design point head	m	30
Net positive suction head required	m	1.56
Head at zero flow rate	m	34.76
Minimum flow rate	m^3/h	11.86
Design point flow rate	m^3/h	75.01

Field data collection has been done by using a local programmable logic controller (PLC) hardwired to the field instrumentation and working as a data logger. One personal computer communicating with the local PLC has been used as a human-machine interface and to export test campaigns measured data for later analysis.

3.3. Design of experiment

Molten salts are used as a heat transfer and storage fluid in CSP plants under various temperature levels. To be able to model the heat transfer and pressure drop characteristics of a heat exchanger working with molten salts without using them during the testing, a combination of fluid parameters and process conditions leading to the same relevant dimensionless numbers as in the original CSP application is used [3]. By not using solar salts, sensible plant management and maintenance simplification can be achieved, in addition to reducing associated safety concerns. For pressure drop, the relevant dimensionless parameter is the Reynolds number shown in equation (3.1), which is defined as a ratio between inertial and viscous forces in the liquid and allows for the characterization of the inherent fluid dynamic behavior of the flow.

$$Re_p = \frac{\rho V D_p}{\mu_b} \tag{3.1}$$

where Re_p – hydraulic Reynolds number; ρ – density; V – velocity; D_p – hydraulic characteristic diameter; μ_b – fluid dynamic viscosity at bulk fluid temperature.

Forced convection dominates heat transfer in the test campaign, as well as in most flows of industrial relevance. In that case, the dimensionless numbers to be considered other than Reynolds are Nusselt and Prandtl [3]. They describe heat transfer between the process and the utility flows and the change in thermophysical properties of the fluids under comparison, respectively [4]:

$$Nu = C \cdot Re_h^X Pr^{0.4} (\frac{\mu_b}{\mu_w})^{0.14} \tag{3.2}$$

$$Re_h = \frac{\rho V D_h}{\mu_b} \tag{3.3}$$

$$Pr = \frac{\nu}{a} \tag{3.4}$$

where C – coefficient based on the geometry and flow regime; Re_h – thermal Reynolds number; D_h – thermal characteristic diameter; μ_w – fluid dynamic viscosity at wall temperature; $\nu = \frac{\mu_b}{\rho}$ – fluid kinematic viscosity; a – thermal diffusivity; X – 0.6 for laminar and 0.8 for turbulent flow.

In the current application, a molten salt flow with a Reynolds number in the range 5700-7800 is simulated. It is characteristic of primary heat exchangers of CO_2 power cycles and reheater, preheater, and part of the evaporator of steam generators with a 550°C turbine inlet temperature. Therefore, in order to model molten salt with water, one has to reach Reynolds and Prandtl numbers as close as possible to the application. The viscosity ratio based on temperature change also has an effect on heat transfer. However, it appears with an exponent of only 0.14 in the Nusselt correlation. The Prandtl number for water is a function of temperature, while the Reynolds number depends on temperature and velocity (assuming constant geometry). For that reason, the temperature of the water was chosen based on Prandtl number similarity, while the velocity of the fluid was identified from the Reynolds number range specified.

The properties dependence on the temperature for water [5] and solar salt (60 wt% $NaNO_3$, 40 wt% KNO_3) [6] are shown in Figure 3.4. One can see that water at temperatures between 10 and 60°C has a Prandtl number almost identical to solar salt at temperatures between 290 and 570°C, which allows for Prandtl number similarity. Yet, density and dynamic viscosity are much higher for solar salt, while conductivity is 14-15% smaller.

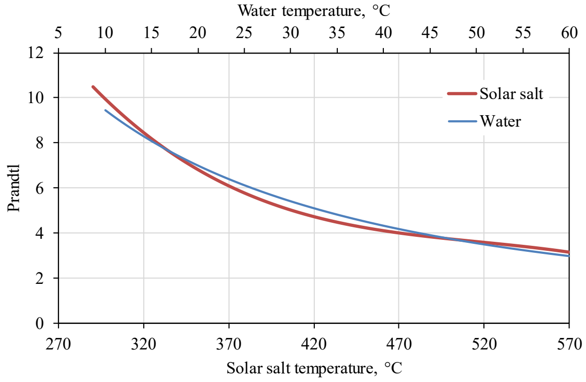

(a)

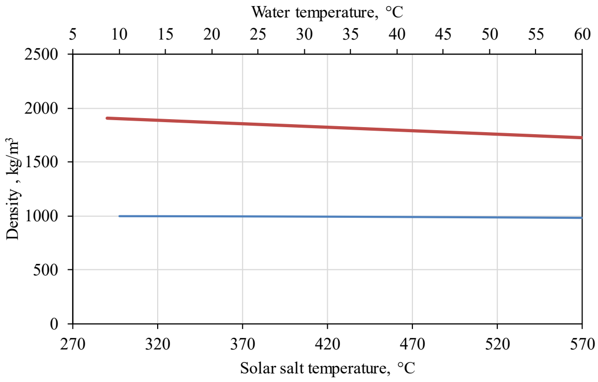

(b)

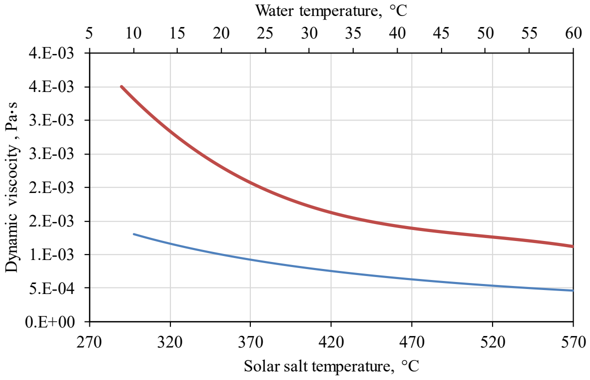

(c)

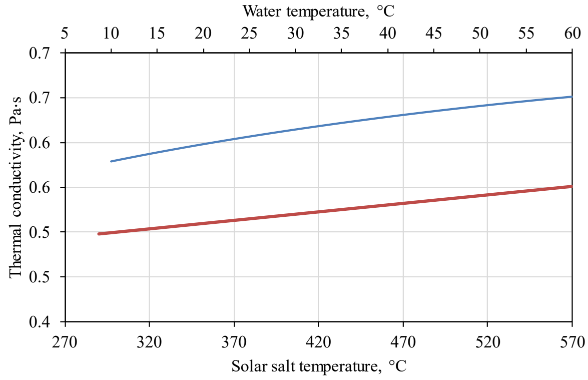

(d)

Figure 3.4. Properties of solar salt and water vs temperature: (a) Prandtl number, (b) density, (c) dynamic viscosity, (d) thermal conductivity

However, as mentioned before, in the Reynolds formulation, the important factor is the ratio between viscous and inertial forces, which can be described by kinematic viscosity shown in Figure 3.5a. This ratio is 20-30% higher for solar salt compared to water, which can be corrected by the decrease of water velocity by the same percentage. In Figure 3.5b one can see the relative change in the dynamic viscosity dependence on temperature is almost identical for solar salt and water, therefore, the dynamic viscosity correction in the Nusselt equation is expected to have a negligible effect.

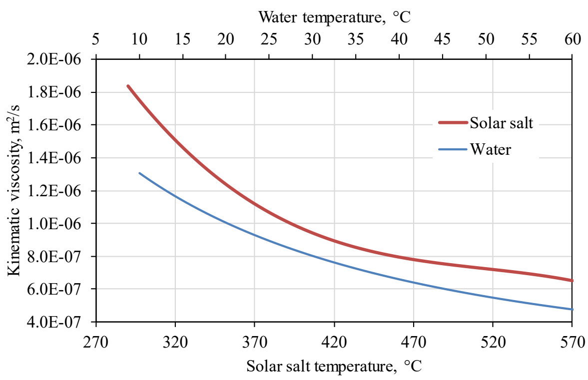

(a)

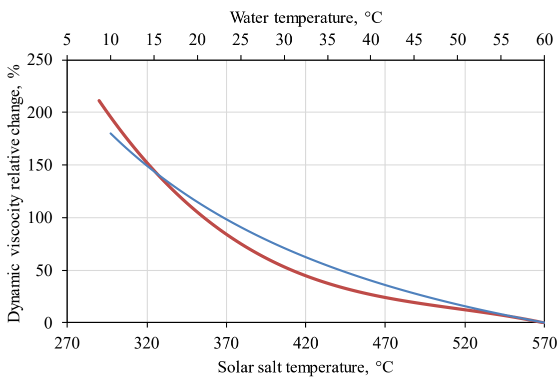

(b)

Figure 3.5. Kinematic viscosity (a) and dynamic viscosity relative change (b) for solar salt and water vs temperature

For different hot water temperatures based on Reynolds numbers range, the hot water flow rate was calculated to be between 20 and 55 m^3/h, as can be seen in Figure 3.6. For all the conditions considered, the flow has a turbulent nature.

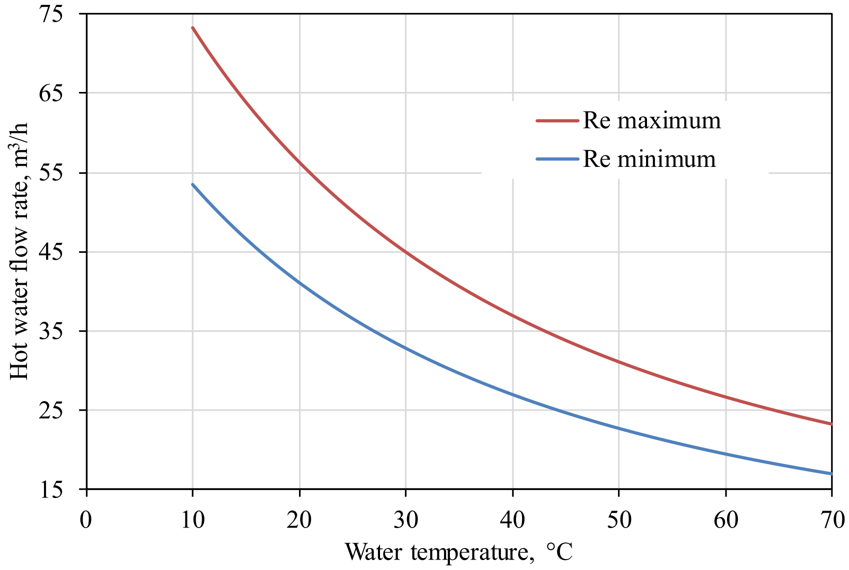

Figure 3.6. Hot water flow rate in the shell for maximum and minimum Reynolds numbers vs water temperature

For the design of the experiment phase, the cold flow temperature was assumed to be 5°C with a constant flow rate of 16 m^3/h. The hot flow temperature was varied between 20, 40, and 60°C, with the flow rate determined by minimum, average, and maximum Reynolds numbers. The test cases are shown in Table 3.10 with volume and mass flows.

Table 3.10. Heat exchanger test cases

Test	$T_{hot\ in}$, °C	Q_{hot}, m^3/h	Q_{cold}, m^3/h	G_{hot}, kg/h	G_{cold}, kg/h
1	60	19.4	16	19090	16000
2	60	23.0	16	22607	16000
3	60	26.6	16	26124	16000
4	40	26.9	16	26737	16000
5	40	31.9	16	31662	16000
6	40	36.9	16	36587	16000
7	20	41.1	16	41025	16000
8	20	48.7	16	48582	16000
9	20	56.2	16	56140	16000

Tests were carried out in two campaigns. The first campaign was done using the smaller baffle spacing 1 and happened on 2025.02.04, 2025.02.06, 2025.02.10, 2025.02.13, 2025.02.18, 2025.02.19, 2025.03.10, 2025.03.11, 2025.03.12, 2025.03.17, 2025.03.18, and 2025.03.25 with data recording done in 5 second intervals. The second campaign with bigger baffle spacing 2 was done on 2025.04.28, 2025.05.05, 2025.05.07, and 2025.05.09 with data recorded in 30 seconds intervals. The change in data recording frequency was made due to the slow nature of thermal processes, on the scale of hours and 5 second recording intervals being excessive.

3.4. Friction factor

Pressure drop characterization was done by calculating the Fanning friction factor for the central zone. It is located around 4.6 shell diameters after the inlet and before the exit of the heat exchanger, making this a zone with developed flow. The pressure drop measured is DP total central shell side (DPIT31). First, the pressure drop associated with the baffles was calculated according to [4] using equation (3.5), after which the pressure drop associated with the tube friction was determined from the total pressure drop following equation (3.6). After that, the low finned tube Fanning friction factor was calculated from equation (3.8).

$$\Delta P_B = K_B N_B \frac{\rho {V_B}^2}{2} \tag{3.5}$$

$$\Delta P_L = \Delta P_{Total} + \Delta P_B \tag{3.6}$$

$$D_p = \frac{({D_S}^2 - N_T\, {D_o}^2)}{D_S + D_o} \tag{3.7}$$

$$\Delta P_L = 2f \frac{L\rho {V_S}^2}{D_p} \tag{3.8}$$

$$f_{HTRI} = \begin{cases} 1.75(\frac{16}{Re}), if\ Re < 1333 \\ 1.75(0.012), if\ 1333 \leq Re \leq 3571 \\ 1.75\left(0.0035 + \frac{0.0264}{Re^{0.42}}\right), if\ Re > 3571 \end{cases} \tag{3.9}$$

where K_B – baffle loss coefficient; N_B – number of baffles; $V_B = \frac{Q}{A_B}$ – baffle velocity with Q – volume flow, A_B – baffle area; f – Fanning friction factor; L – zone length; D_S – shell inner diameter; D_o – tube outer diameter over the fin; D_b – outer bundle diameter; N_T – number of tubes; V_S – fluid velocity in shell.

To calculate the friction factor, all the experimental data was first cleaned following the conditions below to make sure the flow has stabilized enough:

- Hot water flow rate (FIT21) and total pressure drop (DPIT31) rolling coefficients of variation (RCV) should be below 1% for 1 minute window.
- Hot water flow rate (FIT21) should be above 10 m^3/h.
- Shell inlet pressure (PIT36-DPIT31) should be above 150 kPa.
- The sum of differential pressure measurements on the shell side is equal to the total pressure drop within 0.5 kPa (DPIT31+DPIT32+DPIT33+DPIT34+DPIT35=DPIT30).

The resulting Fanning friction factor for low finned tubes calculated from experimental data and form correlations is shown in Figure 3.7. The outcomes of the second test campaign (baffle spacing 2) are well represented by the literature correlations. For the first test campaign (baffle spacing 1), correlations do not properly describe the calculated Fanning friction factor. Such mismatch may be due to the turbulent interaction of the stream and the closely spaced baffles, which is not captured by the correlation.

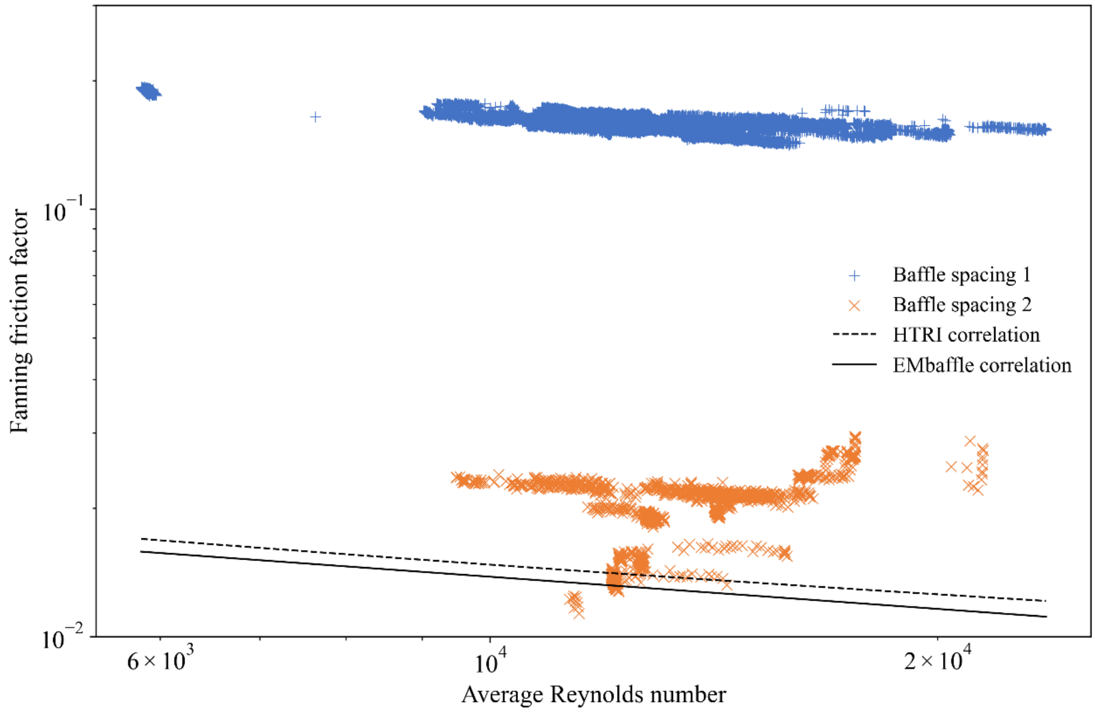

Figure 3.7. Fanning friction factor vs average Reynolds number for low finned tubes

3.5. Nusselt number

During the experiment, the hot water flow rate in the shell side is measured along with its temperature and pressure at the inlet, outlet, and along the shell length. This allows splitting the heat exchanger into zones within which the heat transfer coefficient can be calculated. Two inlet (TT30-TT31, TT31-TT32) and outlet zones (TT36-TT37, TT37-TT38) are characterized by being still in the flow transition area, which will influence the heat transfer phenomenon. Therefore, for determining the pure counterflow stabilized heat transfer, the central zone between TT32 and TT36 is selected.

The process of determining the hot shell side heat transfer coefficient is as follows:

1. The amount of heat exchanged is being determined for all zones based on shell temperature readings and volume flow measured.
2. The volume flow on the cold tube side is calculated based on the whole heat exchanger duty, inlet, and outlet temperature and compared to the design value.
3. The cold tube side fluid temperatures along the tube length are calculated based on the flow rate, inlet temperature, and zone duty.
4. After that, the temperature difference and heat exchange area are calculated for each zone.
5. The cold tube side heat transfer and thermal resistance coefficients, along with the wall thermal resistance, are calculated.
6. Based on the zone duty, temperature difference, and area, the zone's overall heat transfer coefficient is calculated.
7. The hot side thermal resistance is calculated based on the zone's overall heat transfer coefficient, cold side, and tube wall thermal resistance.
8. Based on hot side thermal resistance, the hot-side heat transfer coefficient and Nusselt number are calculated.

Based on this analysis, one can compare the hot shell side heat transfer coefficient and Nusselt number both for the whole heat exchanger and separate zones. The tube side heat transfer coefficient was calculated according to Gnielinski [7] (based on Petukhov-Kirilov equation [8]) with Filonenko friction factor [9]:

$$f = (1.82\, log_{10}\, Re_T - 1.64)^{-2}/4 \tag{3.10}$$

$$Nu_T = \frac{f/2(Re_T - 1000)Pr}{1 + 12.7(\, Pr^{2/3} - 1)\sqrt{f/2}} \tag{3.11}$$

where $Re_T = \frac{\rho \cdot V_T \cdot D_i}{\mu_T}$ – Reynolds number with D_i – internal diameter, μ – dynamic viscosity; G – mass velocity; Pr – Prandtl number; $Nu = \frac{\alpha_T D}{\lambda_T}$ – Nusselt number with α – heat transfer coefficient and λ – thermal conductivity; $_T$ subscripts indicate parameters corresponding to the tube side.

Shell side heat transfer coefficient and Nusselt number were calculated according to [4,10,11]:

$$D_{eff} = D_r + 2\delta h N_{fpi} \tag{3.12}$$

$$D_h = \frac{4(P_T - \pi/4\, {D_{eff}}^2)}{\pi D_{eff}} \tag{3.13}$$

$$Nu = \alpha \frac{D_h}{\lambda} \tag{3.14}$$

$$h' = h(1 + 0.35\, ln \frac{D_f}{D_r}) \tag{3.15}$$

$$h^* = \frac{h'}{\sqrt{\frac{\lambda_S \delta}{2\alpha_S}}} \tag{3.16}$$

$$\eta_f = \frac{tanh\,(\,h^*)}{h^*} \tag{3.17}$$

$$\eta_0 = \frac{A_f \eta_f + A_w}{A} \tag{3.18}$$

where δ – fin thickness; h – fin height; N_{fpi} – fins per meter; D_r – tube root diameter; D_f – tube outside diameter with fin; D_{eff} – finned tube effective diameter; P_T – baffle geometric parameter; η_f – fin efficiency; η_0 – overall surface efficiency; $_S$ subscripts indicate parameters corresponding to the shell side; A_f – fin area; A_w – wall area; A – total tube area.

For each zone, LMTD and total thermal resistance were determined, after which tube side and wall thermal resistance were calculated to determine the shell side thermal resistance. It was used to calculate the shell side heat transfer coefficient:

$$Q = LMTD \cdot UA \tag{3.19}$$

$$R_W = \frac{ln(D_{eff}/D_i)}{2\pi\lambda_W L} \quad (3.20)$$

$$R_T = \frac{1}{\alpha_T 2\pi D_i L} \quad (3.21)$$

$$R_S = \frac{1}{UA} - R_W - R_T \quad (3.22)$$

$$\alpha_s = \frac{1}{\eta_0 R_S 2\pi D_{eff} L} \quad (3.23)$$

where R – thermal resistance; λ_W – tube wall thermal conductivity (Table 3.11); $_S$, $_W$ and $_T$ subscripts indicate parameters corresponding to the shell side, tube wall, and tube side, respectively; D_i – tube internal diameter.

Equations (3.16)-(3.18) and (3.23) are solved iteratively until convergence of the results is achieved.

Table 3.11. Thermal conductivity of SA-789 S31803

T, °C	20	50	75	100	125	150	175	200	225
λ_W, W/(m·K)	14.1	14.6	15	15.4	15.7	16.1	16.5	168	17.2
T, °C	250	275	300	325	350	375	400	425	-
λ_W, W/(m·K)	17.6	17.9	18.3	18.7	19	19.4	19.7	20.1	-

The procedure described is valid only under conditions of thermal equilibrium. Since the experimental setup doesn't have the cooling and cold water is being recirculated back to the cold tank, the temperature of cold water is naturally increasing during the experiment. Furthermore, it was found that the power of the boiler was not able to completely compensate for the heat loss in the heat exchanger. Therefore, a dynamic behavior, like the one represented in Figure 3.8, was observed. This required careful control and monitoring during the experiment to ensure conditions were as close to equilibrium as possible. The maximum flow rate reached in the system was around 42 m^3/h with the thermostatic valve closed (all flow bypassing the boiler) and 32 m^3/h with it being fully open (all flow going to the boiler). Finally, the irregularities in hot water flow could be due to the required net positive suction head (NPSH) being lower than the available one at hot water flow rates above 30 m^3/h.

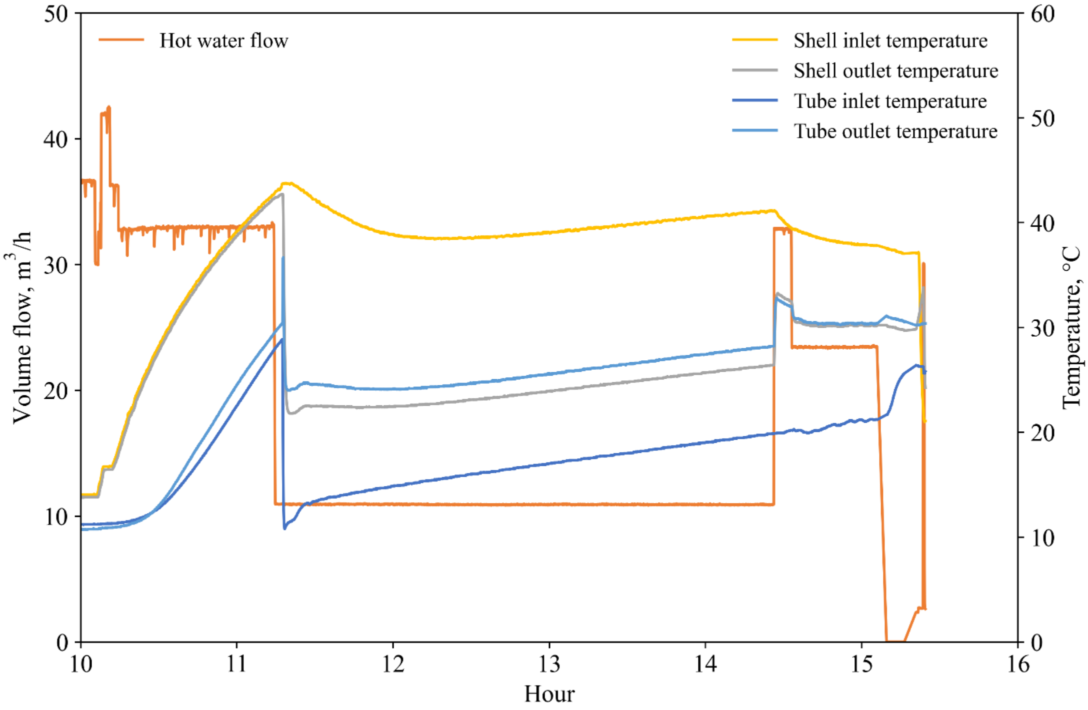

Figure 3.8. Hot water mass flow rate and main temperatures recorded on 2025.02.19

To obtain points closest to the equilibrium, data has been cleaned before successive analysis. Details of data cleaning and algorithms used are reported in Appendix A: Data cleaning. The Nusselt number for points identified with different algorithms (rolling Z-score (RZS), RCV, density-based spatial clustering of applications with noise (DBSCAN)) are shown in Figure 3.9. The obtained points were fitted with equation (3.24), which has an exponent of 0.8 for turbulent flow as in (3.2), and equation (3.25) to obtain both the constant and the exponent from the same equation. The resulting coefficients for both are shown in Table 3.12.

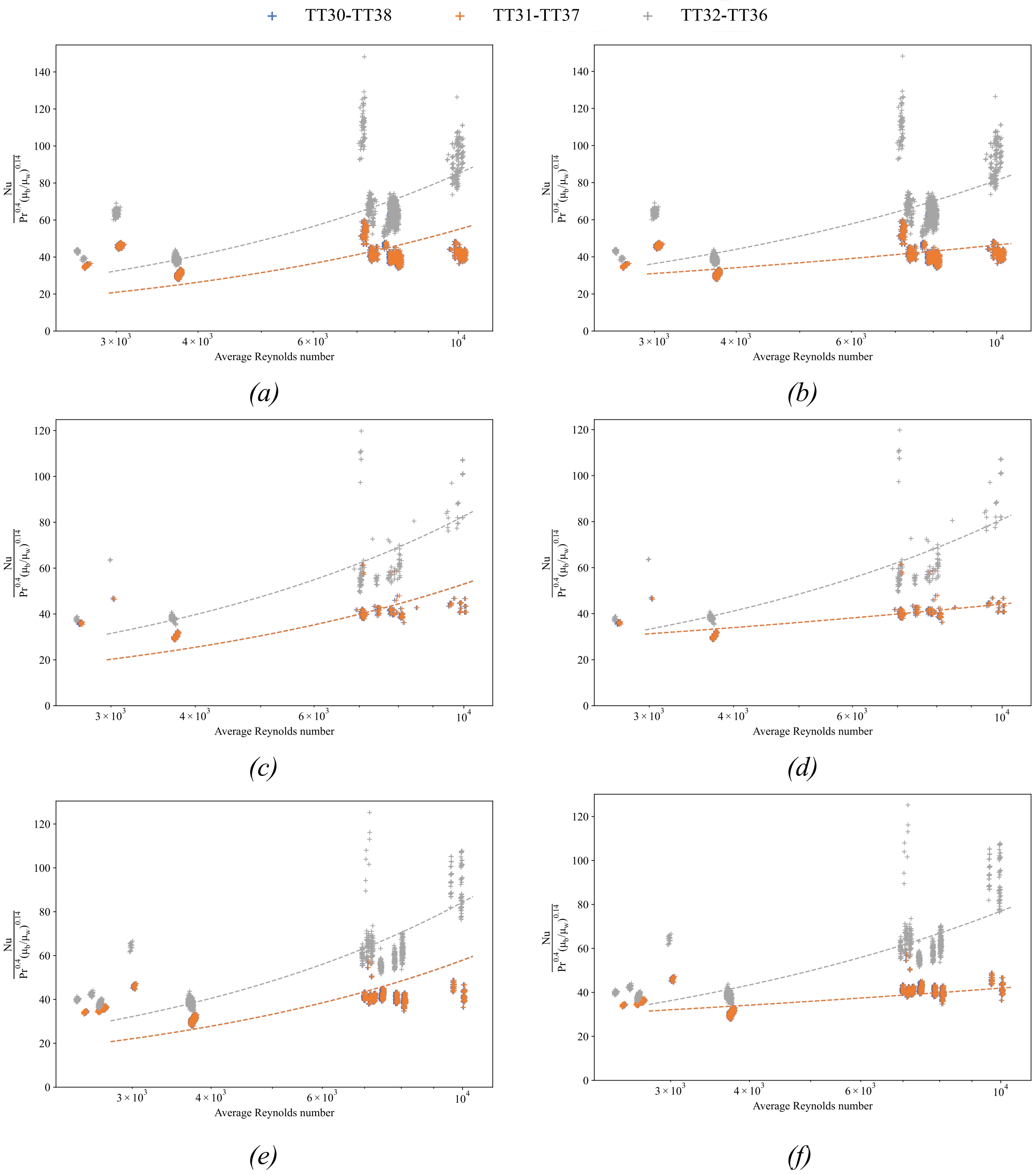

Figure 3.9. Nusselt number dependence on the Reynolds number for RCV (a and b), RZS (c and d), and DBSCAN (e and f) fitted with equations (3.24) and (3.25), respectively

In the case of turbulent flow along the finned tubes, the Reynolds number exponent (X) is usually in the range of 0.75-0.8 (0.8 from [13,14], 0.764 from [15], 0.75 from [16], 0.76 from [17]). This is close to the results obtained using the RZS algorithm for TT32-TT36, which represents the central portion of the heat exchanger with developed longitudinal flow. The coefficient C_1 is around 0.05 for TT32-TT36 and 0.035 for TT30-TT38 and TT31-TT37 zones. At the same time, the constants C_1 and C_2 depend on the baffle design and tube geometric parameters, which are specific for each configuration and cannot be directly compared with literature data.

$$\frac{Nu}{Pr^{0.4}(\frac{\mu_b}{\mu_w})^{0.14}} = C_1 \cdot Re^{0.8} \tag{3.24}$$

$$\frac{Nu}{Pr^{0.4}(\frac{\mu_b}{\mu_w})^{0.14}} = C_2 \cdot Re^{X} \tag{3.25}$$

Table 3.12. Coefficients fitted for equations (3.24) and (3.25) for baffle spacing 1

Outlier detection algorithm	TT32-TT36			TT30-TT38 and TT31-TT37		
	C_1	C_2	X	C_1	C_2	X
RCV	0.054	0.17	0.67	0.035	2.15 and 2.14	0.33
RZS	0.052	0.090	0.74	0.033	3.14	0.29
DBSCAN	0.053	0.24	0.62	0.037	5.4	0.22

During the second campaign, the 1926 lines of data were acquired, with 1666 lines having hot water flow above 5 m^3/h. During the second campaign, the temperature probe TT32 showed values higher than TT31, indicating the wrong positioning. At the same time the TT33 probe wasn't active. Therefore, for the central zone of the heat exchanger, the part between TT34 and TT36 was chosen. The results of the calculation are shown in Figure 3.10, with correlation coefficients shown in Table 3.13. In Figure 3.10a and Figure 3.10b, one can clearly see a big discrepancy between the TT30-TT38 and the rest of the results, which could be due to the inlet and outlet flow transition effect influencing heat transfer. Regarding the results of the TT31-TT37 and TT34-TT36 zones, the values in Figure 3.10c and Figure 3.10d are more in line with each other. In the case of zone TT31-TT37, the heat transfer coefficient is bigger than in smaller baffle spacing 1. Further tests are required to validate this.

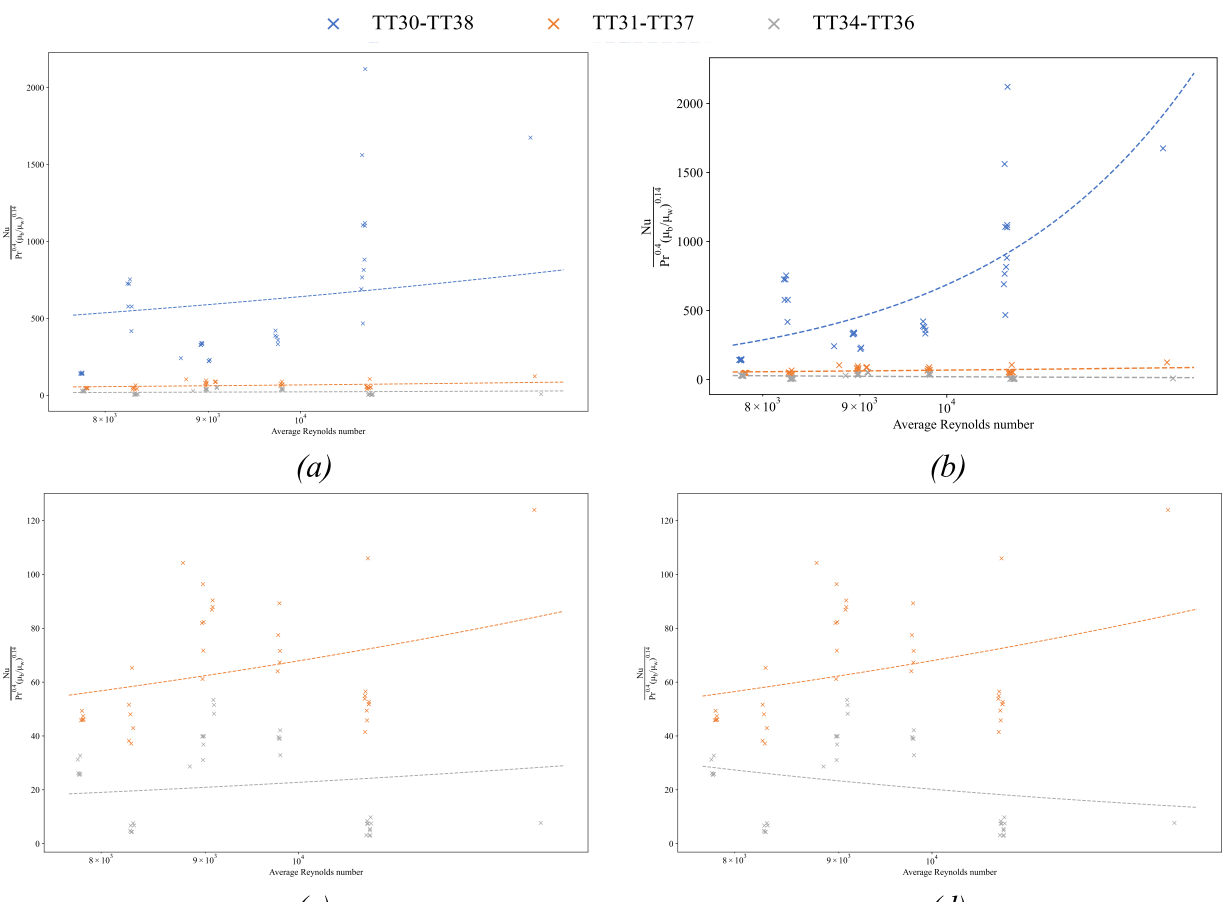

Figure 3.10. Nusselt number dependence on the Reynolds number fitted with equations (3.24) (a and c) and (3.25) (b and d)

Table 3.13. Coefficients fitted for equations (3.24) and (3.25) for baffle spacing 2

TT34-TT36			TT31-TT37			TT30-TT38		
C_1	C_2	X	C_1	C_2	X	C_1	C_2	X
0.014	$5.2\cdot10^{6}$	-1.4	0.043	0.033	0.83	0.405	$1.5\cdot10^{-13}$	3.9

The resulting 240 points from the first and 37 points from the second campaign are shown in Figure 3.11. The experimental setup limits can be seen for both the maximum shell side flow rate and maximum shell side inlet temperature obtained, as was pointed out before. On the other hand, the Reynolds numbers of interest were obtained for an average hot water temperature from 30 to 45°C which would translate to a solar salt temperature from 400 to 480°C.

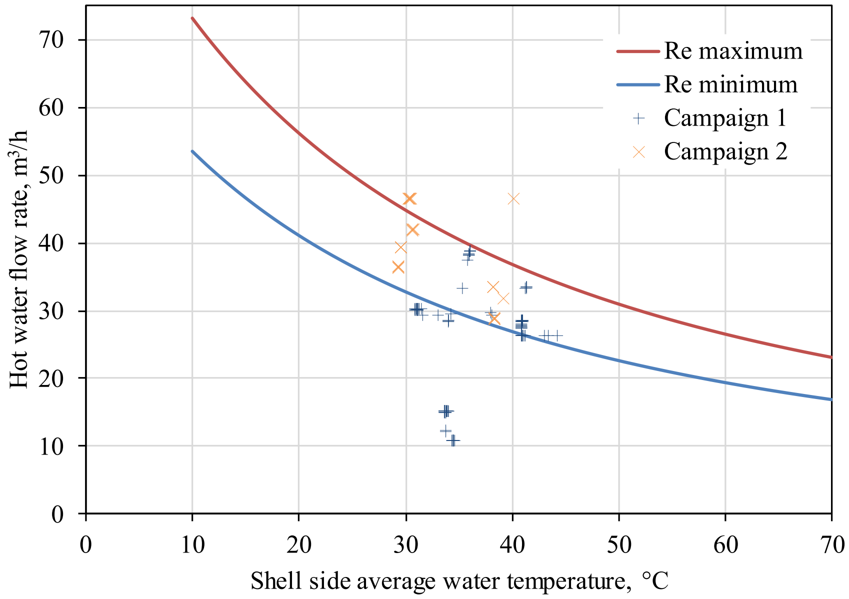

Figure 3.11. Planned and obtained points for baffle spacing 1 using RZS and baffle spacing 2

3.6. Conclusions

The similarity of molten solar salt and water was explored, and the design of the experiment was developed with water temperature ranges based on the Prandtl number similarity and flow rate based on the Reynolds number similarity. This allowed to test the heat exchanger heat transfer characteristics without the need of complex equipment to operate with solar salt. The experimental tests of EMbaffle® heat exchanger with low finned tubes were carried out in two experimental campaigns with two different baffle spacings.

The Fanning friction factor for finned tubes was calculated for both baffle spacings for the central heat exchanger zone with developed longitudinal flow. For the baffle spacing 2, the Fanning friction factor results are close to the correlations. On the other hand, for smaller baffle spacing 1, the calculated Fanning friction factor is not properly described by correlations. This behaviour requires additional investigation.

To characterize the technology heat transfer performance, the shell side Nusselt number was calculated and correlated with the average Reynolds number. Three zones were chosen for calculation: the whole heat exchanger, the central zone with developed longitudinal flow, and the central zone together with flow transition zones. The experimental data for the first campaign was cleaned using the rolling Z-score in order to obtain the data points closest to the thermal equilibrium condition. The resulting correlation coefficients for the central zone were found to be in accordance with the correlations available in the literature for exchanger designs with low finned tubes. For the second campaign, the result indicates that there is an increment of heat transfer with bigger baffle spacing, a behavior that needs to be further investigated.

The heat transfer performance results obtained cover the whole Reynolds range of interest (5700-7800), even if, due to the experimental setup limitations, it was not possible to reach high shell side inlet temperature and high shell side flow rates. This limited the average shell side temperature to 30-45°C, which translates to the solar salt temperature in the range of 400-480°C.

In conclusion, the performance of the new EMbaffle® heat exchanger with low finned tubes and two baffle spacings was experimentally characterized. The friction factor obtained for the smaller baffle spacing requires further investigations, while for the second baffle spacing, results align with the literature correlations. The heat transfer performance for the first baffle spacing is in accordance with the literature data, while for bigger baffle spacing, the results require further investigations. Due to the experimental setup limitations, it was not possible to reach full thermal equilibrium of the system, which limited the heat transfer results accuracy. Based on the analysis done, to confidently describe the heat transfer performance, the experimental setup has to be improved, specifically: the hot water pump operation range should be extended by either increasing the tube diameters or installing the pump with lower NPSH and higher head able to reach higher shell side flow rates; the boiler power should be increased to be able to sustain higher shell side inlet temperatures; and the cold water circuit should be augmented with the cooler to keep the cold water inlet temperature constant. These changes will allow to maintain the constant shell and tube side inlet temperatures and high shell side flow rate, which in turn will allow to reach true thermal equilibrium and cover all the flows and shell side water temperatures needed to replicate conditions for the solar salt primary heat exchanger.

Appendix A: Data cleaning

In this section is reported the analysis of the first campaign data with smaller baffle spacing. Since data acquisition was done in 5 seconds intervals there are a total of 151155 lines of data. First, all the data points with hot water flow below 5 m^3/h were rejected, since these would represent the data registration with the experimental rig not working. To separate the equilibrium points from the remaining 59174 lines, outlier detection algorithms were implemented based on different principles [12]:

- Statistical: rolling Z-score (RZS), rolling coefficient of variation (RCV)
- Density: density-based spatial clustering of applications with noise (DBSCAN) and ordering points to identify the clustering structure (OPTICS)

Along with the algorithms discussed, algorithms based on density (hierarchical density-based spatial clustering of applications with noise (HDBSCAN)), distance (K-nearest neighbors (KNN)) and classification (isolation forest (IF)) were also implemented. However, they could not separate the majority of non-equilibrium points and therefore were not considered further.

Shell and tube inlet and outlet temperatures along with the hot water flow rates were used for outlier detection. The sensitivity of density-based (DBSCAN) and statistical (RZS, RCV) algorithms is shown in Figure 3.12. The only algorithm with the maximum number of outliers not being dependent on the window or sample size is the Z-score with the 1 threshold at a window size of 75 (6 minutes and 15 seconds). For CV at a cutoff threshold of 1%, there is a plateau at the window size of 250 (20 minutes and 50 seconds). For DBSCAN and OPTICS, the results are very similar, and for further analysis, only DBSCAN was considered with EPS (maximum distance between two samples to be considered as in the neighborhood of each other) equal to 0.07 and 30 minimum samples (2 minutes and 30 seconds) to reach the plateau around 93%.

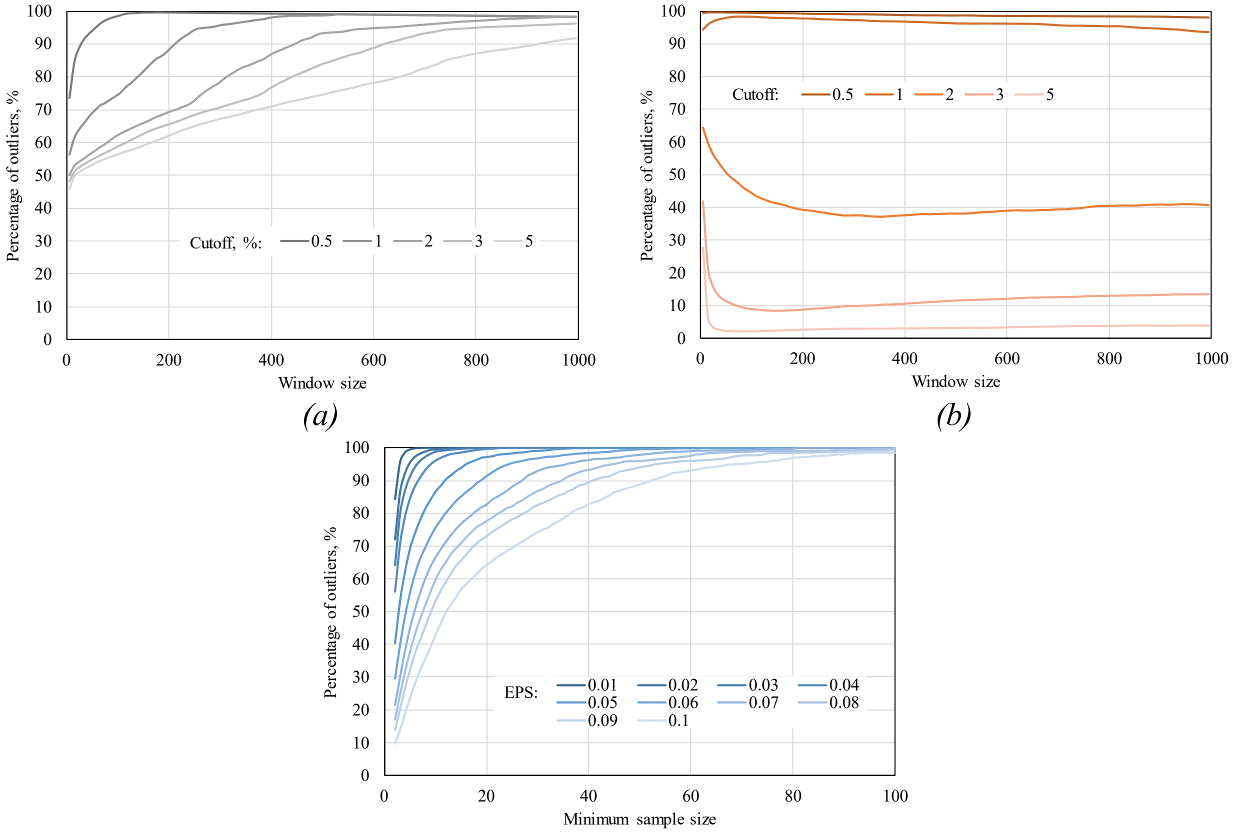

Figure 3.12. Outlier detection results for baffle spacing 1 using RCV (a), RZS (b), and DBSCAN (c)

After the outlier detection, first the lines with calculated cold water flow below 5 m^3/h were deleted, and the Nusselt numbers were calculated for the almost equilibrium points available for the whole heat exchanger and the central baffle space. It should be noted that during the heat transfer calculations, some of the data lines are being deleted due to the negative values obtained in the square root in equation (3.16). Therefore, the final number of points will be lower than the one presented.

3.7. Bibliography

[1] Morris AS. Measurement and instrumentation principles. 3rd ed. Oxford [England] ; Boston: Butterworth-Heinemann; 2001.
[2] Sizing Pressure Performance n.d. https://portal.endress.com/webapp/applicator10/salestool_v73387/index.html#/main/ehapplicator/directEntry.do%3FentryPoint%3DsizingPPA%26visitSource%3Dinside%26linktype%3DListLink%26linklabel%3Dgeneral_menu_engineering_sizingPpa%26undefined (accessed December 19, 2024).
[3] Incropera FP, DeWitt DP, Bergman TL, Lavine AS, editors. Fundamentals of heat and mass transfer. 6. ed. Hoboken, NJ: Wiley; 2007.
[4] Garavaglia M, Grisoni F, Mantegazza M, Rottoli M. Advanced Shell-and-Tube Longitudinal Flow Technology for Improved Performances in the Process Industry. Heat Transfer - Advances in Fundamentals and Applications, IntechOpen; 2023. https://doi.org/10.5772/intechopen.113132.
[5] Lemmon EW, Bell IH, Huber ML, McLinden MO. NIST Standard Reference Database 23: Reference Fluid Thermodynamic and Transport Properties-REFPROP, Version 10.0, National Institute of Standards and Technology 2018. https://doi.org/10.18434/T4/1502528.
[6] Benoit H, Spreafico L, Gauthier D, Flamant G. Review of heat transfer fluids in tube-receivers used in concentrating solar thermal systems: Properties and heat transfer coefficients. Renew Sustain Energy Rev 2016;55:298–315. https://doi.org/10.1016/j.rser.2015.10.059.
[7] Gnielinski V. New equations for heat and mass transfer in turbulent pipe and channel flow. International Chemical Engineering 1976;16:359–67.

[8] Petukhov B, Kirillov P. About heat transfer at turbulent fluid flow in tubes. Thermal Engineering 1958;4:63–8.
[9] Filonenko G. Hydraulic resistance in pipes. Thermal Engineering 1954;1:40–4.
[10] Beale S. Tube banks, single-phase heat transfer in. International encyclopedia of heat and mass transfer, 1997.
[11] Bennett CA, Kistler RS, McGee SM. STG-16 Heat Transfer and Pressure Drop Methods for Longitudinal Flow over Low-Finned Tubes. 2005.
[12] Salano L, Vallerio M, Moioli E, Manenti F. Industrial scale biogas reforming modelling and validation. Chemical Engineering Journal 2025;510:160871. https://doi.org/10.1016/j.cej.2025.160871.
[13] Gentry CC. RODbaffle heat exchanger technology. Chemical Engineering Progress; (USA) 1990;86:7.
[14] Gentry CC, Young RK, Small WM. RODbaffle heat exchanger thermal-hydraulic predictive methods for bare and low finned tubes. 22nd National Heat Transfer Conference, Niagara Falls: 1984, p. 104–9.
[15] Xianhe D, Shiping W, Peisen L, Songjiu D. Effect of the fin shape of transversal outside finned tube on heat transfer of longitudinal flow. J of Che Eng of Chinese Universities 1995;9:387–91.
[16] Obermeier E, Schaber A. Experimental investigation of heat transfer from transverse finned tubes with longitudinal flow. Proceeding of International Heat Transfer Conference 6, Toronto, Canada: Begellhouse; 1978, p. 613–7. https://doi.org/10.1615/IHTC6.1390.
[17] Rampf H, Feuerstein G. Waermeuebergang und Druckverlust an dreiecksfoermigen Rauhigkeiten in turbulenter Ringspaltstoemung. vol. II, Paris, France: 1970.

4. Comparison of equipment for sCO_2, CO_2 mixture, and steam Rankine cycles for CSP

This chapter is based on the article: *"Comparison of sCO_2, CO_2 Mixture, and Steam Rankine Cycles for CSP with Components Sizing: Implications for Cost and Flexibility", published in Conference Proceedings of the European sCO_2 Conference: 6th Edition of the European Conference on Supercritical CO_2 (sCO_2) for Energy Systems, https://doi.org/10.17185/duepublico/83332.*

Abstract

While all commercial concentrating solar power (CSP) plants with central receivers are equipped with the steam Rankine power cycle, supercritical CO_2 (sCO_2) cycles are seen as a promising advancement. They offer higher efficiencies and more compact turbomachinery at high temperatures compared to the steam Rankine cycle, however, sCO_2 cycles face challenges related to high pressures and temperatures, which increase material demands and the mass and cost of heat exchangers. As the need for flexible electricity generation grows, the thermal inertia of the power block, linked to its metal mass, becomes increasingly important. This study examines and compares the component sizes, material usage, and economic and flexibility impacts of sCO_2, CO_2 mixtures, and steam Rankine cycles for commercial-scale CSP applications. All cycles are designed with the same thermal energy input, keeping the solar field and thermal storage constant. Heat exchanger designs, including primary heaters, recuperators, and air-cooled units, follow the ASME Code and are modeled using Aspen Exchanger Design & Rating. Since no commercial sCO_2 turbines exist at this scale, turbine design parameters are estimated using a developed simplified approach. Results are compared with existing studies to assess component-level and system-level implications in terms of cost, performance, and flexibility.

Nomenclature

Acronyms

ACC	air-cooled condenser or cooler
CSP	concentrating solar power
EDR	Aspen Exchanger Design & Rating
FWH	feedwater heater
HE	heat exchanger
HP	high pressure
HTR	high temperature recuperator
ITD	initial temperature difference (K)
LP	low pressure
LTR	low temperature recuperator
MITA	minimum internal temperature approach
OD	outer diameter, mm
PCC	partial cooling cycle
PCHE	printed circuit heat exchanger
PHE	primary heat exchanger
PreC	precompression cycle
RC	recompression cycle
RH	steam cycle reheat
sCO_2	supercritical CO_2
SoA	state-of-art
SR	slenderness ratio
TTD	terminal temperature difference (K)

Symbols

C	cost
D_{hub}	hub diameter (mm)
H	blade height
n_{stages}	number of turbine stages
Q	thermal power (kW)
V	volumetric flow rate (m^3/s)
U	circumferential velocity (m/s)
UA	the overall heat transfer coefficient multiplied by the heat exchange area (MW/K)
δ	pipe thickness, mm
σ_b	bending stress (MPa)
φ	flow coefficient
ψ	loading coefficient
ΔT	temperature difference (K)
ΔP	pressure drop (bar)

SC simple cycle

4.1. Introduction

Even though the steam Rankine cycle which represents the state-of-art (SoA) technology is the only power cycle used in commercial concentrating solar power plants with central receivers so far [1], sCO_2 cycles have been considered as a promising advancement solution in this field. sCO_2 cycles can reach higher efficiencies and will have more compact turbomachinery designs compared to the steam Rankine cycle at high temperatures [2]. On the other hand, the high pressures and temperatures of the sCO_2 cycles present challenges for the materials used and together with high mass flows lead to higher mass and cost of heat exchangers [3]. One approach to enhancing their performance involves transitioning to CO_2 mixture cycles, which offer higher critical temperatures and enable condensation at temperatures as high as 50°C [4]. In this paper, a $SiCl_4$ dopant, stable up to at least 650°C [5,6] is used.

Furthermore, with the increasing need for flexible electricity generation, the thermal inertia of the power block, associated with the metal mass, gains importance. Therefore, to explore the potential, use, and challenges of sCO_2, CO_2 mixtures, and steam Rankine cycle for CSP applications, this work aims to analyze and compare the component sizes, material use, and resulting economic and flexibility implications of the cycles at the component and system level.

4.2. Methodology

This study investigates sCO_2, CO_2 mixtures, and steam Rankine cycles for a commercial scale central receiver CSP plant with molten salt as the heat transfer and storage media, and an air-cooled unit as the heat rejection system [7]. The sCO_2 and CO_2 mixture cycles are designed based on assumptions from [4,8]. The steam Rankine cycle is designed as the state-of-the-art cycle for commercial central receiver plants with reheat and regenerative feedwater heating, according to Kolb [9]. The cycle is simulated through Ebsilon® Professional. The main characteristics of the cycles are provided in Table 4.1.

For sCO_2 simple (SC), recompression (RC), and partial cooling cycles (PCC) are chosen while for CO_2+$SiCl_4$ mixture, simple, precompression (PreC), and recompression ones since they are found to be most promising based on previous literature findings [8,10]. The layout of the CO_2+$SiCl_4$ mixture recompression cycle and its T-s diagram are shown in Figure 4.1. The thermodynamic properties of CO_2 are modeled using Span-Wagner EoS [11], while for CO_2+$SiCl_4$ mixture properties Peng-Robinson EoS [12] and TRAPP model [6,13] with binary interaction parameter equal to 0.06098 [14] is used.

Table 4.1. sCO_2 and CO_2 mixtures power cycles design parameters

Parameter	**Value**	
	sCO_2 and CO_2 mixtures	**Steam**
Turbine inlet temperature, °C	550	
Max pressure in the cycle / turbine inlet pressure, bar	250	125
Cycle minimum temperature, °C	50	
Recuperators MITA, °C	5	-
Feedwater heat exchangers TTD, °C	-	5
PHE Δp, %	2	-
Condenser/cooler Δp, %	2	-
Recuperators hot side Δp, %	1.5	-
Recuperators cold side Δp, %	0.3	-

Parameter	Value	
	sCO_2 and CO_2 mixtures	Steam
Turbine isentropic efficiency, %	92	88
Pump/compressor isentropic efficiency, %	88	80
Motor/generator electrical efficiency, %	97	
Mechanical efficiency, %	99	

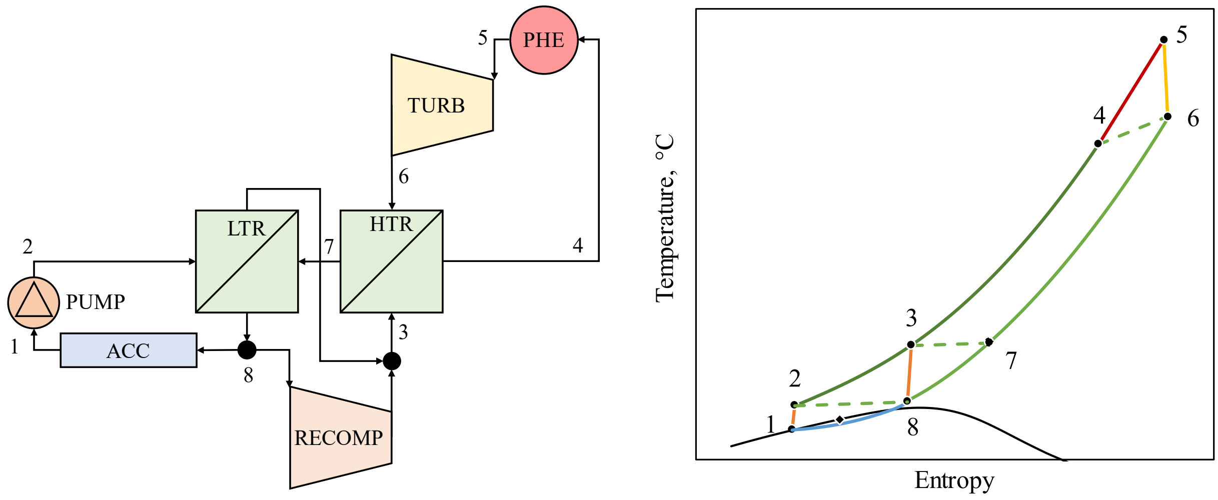

(a) *(b)*

Figure 4.1. Layout (a) and T-s diagram (b) of CO_2+$SiCl_4$ mixture recompression cycle.

The cycles are designed with the same thermal energy input, assuming the same solar field and receiver design for both cycles. The mechanical design of equipment for all cases is performed according to ASME standards with assumptions presented in Table 4.2.

Table 4.2. Power cycles equipment general design parameters

Parameter	Value	Source
PHE power, MWt	280	[7]
Ambient air design temperature, °C	35	-
Equipment design temperature above maximum, °C	+5	[15]
Design pressure above maximum, %	+10	[15]
Thickness allowance, mm	1	-

4.2.1. Materials

Materials used for steam power cycles are widely known and in the case of subcritical cycles comprise 1-2% Cr steels for piping and turbine high-temperature sections with carbon steels for the low-temperature parts [16–18]. Regarding the sCO_2 and CO_2 mixtures cycles it is assumed that the same materials could be used in both cases due to the limited data on the corrosion activity of $SiCl_4$ and positive preliminary results in 316L stainless steel [6].

Subcritical steam material results are generally applicable also for sCO_2, while supercritical water is usually more corrosive than sCO_2 [19]. Multiple sources recommend using stainless steel for temperatures above 400-450°C and even lower [20,21]. But the same criteria (parabolic rate constant) also show that the use of 9-12% Cr steels should not be allowed for temperatures above 500°C in supercritical water. However, in practice, lower alloyed 1-2% Cr steels are used for piping and rotor with 11% Cr stainless steel used for the inner casing [17,22]. In terms of strength, no significant degradation can be seen for 9-12% Cr steels at 550°C [21]. Therefore, it is assumed that 9% Cr steels up to 550°C (pipes, turbine), 2% Cr steels up to 460°C (HTR, SC recuperator), and carbon steels up to 250°C (LTR and ACC) can be applied for both sCO_2 and CO_2 mixtures cycles [19,23].

Special attention should be paid to materials used in the primary heat exchanger, which are in contact with the power cycle working fluid and solar salt. Among the materials for steam generators used and considered before are: Inconel Alloy 800, stainless steels 304 and 304H, 316 and 316H, and various ferritic and carbon steels [24,25]. However since 304, 304H, and 316 stainless steels showed stress corrosion cracking in Solar Two the materials for different sections of the steam generator are chosen as follows [25]: carbon steel for the preheater, 9% Cr steel for the evaporator, and 347 stainless steel for superheater and reheater. For turbine cost estimation the material costs are assumed based on EDR cost database [26] and [27]: 12 USD/kg for 9% Cr steel and 7 USD/kg for 1-2% Cr steel.

4.2.2. Primary heat Exchangers

The data for modeling the PHE are shown in Table 4.3. Since the PHEs for sCO_2 and CO_2 mixtures have operating temperatures close to the superheater, 347 stainless steel is used for the whole heat exchanger. Since both sCO_2 and CO_2 mixtures PHEs are limited by the cold side heat transfer coefficient a minimum 16 mm diameter tube is chosen. For the steam Rankine cycle, the PHEs are designed as two trains, based on the parametric study with the following variables:

- tube outer diameter: 16, 19.05 and 25.4 mm
- tube pitch ratio: 1.25 and 1.5
- tube layout: 30° (45° when 30° is not feasible)

It should be noted that no limitation is imposed regarding shell number. Aspen Exchanger Design & Rating (EDR) V14 [26] is used for all the heat exchanger designs according to the ASME Code [28] and cost estimations, including the primary heaters, regenerative feedwater heaters (FWH), recuperators, and the air-cooled heat rejection unit. Shell and tube heat exchanger design is chosen since it allows for high-power applications and is commercially available with clearly established standards.

Table 4.3. Primary heat exchangers design parameters

Parameter		Value	Source
Material	Preheater	Carbon steel	[25]
	Evaporator	9% Cr steel	
	Superheater, sCO2 and CO2 mixtures PHE	347 steel	
PHE hot end ΔT, °C		20	-
Tube diameter, mm		16/19.05/25.4	-
Maximum tube length, m		15	-
Fouling for hot side, m2·K/W		1.76·10-4	[24]
Fouling for cold side, m2·K/W		8.8·10-5	[24]

4.2.3. Turbines

Turbine design is a complex iterative procedure with many thermal, mechanical, vibrational, and other analyses. In this paper, a preliminary design is assumed to estimate the dimensions and mass based on the previous experience in the literature. A two casings design is adopted with balancing piston and dry gas seals.

The repeated stage flow path is designed with a constant mean diameter, flow coefficient (φ), and loading coefficient ($\psi=\Delta H/u^2$). The main parameters for calculating the turbine geometry are shown in Table 4.4. Blade stagger angles are calculated according to [29]. Since sCO_2 cycles have high mass flows and pressures the bending stress (σ_b) is assumed to be the limiting factor for blade design [30]. Blade height to chord ratio is varied to get the minimum chord length which would satisfy the $\sigma_b \leq$ 130 MPa for nickel alloys and $\sigma_b \leq 100$ MPa for lower-grade materials. Bending stress is calculated based on the correlations proposed by Saravanamuttoo et al.[31].

Table 4.4. sCO_2 and CO_2 mixtures turbines design parameters

Parameter	Value	Source
Rotational speed, Hz	50	-
Reaction degree	0.5	[32]
Pitch-to-chord ratio	0.85	[32]
Axial spacing relative to the chord	0.3	[29]
Blade pitch to mean radius of curvature ratio	0.5	[29]
Balancing piston diameter	$1.1 \cdot D_{hub}$	-
Balancing piston, seals length, mm	500	-
Inlet/ Outlet length, mm	300	-
Rotor diameter under seals, mm	350	[33]
Rotor diameter under bearings, mm	320	-
Bearing length, mm	400	-

For the sCO_2 and CO_2 mixtures axial turbines there is a limited number of complete designs. The comparison of the developed model with the results in the literature is presented in Table 4.5 (hub diameter shown for the first stage).

In [33] the turbine has 58 and 53 rotor and stator blades in the first stage and 47 and 42 in the last stage, while the presented model has 55 and 56 in the first and 36 in the last stage, which shows good accuracy of the simplified approach proposed.

For turbine design circumferential velocity (U) is assumed to be 105 m/s, while $\varphi = 0.75$. Since the increase in the number of stages both increases the turbine isentropic efficiency and reduces the turbine cost [30,33] the single stage loading coefficient should be as low as possible. However, the maximum length of the turbine is limited by rotordynamic behavior, which is out of the scope of this paper. Therefore a slenderness ratio criteria (SR<9), which is defined as a ratio between bearing span and hub diameter, is adopted from [30]. The inner casing is assumed to be made out of 9% Cr steel casting, while the rotor and outer casing out of 2% Cr steel. The thickness of the inner and outer casings is preliminarly calculated as a pipe [34]. The algorithm for turbine design is shown in Figure 4.2. The stage loading coefficient is varied from from $\psi_{min} = 0.65$ to $\psi_{max} = 1.1$ until either the SR criteria is satisfied or the maximum stage loading coefficient or number of stages is reached.

Table 4.5. sCO_2 and CO_2 mixtures turbine model comparison with literature

Reference	[16]				[22]		[33]	
Power, MW	2		50		50		130	
Rotational speed, Hz	175		50		100		50	
Circumferential velocity U, m/s	88		88		132.5		102	
Loading coefficient ψ	1.32		0.66		0.87		1.1	
Flow coefficient φ	0.38		0.76		0.32		1	
Geometry data	Ref.	Calc.	Ref.	Calc.	Ref.	Calc.	Ref.	Calc.
Flow path length, mm	220	172	800	1506	700	740	1800	1515
D_{hub}, mm	160	142	500	498	358	383	620	618
H_{1st} stage, mm	16	17.6	60	62.2	43	41.1	28.7	30
n_{stages}	6	5	11	11	7	7	14	14

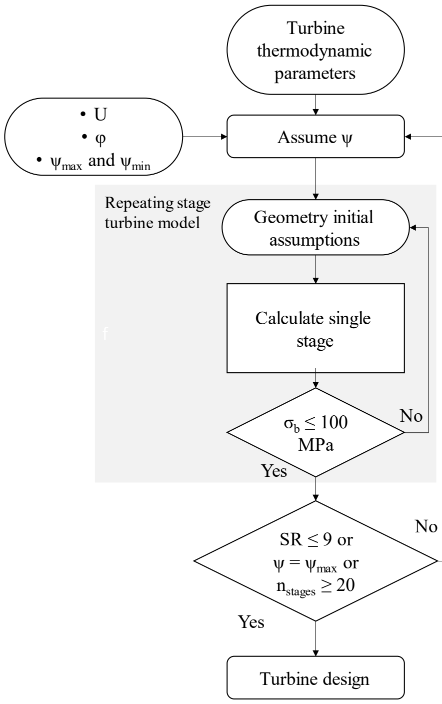

Figure 4.2. Turbine design algorithm.

The preliminary design of the steam turbine is performed by MAN Energy Solutions for the steam Rankine cycle analyzed in this study.

4.2.4. Recuperative system

The data for designing the recuperators for sCO_2 and CO_2 mixtures cycles are shown in Table 4.6.

Table 4.6. sCO_2 and CO_2 mixtures recuperators design parameters

Parameter		**Value**	**Source**
Material	T > 250°C	2% Cr steel	[19,23]
	T < 250°C	carbon steel	
Tube diameter, mm		16	-
Maximum tube length, m		15	-
Fouling for both sides, $m^2 \cdot K/W$		$8.8 \cdot 10^{-5}$	[24]

The closed feedwater heaters (FWH) of the steam cycle are classified into two groups: high pressure (HP) and low pressure (LP). The materials used for the steam cycle can be found in Table 4.7 a as well as the other main design inputs determined according to parametric studies. The materials are selected based on [35].

Table 4.7. Regenerative feedwater heat exchanger design parameters

Parameter		**Value**	
		HP	**LP**
Material	Shell	SA-204 Grd C	SA-516 Grd 70
	Tube	SA-213 T22	SA-210 Grd C
Tube diameter, mm		16	25.4
Tube Layout		30	45
Pitch Ratio		1.5	1.25
Fouling for both sides, $m^2 \cdot K/W$		$8.8 \cdot 10^{-5}$	

As Aspen EDR is not capable of designing the closed feedwater heaters with multiple zones and multiple shell inlets, only one HP and LP HEX are designed with a simplified approach. Both HP and LP FWHs have TEMA Type B-E-U.

4.2.5. Condensers and Coolers

An A-frame air-cooled condenser or cooler (ACC) design is chosen as the configuration for all power cycles since it is the default choice for existing high power CSP plants along with the V-frame.

For sCO_2 and CO_2 mixtures, tube diameters are varied between 13, 16, and 25.4 mm, while air heat up is varied between 15, 20, and 25°C. For the steam cycle, a tube diameter of 25.4 mm emerged as the most economical design. The data for designing the condensers and coolers are shown in Table 4.8. In the case of condensers, there is only one pass, while for CO_2 coolers multiple passes are used.

Table 4.8. Condensers and coolers design parameters

Parameter	**Value**	**Source**
Material	Carbon steel	-
Fan efficiency, %	75	[36]
Cold end ΔT (ITD for the steam condenser), °C	15	-
Hot end ΔT for the steam condenser, °C	5	-
Maximum tube length, m	15	-
Fouling for hot side, $m^2·K/W$	$8.8·10^{-5}$	[24]
Fouling for cold side, $m^2·K/W$	$8.8·10^{-4}$	[37]

4.2.6. Piping

In fossil fuel steam Rankine power plants piping can cost almost as much as a turbine unit [38], while in sCO_2 bigger mass flows will lead to even bigger diameter main piping. Therefore, it is important to estimate the piping for both cycles as well. However, the piping layout is highly dependent on the primary heat exchanger configurations, site limitations, and plant requirements.

The pipe cross sections are determined based on the ASME Code for process piping [34]. The design conditions adapted for both steam Rankine and sCO_2 and CO_2 mixtures cycles are shown in Table 4.9. The working fluid design velocity is based on the value present in both subcritical and supercritical main steam piping [17,22]. For sCO_2 and CO_2 mixtures, 30 m/s is assumed to reach the ρw^2 similar to steam piping and is in line with other literature works [22].

Table 4.9. Piping design parameters

Parameter	**Value**		**Source**
	Steam	**sCO_2 and CO_2 mixtures**	
Material	2% and/or 9% Cr steel	9% Cr steel	-
Design velocity	50	30	[17,22]
Pipes in parallel	2		-

4.3. Results

The results of the equipment modeling are compared with the cost estimates available in the literature. All literature cost estimates and specific costs used are updated to 2023 using CEPCI [39]. The results of the cycles calculation are shown in Table 4.10. Steam Rankine and CO_2 mixture recompression cycles have the highest electrical efficiency (including ACC fan power), followed by mixture and then sCO_2 cycles.

Table 4.10. Cycles results

Working fluid	**H_2O**		**sCO_2**			**CO_2+$SiCl_4$**	
Cycle	**Rank.**	**SC**	**RC**	**PCC**	**SC**	**PreC**	**RC**
Cycle minimum pressure, bar	0.124	100	110	80	72.4	72.4	83.6
PHE inlet temperature, °C	238	376	421	369	361	360	394
Cycle electrical power, MWe	116.1	96.7	108.1	105.4	108.3	109.3	112.5
Electrical efficiency, %	41.5	34.6	38.6	37.7	38.7	39.0	40.2
Same including ACC fan, %	39.7	34.0	37.9	37.0	38.1	38.4	39.7

The design results for steam Rankine cycle PHE with the lowest cost are presented in Table 4.11. The resulting cost is 8.48 MUSD or 72 USD/kWe, which is validated against the design study of a 110 MWe solar tower power plant from [40] by direct scaling due to similar size. Despite the differences in the geometries and fouling resistances, current design has only 6.2% higher specific cost compared to literature (67.8 USD/kWe). It should be noted that up to this point, the steam drum is excluded from the analysis. Assuming the cost of the steam drum to be the same as the superheater as in [41], the overall PHE cost for the steam cycle results in 94.2 USD/kWe specific cost. Earlier studies estimate the cost of HEs alone as 159.9 USD/kWe for 1000 MWth (65.5% of whole PHE cost), 311.1 USD/kWe for 260 MWth (73.8% of whole PHE cost), and 302 USD/kWe for 280 MWth (assuming the same portion of HEs in whole PHE cost) [41–43]. Whereas in the newer study [44] updated to 2023 the cost of HEs is 122.3 USD/kWe for 240 MWth, assuming the HEs cost 70% of the whole PHE. Therefore, the calculations results are slightly under the estimates in the literature, but there is no consensus on the PHEs cost across the sources.

Table 4.11. Primary heat exchangers design parameters for steam cycle

Parameter	**Value**			
	Preheater	**Evaporator**	**Superheater**	**Reheater**
TEMA Type	B-F-U	B-E-U	B-E-U	B-E-U
Tube outer diameter, mm	25.4	25.4	16	25.4
Tube pitch ratio	1.5	1.25	1.5	1.25

The cost of the sCO_2 and CO_2 mixtures PHE varies between 22 and 26 MUSD making it 51.6-61.5% of the correlation from [8]. This can be explained by the use of Inconel 617 in the correlation [8] for all temperature ranges, while in the present analysis a much cheaper stainless steel 347 is used. Therefore, the updated correlation for PHE cost with power above 100MWth without installation (which is assumed to be 20% for PHE [45] in the original correlation) is as follows:

$$C_{PHE}^{2023}\left(UA\left[\frac{MW}{K}\right], \Delta P_{tube}[bar]\right) = k \cdot UA \cdot \Delta P_{tube}{}^{-0.2705}$$
$$k = \begin{cases} 2.610, if\ T_{max} \leq 575°C \\ 4.737, if\ T_{max} > 575°C \end{cases} \tag{4.1}$$

The overall metal mass of the steam turbine designed for this study is concluded to be 165 tons, 125 and 40 tons for casing and rotor, respectively. Subsequently, the material cost of the steam turbine is 1.16 MUSD. According to Akar et al. [46] the material costs contribute only to 5.75% of the overall manufacturing costs of steam turbines with standard design and high manufacturing volume for geothermal application. Assuming that the breakdown applies also to steam turbines for CSP plants, the resulting cost is 20.07 MUSD leading to 172.9 USD/kWe. For validation, a subcritical 325 MW plant [38] is scaled down according to [47], and the cost calculated is 198.6 USD/kWe. Based on the study [43], the bid cost of the 50 MW turbine is scaled up according to [47] to 160.0 USD/kWe, while the estimate is 193.3 USD/kWe assuming 20% installation cost and generator cost from [45]. On the other hand, the cost function given in [48] estimates the cost of the steam turbine as 236.7 USD/kWe or 36.9% higher than this study. Therefore, this study's results are on the lower end of the literature data which gives a cost of 160-195 USD/kWe.

The results of sCO_2 and CO_2 mixtures turbine model are shown in Table 4.12. Assuming the same material cost contribution as in the steam turbine the resulting cost of the turbines is 3.52-4.07 MUSD, which is 10.9-14.3% lower than the correlation results [45] showing a good agreement.

Table 4.12. sCO_2 and CO_2 mixtures turbines parameters

Working fluid	sCO_2			CO_2+$SiCl_4$		
Cycle	**SC**	**RC**	**PCC**	**SC**	**PreC**	**RC**
ψ	0.65	0.75	0.74	0.65	0.65	0.65
D_{hub}, mm	615	596	617	629	629	614
n_{stages}	16	12	17	14	15	15
Flow path length, m	2.4	2.5	2.7	2.1	2.3	2.7
SR	8.3	8.8	8.8	7.6	8.0	8.8
Mass rotor, tons	9.2	8.9	9.6	8.7	9.0	9.5
Mass casings, tons	17.7	20.0	18.7	16.5	18.4	18.6

Due to the simplified design of FWHs for the steam Rankine cycle; the FWH costs are expected to be underestimated. For comparison, the cost function provided in [49] is calibrated with the CSP plant inventory listed in [41], which includes vendor data, and in-house cost data for power block. The updated FWH cost function is presented in Eqn. 2.

$$C_{FWH}^{2023}(Q[kW], TTD[K]) = 28 \cdot Q \cdot \left(\frac{1}{TTD + a}\right)^{0.1} \quad \text{where } a_{LP} = 3, a_{HP} = 6 \qquad (4.2)$$

The costs of designed heat exchangers are found to be 46.6% and 51.2% of the costs calculated by Eqn. 2 for HP FWH and LP FWH, respectively. This difference in the cost estimations is regarded acceptable due to the simplified design of FWHs with a single-zone approach where actual FWHs have multiple zones such as condensing and drain cooling zones [35], and uncertainty of the materials used in the reference FWHs. For improved reliability and accuracy, the costs are calculated by Eqn. (2) for the FWHs of this study for further analysis and comparison. Finally, a similar approach with inventory data [41] calibrated cost correlation [50] is employed for the deaerator.

For sCO_2 and CO_2 mixtures recuperators, the costs obtained are above the ones predicted from the correlation [45]. In Figure 4.3 the optimized costs from Aspen EDR are compared with cost correlations based on heat exchanger effectiveness. One can see a general increase in the cost with further effectiveness increase above 95% as can be seen also in the PCHE literature before [51]. It should be noted that special baffle designs could improve the economics of sCO_2 and CO_2 mixtures recuperative heat exchangers [52].

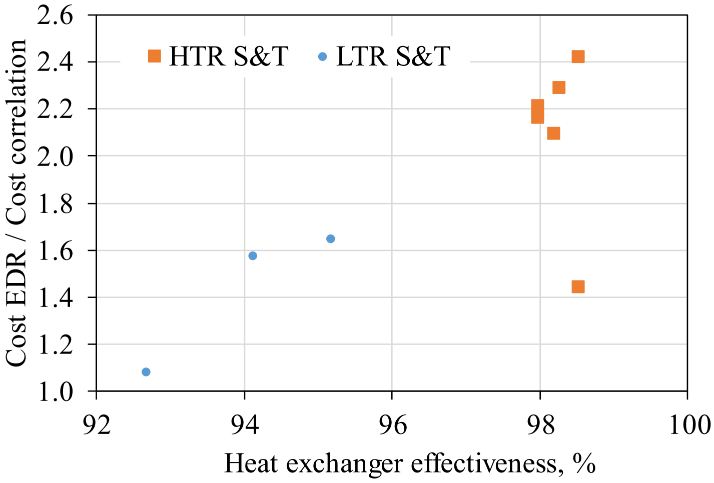

Figure 4.3. Recuperative system cost.

The cost of the air-cooled heat rejection unit for the steam cycle is calculated as 15.8 MUSD, resulting in the specific cost of 136.0 USD/kWe for 15°C ITD. In the study [53] the costs vary significantly based on ITD used from 236.7 USD/kWe for 16°C ITD to 157.3 USD/kWe for 24°C ITD. However, these numbers include also air removal equipment and support for start-up, training, and testing. The paper [54] focused on the 20 MW power plant gives a specific cost of 154.9 USD/kWe for ITD of around 30°C for ACC frame and fan. Therefore, current study results are within the literature range, but with current ITD higher costs of ACC are expected.

In the case of sCO_2 and CO_2 mixtures cycles the air temperature increase in the ACC is assumed to be 25°C [55] for cost correlation [45], while the fan's electric power is estimated to be 1% of thermal power [8]. A comparison of results between the Aspen EDR and correlation is presented in Figure 4.4. One can see that either the cost correlations or power consumption is underrated. Since the cost of the ACC is not significant in the final cycle cost, it is better to assume a 20-30% higher cost and lower fan power [56]. It should be noted that while for sCO_2 the resulting pressure drop is on average 75% of design, for CO_2+$SiCl_4$ mixture ACCs it is within 16-26%. This means that in the case of condensing cycle pressure drop in the air-cooled condenser can be assumed to be 0.5% of inlet pressure instead of 2% currently.

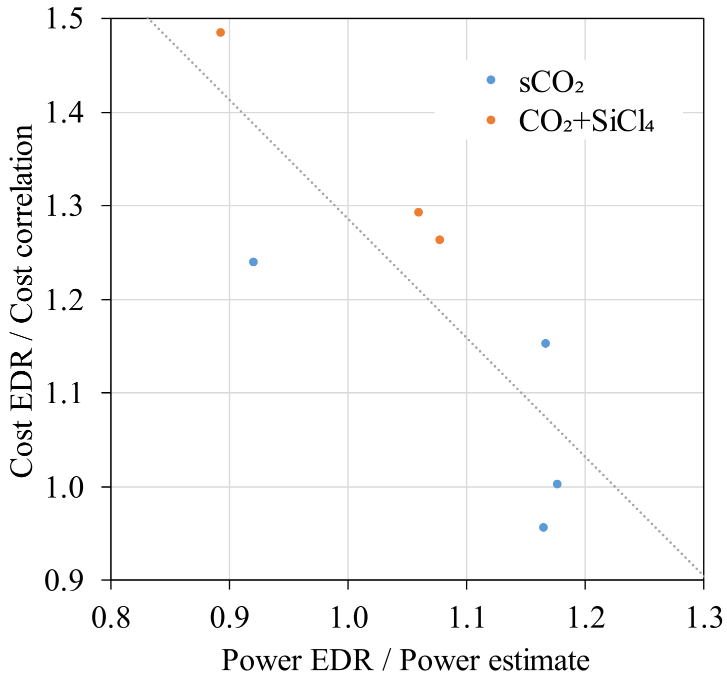

Figure 4.4. Condensers and coolers Cost vs Power.

The results of the main piping are presented in Table 4.11 for the cycles with both 2% Cr and 9% Cr Steel, A335 P22 and P91, respectively. One can see a significant increase in piping dimensions including outer diameter (OD) and thickness (δ) moving from steam to sCO_2 and CO_2 mixtures cycles due to both higher volume flow (V) and higher pressure in the latter case. The mass per meter for steam cycles main and reheat piping (accounting for 2 parallel pipes used) is 859 kg/m for P22 and 356 kg/m for P91, while for sCO_2 and CO_2 mixtures cycles it is between 1322 and 2445 kg/m.

Table 4.13. Main piping parameters

Fluid	Cycle	V, m³/s	Steel	OD, mm	δ, mm	Mass, kg/m
H_2O	Main	2.7	2% Cr	267	42	462
			9% Cr	217	16	162
	To RH	9.6	2% Cr	358	4	73
			9% Cr	355	3	53
	From RH	5.6	2% Cr	460	15	323
				444	7	141
sCO_2	SC	8.6		574	74	1824
	RC	11.5		666	86	2445
	PC	8.2	9% Cr	563	72	1750
CO_2+ $SiCl_4$	SC	6.2		490	63	1334
	PC	6.2		489	63	1322
	RC	8.6		576	74	1832

For the steam Rankine cycle, the pump costs are computed according to [57] and equal 10.47 USD/kWe, while FWHs are 10.5 USD/kWe. Adding all the calculated costs the steam power cycle main equipment cost is 425.8 USD/kWe with 40.6% being the turbine cost, followed by 31.9% for ACC and 22.1% for PHE. However, the costs of PHE and ACC from the literature are both higher and are highly variable. If conservative assumptions from the literature are used the steam cycle main equipment cost reaches up to 800 USD/kWe. The whole power block with PHE and auxiliary systems cost is estimated as 1286-1350 USD/kWe in [44] and 1196-1270 USD/kWe in [43]. Therefore, taking into account that the additional costs are expected for installation (20-30%) and auxiliary equipment the cost of main equipment is considered reasonable.

In the case of sCO_2 and CO_2 mixtures, the compressors and pumps costs are calculated as compressors from [45]. For CO_2 and CO_2 mixture SC they are 82 and 63 USD/kWe respectively, while for the rest of the cycles they vary between 103 and 124 USD/KWe. The cost of PHE is consistent between cycles and is 210-243 USD/kWe. The same can be seen in the case of the turbine which costs 32.5-38.3 USD/kWe and ACC which costs 63-80 USD/kWe for most cycles, except the 117 USD/kWe for PCC. The main portion of the cost of the cycle is due to heat exchangers and specifically the recuperative system, the high costs of which are due to high effectiveness. The cost of the recuperator is 288 and 639 USD/kWe for the sCO_2 and CO_2 mixture cycle respectively, HTR cost varies between 334 and 628 USD/kWe, while for LTR it is between 191 and 504 USD/kWe. The overall cost of cycles equipment for sCO_2 SC is 707 USD/kWe, 1592 USD/kWe for RC, 1056 USD/kWe for PCC, and 1056 USD/kWe for PCC. While for CO_2 mixture SC it is 1034 USD/kWe, 944 USD/kWe for PreC, and 1392 USD/kWe for RC. Compared to literature correlations the cost of all equipment is almost the same for sCO_2 PCC and CO_2 mixture PreC, while recompression cycles are 384 and 291 USD/kWe above. The sCO_2 has a 119 USD/kWe lower cost, while the mixture one has 213 USD/kWe.

The masses of equipment at high temperatures are shown in Figure 4.5. The mass of steam PHE is 1.7-2.2 times lighter than in the case of sCO_2 and CO_2 mixtures, while the steam turbine mass is 6 times higher. In general, sCO_2 and CO_2 mixtures cycles have a significantly higher mass (4-14 times) mainly due to recuperators. One can see that PHE mass is almost constant across the sCO_2 and CO_2 mixtures cycles, while turbine mass is insignificant compared to heat exchangers. However, the main concern is the recuperator especially the high-temperature part, which has both high mass and is subjected to high temperatures. It should be noted that in current work recuperators masses are overestimated due to high effectiveness and adherence to shell and tube design. In the design done according to [58] lower mass and cost by a factor of 2 for HTR and 1.5 for LTR for shell and tube heat exchangers is expected. Another option is to move towards a different heat exchanger design to reduce the mass and increase flexibility, such as PCHE which is widely applied for sCO_2 cycles in literature. In that case, an order of magnitude reduction in mass is expected [59] which will make both cycles masses on par. However, currently, PCHEs can only reach tens of MWth and face scalability problems, which limit their application for the proposed hundreds of MWth range design [60].

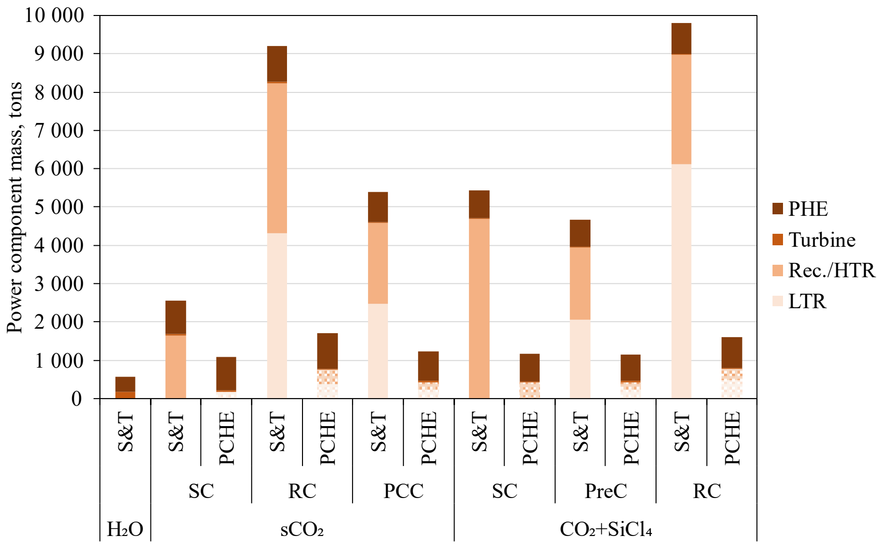

Figure 4.5. sCO_2 and CO_2 mixtures cycles mass distribution

4.4. Conclusions

Preliminary design of equipment for steam Rankine cycle and sCO_2 and CO_2 mixtures cycles were carried out with results compared to correlations and data available in the literature. Heat exchangers were designed with commercial software and high-temperature piping was sized according to ASME standards. Steam turbine preliminary design was obtained from the industrial partner, while for sCO_2 and CO_2 mixtures cycles a simplified approach was developed.

In the case of the steam Rankine cycle, the primary heat exchanger cost is found to be in good agreement with other research work but below most literature estimates. However, within the literature, the costs for only HEs vary by a factor of 2, which makes this piece of equipment both a significant part of the cycle cost and very uncertain. The air-cooled condenser designed in this study was found to be within the literature cost results, but on the lower side accounting for ITD influence. The turbine cost calculated is equal to lower values found in literature, while most of the literature costs are around 10-15% higher. On the other hand, it was concluded that the detailed feedwater heater design is crucial to determine their cost since there is a wide range of FWHs estimates in literature with significant deviation from the simplified design obtained in current work. Most of the steam power cycle cost is due to PHE, turbine, and ACC, as expected, among which PHE has the highest costs in literature and the highest uncertainty.

In the case of sCO_2 and CO_2 mixtures cycles the primary heat exchanger for 550°C TIT application was designed with a 347H stainless steel which reduces the overall cost by around a factor of 2 compared to literature results. Turbines preliminary design and cost estimation give results 10.9-14.3% lower than literature correlations. Designed recuperators have a significantly higher cost compared to the literature. Analysis shows that this is due to very high exchangers efficiencies and similar trends are found in the literature for PCHEs. Therefore, simplified correlations based on UA can be used only for heat exchangers with effectiveness below 92-93%. Based on ACC design results it was found that either the cost or fan power has to be increased by 20-30% with cost being more preferable since it is not significant for sCO_2 and CO_2 mixtures cycles. On the other hand, for condensing CO_2 mixtures cycles the working fluid pressure drop can be decreased from 2% of inlet pressure to 0.5%. The rest of the equipment, however, doesn't show significant sensitivity to the transition from sCO_2 to CO_2 mixtures.

Regarding the cost, for both cycles, only the main equipment was considered. Calculation results of the steam cycle give values of around 425 USD/kWe, however, based on conservative literature values the cost can be up to 800 USD/kWe. The sCO_2 simple cycle has equipment cost of 707 USD/kWe which is between average and the conservative steam Rankine power cycle values, followed by precompression cycle with a cost of 944 USD/kWe, sCO_2 partial cooling and CO_2 mixture simple cycles with a cost of 1057 and 1034 USD/kWe, and sCO_2 and CO_2 mixture recompression cycles with 1593 and 1392 USD/kWe. The difference in cycles working principles leads to different cost distributions. For the steam Rankine cycle, most of the power unit cost is due to the PHE, turbine, and air-cooled condenser. On the other hand, for supercritical and transcritical cycles, most of the cost is associated with the recuperative system and primary heat exchanger, which is due to a significant portion of heat being recuperated and large mass flows. It should be noted that for the steam cycles, there are commercial estimates available based on vendors, who already produced equipment on a similar scale, while for sCO_2 the best data available are correlations based on vendor quotes, cost estimates, and published literature, while the equipment wasn't yet produced at that scale.

Regarding flexibility, there are two main considerations: the amount of heat needed to be supplied to the cycle equipment to reach the operating temperature and the limiting factor of thermal stress in high-temperature parts of the cycle. In the first case, the steam Rankine PHE mass is around two times smaller than sCO_2 and CO_2 mixtures cycles PHEs, while the average operating temperature is lower for the steam cycle. The turbine mass is around 6 times higher in the steam case, while the

Rankine cycle regenerative system is around 100 tons and much lighter than sCO_2 and CO_2 mixtures recuperative systems. However, it should be noted that a different recuperator heat exchanger technology could reduce the weight by an order of magnitude. Regarding the thermal stresses, sCO_2 and CO_2 mixtures cycles have higher pipe and turbine casing thickness due to around two times higher maximum pressure and large volume flows. On the other hand, the length of pipes may be expected to be shorter in the case of sCO_2 and CO_2 mixtures due to the lack of reheat. Finally, the thick drum walls of the steam cycle should be taken into consideration.

From the operation and maintenance point of view steam Rankine cycle will require water treatment facility, while for sCO_2 and CO_2 mixture cycles the working fluid management system is needed to fill, empty and regulate the amount of fluid in the cycle and cycle minimum pressure in the case of sCO_2. For CO_2 mixture there is also a need of a hot well similar to the Steam Rankine cycle one.

Further studies will focus on the reduction of sCO_2 and CO_2 mixture recuperators cost and weight along with the thermal inertia estimation and techno-economic optimization of the most promising cycles.

4.5. Bibliography

[1] Power Tower | Concentrating Solar Power Projects | NREL n.d. https://solarpaces.nrel.gov/by-technology/power-tower (accessed September 4, 2024).

[2] Mehos M, Turchi C, Vidal J, Wagner M, Ma Z, Ho C, et al. Concentrating Solar Power Gen3 Demonstration Roadmap. NREL, SNL; 2017. https://doi.org/10.2172/1338899.

[3] Brun K, Friedman P, Dennis R. Fundamentals and applications of supercritical carbon dioxide (sCO2) based power cycles. Woodhead publishing; 2017.

[4] Crespi F, Rodríguez De Arriba P, Sánchez D, Ayub A, Di Marcoberardino G, Invernizzi CM, et al. Thermal efficiency gains enabled by using CO2 mixtures in supercritical power cycles. Energy 2022;238:121899. https://doi.org/10.1016/j.energy.2021.121899.

[5] Nakayama M, Miyamoto S, Ogawa T, Osae S, Tomono K, Sumimoto M, et al. Thermal decomposition of tetrabromosilane and deposition of crystalline silicon. Materials Science in Semiconductor Processing 2014;23:93–7. https://doi.org/10.1016/j.mssp.2014.02.045.

[6] Doninelli M, Di Marcoberardino G, Iora P, Gelfi M, Invernizzi CM, Manzolini G. Silicon Tetrachloride as innovative working fluid for high temperature Rankine cycles: Thermal Stability, material compatibility, and energy analysis. Applied Thermal Engineering 2024;249:123239. https://doi.org/10.1016/j.applthermaleng.2024.123239.

[7] System advisor model (SAM) case study: Gemasolar. NREL 2013:6.

[8] Morosini E, Villa E, Quadrio G, Binotti M, Manzolini G. Solar tower CSP plants with transcritical cycles based on CO2 mixtures: A sensitivity on storage and power block layouts. Solar Energy 2023;262:111777. https://doi.org/10.1016/j.solener.2023.05.054.

[9] Kolb G. An evaluation of possible next-generation high temperature molten-salt power towers. Albuquerque, USA: Sandia National Laboratories; 2011. https://doi.org/10.2172/1035342.

[10] Neises T, Turchi C. Supercritical carbon dioxide power cycle design and configuration optimization to minimize levelized cost of energy of molten salt power towers operating at 650 °C. Solar Energy 2019;181:27–36. https://doi.org/10.1016/j.solener.2019.01.078.

[11] Span R, Wagner W. A New Equation of State for Carbon Dioxide Covering the Fluid Region from the Triple-Point Temperature to 1100 K at Pressures up to 800 MPa. J Phys Chem Ref Data 1996;25:1509–96. https://doi.org/10.1063/1.555991.

[12] Peng D-Y, Robinson DB. A New Two-Constant Equation of State. Ind Eng Chem Fund 1976;15:59–64. https://doi.org/10.1021/i160057a011.

[13] Ely JF, Hanley HJ. A computer program for the prediction of viscosity and thermal conductivity in hydrocarbon mixtures. vol. 13. US Department of Commerce, National Bureau of Standards; 1981.

[14] Doninelli M, Morosini E, Di Marcoberardino G, Invernizzi CM, Iora P, Riva M, et al. Experimental investigation of the CO2+SiCl4 mixture as innovative working fluid for power cycles: Bubble points and liquid density measurements. Energy 2024:131197. https://doi.org/10.1016/j.energy.2024.131197.

[15] Cunningham S, Rhodes M, Bulnes FK, Wade J, Khawly GN. The Design, Fabrication, and Installation of the Inconel 740H Piping System for a 10 MW sCO2 Pilot Plant 2024.

[16] Glos S, Musch C, Stueer C, Schlehuber D, Wechsung M. Design of an axial sCO2 turbine for a demo plant in an industrial environment. Conference Proceedings of the European sCO2 Conference5th European sCO2 Conference for Energy Systems: March 14-16 2023;2023:162. https://doi.org/10.17185/DUEPUBLICO/77286.

[17] Characteristics of turbounits. Tomsk Polytechnic University Publishing House; 2014.
[18] Kosiak IUF. Steam turbine K-300-240 KhTGZ. Moscow, Russia: Energoizdat; 1982.
[19] Subbaraman G, Kung S, Saari H. Materials for Supercritical CO2 Applications. 8th International sCO2 Power Cycles Symposium, San Antonio, Texas: 2024, p. 59.
[20] Marchionni M, Bianchi G, Tassou SA. Review of supercritical carbon dioxide (sCO2) technologies for high-grade waste heat to power conversion. SN Appl Sci 2020;2:611. https://doi.org/10.1007/s42452-020-2116-6.
[21] Pint BA, Pillai R, Keiser JR. Defining Temperature Limitations for Steels in sCO2 Applications. vol. 38, San Antonio, Texas: 2022, p. 8.
[22] Glos S, Lippe P, Schlehuber D, Kobler S, Wechsung M. Design considerations of sCO2 turbines developed within the CARBOSOLA project. Conference Proceedings of the European sCO2 Conference4th European sCO2 Conference for Energy Systems: March 23-24 2021;2021:106. https://doi.org/10.17185/DUEPUBLICO/73952.
[23] Li K, Zhu Z, Xiao B, Luo J-L, Zhang N. State of the art overview material degradation in high-temperature supercritical CO2 environments. Progress in Materials Science 2023;136:101107. https://doi.org/10.1016/j.pmatsci.2023.101107.
[24] Investigation of thermal storage and steam generator issues. 1993. https://doi.org/10.2172/10189397.
[25] Moore R, Siegel N, Kolb G, Vernon M, Ho C. Design considerations for concentrating solar power tower systems employing molten salt. 2010. https://doi.org/10.2172/1008140.
[26] Aspen Exchanger Design and Rating (EDR) | AspenTech n.d. https://www.aspentech.com/en/products/engineering/aspen-exchanger-design-and-rating (accessed July 25, 2023).
[27] Turchi C, Gage S, Martinek J, Jape S, Armijo K, Coventry J, et al. CSP Gen3: Liquid-Phase Pathway to SunShot. Appendix 12: Project Reports. 2021. https://doi.org/10.2172/1807668.
[28] BPVC Section VIII-Rules for Construction of Pressure Vessels Division 1. ASME; 2023.
[29] Ainley D, Mathieson G. A method of performance estimation for axial-flow turbines 1951.
[30] Salah S. Design and analysis of supercritical carbon-dioxide axial turbines. City, University of London, 2023.
[31] Saravanamuttoo HIH, Cohen H, Rogers GFC. Gas turbine theory. 5. ed. Harlow: Prentice Hall; 2007.
[32] Abdeldayem AS, Salah SI, Aqel OA, White MT, Sayma AI. Design of a 130 MW Axial Turbine Operating with a Supercritical Carbon Dioxide Mixture for the SCARABEUS Project. IJTPP 2024;9:5. https://doi.org/10.3390/ijtpp9010005.
[33] Abdeldayem A, Paggini A, Diurno T, Orazi C, White M, Ruggiero M, et al. Integrated Aerodynamic and Mechanical Design of a Large-Scale Axial Turbine Operating With Supercritical Carbon Dioxide Mixtures. Volume 12: Supercritical CO2, Boston, Massachusetts, USA: American Society of Mechanical Engineers; 2023, p. V012T28A012. https://doi.org/10.1115/GT2023-102236.
[34] ASME Code for Pressure Piping, B31. ASME; 2014.
[35] Grunsky A. Feedwater Heater Maintenance Guide. Palo Alto, USA: EPRI; 2002.
[36] Summary of ISO 12759. Fans – Efficiency classification of fans. n.d.
[37] SASOL, Lake Charles, Louisiana, USA, Swan WP, Fernandes DP, Center for Abnormal Situation Management Research, Lamar University, Beaumont, Texas 77710, USA, Khade A, Cen DH, et al. Abnormal Situation Management: Detection of Fouling and Longitudinal Bypass in Heat Exchangers. IJCEA 2018;9:9–15. https://doi.org/10.18178/ijcea.2018.9.1.691.
[38] Pauschert D. Study of Equipment Prices in the Power Sector. Washington, D.C., U.S.A: The International Bank for Reconstruction and Development/THE WORLD BANK GROUP; 2009.
[39] Chemical Engineering Plant Cost Index (CEPCI) n.d. https://www.training.itservices.manchester.ac.uk/public/gced/CEPCI.html?reactors/CEPCI/index.html (accessed December 2, 2024).
[40] González-Gómez PA, Gómez-Hernández J, Briongos JV, Santana D. Thermo-economic optimization of molten salt steam generators. Energy Conversion and Management 2017;146:228–43. https://doi.org/10.1016/j.enconman.2017.05.027.
[41] Kelly BD. Advanced Thermal Storage for Central Receivers with Supercritical Coolants. Lakewood, USA: ABENGOA SOLAR; 2010. https://doi.org/10.2172/981926.
[42] Mancini T, Gary J, Kolb G, Ho C. Power Tower Technology Roadmap and cost reduction plan. 2011. https://doi.org/10.2172/1011644.
[43] Turchi CS, Boyd M, Kesseli D, Kurup P, Mehos MS, Neises TW, et al. CSP Systems Analysis - Final Project Report. 2019. https://doi.org/10.2172/1513197.
[44] Dersch J, Paucar J, Polkas T, Schweitzer A, Stryk A. Blueprint for Molten Salt CSP Power Plant Final report of the project "CSP-Reference Power Plant" No. 0324253 2021.
[45] Weiland NT, Lance BW, Pidaparti SR. sCO2 Power Cycle Component Cost Correlations From DOE Data Spanning Multiple Scales and Applications. Volume 9: Oil and Gas Applications; Supercritical CO2 Power Cycles; Wind Energy, Phoenix, Arizona, USA: American Society of Mechanical Engineers; 2019, p. V009T38A008. https://doi.org/10.1115/GT2019-90493.
[46] Akar S, Augustine C, Kurup P, Mann M. Global Value Chain and Manufacturing Analysis on Geothermal Power Plant Turbines. Renewable Energy 2018.
[47] Bejan A, Tsatsaronis G, Moran MJ. Thermal design and optimization. John Wiley & Sons; 1995.

[48] Roosen P, Uhlenbruck S, Lucas K. Pareto optimization of a combined cycle power system as a decision support tool for trading off investment vs. operating costs. International Journal of Thermal Sciences 2003;42:553–60. https://doi.org/10.1016/S1290-0729(03)00021-8.
[49] Fernández-Torrijos M, Marugán-Cruz C, Sobrino C, Santana D. The water cost effect of hybrid-parallel condensing systems in the thermo-economical performance of solar tower plants. Applied Thermal Engineering 2022;202:117801. https://doi.org/10.1016/j.applthermaleng.2021.117801.
[50] Ameri M, Ahmadi P, Hamidi A. Energy, exergy and exergoeconomic analysis of a steam power plant: A case study. Int J Energy Res 2009;33:499–512. https://doi.org/10.1002/er.1495.
[51] Le Pierres R. Technology Development Needs for sCO2 Heat Exchangers, San-Diego, USA: 2015, p. 16.
[52] Naumov V, Mantegazza M, Doninelli M, Di Marcoberardino G, Iora P, Rottoli M. Comparison of Shell and Tube Heat Exchangers for CO2 and CO2+SiCl4 Mixtures Transcritical Cycles 2024. https://doi.org/10.5281/zenodo.13986989.
[53] Davis G, Selkowitz S, Brook M. Comparison of Alternate Cooling Technologies for California Power Plants Economic, Environmental and Other Tradeoffs. Public Interest Energy Research California Energy Commission 2004.
[54] Luceño JA, Martín M. Two-step optimization procedure for the conceptual design of A-frame systems for solar power plants. Energy 2018;165:483–500. https://doi.org/10.1016/j.energy.2018.09.177.
[55] Illyés V, Morosini E, Doninelli M, David P-L, Guerif X, Werner A, et al. Design of an Air-Cooled Condenser for CO2-Based Mixtures: Model Development, Validation and Heat Exchange Gain with Internal Microfins. Volume 9: Supercritical CO2, Rotterdam, Netherlands: American Society of Mechanical Engineers; 2022, p. V009T28A016. https://doi.org/10.1115/GT2022-82438.
[56] Neises T. Influence of the air-cooled supercritical carbon dioxide recompression cycle design-point on molten salt power tower techno-economic performance. Solar Energy 2023;264:112073. https://doi.org/10.1016/j.solener.2023.112073.
[57] Silveira JL, Tuna CE. Thermoeconomic analysis method for optimization of combined heat and power systems. Part I. Progress in Energy and Combustion Science 2003;29:479–85. https://doi.org/10.1016/S0360-1285(03)00041-8.
[58] Weiland N, Thimsen D. A practical look at assumptions and constraints for steady state modeling of sCO2 Brayton power cycles, San Antonio, Texas: National Energy Technology Laboratory (NETL), Pittsburgh, PA, Morgantown, WV …; 2016.
[59] Doninelli M, Di Marcoberardino G. On the Design of Recuperator for Transcritical Cycle Adopting CO2-Based Mixture as Working Fluid: A Focus on Transport Properties Prediction. Energy Technology 2024;12:2300677. https://doi.org/10.1002/ente.202300677.
[60] Lariviere B, Marion J, Macadam S, McDowell M, Lesemann M, McClung A, et al. sCO2 power cycle development and STEP Demo pilot project. Conference Proceedings of the European sCO2 Conference4th European sCO2 Conference for Energy Systems: March 23-24 2021;2021:352. https://doi.org/10.17185/DUEPUBLICO/73979.

Part 2: New dopants for CO_2 mixture power cycles for CSP

In Part 2, the new dopants are proposed, their preliminary techno-economic performance is assessed, and the experimental characterization is carried out.

In Chapter 5, a preliminary techno-economic analysis of CO_2 mixture power cycles with germanium tetrachloride ($GeCl_4$) and trichlorofluorosilane (Cl_3FSi) is carried out in the CSP plant. The working fluid composition is optimized to achieve maximum efficiency. After this, the CSP plant is modeled to obtain the annual power generation and capital cost with solar multiple and thermal energy storage size optimization to reach the minimum LCOE.

In Chapter 6, the hexafluoropropylene (C_3F_6) and germanium tetrachloride ($GeCl_4$) thermal stability results are presented. The measurement and uncertainty calculation methodology are presented and applied to the dopants tested.

5. Preliminary analysis of CO_2+$GeCl_4$ and CO_2+Cl_3FSi mixtures CSP plants

This chapter is based on the article: *"Preliminary analysis of CO_2+$GeCl_4$ and CO_2+Cl_3FSi mixtures for CSP application", under review in SolarPACES Conference Proceedings: SolarPACES 2025, 31st International Conference on Concentrating Solar Power, Thermal, and Chemical Energy Systems.*

Abstract

The steam Rankine power cycle is currently used in all concentrating solar power (CSP) plants with central receivers. It could be replaced by the supercritical CO_2 (sCO_2) cycles since they offer higher efficiencies and more compact turbomachinery at high temperatures. Their performance could be further improved by using dopants with high critical temperatures to allow for condensation at temperatures typical for air-cooled condensers. This work focuses on the preliminary analysis of CO_2+$GeCl_4$ and CO_2+Cl_3FSi mixtures cycles for CSP plants applications at 550 and 700°C turbine inlet temperature levels representative of Gen2 and Gen3 CSP plants. The results indicate a competitive techno-economic performance of both CO_2+$GeCl_4$ and CO_2+Cl_3FSi mixtures cycles compared to various sCO_2 cycles configurations.

5.1. Introduction

Concentrated solar power (CSP) plants hold significant potential for producing renewable energy. The cost of electricity from CSP plants is higher than from PV and wind plants. Nonetheless, the introduction of CSP plants may improve the electric grid stability by leveraging the dispatchability offered by the inexpensive thermal energy storage technology (TES). Reducing electricity costs can be achieved by lowering equipment expenses and enhancing plant efficiency. The closed CO_2 cycles provide a thermal efficiency benefit compared to the steam Rankine and helium Brayton ones at high turbine inlet temperatures, making them a promising option for Gen3 CSP plants [1,2]. Closed sCO_2 cycles efficiency could be increased through the addition of dopants with high critical parameters, transitioning from supercritical to transcritical cycle while maintaining the same minimum cycle temperature. Improvements in cycle thermal efficiency resulting from the use of CO_2-based mixtures been thoroughly examined for C_6F_6, N_2O_4, SO_2, $SiCl_4$ and $TiCl_4$ [3]. But at high temperatures, only a limited number of dopants satisfy the requirements for thermochemical stability and compatibility with the material. A $SiCl_4$ dopant has been recently experimentally investigated and showed both good thermal stability [4] and techno-economic performance [5]. The objective of this work is the preliminary analysis of CO_2+$GeCl_4$ and CO_2+Cl_3FSi mixtures (dopants similar to the one experimentally tested) in CSP power plant cycles. Power cycles with the best thermodynamic efficiency do not necessarily yield the best techno-economic performance [5–7]. Therefore, the current paper focuses on optimizing both the power cycle and the whole CSP plant with proposed mixtures to compare their techno-economic performance with sCO_2 cycles. This work is part of the EU funded TOPCSP project [8].

5.2. Methodology

5.2.1. Power cycle model

The parameters of chosen fluids are shown in Table 5.1, taken from the NIST ThermoData Engine (TDE) in Aspen Plus. Power cycles were modelled in Aspen Plus V14 [9] using Span and Wagner EoS for sCO_2 [10] and Peng-Robinson EoS [11] for mixtures. No experimental data for chosen CO_2 mixtures were identified in the literature; therefore, the binary interaction parameters (kij) were assumed to be zero for preliminary thermodynamic analysis, which should not significantly influence the cycle performance [12]. Since both new dopants are based on Ge-Cl, Si-Cl, and Si-F bonds with high bond energies, they are expected to be stable up to 700°C.

Table 5.1. Parameters of working fluids

CAS	Formula	T_{melt}, °C	T_{boil}, °C	T_{cr}, °C	P_{cr}, bar	Z_{cr}	ω	NFPA 704		
								H	F	R
124-38-9	CO_2	-57	-78	31	73.8	0.274	0.224	0	0	0
10038-98-9	$GeCl_4$	-51	83	280	38.6	0.271	0.218	3	0	2-w
14965-52-7	Cl_3FSi	-	10	165	35.7	0.307	0.198	3	0	2

where H – health; F – flammability; R – reactivity; w – reacts violently with water; 1- 4 – degree of hazard

Pressure-Temperature envelopes of CO_2+$GeCl_4$, and CO_2+Cl_3FSi mixtures together with critical points for different compositions are shown in Figure 5.1. To ensure reliable power cycle operation only mixtures with critical temperatures above 60°C are considered which limits the maximum CO_2 molar composition to 87% for CO_2+Cl_3FSi and 95% for the CO_2+$GeCl_4$.

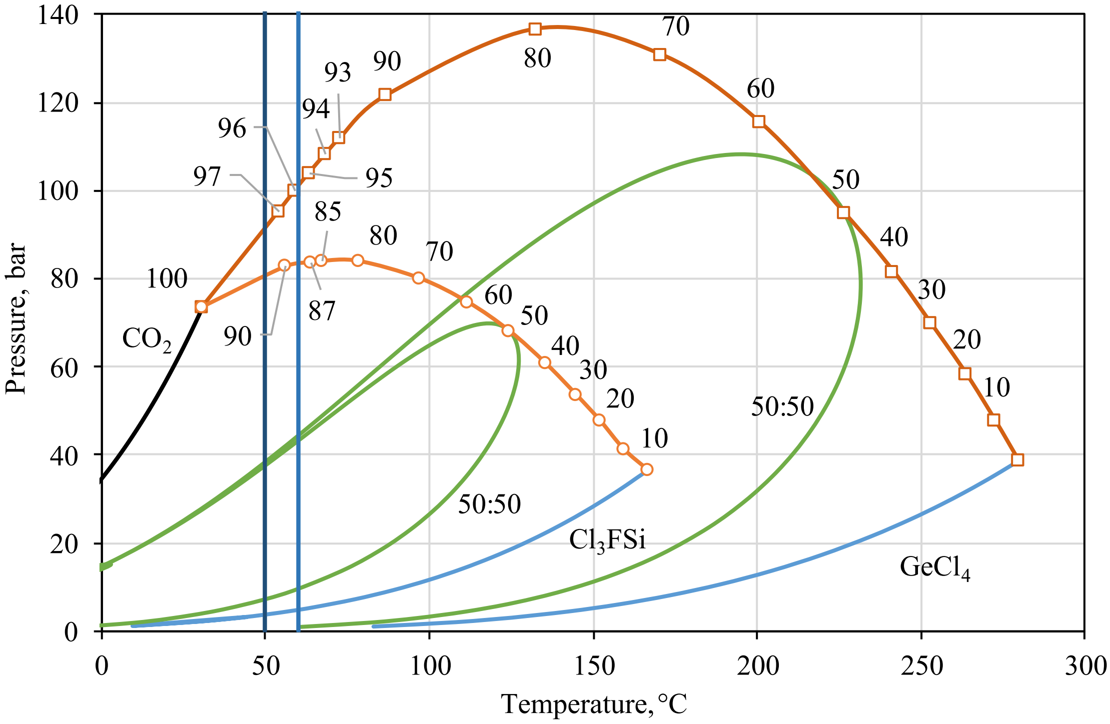

Figure 5.1. Critical point locuses on P-T diagram with circles for CO_2+Cl_3FSi and squares for CO_2+$GeCl_4$ mixtures with different CO_2 molar fractions (black line is pure CO_2, blue lines are pure $GeCl_4$ and Cl_3FSi vapor pressure curves; green lines are 50:50 P-T envelopes).

The most promising power cycle layouts were selected for the comparison: simple, recompression, and partial cooling power cycles with sCO_2 were modeled, while for CO_2+$GeCl_4$, and CO_2+Cl_3FSi mixtures simple, recompression and precompression cycles were chosen based on previous results in the literature [5–7] (Figure 2.1).The design parameters of power cycles are shown in Table 5.2 and are similar to previous studies [5,13].

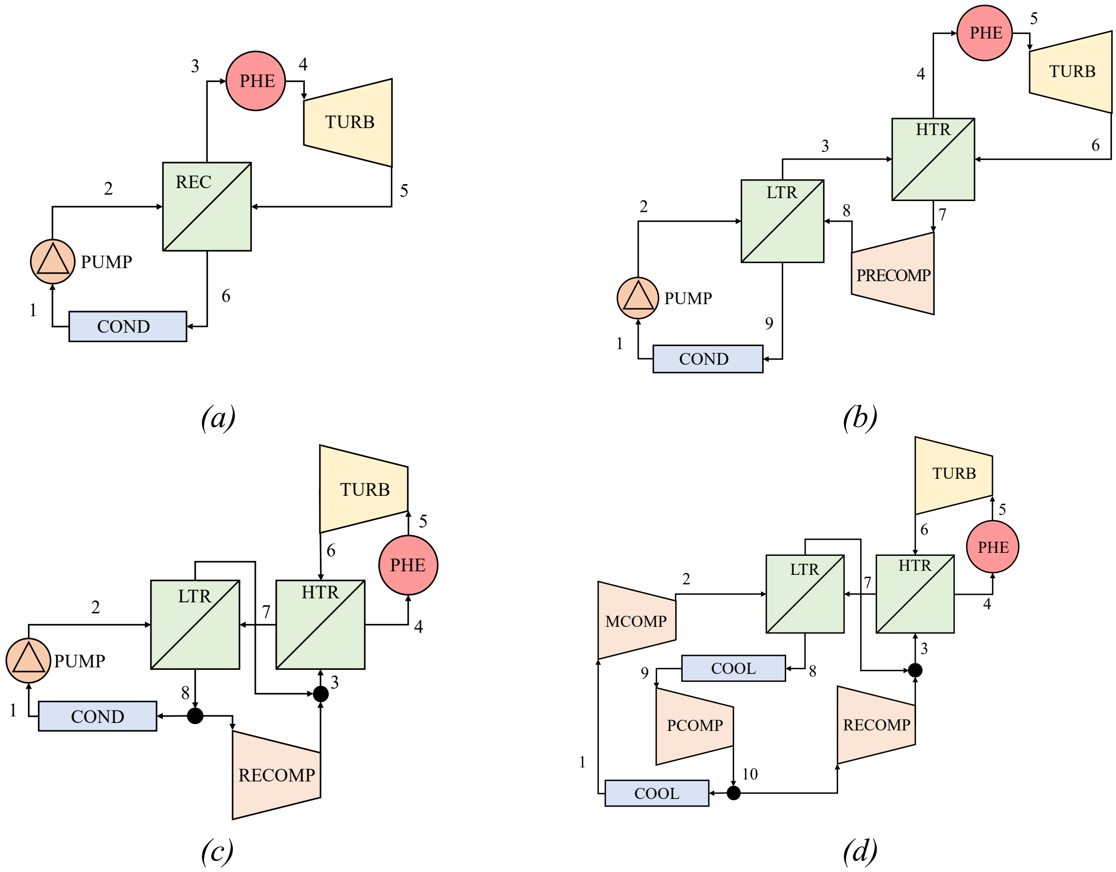

Figure 5.2. Layout of simple (a), precompression (b), recompression (c) and partial cooling (d) cycles. PHE – primary heat exchanger; TURB – turbine; LTR – low-temperature recuperator; HTR – high-temperature recuperator; PUMP – pump; PCOMP – partial cooling compressor; PRECOMP – precompressing compressor; RECOMP – recompressing compressor; MCOMP – main compressor; COND – air-cooled condenser.

Table 5.2. Power cycles design assumptions

Parameter	Value
TIT, °C	550, 700
P_{max}, bar	250
T_{min}, °C	50
$T_{air,des}$, °C	35
Recuperator minimum internal temperature approach, °C	5
ΔP_{PHE}, cooler/condenser, %	2
$\Delta P_{recuperator}$ hot/cold side, %	1.5/0.3
$\eta_{turbine,is}/\eta_{pump/compressor,is}$, %	92/88
η_{el}/η_{mech}, %	97/99
Fan power, % of rejected heat	1
Cooler/condenser ΔT_{air}, °C	25

The study objective is to assess the performance of proposed dopants in CSP power cycles. Cycle electrical efficiencies were calculated assuming separate shafts for turbomachines:

$$\eta_{cycle,el} = (P_t \cdot \eta_{mech} \cdot \eta_{el} - (P_p + P_c)/(\eta_{mech} \cdot \eta_{el}) - P_{fan})/Q_{PHE} \qquad (5.1)$$

where $\eta_{cycle,el}$ – electrical cycle efficiency, %; P_t – turbine power, MWe; P_p – pump power, MWe; P_c – compressors power, MWe; P_{fan} – cooler/condenser fan power, MWe; Q_{PHE} – PHE thermal power, MWth; η_{mech} – generator/motor mechanical efficiency, %; η_{el} – generator/motor electrical efficiency, %.

5.2.2. CSP plant model

The tower concentrated solar power plant layout is shown in Figure 5.3a. An arrangement of heliostats is used to concentrate sunlight onto a central receiver located at the top of the tower, where the salt/sodium is heated. Then this heat is saved in molten salt within thermal energy storage. Hot salt from TES is pumped through the PHE, providing the thermal energy to the power cycle for electricity generation. Throughout the day, thermal energy is provided to the power cycle, with any surplus being stored in thermal energy storage; during other periods, the heat for the power cycle is sourced from this stored energy. The CSP plant model created for the assessment of annual performance is illustrated in Figure 5.3b. The primary elements of the CSP plant that have been thoroughly modeled include (i) the solar field, (ii) the receiver, (iii) the TES, and (iv) the power cycle. The CSP plant model used was already presented in paper [5] and for the full list of assumptions, the reader is invited to consult it.

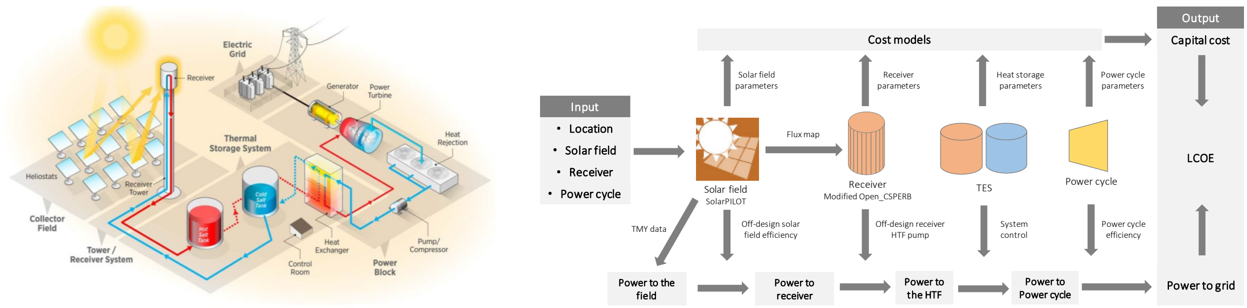

(a) *(b)*

Figure 5.3. CSP system scheme adapted from [2] (a) and model (b).

Moving forward, the same assumptions are made except when stated otherwise. The following changes were implemented to the model:

1. Condenser/cooler fan power dependence on the air temperature was added based on equations from [14,15].
2. Primary heat exchanger cost model was updated based on [16].
3. For cold storage temperatures below 403°C the NaCl-KCl-$ZnCl_2$ 13.8-41.9-44.3 %mol (8.1-31.3-60.6 %wt) salt is used [17].

Typical meteorological year data was taken from the PVGIS-SARAH3: 2005-2023 tool [18] for 37.40°N, 6.01°W in Seville(Spain), following the paper [19]. The mean daily value of DNI is 6.2 kWh/m² with 95% DNI at 880 W/m², an average ambient temperature of 19°C, and wind velocity of 2.3 m/s. It should noted that, the average DNI in the location is 5.68 kWh/m² based on the data from 2000-2012 [19], while NASA SSE gives a value of 6.18 kWh/m². These two values, however, are both higher than 4.86 kWh/m², characteristic of the data usually used for the location from typical meteorological year data available in SAM.

An initial solar multiple (SM) of 2.5 is assumed according to the Gemasolar power plant, located in Fuentes de Andalucía, Spain, about 40 miles east of Sevilla [20]. The initial PHE thermal power is assumed to be 280 MWth to get the net power around 100 MWe [20], which leads to receiver power of 760 MWth at the design point. The number of flow paths, panels, and tube diameters of each receiver was chosen based on the maximum fictitious power (7.3) taking into account the maximum sodium speed of 2.44 m/s [21]:

$$Q_{fictitious} = Q_{rec,output} - \frac{P_{HTF\,pump}}{\eta_{cycle,el}} \tag{5.2}$$

where $Q_{fictitious}$– receiver fictitious power, MWth;$P_{HTF\,pump}$– receiver HTF pump power, MWe;$Q_{rec,output}$– receiver output power, MWth.

The economic assumptions were 30 years of service with a 6.5% CRF to calculate LCOE according to the equation (5.3) [22]:

$$LCOE = \frac{TCC \cdot CRF + FOC}{EE} + VOC \tag{5.3}$$

where *LCOE* – levelized cost of electricity, USD_{2020}/MWh;*TCC* – total capital cost, USD_{2020}; *CRF* – capital recovery factor; *FOC* – fixed operating costs, USD_{2020}; *VOC* – variable operating costs, USD_{2020}/MWh; *EE* – electric energy output per year, MWh/yr.

5.3. Results

5.3.1. Power cycles performance

The mixture power cycles optimization is shown in Figure 5.4. For CO_2+Cl_3FSi mixture points with condensation temperatures below 60°C (above 87%mol. CO_2) are shown but not considered for calculation. For the CO_2+$GeCl_4$ recompression cycle, the use of CO_2 fraction below 95% leads to a two-phase condition at the recompressor inlet and was therefore not considered, while the increase of the CO_2 fraction above 96% leads to a reduction of the critical temperature below 60°C. This makes 95% the optimal point for both TIT, but raises questions about secure operation with limitations being so close.

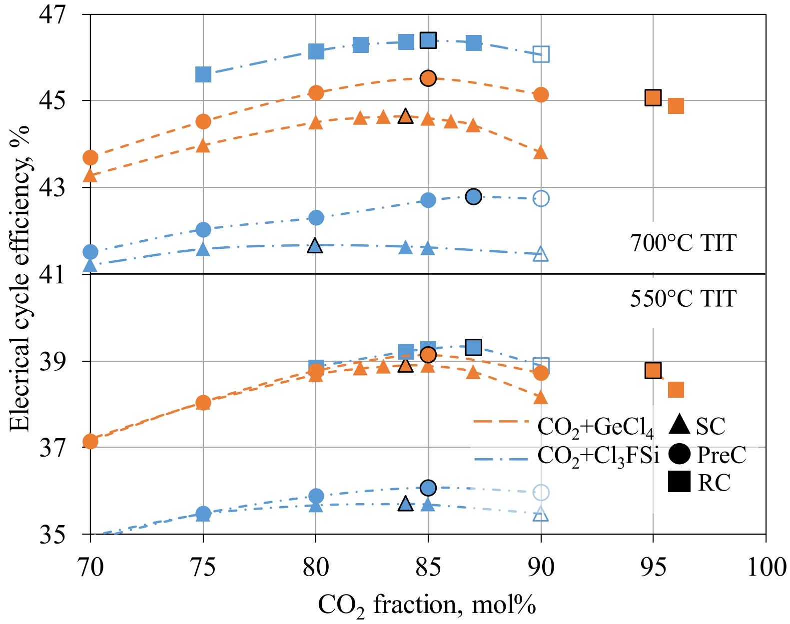

Figure 5.4. Power cycles CO_2 fraction optimization results at 550°C and 700°C TIT

The cycles optimization results are shown in Table 5.3. The recompression CO_2+Cl_3FSi cycle has the highest efficiency at 550°C TIT, followed by CO_2+$GeCl_4$ precompression, simple and recompression ones. At 700°C TIT electrical efficiency is reducing starting from the recompression CO_2+Cl_3FSi cycle and followed by CO_2+$GeCl_4$ precompression, recompression, and sCO_2 recompression cycles. This makes the simple and precompression cycles with the CO_2+$GeCl_4$ mixture more efficient than the sCO_2 recompression and partial cooling ones while having a simpler layout.

Table 5.3. Power cycles results

Parameter	**Value**								
Cycle fluid	**sCO_2**			**CO_2+$GeCl_4$**			**CO_2+Cl_3FSi**		
Cycle type	**SC**	**RC**	**PCC**	**SC**	**RC**	**PreC**	**SC**	**RC**	**PreC**
TIT, °C	550								
CO_2 fraction, mol%	-	-	-	84	95	85	84	87	85
P_{min}, bar	100	110	80/120	-	-	70	-	-	65
$T_{in\ PHE}$, °C	376.0	420.7	368.5	364.3	401.2	363.3	287.1	361.6	289.2
$T_{in\ cond./cool}$, °C	111.8	95.1	82.9/86.8	87.4	97.8	86.4	98.5	101.9	99.5
P_t/ Q_{PHE}, %	53.5	63.2	62.2	52.1	63.4	56.5	50.9	67.5	55.4
$P_{p/MC}$/ Q_{PHE}, %	16.1	12.1	6.4	10.1	10.7	10.1	12.0	11.7	3.9
$P_{RC/PC}$/ Q_{PHE}, %	-	9.1	6.9/7.9	-	10.0	3.9	-	12.3	12.0
UA_{HTR}/ Q_{PHE}, 10^3/K	58.6	103.1	52.9	118.4	79.4	48.7	37.7	46.6	27.2
UA_{LTR}/ Q_{PHE}, 10^3/K	-	124.8	66.9	-	82.9	90.9	-	121.7	21.8
$\eta_{cycle,th}$, %	37.34	42.00	41.00	41.97	42.71	42.53	38.83	43.55	39.47
$\eta_{cycle,el}$, %	33.92	38.04	37.06	38.90	38.77	39.13	35.70	39.31	36.07
Spec. power, kJ/kg	75.18	62.46	85.43	70.24	66.09	71.78	77.58	64.87	79.65
TIT, °C	700								
CO_2 fraction, mol%	-	-	-	84	95	85	80	85	87
P_{min}, bar	90	105	70/115	-	-	65	-	-	60
$T_{in\ PHE}$, °C	502.6	552.8	486.6	489.0	533.1	484.7	308.8	472	409.8
$T_{in\ cond./cool}$, °C	131.5	102.4	92.5/91.5	87.4	100.7	86.5	97.2	100.6	101.9
P_t/ Q_{PHE}, %	62.4	69.7	70.1	56.9	68.0	63.9	55.3	71.3	64.6
$P_{p/MC}$/ Q_{PHE}, %	18.4	11.7	5.8	9.1	10.3	5.8	10.5	9.8	7.0
$P_{RC/PC}$/ Q_{PHE}, %	-	9.1	7.1/9.1	-	8.6	8.9	-	11.0	11.0
UA_{HTR}/ Q_{PHE}, 10^3/K	59.0	114.7	55.4	114.8	90.2	52.4	34.7	50.0	29.7
UA_{LTR}/ Q_{PHE}, 10^3/K	-	101.9	54.4	-	62.6	85.8	-	103.3	23.2
$\eta_{cycle,th}$, %	43.95	48.86	48.15	47.80	49.06	49.16	44.84	50.57	46.63

Parameter	Value								
$\eta_{cycle,el}$, %	40.15	44.73	43.94	44.64	45.06	45.51	41.66	46.38	42.79
Spec. power, kJ/kg	101.44	84.29	119.67	89.42	85.91	94.15	98.05	86.14	107.43

where MC – main compressor; PC – pre- o partial cooling compressor; RC – recompressing compressor

5.3.2. CSP plant performance

The solar field efficiencies are shown in Figure 5.5. Because of the smaller sodium receiver, the maximum efficiency of the 700°C field is lower, though the overall distribution remains similar.

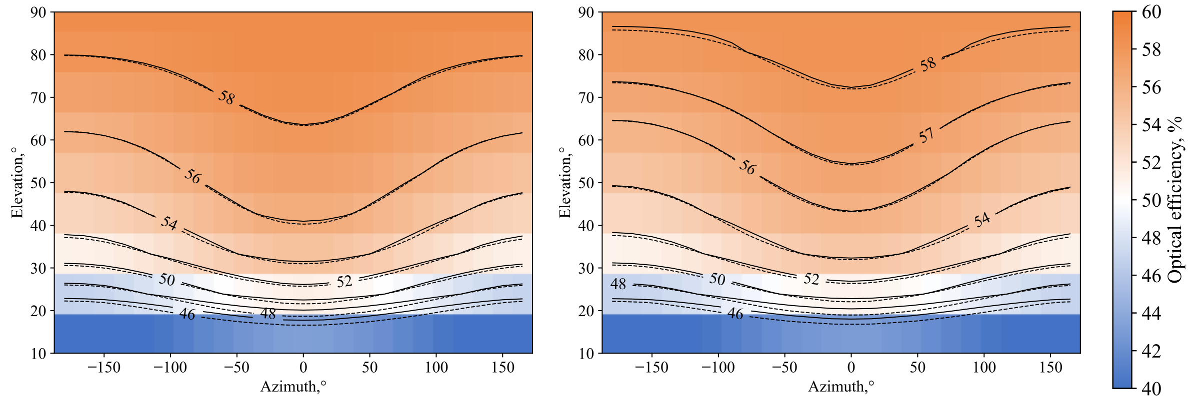

(a) *(b)*

Figure 5.5. Off-design solar field optical efficiency map for 550°C (a) and 700°C TIT (b) cases with solid lines (——) representing original efficiency levels and dashed lines (– –) indicating interpolated values

The receiver designs optimized for maximum fictitious power are shown in Table 2.1. Higher PHE inlet temperature leads to higher average HTF temperature in the receiver, lower receiver efficiency, and higher pumping power.

Table 5.4. Receivers design parameters

Parameter	Value								
Cycle fluid	sCO_2			CO_2+$GeCl_4$			CO_2+Cl_3FSi		
Cycle type	SC	RC	PCC	SC	RC	PreC	SC	RC	PreC
TIT, °C					550				
Heliostats					10480				
Flow paths					2				
Panels per path			3				4	3	4
D_{tube}, mm	34	50	34	32	42	32	32	32	32
$\Delta P_{receiver}$, bar	44.4	42.5	44.1	45.9	44.2	45.9	48.2	45.8	48.3
$N_{HTF\ pump}$, MWe	7.56	9.81	7.19	7.32	8.85	7.27	5.34	7.18	5.4
$\eta_{receiver}$, %	90.5	90.1	90.6	90.7	90.4	90.7	91.2	90.7	91.2
TIT, °C					700				
Heliostats					10545				
Flow paths	12	14	10	10	12	10	12	10	8
Panels per path					1				
D_{tube}, mm	50	60	60	42	50	42	20	34	32
$\Delta P_{receiver}$, bar	18.0	17.8	18.2	18.2	17.9	18.2	19.2	18.3	18.6
$N_{HTF\ pump}$, MWe	7.02	9.36	6.56	6.64	8.31	6.50	3.66	6.17	4.87
$\eta_{receiver}$, %	86.9	86.1	87.2	87.2	86.5	87.2	89.3	87.4	88.2

5.3.3. CSP plant optimization results

The solar multiple and hours of thermal energy storage were optimized to reach minimum LCOE. In Figure 5.6, one can see the sensitivity of LCOE to SM and TES size for all working fluids and two TIT temperature levels for cycles with minimum optimum LCOE: sCO_2 partial cooling cycle, simple and precompression CO_2+$GeCl_4$ mixture cycles, and simple CO_2+Cl_3FSi cycles.

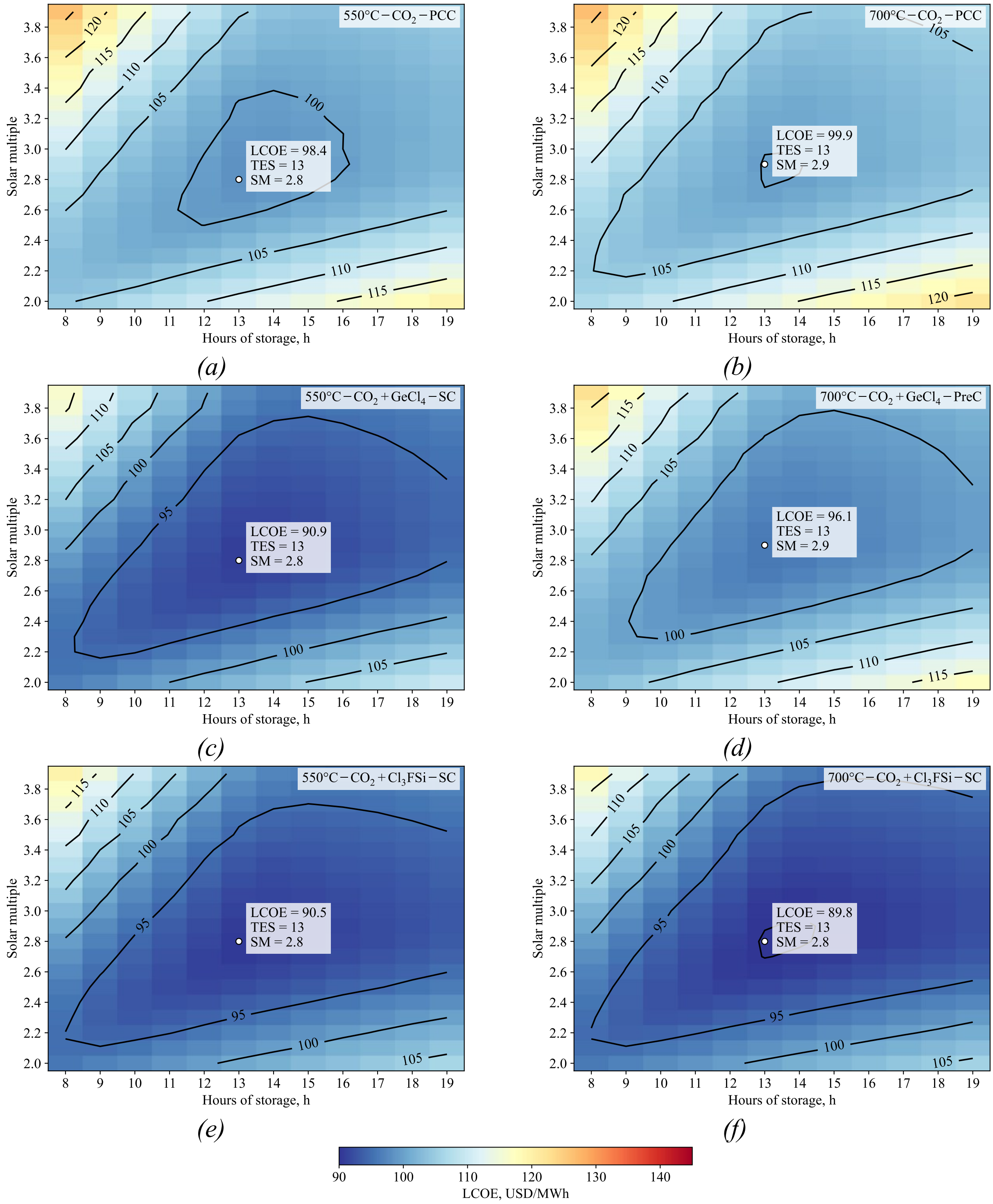

Figure 5.6. SM and TES sensitivity for cycles using CO_2 (a, b), CO_2+$GeCl_4$ (c, d), and CO_2+Cl_3FSi (e, f) with minimum LCOE at 550 and 700°C TIT respectively.

The results of optimized CPS plants are shown in Table 5.5. The optimum SM is 2.8-2.9, lower than the values of 3.2-3.5 previously reported in the literature [5,23] which is due to the higher annual direct irradiance in the current case (6.2 vs. 4.86 kWh/m^2).

Table 5.5. Optimum CSP plants parameters

Parameter	**Value**								
Cycle fluid	**sCO_2**			**CO_2+$GeCl_4$**			**CO_2+Cl_3FSi**		
Cycle type	**SC**	**RC**	**PCC**	**SC**	**RC**	**PreC**	**SC**	**RC**	**PreC**
TIT, °C					550				
TES capacity, h					13				
SM	2.8	2.9				2.8			
$\eta_{sol.\ to\ th.}$, %	42.90	41.99	42.91	42.98	42.78	42.98	43.29	42.98	43.28
$\eta_{sol.\ to\ el.}$, %	13.69	14.91	15.03	15.82	15.56	15.92	14.75	16	14.87
CF, %	62.35	63.34	62.39	62.38	62.16	62.4	62.73	62.4	62.71
EE, GWh/year	454.5	494.9	498.7	525.0	516.5	528.3	489.5	530.9	493.5
Heliostats, MUSD					216.4				
R&T, MUSD					119.3				
TES, MUSD	91.2	114.3	87.9	86.2	104.5	85.8	63.9	85.2	64.3
Power cycle, MUSD	54.7	92.2	84.0	63.3	84.3	76.4	49.5	86.2	59.4
TCC, MUSD	603.6	676.9	635.0	608.0	655.5	623.4	564.3	634.3	576.7
LCOE, USD_{2020}/MWh	102.0	104.4	98.4	90.9	98.2	92.3	90.5	93.3	91.5
TIT, °C					700				
TES capacity, h				13					14
SM				2.9			2.8	2.8	2.9
$\eta_{sol.\ to\ th.}$, %	39.97	39.52	40.16	40.16	39.77	40.17	41.97	40.85	41.03
$\eta_{sol.\ to\ el.}$, %	15.03	16.40	16.62	16.89	16.72	17.25	16.78	17.91	16.74
CF, %	62.66	62.13	62.84	62.84	62.39	62.87	62.55	61.64	63.98
EE, GWh/year	502.0	547.5	555.1	564.1	558.3	575.9	560.3	598.1	559
Heliostats, MUSD					217.7				
R&T, MUSD	156.8	160.0	156.2	156.3	158.5	156.1	152.4	155.6	153.9
TES, MUSD	110.0	139.4	103.4	104.4	126	102.7	69.3	100.9	85.8
Power cycle, MUSD	80.8	130.1	100.5	88.6	111.8	96.2	71.9	105.2	83.5
TCC, MUSD	705.0	804.1	720.0	707.0	763.9	713.9	639.7	722.2	675.6
LCOE, USD_{2020}/MWh	106.9	111.2	99.9	97.0	104.6	96.1	89.8	94.3	93.9

where $\eta_{sol.\ to\ th.}$– annual solar to thermal efficiency; $\eta_{sol.\ to\ el.}$– annual solar to electric efficiency; CF – capacity factor; R&T – receiver and tower cost

The distribution of optimized CPS plant cycles specific costs is shown in Figure 5.7a. The most expensive components for all cycles are recuperators and primary heat exchangers, followed by compressors/pumps. The lower portion of regenerated heat also leads to significantly lower costs of recuperators for simple and precompression cycles with the CO_2+Cl_3FSi mixture, making them one of the cheapest components. In Figure 5.7b the distribution of TCC, electricity output, and LCOE are shown. The increase in electricity generation in most mixtures cases does not compensate for the increase in the cost of using a more complex cycle layout.

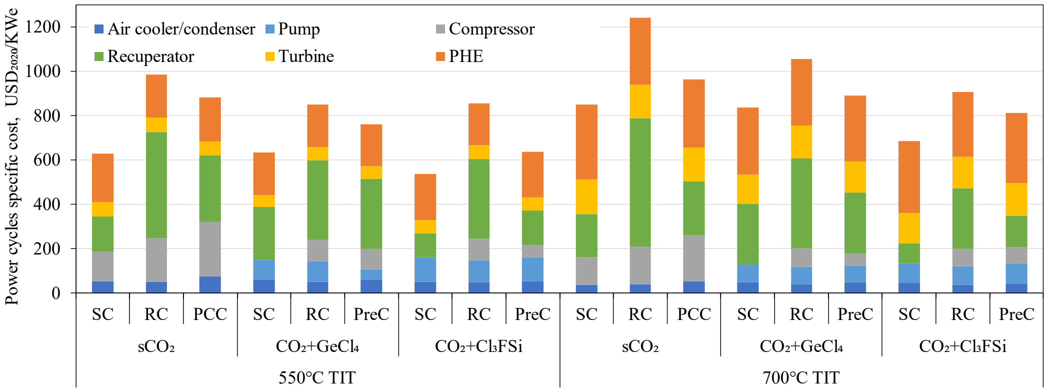

(a)

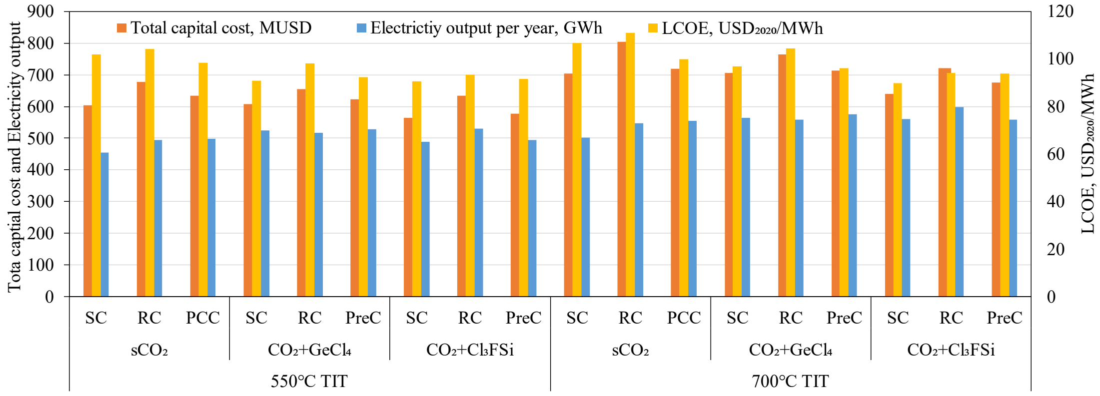

(b)

Figure 5.7. Power cycles cost distribution (a) and total capital cost, electricity generated and LCOE (b) for the optimum CSP plant case.

5.4. Conclusions

Preliminary analyses indicate that both CO_2+$GeCl_4$ and CO_2+Cl_3FSi mixture-based power cycles offer a reduction in LCOE compared to conventional sCO_2 cycles at both TIT levels. Among the power cycle configurations, the simple and precompression cycles are the most promising, while for sCO_2, the partial cooling layout achieves the lowest LCOE, followed by the simple and recompression layouts.

In general, simpler power cycle layouts exhibit lower efficiencies and reduced PHE inlet temperatures, which increases solar receiver efficiency. Nevertheless, their overall solar-to-electric efficiency at the CSP plant level remains lower. Their primary advantage lies in reduced costs of both the power cycle and thermal energy storage. Therefore, for mixtures, the simple cycle consistently results in one of the lowest LCOE.

For more accurate assessment, experimental data is needed to accurately tune the thermodynamic and transport properties models to be able to precisely characterize both efficiencies and economic performance of proposed mixtures in CSP plants.

5.5. Bibliography

[1] Turchi C, Gage S, Martinek J, Jape S, Armijo K, Coventry J, et al. CSP Gen3: Liquid-Phase Pathway to SunShot. 2021. https://doi.org/10.2172/1807668.

[2] Mehos M, Turchi C, Vidal J, Wagner M, Ma Z, Ho C, et al. Concentrating Solar Power Gen3 Demonstration Roadmap. NREL, SNL; 2017. https://doi.org/10.2172/1338899.
[3] Manzolini G, Binotti M, Bonalumi D, Invernizzi C, Iora P. CO2 mixtures as innovative working fluid in power cycles applied to solar plants. Techno-economic assessment. Solar Energy 2019;181:530–44. https://doi.org/10.1016/j.solener.2019.01.015.
[4] Doninelli M, Di Marcoberardino G, Iora P, Gelfi M, Invernizzi CM, Manzolini G. Silicon Tetrachloride as innovative working fluid for high temperature Rankine cycles: Thermal Stability, material compatibility, and energy analysis. Applied Thermal Engineering 2024;249:123239. https://doi.org/10.1016/j.applthermaleng.2024.123239.
[5] Naumov V, Doninelli M, Di Marcoberardino G, Iora P. Solar tower power plants with CO2 +SiCl4 mixtures transcritical cycles. Renewable Energy 2025:122518. https://doi.org/10.1016/j.renene.2025.122518.
[6] Neises T, Turchi C. Supercritical carbon dioxide power cycle design and configuration optimization to minimize levelized cost of energy of molten salt power towers operating at 650 °C. Solar Energy 2019;181:27–36. https://doi.org/10.1016/j.solener.2019.01.078.
[7] Morosini E, Villa E, Quadrio G, Binotti M, Manzolini G. Solar tower CSP plants with transcritical cycles based on CO2 mixtures: A sensitivity on storage and power block layouts. Solar Energy 2023;262:111777. https://doi.org/10.1016/j.solener.2023.05.054.
[8] Doctoral Network | TOPCSP 2022. https://topcsp.eu/ (accessed April 24, 2024).
[9] Aspen Plus | Leading Process Simulation Software | AspenTech n.d. https://www.aspentech.com/en/products/engineering/aspen-plus (accessed June 28, 2023).
[10] Span R, Wagner W. A New Equation of State for Carbon Dioxide Covering the Fluid Region from the Triple-Point Temperature to 1100 K at Pressures up to 800 MPa. J Phys Chem Ref Data 1996;25:1509–96. https://doi.org/10.1063/1.555991.
[11] Peng D-Y, Robinson DB. A New Two-Constant Equation of State. Ind Eng Chem Fund 1976;15:59–64. https://doi.org/10.1021/i160057a011.
[12] Di Marcoberardino G, Morosini E, Manzolini G. Preliminary investigation of the influence of equations of state on the performance of CO2 + C6F6 as innovative working fluid in transcritical cycles. Energy 2022;238:121815. https://doi.org/10.1016/j.energy.2021.121815.
[13] Illyés V, Morosini E, Doninelli M, David P-L, Guerif X, Werner A, et al. Design of an Air-Cooled Condenser for CO2-Based Mixtures: Model Development, Validation and Heat Exchange Gain with Internal Microfins. Volume 9: Supercritical CO2, Rotterdam, Netherlands: American Society of Mechanical Engineers; 2022, p. V009T28A016. https://doi.org/10.1115/GT2022-82438.
[14] Morosini E, Gentile G, Binotti M, Manzolini G. Techno-economic assessment of small-scale solar tower plants with modular billboard receivers and innovative power cycles. J Phys: Conf Ser 2022;2385:012109. https://doi.org/10.1088/1742-6596/2385/1/012109.
[15] Dario A, Astolfi M, Binotti M, Macchi E, Silva P. Part-load operation of coal fired sCO2 power plants. Conference Proceedings of the European sCO2 Conference3rd European Conference on Supercritical CO2 (sCO2) Power Systems 2019: 19th-20th September 2019 2019:68. https://doi.org/10.17185/DUEPUBLICO/48897.
[16] Naumov V, Gedik E, Petersen N, Di Marcoberardino G, Iora P, Wirsum M. Comparison of sCO2, CO2 mixture, and steam Rankine cycles for CSP with components sizing: implications for cost and flexibility. 6th Edition of the European Conference on Supercritical CO2 (sCO2) for Energy Systems, Conference Proceedings of the European sCO2 Conference, Delft, Netherlands: DuEPublico: Duisburg-Essen Publications Online; 2025, p. 244--254. https://doi.org/10.17185/DUEPUBLICO/83332.
[17] Manzolini G, Lucca G, Binotti M, Lozza G. A two-step procedure for the selection of innovative high temperature heat transfer fluids in solar tower power plants. Renewable Energy 2021;177:807–22. https://doi.org/10.1016/j.renene.2021.05.153.
[18] JRC Photovoltaic Geographical Information System (PVGIS) - European Commission n.d. https://re.jrc.ec.europa.eu/pvg_tools/en/ (accessed May 28, 2025).
[19] Moreno-Tejera S, Silva-Pérez MA, Lillo-Bravo I, Ramírez-Santigosa L. Solar resource assessment in Seville, Spain. Statistical characterisation of solar radiation at different time resolutions. Solar Energy 2016;132:430–41. https://doi.org/10.1016/j.solener.2016.03.032.
[20] System advisor model (SAM) case study: Gemasolar. NREL 2013:6.
[21] Wang S, Asselineau C-A, Fontalvo A, Wang Y, Logie W, Pye J, et al. Co-optimisation of the heliostat field and receiver for concentrated solar power plants. Applied Energy 2023;348:121513. https://doi.org/10.1016/j.apenergy.2023.121513.
[22] National Renewable Energy Laboratory. System Advisor Model Version 2022.11.21 (SAM 2022.11.21). NREL SAM 2022. https://https://sam.nrel.gov (accessed February 22, 2024).
[23] Rodríguez-deArriba P, Crespi F, Pace S, Sánchez D. Mapping the techno-economic potential of next-generation CSP plants running on transcritical CO 2 -based power cycles. Energy 2024:133142. https://doi.org/10.1016/j.energy.2024.133142.

6. New CO_2 dopants experimental investigation results

The experimental apparatus used for new dopants thermal stability characterization shown in Figure 6.1 was previously described in literature [1]. It consists of an experimental circuit, thermostatic bath, muffle furnace, and data acquisition system. A thermostatic bath is used to control the tested fluid temperature to obtain the vapor pressure curve, while a muffle furnace is used to apply the thermal stress.

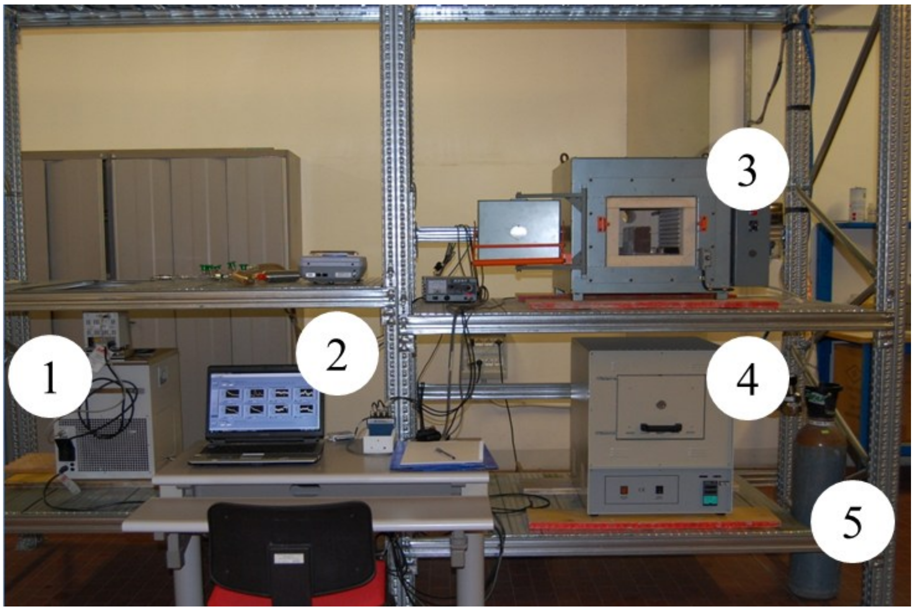

Figure 6.1. Main equipment used for the thermal stability test: (1) thermostatic bath, (2) data acquisition system, (3) electric oven, (4) muffle furnace, (5) helium for leakage tests.

The experimental circuit shown in Figure 6.2 consists of a metal vessel, valves, pressure transducers, a temperature probe, and connecting tubes. It is first tested for leakages using helium and then filled with fluid of interest. The list of equipment used with its characteristics is shown in Table 6.1.

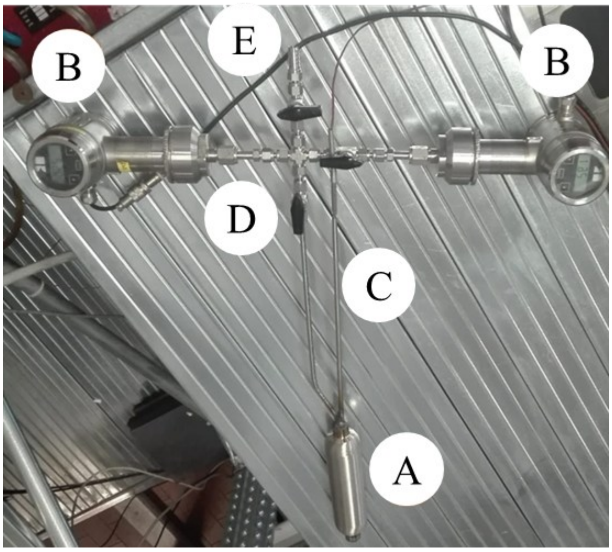

Figure 6.2. Main components of the thermal stability test circuit: (A) 316L vessel, (B) pressure transducer, (C) temperature probe housing, (D) vessel valve, (E) circuit main valve.

The metal vessel has a pressure transducer and thermocouple to measure pressure and temperature inside. The test is based on a comparison of vapor pressure curves before and after the thermal stress of the fluid.

The thermal stability test consists of the following steps:

1. evacuation of the system with a vacuum pump,
2. loading of the specified mass of fluid,
3. measurement of the fluid vapor pressure in the thermostatic bath,
4. 100-hour thermal stress in the muffle furnace at a constant temperature.

At first the reference vapor pressure curve is obtained using the fresh fluid. Steps 3 and 4 are then repeated until the desired stress temperature or fluid degradation is reached.

Table 6.1. Instruments used for thermal stability tests

Equipment	**Manufacturer**	**Model**	**Characteristics**	
Vacuum pump	Alcatel	2012A	Vacuum down to 1/1000 mbar	
Sample cylinder	Swagelok	-	Material: AISI 316L Internal Volume: 150 cm^3	
Needle valves	Swagelok	SS-4H-V13	Material: AISI 316L	
Equipment	**Manufacturer**	**Model**	**Measurement range**	**Accuracy**
Scale	Mettler-Toledo	MS12002TS FS	up to 12.2 kg	0.1 g
Thermostatic bath	Julabo	Julabo FP 40	-45-150°C	0.1 °C
Pressure transmitter 1 (C_3F_6 tests)	Keller	Klay 2000-SAN	Adjustable (1-5 bar used)	0.1 % of full-scale
Pressure transmitter 2 ($GeCl_4$ tests)	Wika	S-20	6 bar	0.25% of full-scale
Thermocouple	Tersid	Type K	-200-1270 °C	Tolerance class I

Total uncertainty of experimental results was calculated based on instrumental uncertainty and standard deviation of the variable:

$$u(x) = \sqrt{u_{instrumental}(x)^2 + \sigma(x)^2} \tag{6.4}$$

$$\sigma(x) = \sqrt{\frac{\sum(x_i - \bar{x})^2}{n}} \tag{6.5}$$

where $u_{instrumental}$ – uncertainty of the measuring instrument; x_i are acquisitions of parameter made for a single point; $\bar{x}$ – average value of the parameter in a point; $n = 120$ acquisitions during 10 minutes with 5 seconds interval.

The thermocouple has 1.5°C tolerance in the temperature range of interest, while the standard deviation of temperature is very small across all experiments. This makes the thermocouple the main source of total temperature uncertainty. For pressure measurements, the main uncertainty contribution is also instrumental and comes from pressure transmitters but depends on the transmitter and measurement span used.

The thermodynamic properties of the fluids used in tests and modelling are shown in Table 6.2 [2]. Vapor pressure curves of pure fluids were calculated using the Antoine equation (6.6) with parameters from [3] shown in Table 6.3.

Table 6.2. Thermodynamic properties of fluids

Property	**CO_2**	**C_3F_6**	**$GeCl_4$**
CAS number	124-38-9	116-15-4	10038-98-9

Property	CO_2	C_3F_6	$GeCl_4$
Molar mass, g/mol	44.0	150.0	214.4
Acentric factor	0.224	0.205	0.218
Critical pressure, bar	73.8	29.0	38.6
Critical temperature, °C	31.1	94.8	280
Critical compressibility	0.274	0.254	0.271
Triple point temperature, °C	-56.6	-156.5	-51
Boiling temperature, °C	-78.4	-29.6	83

$$log10(P) = A - \frac{B}{T + C} \tag{6.6}$$

where P – vapor pressure in bar; T – temperature in K; A, B, C – parameters.

Table 6.3. Antoine equation parameters of fluids [3]

Parameter	C_3F_6	$c\text{-}C_4F_8$	$GeCl_4$
A	4.51288	4.254	3.68225
B	1028.267	1007.399	1080.101
C	-14.694	-30.205	-63.588

6.1. Hexafluoropropylene (C_3F_6)

Following the successful tests of C_6F_6 [4], it was decided to consider the hexafluoropropylene (C_3F_6) as a possible dopant. Since the C_3F_6 was planned to be used in the CO_2 mixture, the EoS was tuned to represent the mixture thermodynamic properties. In the literature, the Peng-Robinson (PR) Equation of State (EoS) with the Mathias-Copeman alpha function was used to obtain the binary interaction parameter $k_{ij} = 0$ [5]. In the current work, the PR EoS in standard formulation was used with Boston-Mathias alpha function and Van der Waals mixing rules. The data from [5,6], available in Aspen Plus NIST TDE [2], was used to regress the binary interaction parameter $k_{ij} = 0.02305 \pm 0.00236$. In Figure 6.3, one can see the comparison of VLE data and modeling results with good accuracy. The 40°C isotherm is an outlier and was previously modeled using the PR EoS with Wong-Sandler mixing rules and the NRTL activity coefficient model [6], while the current model uses the standard PR EoS formulation. The resulting critical parameters dependence on the mixture composition is shown in Figure 6.4, with mixtures with C_3F_6 above 70 mol% having critical temperatures above 50°C.

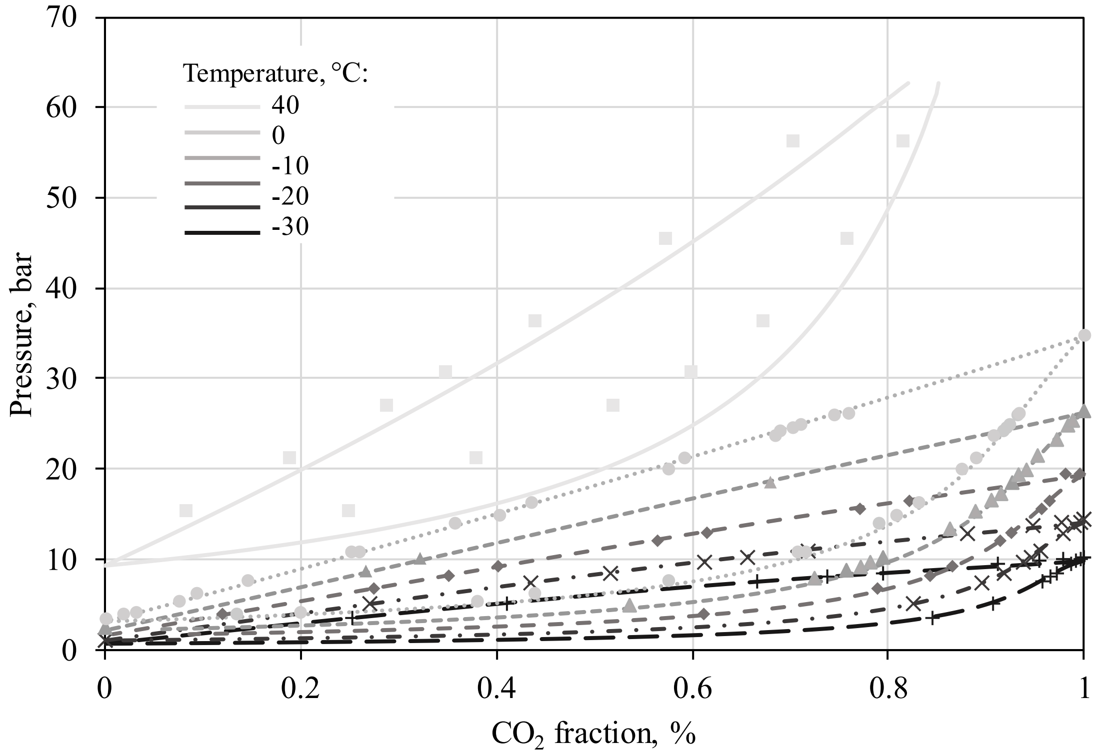

Figure 6.3. Equilibrium CO_2+C_3F_6 liquid and vapor pressure dependence on the composition for different temperatures (lines for model and markers for experimental data).

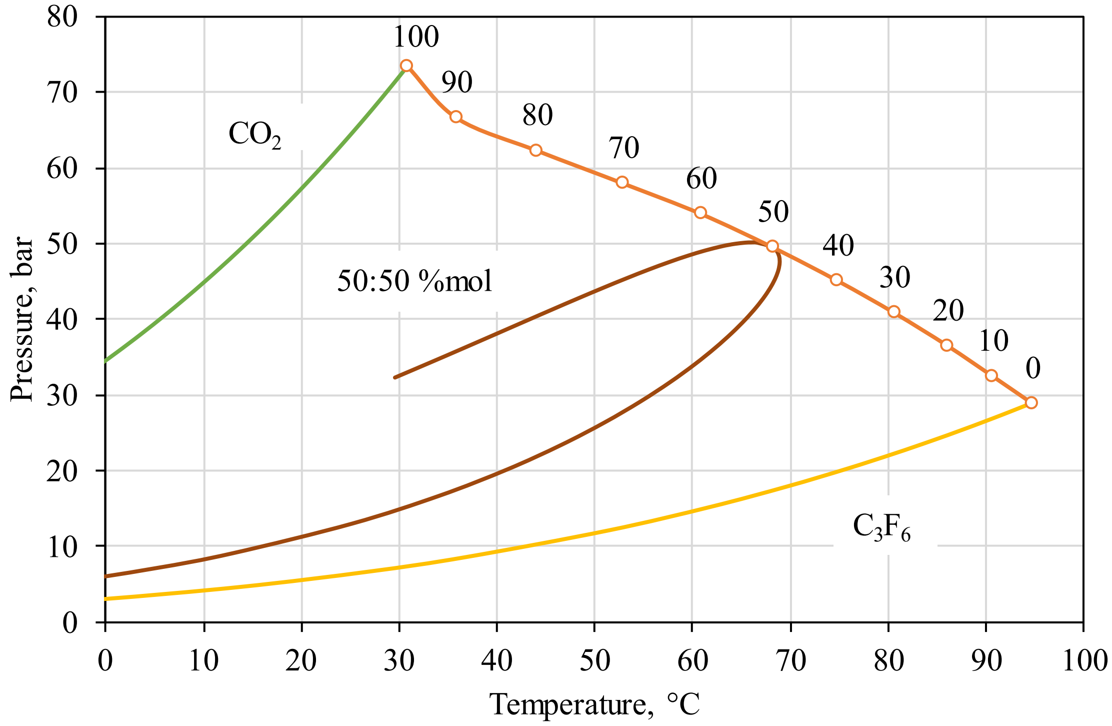

Figure 6.4. Critical point locuses on P-T diagram for CO_2+C_3F_6 with different CO_2 molar fractions (the green line is the pure CO_2 and the yellow line is the pure C_3F_6 vapor pressure curves; the brown line is the 50:50 P-T envelope).

As discussed previously, the experimental characterization of the working fluid began with the evaluation of its thermal stability. The fresh fluid vapor pressure curve was measured and compared with experimental literature data shown in Figure 6.5 [5,7–22]. The experimental results with uncertainties are available in Table 6.4. For further analysis, the vapor pressure curve was calculated using the Antoine equation from [3].

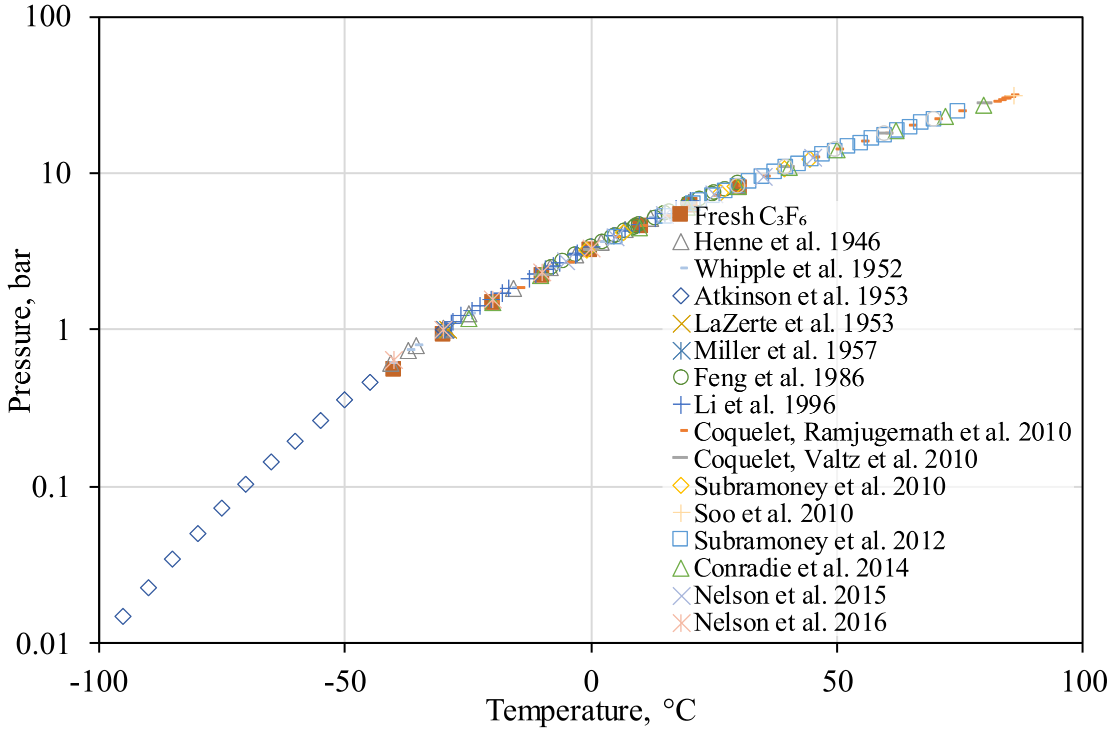

Figure 6.5. Measured hexafluoropropylene (C_3F_6) vapor pressure comparison with the experimental data

The thermostability tests for C_3F_6 were carried out at 400°C. After 100 hours of exposure, the vapor pressure curve showed the formation of fluid with a higher critical point than C_3F_6. In Figure 6.6 are shown the C_3F_6 vapor pressure curve, experimental curves used as a reference, and after thermal stress. It was found that, according to literature, C_3F_6 at medium temperatures turns mainly into i-C_4F_8, which is a highly toxic gas [10,23]. This "chain-elongation behavior contrasts with the familiar cracking" [23] and explains the decrease of vapor pressure after the thermal stability test. To illustrate this, the c-C_4F_8 vapor pressure curve calculated with Antoine equation (6.6) with parameters from Table 6.3 is added, since the thermodynamic parameters of i-C_4F_8 are not available. Therefore, the thermal stability was not confirmed, and the dopant was abandoned for high-temperature applications.

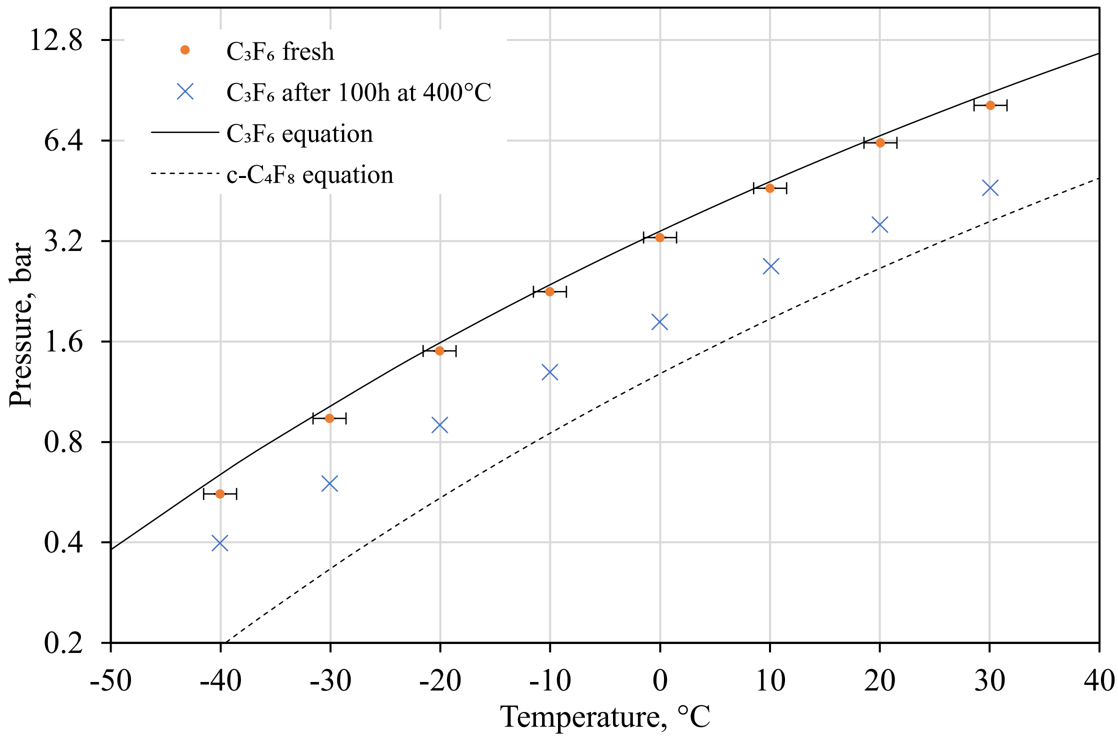

Figure 6.6. Hexafluoropropylene (C_3F_6) vapor pressure thermal stress results at after 100 hour exposure to 400°C

Table 6.4. Fresh C_3F_6 vapor pressure experimental results with uncertainty

Temp., °C	**U(T), °C**	**Pres., bar**	**U(P), bar**
-40.049	1.500	0.559	0.001
-30.089	1.500	0.941	0.001
-20.071	1.500	1.498	0.002
-10.027	1.500	2.254	0.003
-0.002	1.500	3.277	0.004
10.017	1.500	4.604	0.005
20.061	1.500	6.296	0.007
30.081	1.500	8.153	0.009

6.2. Germanium tetrachloride ($GeCl_4$)

The 100 grams of germanium tetrachloride at 99.99% were acquired from Thermo Fisher Scientific Inc. In previous experiments, it was found to be stable at 950°C in a quartz tube [24]. The pure $GeCl_4$ data is widely available in the literature [24–28], therefore, an Antoine equation with parameters from [3], shown in Table 6.3, was used to represent the vapor pressure curve literature data. The measured pressure curves for fresh fluid and after the thermal stress are shown in Figure 6.7. Up to around 60°C, the experimental results obtained are in accordance with the equation, considering the measurement uncertainty. At higher temperatures, all fluid in the cylinder is in the gas phase. The experimental results with uncertainties are available in Table 6.5. After thermal stress, the pressure curve behaves as an ideal gas, indicating the full decomposition of $GeCl_4$. Therefore, the thermal stability of $GeCl_4$ in 316L was not confirmed, and the dopant was abandoned for high-temperature applications.

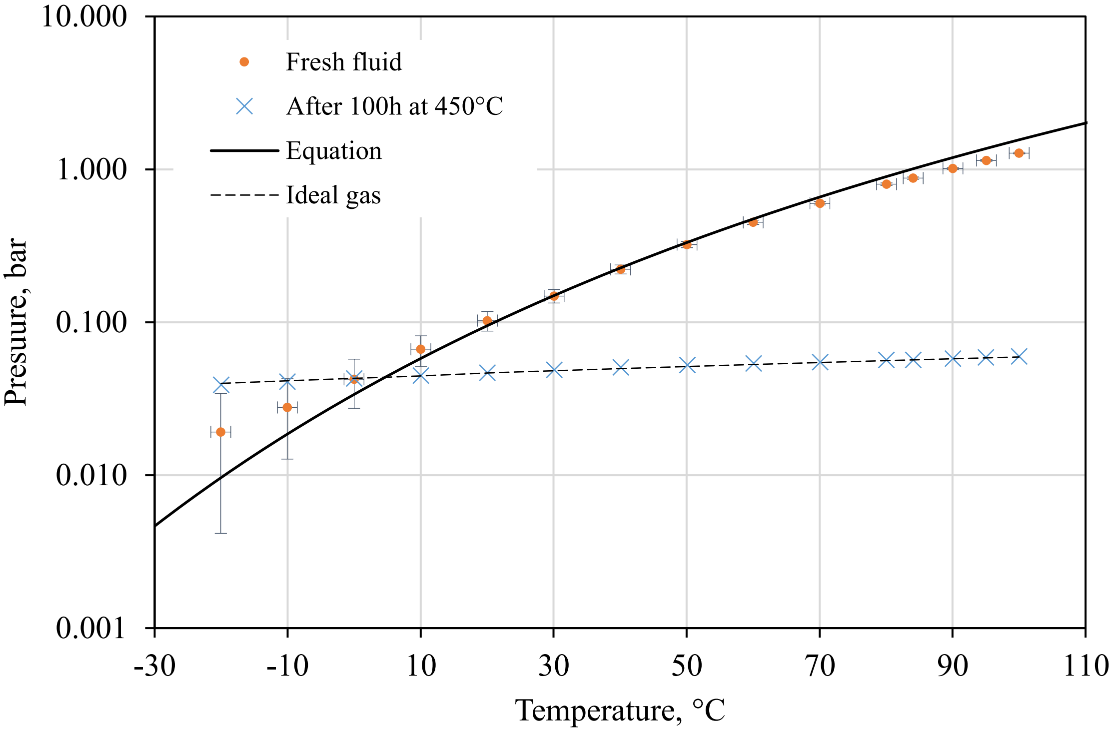

Figure 6.7. Germanium tetrachloride ($GeCl_4$) vapor pressure from literature, experimental reference results and after thermal stress

Table 6.5. Fresh $GeCl_4$ vapor pressure experimental results with uncertainty

Temperature, °C	U(T), °C	Pressure, bar	U(P), bar
-20.044	1.500	0.019	0.015
-10.039	1.500	0.028	0.015
-0.018	1.500	0.042	0.015
10.036	1.500	0.067	0.015
20.039	1.500	0.103	0.015
30.080	1.500	0.149	0.015
40.079	1.500	0.222	0.015
50.066	1.500	0.322	0.015
60.011	1.500	0.450	0.015
70.045	1.500	0.600	0.015
80.060	1.500	0.801	0.015
84.069	1.501	0.876	0.016
90.057	1.501	1.015	0.016
95.085	1.500	1.144	0.016
100.014	1.503	1.279	0.016

After the thermal stress test, the vessel was examined in MetalLabs [29] Metallurgy Group of UniBs to determine the impact on the material and identify the traces of reactions that took place [30]. Possible reactions were identified based on a literature review. First, the $GeCl_4$ could react with the silicon (Si) present in the alloy [31]. At 300°C $GeCl_4$ reacts with silicon, forming $GeCl_2$, GeCl, elemental Ge bonded to Si, and SiCl. At 500°C SiCl, $SiCl_2$, and Ge bonded to Si are formed. The second reaction that could have been happening is the formation of $GeCl_2$ when vapor $GeCl_4$ passes over Ge at 300°C [32]. Germanium dichloride ($GeCl_2$) and SiGe are solids, while SiCl, GeCl and $SiCl_2$ are gases, with the last two being highly unstable. Chlorine could also react with chromium, nickel and iron in the alloy to form different types of solid metal chlorides highly soluble in water.

A section of the vessel with the base and shell weld was cut off underwater, with a further central cut done as shown in Figure 6.8. Scanning electron microscopy (SEM) analysis was used to determine the weight composition of material in different parts of the vessel, with more information available in Appendix A: SEM analysis.

Figure 6.8. The 316L vessel after $GeCl_4$ thermal stress for 100h at 450°C

Based on the SEM analysis conducted, there is germanium present on the surface and in the cracks of the part of the vessel analyzed. There is also chlorine to be found on the surface, but it is concentrated in the threads and in the transition area between the base and the shell and is absent on the shell surface. The concentration of silicon is also higher on the surface than in the bulk material in almost all points analyzed. There are formations made primarily of Ge Fe and Ni in the transition zone and shell. The cracks are present only on the threads and could have been there even before the test. Overall, the interactions observed are rather mild, likely due in part to the limited exposure duration (100 hours) and the small quantity of fluid used (on the order of a few grams), and are insufficient to draw definitive conclusions.

6.3. Conclusions

The vapor pressure curves of fresh hexafluoropropylene (C_3F_6) and germanium tetrachloride ($GeCl_4$) were measured. The results were found to be in accordance with the literature data within the measurement uncertainty. For the C_3F_6 Peng-Robinson EoS, the binary interaction parameter was regressed based on literature data. Hexafluoropropylene and germanium tetrachloride were thermally stressed for 100 hours at 400°C and 450°C, respectively. Based on the big discrepancy between the fresh and stressed fluid vapor pressure curves, both fluids were found to be thermally unstable at the temperatures of the test.

The vapor pressure of $GeCl_4$ after thermal stress resembles that of an ideal gas, which could indicate that all fluid in the vessel has turned into solid and gas with very low critical pressure. In the case of C_3F_6, the vapor pressure after thermal stress is lower than in the fresh fluid, which is contradictory to the usual thermal decomposition processes. However, these results are in accordance with literature, which indicates the formation of i-C_4F_8 with higher critical temperature during heating. Therefore, neither new dopant is applicable to CSP plant power cycles due to low thermal stability.

6.4. Bibliography

[1] Pasetti M, Invernizzi CM, Iora P. Thermal stability of working fluids for organic Rankine cycles: An improved survey method and experimental results for cyclopentane, isopentane and n -butane. Applied Thermal Engineering 2014;73:764–74. https://doi.org/10.1016/j.applthermaleng.2014.08.017.

[2] NIST Standard Reference Database 103b. NIST 2010.
[3] NIST Chemistry WebBook n.d. https://webbook.nist.gov/chemistry/ (accessed December 15, 2025).
[4] Di Marcoberardino G, Morosini E, Di Bona D, Chiesa P, Invernizzi C, Iora P, et al. Experimental characterisation of CO2 + C6F6 mixture: Thermal stability and vapour liquid equilibrium test for its application in transcritical power cycle. Applied Thermal Engineering 2022;212:118520. https://doi.org/10.1016/j.applthermaleng.2022.118520.
[5] Nelson WM, Benecke TP, Ramjugernath D. Phase equilibrium data for binary mixtures of carbon dioxide with {1,1,2,3,3,3-hexafluoro-1-propene or 2,2,3-trifluoro-3-(trifluoromethyl)oxirane} at temperatures between (233 and 273) K. Fluid Phase Equilibria 2016;425:114–9. https://doi.org/10.1016/j.fluid.2016.05.004.
[6] Nelson WM, Subramoney SC, Valtz A, Coquelet C, Richon D, Naidoo P, et al. Vapor−Liquid Equilibrium Data for Binary Systems Consisting of Either Hexafluoropropene (HFP) or 2,2,3-Trifluoro-3-(trifluoromethyl)oxirane (HFPO) with Carbon Dioxide (R-744) or 2,2-Dichloro-1,1,1-trifluoroethane (R-123). J Chem Eng Data 2011;56:74–8. https://doi.org/10.1021/je100841y.
[7] Henne AL, Waalkes TP. Fluorinated derivatives of propane and propylene. VI. Journal of the American Chemical Society 1946;68:496–7.
[8] Young EG, Murray WS. The Structure of C_3 F_6. J Am Chem Soc 1948;70:2814–5. https://doi.org/10.1021/ja01188a508.
[9] Whipple GH. Vapor-Liquid Equilibria of Some Fluorinated Hydrocarbon Systems. Ind Eng Chem 1952;44:1664–7. https://doi.org/10.1021/ie50511a050.
[10] Atkinson B, Trenwith A. The thermal decomposition of tetrafluorethylene. Journal of the Chemical Society (Resumed) 1953:2082–7.
[11] LaZerte JD, Hals LJ, Reid TS, Smith GH. Pyrolyses of the Salts of the Perfluoro Carboxylic Acids[1]. J Am Chem Soc 1953;75:4525–8. https://doi.org/10.1021/ja01114a040.
[12] Miller WT, Fainberg AH. Preferential Replacement Reactions of Highly Fluorinated Alkyl Halides. I. Preparation of Certain Fluorinated Allyl Iodides[1,2]. J Am Chem Soc 1957;79:4164–9. https://doi.org/10.1021/ja01572a049.
[13] Feng G, Liu H, Hu Y. Vapor-liquid equilibria of Freon 22 and hexafluropropylene binary system under moderate pressures. Journal of East China University of Science and Technology 1986.
[14] Li C, Feng Y, Wu Z. Vapor Pressure of Hexafluoropropylene. Journal of East China University of Science and Technology 1996:64–6.
[15] Coquelet C, Ramjugernath D, Madani H, Valtz A, Naidoo P, Meniai AH. Experimental Measurement of Vapor Pressures and Densities of Pure Hexafluoropropylene. J Chem Eng Data 2010;55:2093–9. https://doi.org/10.1021/je900596d.
[16] Coquelet C, Valtz A, Naidoo P, Ramjugernath D, Richon D. Isothermal Vapor−Liquid Equilibrium Data for the Hexafluoropropylene (R1216) + Propylene System at Temperatures from (263.17 to 353.14) K. J Chem Eng Data 2010;55:1636–9. https://doi.org/10.1021/je900703f.
[17] Subramoney SC, Nelson WM, Valtz A, Coquelet C, Richon D, Naidoo P, et al. Pure Component and Binary Vapor−Liquid Equilibrium + Modeling for Hexafluoropropylene and Hexafluoropropylene Oxide with Toluene and Hexafluoroethane. J Chem Eng Data 2010;55:411–8. https://doi.org/10.1021/je900400v.
[18] Subramoney SC, Valtz A, Coquelet C, Richon D, Naidoo P, Ramjugernath D. Vapor–Liquid Equilibrium Measurements and Modeling for the Ethane (R-170) + 1,1,2,3,3,3-Hexafluoro-1-propene (R-1216) Binary System. J Chem Eng Data 2012;57:2947–55. https://doi.org/10.1021/je300431n.
[19] Conradie FJ, Crouse PL, Courtial X, Nelson WM, Van Der Walt IJ, Ramjugernath D. Isothermal Vapor–Liquid Equilibrium Data for the 1,1,2,2-Tetrafluoroethene + 1,1,2,3,3,3-Hexafluoroprop-1-ene Binary System: Measurement and Modeling from (248 to 283) K. J Chem Eng Data 2014;59:82–8. https://doi.org/10.1021/je400828j.
[20] Nelson WM, Williams-Wynn M, Subramoney SC, Ramjugernath D. Isothermal Vapor–Liquid Equilibrium Data for the Binary System 1,1,2,3,3,3-Hexafluoro-1-propene (R1216) + 2,2,3-Trifluoro-3-(trifluoromethyl)oxirane from (268.13 to 308.19) K. J Chem Eng Data 2015;60:568–73. https://doi.org/10.1021/je5006938.
[21] Hashemi H, Nelson WM, Babaee S, Naidoo P, Ramjugernath D. Isothermal Vapor–Liquid Equilibrium Data for the Binary Systems Consisting of 1,1,2,3,3,3-Hexafluoro-1-propene and Either Methylcyclohexane, Cyclohexane, *n* -Hexane, 2-Methyltetrahydrofuran, or 2,2,3,3,4,4,4-Heptafluoro-1-butanol. J Chem Eng Data 2019;64:5232–7. https://doi.org/10.1021/acs.jced.9b00441.
[22] Soo C-B, Théveneau P, Coquelet C, Ramjugernath D, Richon D. Determination of critical properties of pure and multi-component mixtures using a "dynamic–synthetic" apparatus. The Journal of Supercritical Fluids 2010;55:545–53. https://doi.org/10.1016/j.supflu.2010.10.022.
[23] Poutsma ML. Chain elongation during thermolysis of tetrafluoroethylene and hexafluoropropylene: Modeling of mechanistic hypotheses and elucidation of data needs. Journal of Analytical and Applied Pyrolysis 2011;92:25–42. https://doi.org/10.1016/j.jaap.2011.04.006.
[24] Laubengayer AW, Tabern DL. Germanium. XIV. J Phys Chem 1926;30:1047–8. https://doi.org/10.1021/j150266a005.
[25] Toczylkin L, Young C. Vapour pressures of some liquids of quasi-spherical molecules near their critical points and the applicability of the principle of corresponding states. Australian Journal of Chemistry 1977;30:1591–3. https://doi.org/10.1071/CH9771591.
[26] Liebhafsky HA. Gmelins Handbuch der Anorganischen Chemie. J Am Chem Soc 1959;81:3487–8. https://doi.org/10.1021/ja01522a095.

[27] Gray DE, Wise H. *American Institute of Physics Handbook*. Physics Today 1957;10:36–8. https://doi.org/10.1063/1.3060136.
[28] Stull DR. Vapor Pressure of Pure Substances. Organic and Inorganic Compounds. Ind Eng Chem 1947;39:517–50. https://doi.org/10.1021/ie50448a022.
[29] Gruppo di Metallurgia - English n.d. https://metallurgia.unibs.it/english (accessed March 18, 2026).
[30] Putelli L, Di Marcoberardino G, Gelfi M, Invernizzi CM, Iora PG, Manzolini G. Preliminary Analysis of High-Temperature Corrosion of Metallic Alloys With CO2 and CO2-Based Working Mixtures for Power Plants Applications, American Society of Mechanical Engineers Digital Collection; 2022. https://doi.org/10.1115/GT2022-84197.
[31] Lapiano-Smith DA, McFeely FR. The chemisorption and reaction of GeCl4 with Si(100). Thin Solid Films 1993;225:187–90. https://doi.org/10.1016/0040-6090(93)90153-G.
[32] Greenwood NN, Earnshaw A. Chemistry of the Elements. Elsevier; 1997. https://doi.org/10.1016/C2009-0-30414-6.
[33] METALCOR. 1.4404 (AISI 316 L), S31603 | Datasheet | METALCOR n.d. https://www.metalcor.de/en/datenblatt/12/ (accessed March 17, 2026).

Appendix A: SEM analysis

The AISI 316L alloy chemical composition is available in Table 6.6 [33].

Table 6.6. The AISI 316L alloy chemical composition [33]

	Chemical composition, wt%								
	C	Si	Mn	P	S	Cr	Mo	Ni	N
Min	-	-	-	-	-	16.5	2.00	10.0	-
Max	0.03	1.00	2.00	0.045	0.015	18.5	2.50	13.0	0.11

A section of the vessel with the base and shell weld was cut off under water with a further central cut done as shown in Figure 6.8. Scanning Electron Microscopy was used with all elements analyzed and results normalized. Results for the base of the vessel are shown in Figure 6.9 with corresponding chemical compositions in Table 6.7. In the case of Figure 6.9a point 1 the composition in the bulk is within the specification for 316L alloy in Table 6.6 with a little excess of chromium. The pockets in Figure 6.9b, Figure 6.9c, Figure 6.9d and Figure 6.9e are probably due to impurities in metal such as oxygen and sulfur in the form of manganese sulfides and others. The cracks in the rest of figures in the thread could have occurred before exposure to the germanium tetrachloride during the production process. On all surfaces analyzed, there are traces of chlorine, including inside the cracks. In Figure 6.9e in point one there is a significant percentage of germanium to be found. All surfaces also have a presence of silicone, and at most points, its concentration is higher than in the original material. This could be due to the silicon oxidation or as a result of silicon used in flux during the welding process.

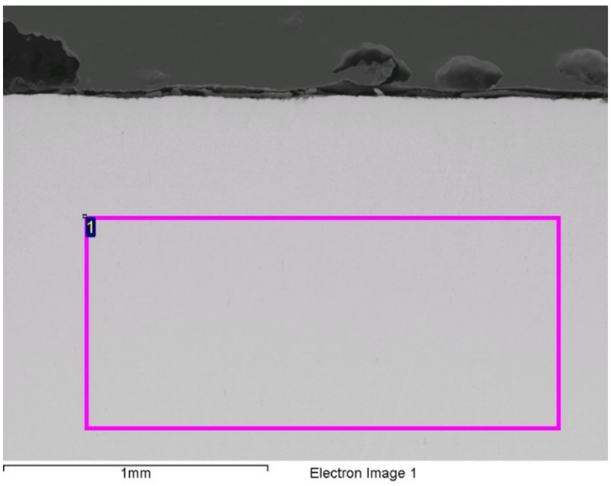

(a)

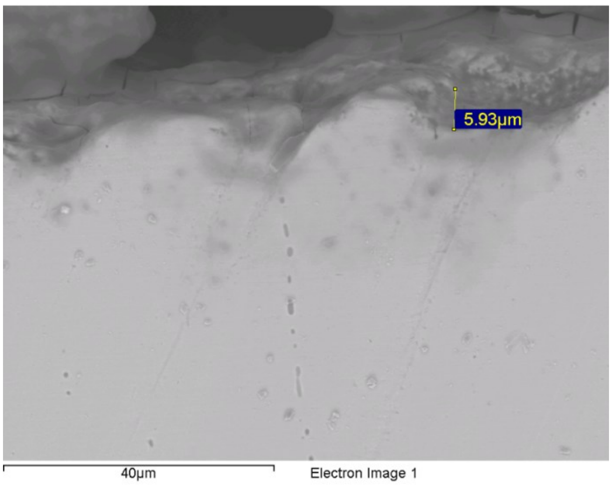

(b)

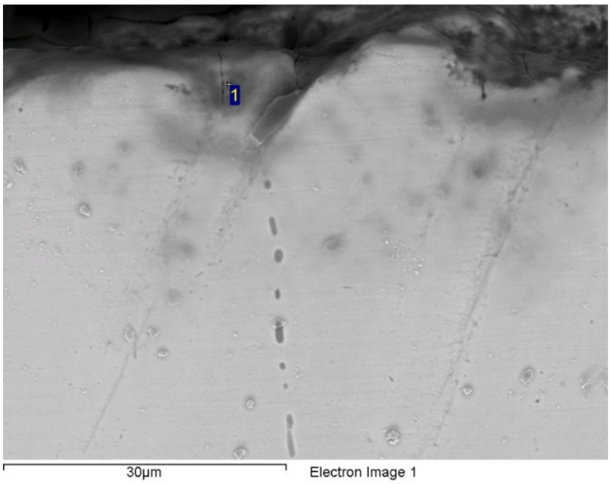
1
30µm
Electron Image 1

(c)

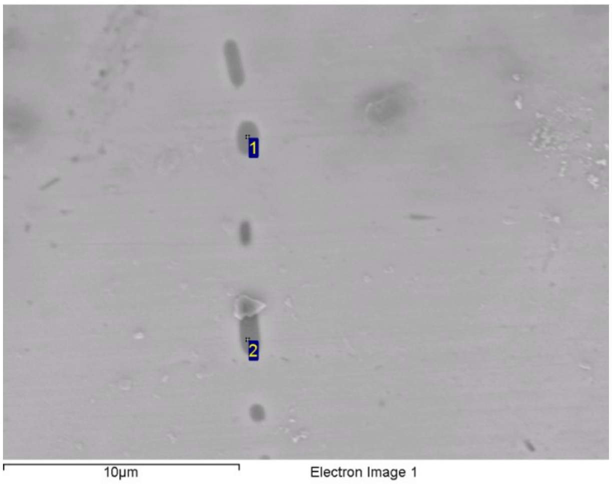
1
2
10µm
Electron Image 1

(d)

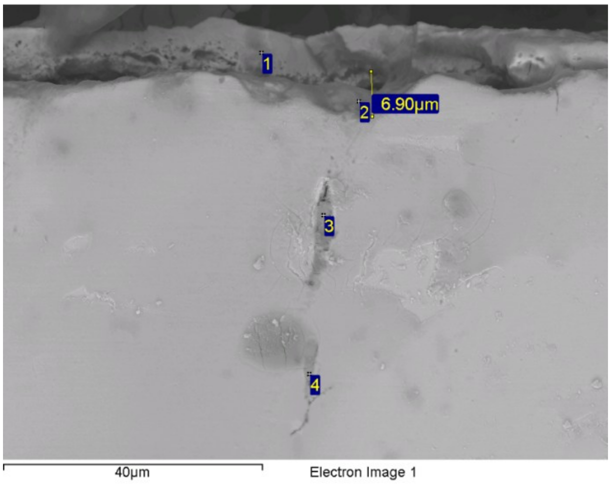
1
6.90µm
2
3
4
40µm
Electron Image 1

(e)

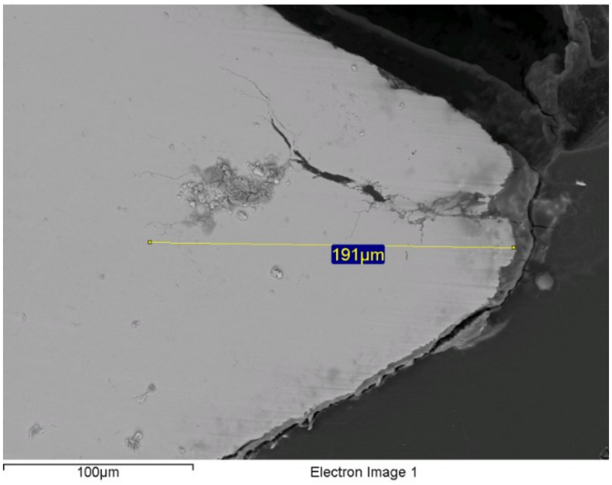
191µm
100µm
Electron Image 1

(f)

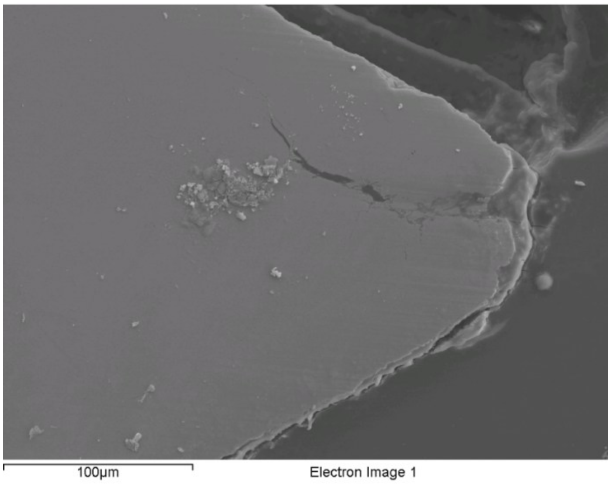
100µm
Electron Image 1

(g)

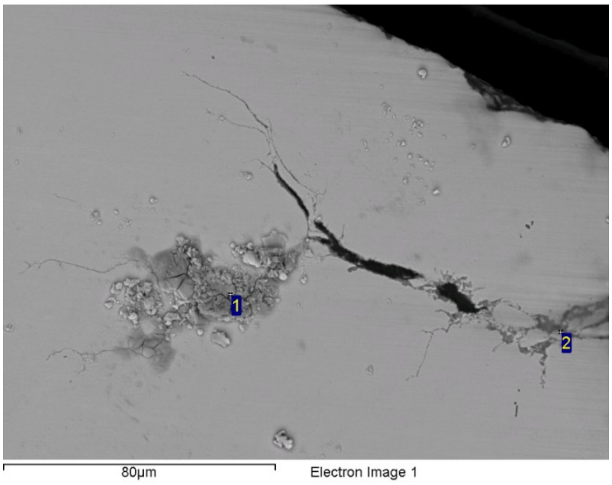
1
2
80µm
Electron Image 1

(h)

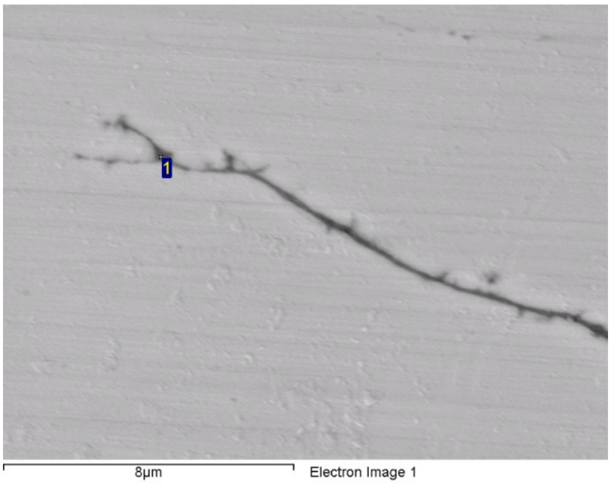

(i)

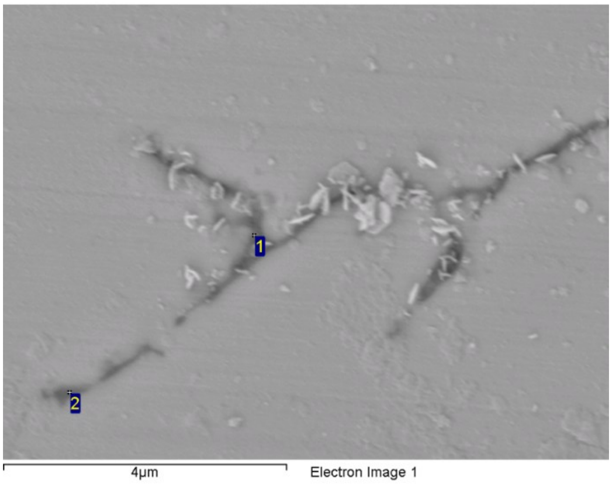

(j)

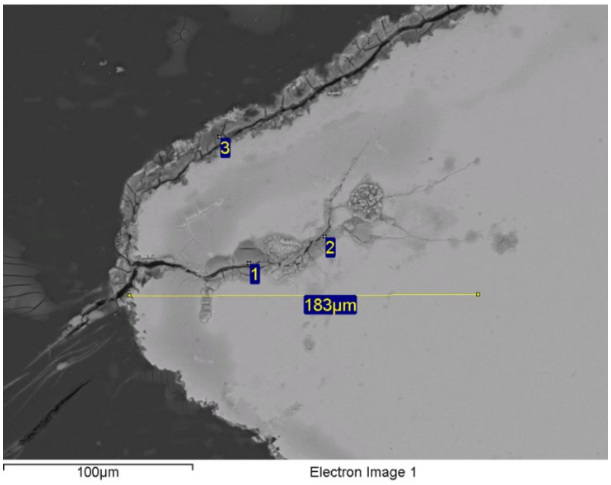

(k)

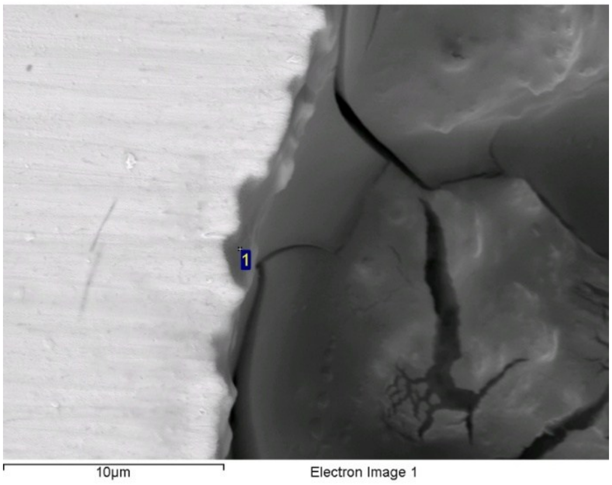

(l)

Figure 6.9. The SEM analysis of the base of vessel section

Table 6.7. The chemical composition of vessel base section in points from Figure 6.9

Figure	Point	Chemical composition, wt%												
		C	**O**	**Al**	**Si**	**S**	**Cl**	**Cr**	**Mn**	**Fe**	**Ni**	**Mo**	**Ge**	**Cu**
Figure 6.9a	1	-	-	-	0.61	-	-	18.76	1.47	64.99	11.44	2.72	-	-
Figure 6.9c	1	-	17.53	-	0.73	1.61	2.90	18.94	1.37	48.64	8.28	-	-	-
Figure 6.9d	1	14.30	-	-	-	11.27	-	13.29	14.82	40.02	6.31	-	-	-
Figure 6.9d	2	10.89	-	-	-	15.33	-	12.88	22.17	33.67	5.06	-	-	-
Figure 6.9e	1	-	9.69	-	1.75	-	3.50	5.72	-	38.91	9.68	-	30.76	-
Figure 6.9e	2	-	9.83	-	0.76	-	1.89	19.91	1.42	53.57	9.72	-	2.90	-
Figure 6.9e	3	-	20.00	-	0.49	18.52	2.70	21.72	-	32.79	3.78	-	-	-
Figure 6.9e	4	11.31	8.24	-	-	26.12	-	25.75	-	25.07	2.77	-	-	0.75
Figure 6.9h	1	-	13.58	-	-	-	17.83	13.46	0.94	47.22	6.97	-	-	-
Figure 6.9h	2	-	12.81	-	3.23	-	2.28	16.47	1.17	53.71	10.33	-	-	-
Figure 6.9i	1	-	6.73	-	0.85	-	1.59	20.59	61.20	9.04	1.59	-	-	-
Figure 6.9j	1	-	6.45	-	0.87	-	0.50	22.57	1.05	59.86	8.70	-	-	-
Figure 6.9j	2	-	5.75	-	1.61	-	0.22	19.03	1.02	63.40	8.97	-	-	-
Figure 6.9k	1	-	36.11	0.82	1.54	-	7.64	21.37	-	27.63	4.87	-	-	-
Figure 6.9k	2	-	30.44	-	-	-	2.46	10.95	-	46.23	9.92	-	-	-
Figure 6.9k	3	-	48.57	0.86	9.98	-	13.62	13.91	-	10.83	2.23	-	-	-
Figure 6.9l	1	19.68	13.85	-	0.51	-	1.58	17.71	1.17	33.86	5.28	-	6.37	-

Results for the base-shell transition section of the vessel are shown in Figure 6.10 with corresponding chemical compositions in Table 6.8. For the bulk of material in Figure 6.10a, point 1, the composition is within the specification for alloy 316L. On all the surfaces there is some germanium, chlorine, and silicon with concentrations higher than in the original material in most cases. There are also formations primarily made of Ge, Fe and Ni in point 1 in Figure 6.10d and Figure 6.11b in the shell.

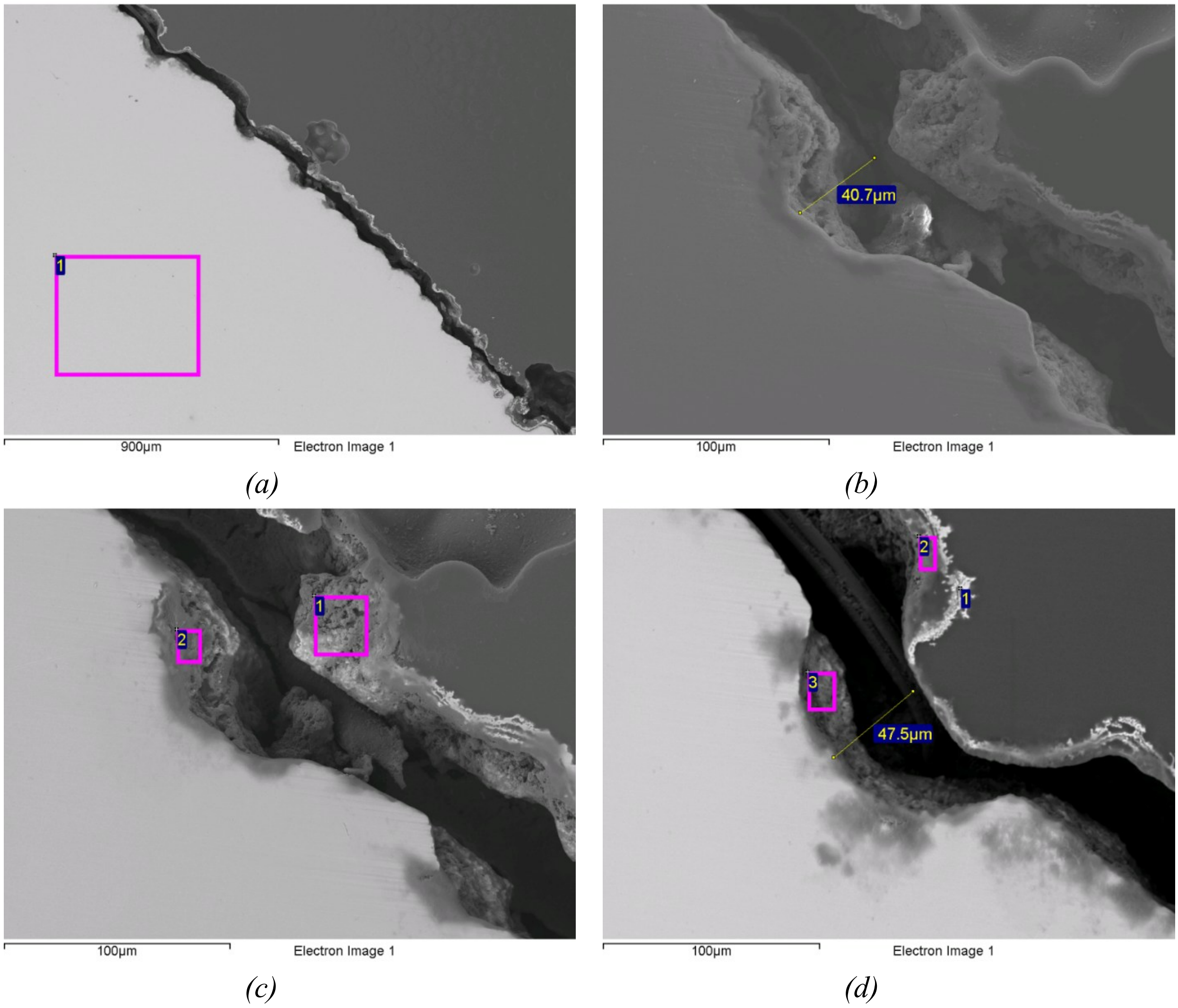

Figure 6.10. The SEM analysis of the vessel base-shell transition section

Table 6.8. The chemical composition of vessel transition section in points from Figure 6.10

Figure	**Point**	**Chemical composition, wt%**											
		C	**O**	**Mg**	**Si**	**Cl**	**Ca**	**Cr**	**Mn**	**Fe**	**Ni**	**Mo**	**Ge**
Figure 6.10a	1	-	-	-	-	-	-	17.34	1.55	67.39	11.20	2.52	-
Figure 6.10c	1	-	38.68	-	2.79	1.95	-	1.49	-	17.90	22.54	-	14.63
Figure 6.10c	2	50.08	26.63	-	0.41	1.28	0.36	0.76	-	9.51	6.88	-	4.10
Figure 6.10d	1	19.98	5.41	2.00	-	-	-	0.58	-	24.06	17.93	-	30.04
Figure 6.10d	2	56.37	24.24	-	0.73	0.41	-	0.62	-	5.17	7.30	-	5.16
Figure 6.10d	3	44.62	30.39	-	0.90	0.36	0.39	4.89	0.78	12.16	3.22	-	2.27

Results for the shell part of the vessel are shown in Figure 6.11 with corresponding chemical compositions in Table 6.9. There is germanium and silicone on the surfaces, with silicon concentrations higher than in the alloy 316L. But there are no traces of chlorine in any of the points measured, which could be due to the primary formation of volatile in this zone. This could be due to the different microstructure because of welding between the base and shell zones, reducing the corrosion resistance in the base and transition zones.

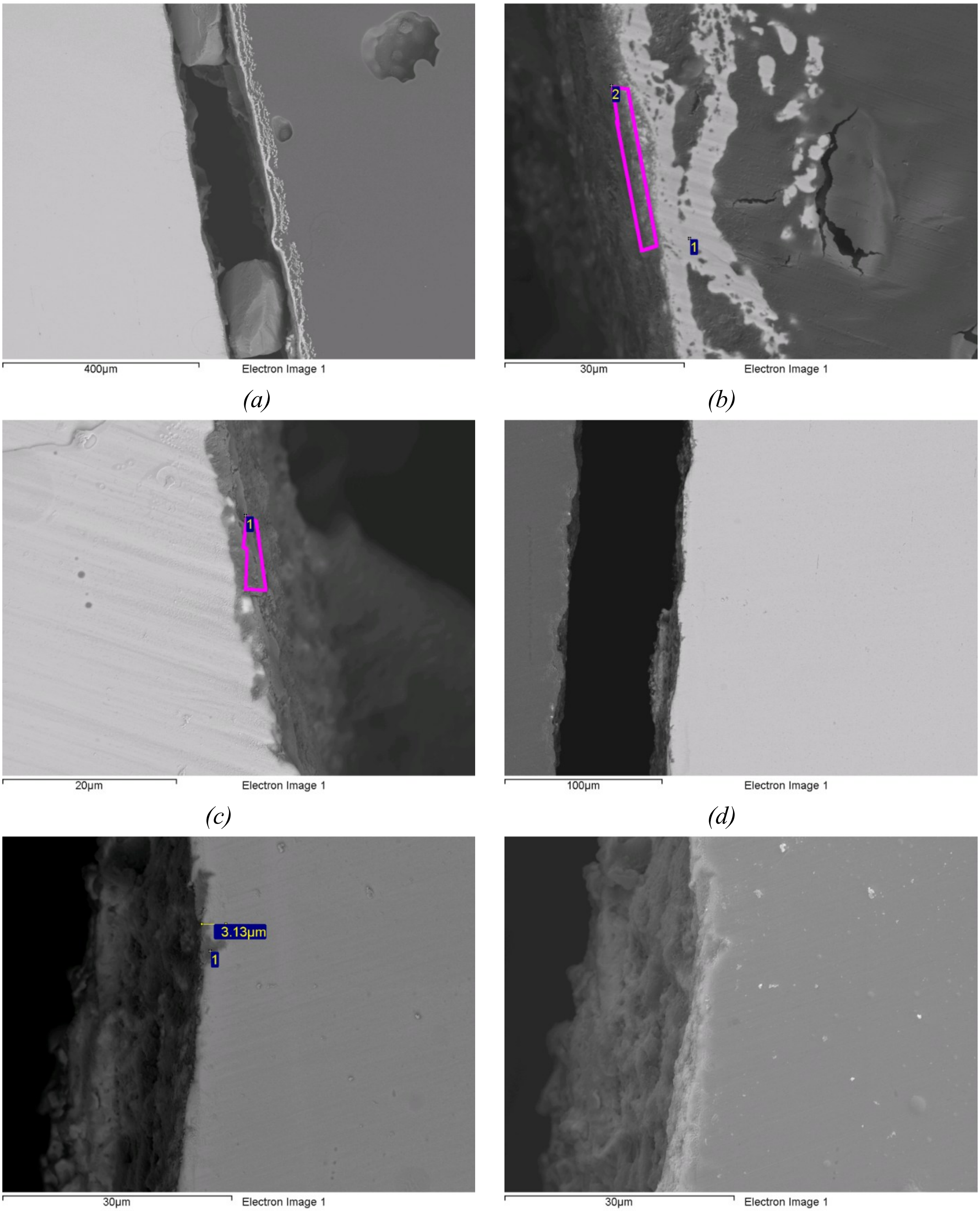

(a) *(b)* *(c)* *(d)* *(e)* *(f)*

Figure 6.11. The SEM analysis of the vessel shell section

Table 6.9. The chemical composition of vessel shell section in points from Figure 6.11

Figure	**Point**	**Chemical composition, wt%**										
		C	**O**	**Mg**	**Si**	**S**	**Ca**	**Cr**	**Mn**	**Fe**	**Ni**	**Ge**
Figure 6.11b	1	7.95	-	2.54	-	-	-	-	-	40.41	13.06	36.03
Figure 6.11b	2	50.88	24.39	0.47	1.26	1.12	0.19	0.36	-	11.48	4.16	5.70
Figure 6.11c	1	49.66	20.71	-	1.32	-	-	4.46	0.73	18.05	2.81	2.26
Figure 6.11e	1	43.18	12.54	-	1.10	-	0.48	7.27	0.48	28.53	5.76	0.66

Part 3: Technoeconomic analysis of CSP plants with sCO_2 and CO_2 mixture power cycles

Part 3 focuses on the techno-economic analysis of both sCO_2 and CO_2 mixture power cycles in CSP plants, exploring the influence of the cycle layout and CSP plant design parameters.

In Chapter 7, the sCO_2 and CO_2+$SiCl_4$ mixture cycles techno-economic parameters are compared in second (Gen2) and third (Gen3) generation CSP plants. The two technology levels are characterized by the 550 and 700°C *TIT and the use of solar salt and sodium/chloride salt as HTF and TES in the CSP plant. The CSP plant SM and TES size are optimized, and the results of different working fluids and power cycles are compared.*

In Chapter 8, the impact of the heat rejection unit design on the techno-economic performance of the sCO_2 and CO_2+$SiCl_4$ mixture cycles is evaluated. The simple recuperated power cycles are modeled in design and off-design conditions and then integrated into the Gen2 CSP plant with optimized SM and TES size to assess the influence of the heat rejection unit design on the levelized cost of electricity.

7. sCO_2, CO_2+$SiCl_4$ mixture and steam Rankine power cycles in CSP plants

This chapter is based on the article: *"Solar Tower Power Plants with CO_2+ $SiCl_4$ Mixtures Mixtures Transcritical Cycles", published in Renewable Energy Journal, January 2025, 122518, https://doi.org/10.1016/j.renene.2025.122518*

Abstract

The temperature potential of CSP plants is not fully utilized using conventional steam cycles. The next step could be using supercritical CO_2 cycles with high-temperature receivers. These cycles can be improved by using the dopants to increase the critical temperature and move towards transcritical cycles, allowing for higher efficiency and lower cost of the power cycle equipment. A CSP plant model to calculate the annual electricity generation and levelized cost of electricity is developed and validated against the results of SAM and SolarTherm. A comparison of steam, sCO_2, and CO_2+$SiCl_4$ mixture cycles is carried out considering 550 and 700°C TIT levels representative of Gen2 and Gen3 CSP technologies. The CO_2+$SiCl_4$ mixture recompression cycle achieves the highest efficiency, followed by mixture precompression and sCO_2 recompression cycles. On the other hand, the lowest LCOE at 550°C TIT is achieved with solar multiple of 3.4 and 15 hours of TES using the CO_2+$SiCl_4$ mixture simple recuperated cycle (110.7 USD/MWh to be compared to steam Rankine cycles value of 113.3 USD/MWh and 118.2 USD/MWh of sCO_2 partial cooling cycle), because of the power cycle lower cost. At 700°C TIT, the precompression mixture cycle achieves the lowest LCOE of 113.0 USD/MWh compared to 117.2 USD/MWh of the sCO_2 partial cooling cycle. Therefore, the CO_2+$SiCl_4$ mixture cycles have higher efficiency and lower LCOE compared to sCO_2 cycles, while the lowest LCOE is achieved by the simple and precompression mixture cycle at 550 and 700°C TIT respectively.

Nomenclature

Acronyms	
BoP	Balance of plant
CRF	capital recovery factor, %
CSP	concentrating solar power
DNI	direct normal irradiance
EE	electric energy, MWh
EoS	Equation of state
FOC	fixed operating costs, USD
HTF	Heat transfer fluid
HTR	high-temperature recuperator
ITD	internal temperature difference
LCOE	levelized cost of electricity, USD/MWh
LTR	low-temperature recuperator
MITA	minimum internal temperature difference, °C
PCC	partial cooling cycle
PHE	primary heat exchanger
PreC	precompression cycle
TES	thermal energy storage
TIT	turbine inlet temperature, °C
UA	Overall heat transfer coefficient and the heat transfer area product, MW/K
VOC	variable operating costs, USD/MWh
Symbols	
η	efficiency, %
Q	thermal power, MW
wt%	mass fraction
mol%	mole fraction
Subscripts	
$_{bol}$	boiling
$_{c}$	compressor
$_{cr}$	critical
$_{el}$	electrical
$_{limit}$	thermal limit
$_{mech}$	mechanical
$_{melt}$	melting

RC	recompression cycle	p	pump
SC	simple recuperated cycle	rec	receiver
sCO_2	supercritical CO_2	t	turbine
SM	solar multiple		
TCC	total capital cost, USD		

7.1. Introduction

Solar power is a renewable energy source that has great potential for energy transition. Two main technologies make use of solar energy today for electricity production: photovoltaic solar panels and concentrating solar power (CSP) plants. The latter is characterized by the higher levelized cost of electricity (LCOE) compared to both PV and wind power plants [1]. However, the use of CSP plants can be beneficial to the electric grid because of the dispatchability provided by the low-cost thermal energy storage technology (TES). The primary advantages of tower CSP plants over other CSP technologies are high power and high solar concentration which lead to lower specific costs, higher turbine inlet temperature, and higher electric efficiencies. The technology is very flexible since one can choose from different types of heliostats, receivers, heat transfer fluids (HTF), heat storage systems, and power cycles.

Most new large-scale CSP projects use a central receiver tower with molten salt as HTF [2]. For new tower designs, the standard installed capacity is around 100 MW, while TES is 8-16 hours, making them very flexible throughout the day. Most CSP plants today use direct TES systems with solar salt and steam Rankine cycle for power generation with turbine inlet temperatures (TIT) up to 560°C. The increase in turbine inlet temperature using the steam Rankine cycle is limited by high-temperature corrosion and creep phenomena. However, temperatures up to 1000°C can be attained for liquid metal and solid particle HTF [3], and up to around 1300°C at the receiver [4,5]. The closed CO_2 cycles offer a thermal efficiency advantage over both the steam Rankine and helium Brayton cycles at TIT > 600°C and can reach more than 50% at 800°C TIT [6,7]. Different CO_2 cycle layouts have been extensively studied in the past, including precompression and recompression cycles by Dekhtyarev in 1962 [8], simple recuperated, recompression, partial cooling, and partial cooling with improved regeneration cycles by Angelino in 1969 [9], and various cycles for nuclear application by Dostal et al. in 2004 [10]. New CSP plants use dry cooling systems, therefore, the cycle minimum temperature will be above the critical temperature of the CO_2 leading to non-condensing and fully supercritical CO_2 (sCO_2) cycles [11]. However, sCO_2 cycles require high operating pressures (comparable to supercritical steam cycles) and complex layouts to improve internal heat recovery. Moreover, compression of sCO_2 near critical point entails technical challenges due to density strong dependence on temperature at compressor intake, which depends on the cooler capabilities.

The efficiency of closed sCO_2 cycles can be improved by using dopants with high critical parameters, moving from supercritical to transcritical cycles at the same minimum cycle temperature [12,13]. Thermal efficiency gain derived from the adoption of CO_2-based mixtures, compared to pure sCO_2, is confirmed in many previous literature works. For Gen2 (TIT 550°C) plants, C_6F_6 has been extensively investigated as a dopant and reached thermal efficiency of 42.2% in precompressed cycle [14,15]. Dopants N_2O_4 and $TiCl_4$ achieve respectively 46.7% and 51% thermal efficiency in Gen3 (TIT 700°C) plants using a simple recuperative layout [16–18]. However, at such high-temperature applications, only a handful of dopants meet the criteria of thermo-chemical stability and material compatibility. The CO_2+C_6F_6 mixture proved to be not thermally stable at temperatures above 600°C [15] and has compatibility issues with Inconel 625 at 550°C [19]. At the same time, N_2O_4 reversibly decomposes at high temperatures and is strongly corrosive, while $TiCl_4$ quickly hydrolyses in contact with humid air posing serious challenges in fluid loading and management. Therefore, the main challenge for CO_2 dopant selection is thermal stability at maximum cycle operating temperature. Recently, within the H2020 SCARABEUS [20] and DESOLINATION projects [21], a new $SiCl_4$

dopant that could be stable up to 900°C [22] has been introduced. Bubble points of the CO_2+$SiCl_4$ mixture have recently been measured [23], allowing for the characterization of the power cycle performance. A recent test in our Fluid Test Laboratory confirms the high thermal stability of $SiCl_4$ with no degradation after prolonged thermal stress at 650°C in contact with common stainless steel AISI 316L [24]. Therefore, there is a lot of potential for CO_2+$SiCl_4$ mixture usage in high-temperature CSP applications.

Most of the research at this point is focused on power cycle efficiency optimization, however, the minimum electricity cost does not match these conditions [25]. Some studies pointed out that cycles operating with lower efficiency and at lower temperatures, characteristic of Gen2 CSP plants, might have lower LCOE compared to Gen3 CSP plants [26,27]. Moreover, most of the studies focused on sCO_2 cycles in CSP plants have no comparison with the state-of-the-art Gen2 CSP plant technology, which is a steam Rankine cycle. Compared with previous literature, the present paper intends to carry out a techno-economic evaluation of the sCO_2, CO_2+$SiCl_4$ mixture, and steam Rankine cycles in Gen2 and Gen3 CSP plants. Moreover, one primary objective of this research is to improve the understanding of the optimal design conditions for CO_2 based mixture cycles in CSP plants. The developed CSP model is introduced and validated against the results of SAM and SolarTherm for steam and sCO_2 cycles based on electricity output, capital costs, and LCOE. The comparison is conducted for Gen2 and Gen3 CSP plants (TIT 500 and 700°C respectively) at optimum cycles electrical efficiency, using both same and optimized for minimum LCOE solar multiple and thermal energy storage sizes.

7.2. Methodology

7.2.1. CSP plant model

A tower CSP plant layout is shown in Figure 7.1(a). First, an array of heliostats is used to focus sunlight onto a central receiver mounted on the tower. When there is enough light incident on the receiver, the salt from the TES cold tank is heated and transported to the hot tank. At the same time, salt from the hot TES tank is pumped through the primary heater supplying the heat to the power cycle to generate electricity. That way during the day thermal power is supplied to the power cycle, while excess is stored in TES, while the rest of the time the heat is supplied to the power cycle from TES.

For a techno-economic analysis, it is important to model the entire CSP plant and not only the power unit. This is done to account for the cycle parameter's influence on the receiver and TES, the cost of the power cycle equipment, and the CSP plant overall. The structure of CSP plant model developed for annual performance calculation shown in Figure 7.1(b). It includes several modules and software, each responsible for the part of the plant. The main components of the CSP plant that have been modeled in detail are (i) the solar field, (ii) the receiver, (iii) the TES, and (iv) the power cycle. The latter has been modeled in Aspen Plus V14 [28] software with the assumptions detailed in the following section 7.2.2.

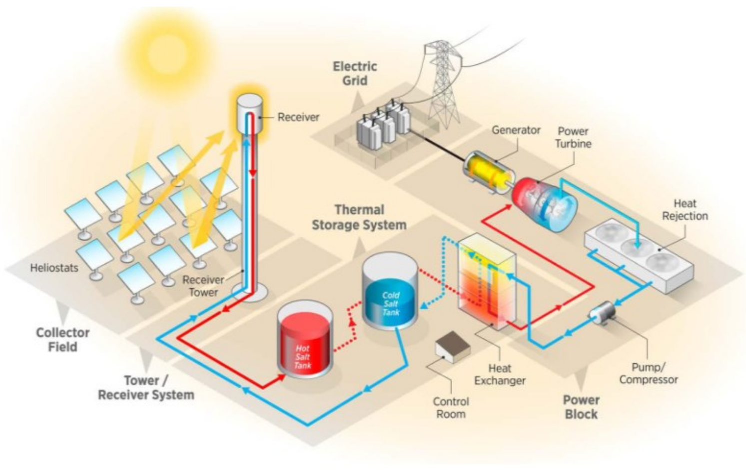

(a)

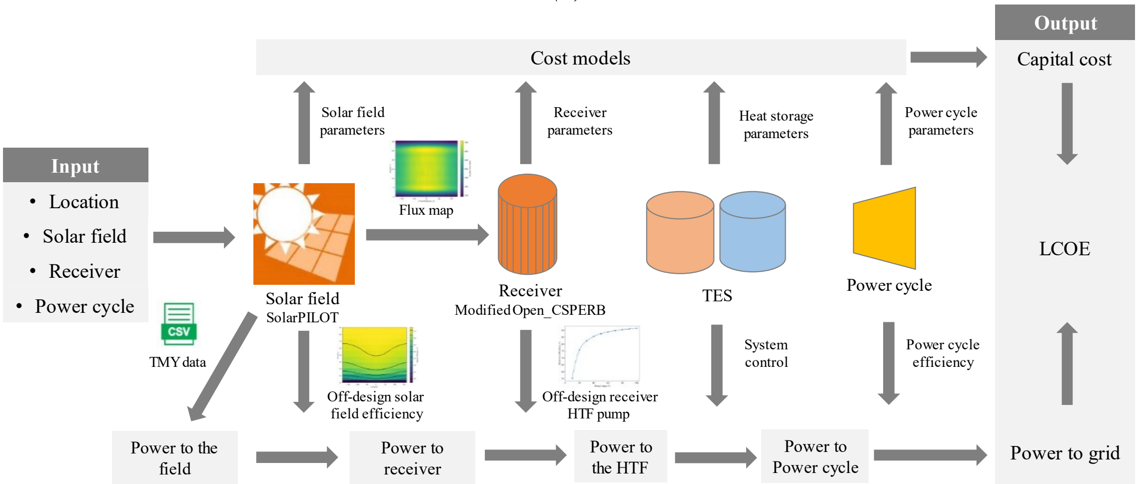

(b)

Figure 7.1. CSP system layout adapted from [29] (a) and model structure (b)

The starting point of the CSP plant modeling is the solar field. SolarPILOT [30] is used through Python API [31] for generating the solar field, flux maps for the receiver, and off-design optical efficiency map of the solar field. The annual simulation for solar field optimization is based on 8 representative days of the year. The solar field off-design optical efficiency is calculated based on the 10x24 discretization grid [32] and interpolated using the bivariate spline from the SciPy Python module [33]. Python module “sunposition” is used for calculating the solar zenith and azimuth angles based on algorithms from [34] with uncertainties of ±0.0003°.

Regarding the receiver model, the Open_CSPERB Python module [35], which solves the energy balances of an external cylindrical receiver, is adopted to calculate the receiver efficiency (which includes reflection, emission, and convection losses) in both design and off-design conditions. The properties of sodium and salts are calculated according to [36]. The code was modified to calculate the pressure drop including a cold riser static pressure head and HTF pump power based on the assumptions in Table 7.1. The off-design performance of the system is calculated assuming that receiver power input is the main parameter affecting the efficiency [37]. Therefore receiver efficiency and HTF pump power are calculated for the input power portion from 0.1 to 1 with 0.1 step and are interpolated during the annual calculation with cubic spline from the SciPy [38].

Thermal energy storage is made of two tanks, whose height is calculated according to Table 7.1. The diameter of each tank is determined based on the TES size and amount of salt required to store.

Table 7.1. CSP model design assumptions

Parameter	Value	Source
	Solar field	
Direct Normal Irradiation, W/m^2	840	
Sun location	Noon at summer solstice	
	Receiver	
Z-shaped manifold pressure loss coefficient	3.5	[39]
90 degree bend pressure loss coefficient	0.13	[39]
Manifold inlet pressure loss coefficient	0.6	[39]
Manifold outlet pressure loss coefficient	0.5	[39]
Receiver tube spacing, mm	2	Assumed
HTF pump efficiency, %	85	[40]
Ambient temperature, °C	20	Assumed
Wind Hellmann exponent	0.34	[41]
Wind speed at 10 m, m/s	2	Assumed
	Thermal energy storage	
Storage fluid height, m	12.2	[29,42]
Tank additional space, %	20	[26]
Power cycle condenser		
Condenser/cooler ITD, °C	15	[43]
Cooler air temperature increase, °C	25	Assumed

The annual production of electricity is calculated with one-hour steps taking into account the start-up and shut-down (heliostat minimum tracking angle, field minimum output power fraction, startup energy), thermal energy losses in TES, and additional electrical consumption (heliostats solar tracking, PHE pump power) according to the assumptions in Table 9.11.

Table 7.2. CSP model annual calculation assumptions

Parameter	Value	Source
Heliostat minimum angle, °	8	
Field minimum output minimum power fraction	0.25	
Receiver startup energy fraction, %	25	
Cycle startup energy fraction, %	50	[40]
Heliostat track power, kWe	0.055	
Storage fluid pressure drop in PHE, bar	5	
Initial hot TES tank fill fraction, %	30	
Wetted heat loss coefficient in TES, W/m^2 K	0.136	[44]

The previously mentioned modules and software were complemented with the heat exchangers, power cycle models, and operation logic responsible for the TES functioning, limitations, and start-up procedures.

7.2.2. Power cycle modeling

Standard steam Rankine cycle along with the sCO_2 and CO_2+$SiCl_4$ mixture cycles are considered. The chosen parameters of considered fluids are shown in Table 7.3. The sCO_2 cycle was calculated using the Span-Wagner EoS [45]. The binary interaction parameter for the CO_2+$SiCl_4$ mixture using Peng-Robinson EoS was equal to 0.06098 [46].

Table 7.3. Parameters of considered working fluids

CAS	**Formula**	**T_{melt}, °C**	**T_{boil}, °C**	**T_{cr}, °C**	**P_{cr}, bar**	**NFPA 704**			**T_{limit}, °C**
						Heal.	**Flamm.**	**React.**	
7732-18-5	H_2O	0	100	373.9	220.6	0	0	0	>700
124-38-9	CO_2	-57	-78	31	73.8	2	0	0	>700
10026-04-7	$SiCl_4$	-69	58	233.9	35.9	3	0	2-w	650 in stainless steel, >700 in general

The main sCO_2 and CO_2+$SiCl_4$ mixture power cycles configurations considered for analysis were chosen from the literature to reach the lowest LCOE [25,27]. They are shown in Figure 7.2: simple recuperated (SC), precompression (PreC), recompression (RC), and partial cooling (PCC) cycles. Most of the cycles can use and advantage of CO_2 mixtures by compression in the liquid phase, which can be seen in T-s diagrams. In the case of a partial cooling cycle, a CO_2 mixture was considered but proved unsuitable due to the saturated steam compression and subsequent very low efficiency. All power cycles were modeled according to the assumptions presented in Table 7.4 [17,27].

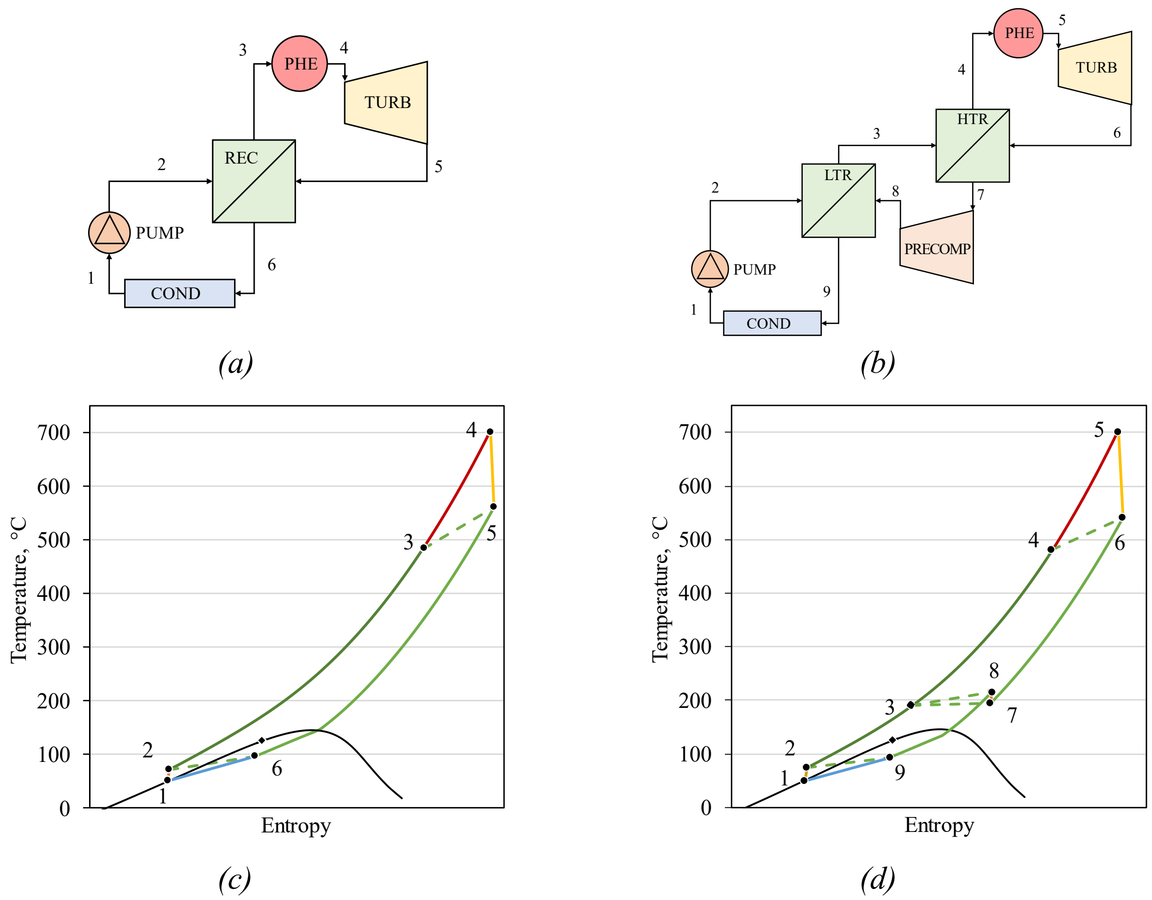

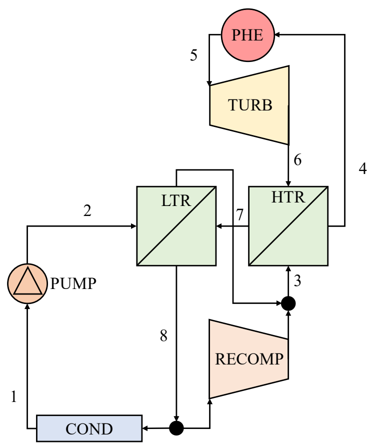

(e)

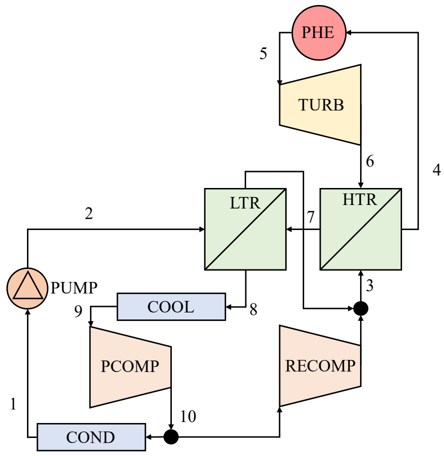

(f)

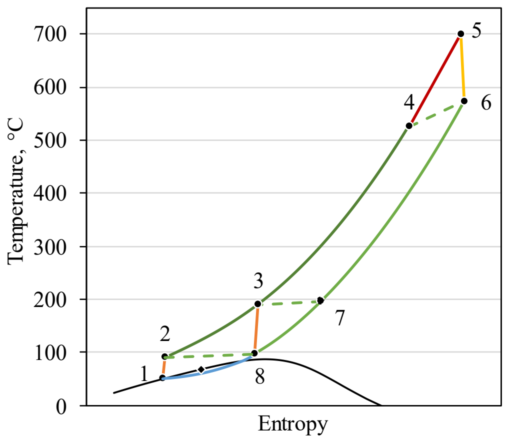

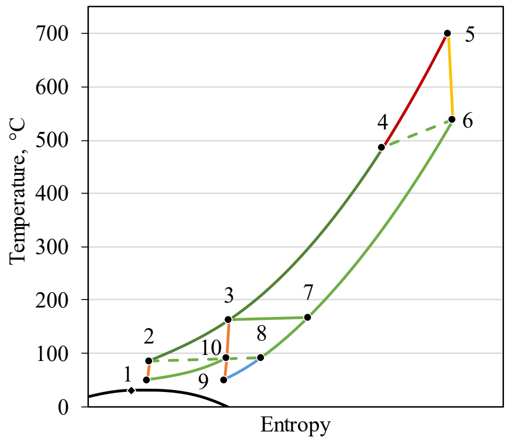

(g) *(h)*

Figure 7.2. Layout and T-s diagram of recuperated simple (a, c), precompression (b, d), recompression (e, g), and partial cooling (f, h) cycles considered in the analysis. PHE – primary heat exchanger; TURB – turbine; REC – recuperator; LTR – low-temperature recuperator; HTR – high-temperature recuperator; PUMP – pump; PRECOMP – precompressor; RECOMP – recompressing compressor; PCOMP – partial cooling compressor; COND – air cooled condenser; COOL – air cooled cooler;

Table 7.4. Power cycle assumptions

Parameter	**Value**
TIT, °C	550, 700
Max pressure in the cycle, bar	250
Cycle minimum temperature, °C	50
Recuperators MITA, °C	5
Condenser/cooler Δp, %	2
Recuperators hot side Δp, %	1.5
Recuperators cold side Δp, %	0.3
PHE Δp, %	2
Turbine isentropic efficiency, %	92
Pump/compressor isentropic efficiency, %	88
Motor/generator electrical efficiency, %	97
Fluid machines mechanical efficiency, %	99

The CSP plants capacity is assumed to be around 100 MWe. For compressors and pumps with power lower than 37 MW, electric motors can be used [47]. Therefore, the electrical efficiency of the cycle was calculated according to equation (7.1) assuming separate shafts for the turbine, pumps, and compressors.

$$\eta_{cycle,el} = \frac{P_t \cdot \eta_{mech} \cdot \eta_{el} - (P_p + P_c)/(\eta_{mech} \cdot \eta_{el})}{Q_{PHE}} \tag{7.1}$$

where $\eta_{cycle,el}$ – cycle electrical efficiency, %; P_t – turbine power, MW; P_p – pump power, MW; P_c – compressors power if used, MW, Q_{PHE} – power supplied to the cycle in the PHE, MW; η_{mech} – mechanical efficiency, %; η_{el} – electrical efficiency, %.

7.2.3. CSP plant economic assumptions

The cost assumptions for the solar field, tower, fixed and variable operating costs, contingency rate, and EPC rate were taken from SAM [40] and can be seen in Table 7.5. For validation of the high-temperature CSP plant with sodium and chloride salt receiver, the "SunShot" assumptions were used [48]. A solar salt receiver cost was based on the correlation from SAM [40], while for high-temperature cases the cost of the receiver, salt pumps, riser, downcomer, sodium loop, and sodium-to-salt heat exchanger was calculated based on correlations from [49,50]. The cost of TES was calculated according to [36] apart from the validation stage when the cost of chloride salt was equal to 0.7 USD/kg [49]. The cost of the steam power cycle and balance of plant (BoP) was taken from [40]. The cost of sCO_2 and CO_2 mixture cycles equipment was calculated according to [47] with CO_2 mixture pumps calculated as compressors. Since in [47] there are only correlations for coal and gas-fired primary heaters, the cost of the PHE was calculated based on [51] for validation and using CSP specific correlation from [27] for the study. The discount rate was assumed based on the recommendations from [52] and is close to the rate used in [48]. The calculated CRF was equal to 6.5%.

Table 7.5. CSP model economic assumptions

Parameter	Value	Source
Installation costs for recuperators, %	5	[47]
Installation costs for the rest of equipment, %	20	[47]
Heliostat field cost, USD/m^2	127	[40]
Site improvement cost, USD/m^2	16	[40]
FOC, USD/kW-yr	66	[40]
VOC, USD/MWh	3.5	[40]
Contingency rate, %	7	[40]
EPC rate, %	13	[40]
Land cost, USD/acre	1000	[40]
Real discount rate, %	5	[52]
Lifetime, years	30	Assumed

The economic assumptions were integrated into the CSP plant model shown in Figure 7.1 to calculate annual electricity output, plant total capital cost (TCC), and LCOE. The LCOE is calculated according to the equation (1) [40].

$$LCOE = \frac{TCC \cdot CRF + FOC}{EE} + VOC \tag{7.2}$$

where $LCOE$ – levelized cost of electricity, USD_{2020}/MWh; TCC – total capital cost, USD_{2020}; CRF – capital recovery factor; FOC – fixed operating costs, USD_{2020}; VOC – variable operating costs, USD_{2020}/MWh; EE – electric energy output per year, MWh/yr.

7.2.4. CSP plant model validation

During the validation, different input assumptions were chosen in each case based on the reference used (detailed data is available in Supplementary materials Validation). First, the modified receiver model was compared against other models and experimental results and showed efficiency deviation within 1% and pressure drop deviation within 10%.

After that, the CSP plant model showed deviations in electricity output per year within 3% compared with the default SAM tower CSP case, below 5% compared to the SolarTherm and SAM for sCO_2 cycles with high-temperature receivers using sodium and chloride salts as HTF [40,48,53]. The deviations for TCC and LCOE were within 1.5% and 2.5% for CSP plants with a steam cycle, within 4.5% and 5% for the sCO_2 cycle using a chloride salt receiver, and within 2% and 3.5% using a sodium receiver.

7.2.5. CSP modeling approach

The CSP plants used in this paper for comparison of different power cycles were modeled according to the assumptions in Table 7.6. Hours of storage and solar multiple for the initial CSP plants were assumed according to the Gemasolar power plant, located in Fuentes de Andalucía, Spain, about 40 miles east of Sevilla. The solar field design power was chosen based on the power cycle thermal power of 280 MWth [53]. The design point DNI was assumed to be not exceeded 95% of hours, with DNI above zero [54]. The design temperature for air coolers and condensers was assumed to be 35°C which is not exceeded in 96% of operating hours in the location [55]. The receiver dimensions were assumed according to [32,53] and scaled for increased power input. Dimensions were kept constant within the same TIT to maintain flux density. The same flux density, HTF type and maximum temperature would allow the same tube materials to be used, which is essential for fair cost estimations [56,57]. For the Gen2 CSP plant solar salt was used as a heat transfer and storage fluid. For Gen3 sodium was used as an HTF due to lower LCOE [27], while for TES chloride salt similar to the one used in [49] was chosen from [36]. Tower height was obtained from SAM optimization for the steam power cycle.

Table 7.6. CSP plant model assumptions for two temperature levels

Parameter	Value	
TIT, °C	550	700
Design point DNI, W/m^2	840	
Solar field design power, MWth	700	
Tower height, m	220	
Receiver dimensions DxH, m	18.1x20.9	19.1x18.8
HTF		Sodium
TES fluid	Solar salt	NaCl-KCl-$MgCl_2$ (20.5-30.9-48.6 wt%)
Cycle fluid	Steam, sCO_2, CO_2+$SiCl_4$	sCO_2, CO_2+$SiCl_4$
Sun location	Noon at summer solstice	
CSP plant location	Sevilla, Spain	
Initial solar multiple (SM)	2.5	
Heliostat dimensions, m	12.2x12.2	
Heliostat reflectivity, %	95	

Parameter	Value	
Solar field availability, %	95	
Receiver tube absorptivity, %	94	
Receiver tube emissivity, %	88	
ΔT between HTF/TES and TES/power cycle fluid, °C	20	
Initial TES size, h	15	
Fan power as a fraction of cooler/condenser heat rejection, %	Steam 2	sCO_2, CO_2+SiCl_4 1
Ambient design temperature for cooler/condenser, °C	35	

The number of flow paths, panels, and tube diameters of each receiver was chosen based on the maximum fictitious power (7.3) taking into account the maximum sodium speed of 2.44 m/s [32].

$$Q_{fictitious} = Q_{rec,output} - \frac{P_{HTF\ pump}}{\eta_{cycle,el}} \tag{7.3}$$

To fairly compare cycles with different TES cold temperatures, specific cost, and efficiency it is important to provide optimal CSP plant conditions in each case. The main CSP plant parameters are the hours of storage and solar multiple which determine the ratio between TES, solar field, and power cycle sizes. After the modeling of the initial CSP plant the solar field and receiver parameters are fixed, while the TES and power cycle sizes are optimized to reach minimum LCOE.

7.3. Results and Discussion

7.3.1. Power cycles performance

The optimum minimum pressure for CO_2+SiCl_4 and sCO_2 cycles was optimized to reach maximum electrical cycle efficiency with a 5 bar step. In the case of mixture cycles also composition was optimized based on the electrical efficiency as can be seen in Figure 7.3. The optimum CO_2 fraction for simple, precompression and recompression cycles was chosen to be 80%, 80%, and 91% at 550°C TIT and 75%, 80% and 92% at 700°C TIT.

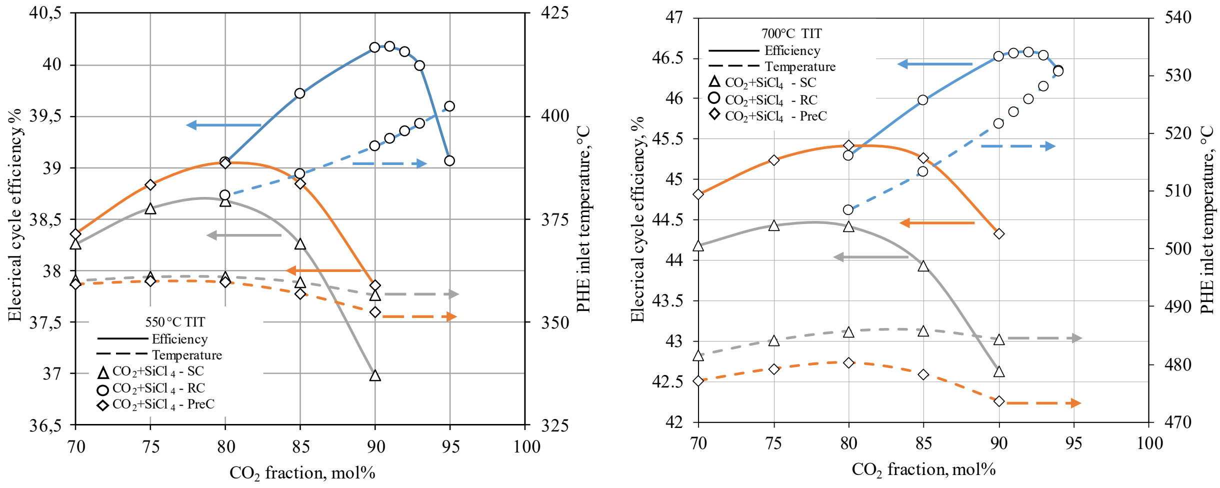

(a) *(b)*

Figure 7.3. Considered power cycles parameters: electrical efficiency and PHE inlet temperature at 550°C (a) and 700°C TIT (b)

The optimum minimum pressures and mixture compositions with the considered power cycle parameters are presented in Table 7.7. The steam cycle parameters were taken from [40] and are consistent with values in [14]. The simple, recompression, and partial cooling cycles optimum minimum pressures are close to literature results accounting for higher TIT and minimum cycle temperature [25]. Mixture cycles on average have higher efficiency and lower PHE inlet temperature, which positively affects the TES size and therefore cost. In all cases, a partial cooling cycle allows for lower PHE inlet temperature while not significantly reducing the electrical efficiency. The same effect can be seen in the case of the mixture precompression cycle. These cycles parameters are used for further analysis of the whole CSP plant assuming only the design point operation of the power cycle.

Table 7.7. Optimized power cycles parameters

Parameter	Value														
TIT, °C	550								700						
Cycle fluid	H_2O	sCO_2				CO_2+SiCl_4			sCO_2				CO_2+SiCl_4		
Cycle	Rankine	SC	PreC	RC	PCC	SC	PreC	RC	SC	PreC	RC	PCC	SC	PreC	RC
Optimised CO_2 fraction, mol%	-	-	-	-	-	80	80	91	-	-	-	-	75	80	92
Optimized minimum pressure, bar	-	100	130/145	110	80/120	-	65	-	90	115/135	105	70/115	-	60	-
PHE inlet temperature, °C	-	376.0	437.4	420.7	368.5	361.0	359.5	394.4	502.6	556.0	552.8	486.6	484.1	480.2	525.9
Condenser/cooler inlet temperature, °C	-	111.8	77.2	95.1	82.9/86.8	92.6	92.4	94.1	131.5	80.7	102.4	92.5/91.5	96.6	92.4	95.8
Cycle thermal efficiency, %	41.2	37.3	40.0	42.0	41.0	41.2	41.9	43.5	44.0	46.8	48.9	48.2	47.1	48.6	50.0
Electric efficiency, %	39.6	34.6	36.7	38.6	37.7	38.7	39.0	40.2	40.7	43.2	45.2	44.5	44.4	45.4	46.6
Specific power, kJ/kg	-	75.2	52.2	62.5	85.4	74.2	75.4	69.8	101.4	79.4	84.3	119.7	91.7	99.3	91.5
HTR or recuperator UA/Q_{PHE}, 1000/K	-	58.6	137.9	103.1	52.9	98.6	52.9	48.9	59.0	119.1	114.7	55.4	96.3	51.6	83.6
LTR UA/Q_{PHE}, 1000/K	-	-	248.3	197.5	107.5	-	118.5	110.3	-	146.6	146.3	77.5	-	104.7	164.5

7.3.2. CSP plants initial parameters

The solar field and flux maps generated from SolarPILOT are shown in Figure 7.4. The solar fields dimensions and efficiencies are pretty close for 550°C and 700°C TIT cases with maximum values reaching 72.2% which is due to the same power to the receiver and height of the tower. The maximum flux in the 550°C TIT receiver with solar salt is 982 kW/m^2, while for the sodium 700°C TIT receiver it is 1041 kW/m^2 which is within the limits of allowable flux density (1.2-1.3 MW/m^2 [58]) and close to optimum values of around 1.1 MW/m^2 [32].

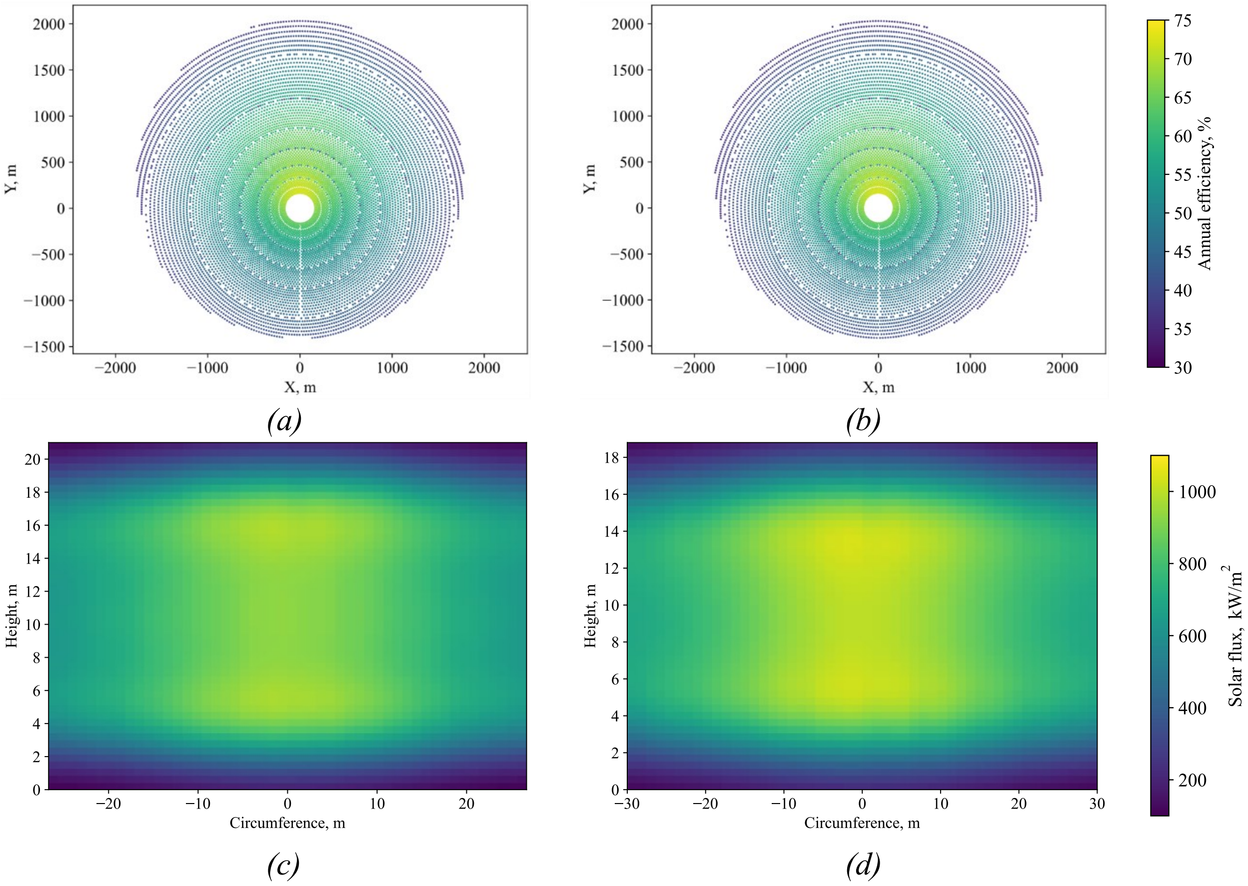

Figure 7.4. Solar field and flux map of receivers at 550°C (a, c) and 700°C TIT (b, d)

After obtaining the flux maps and power cycle parameters receiver flow path design was optimized to reach maximum fictitious power (7.3) at the design point. The parameters of the solar field and receiver are shown in Table 7.8. Since receiver output power is very close for all studied cases, the temperature increase (which is proportional to the HTF enthalpy increase in the receiver), is inversely proportional to the mass flow based according to energy balance. Therefore, the transition from steam to sCO_2 and CO_2 mixture cycles with a TIT of 550°C leads to the bigger mass flow rate of HTF and favors fewer panels to reduce pressure drops. In the case of a TIT of 700°C, the amount of panels is around 12-14 which is similar to the 16 panels results in [32] which were calculated with parameters close to the mixture precompression cycle.

Table 7.8. Solar field and receiver parameters

Parameter	**Value**														
TIT, °C	**550**								**700**						
Cycle fluid	**H_2O**	**sCO_2**				**CO_2+SiCl_4**			**sCO_2**				**CO_2+SiCl_4**		
Cycle type	**Rankine**	**SC**	**PreC**	**RC**	**PCC**	**SC**	**PreC**	**RC**	**SC**	**PreC**	**RC**	**PCC**	**SC**	**PreC**	**RC**
Solar multiple								2.5							
Heliostat number				11309								11390			
Flow paths				2					12			14			12
Panels per flow path	5				3							1			
Tube outer diameter, mm	40		60	50		40			50	60			40		50
HTF mass flow, kg/s	1698	2692	4109	3754	2584	2483	2464	3007	2765	3759	3680	2575	2546	2481	3126
Receiver pressure drop, bar	48.5	43.6	41.6	42.5	43.4	43.3	43.2	44.4	18.0	17.8	17.8	18.2	18.2	18.2	17.9
Temperature rise across the receiver, °C	280	174	113	129	181	189	190	156	197	144	147	213	216	220	174
HTF pump power, MW	5.4	7.5	11.2	9.9	7.2	6.8	6.8	8.6	7.1	9.7	9.5	6.7	6.6	6.5	8.0
Receiver efficiency, %	91.5	90.8	90.0	90.2	90.8	90.8	90.8	90.7	87.0	86.2	86.2	87.6	87.7	87.7	86.7

The efficiencies of receivers mainly depend on the temperature of HTF inside (and therefore tube temperatures), because it highly influences the radiative losses. This leads to 550°C TIT receivers having higher efficiencies than in the 700°C TIT case. The same effect can be seen within the same TIT cases when a receiver efficiency increases with the increase of the temperature rise in the PHE as shown in Figure 7.5. During maximization of the fictitious power the balance between the receiver output power (determined by efficiency) and HTF pump power (determined by pressure drop) is found. The close output powers for both TIT cases lead to similar values of optimum HTF pump powers. However, due to lower efficiency, the 700°C TIT receiver design favors higher HTF pump power values. The mass flow rate being inversely proportional to PHE temperature rise leads to identical trends of HTF pump power for both TIT cases.

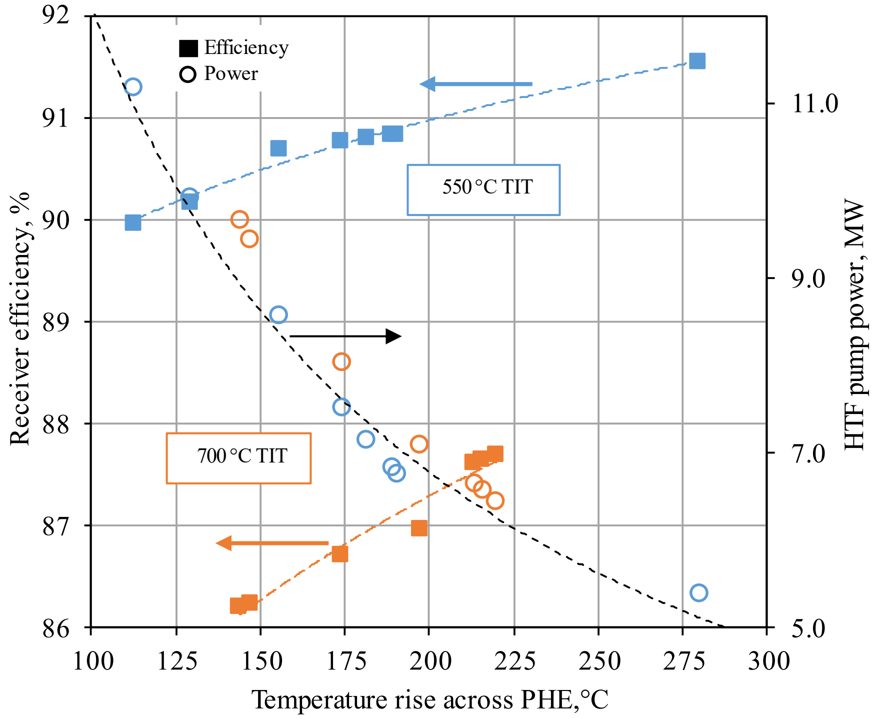

Figure 7.5. Influence of temperature rise across the PHE on receiver efficiency and HTF pump power.

For the obtained solar fields and receiver designs in Table 7.8, power cycles were sized based on the initial SM from Table 7.6. That way different power cycles can be compared in a CSP plant with the same solar field, and SM, while in section 7.3.4 power cycle sizes will be varied to reduce LCOE. The electric power and specific cost of different power cycles are presented in Supplementary materials B. The resulting specific costs of power cycles are similar to the ones presented in the literature for sCO_2 and CO_2 mixture: 861 and 757-1106 USD/kWe for simple cycle, 1076 and 866-1020 USD/kWe for precompression cycle, 1088-1176 and 1115 USD/kWe for recompression cycle for 500°C TIT and 924 USD/kWe for simple and 1114 USD/kWe for recompressed sCO_2 cycles for 700°C TIT [26,27]. The sCO_2 simple cycle recuperative system UA is more than 3 times smaller than in the precompression and recompression cycle and more than 1.5 times than in the partial cooling cycle. The transition to CO_2 mixture leads to the lower specific cost of the power cycle due to the lower recuperative system UA, power of the turbine, and compressors/pumps.

Most of the sCO_2 and CO_2 mixture power cycles cost is comprised of the primary heat exchanger and the recuperative system as can be seen in Figure 7.6. The recuperative system cost difference is similar to the UA one (Table 7.7) but is less significant due to the recuperator cost correlation. The PHE and recuperative system together comprise 57-75% of the power cycle cost and are followed by compressors/ pumps, turbines, and air cooler/condenser. However, it should be noted that in the current calculation, the same correlations were used for the cost of the compressor and pump, therefore the cost of the pumps could be lower. The main variation in the specific cost between the sCO_2 and CO_2 mixture cycles is due to the cost of the recuperative system.

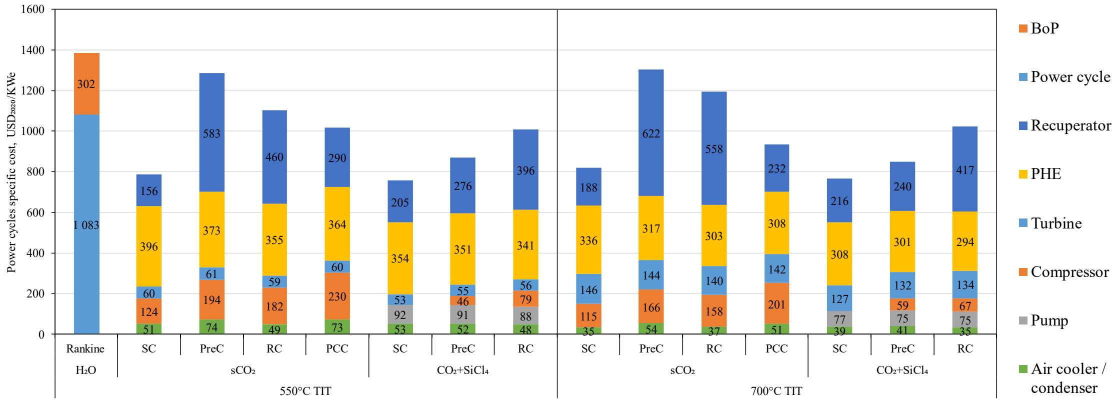

Figure 7.6. Power cycles specific cost distribution for the initial case

7.3.3. CSP plants off-design performance

Moving forward to the off-design performance of the CSP plant, the solar field optical efficiency tables were obtained from SolarPILOT and interpolated for further calculations. Comparison between the original and interpolated data can be seen in Figure 7.7 based on lines of constant efficiency. The optical efficiency at 550°C is higher mainly due to the higher image intercept efficiency (spillage efficiency) caused by smaller 700°C receiver dimensions.

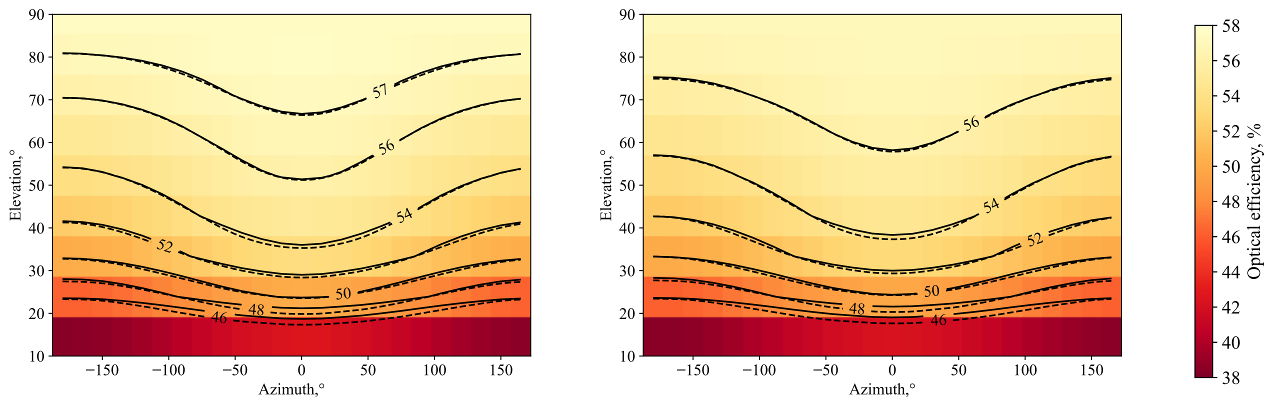

(a) *(b)*

Figure 7.7. Solar field optical efficiency map at 550°C (a) and 700°C TIT (b) with straight lines (——) for original efficiency levels and dashed lines (— —) for interpolated

Receiver efficiency and HTF pump power were calculated for optimized receiver flow path design varying the flux map intensity (section 7.2.1) and interpolated as shown in Figure 7.8. The trends of receiver efficiency and HTF pump power are very similar for all cycles and TIT with the maximum level determined by temperature rise across PHE.

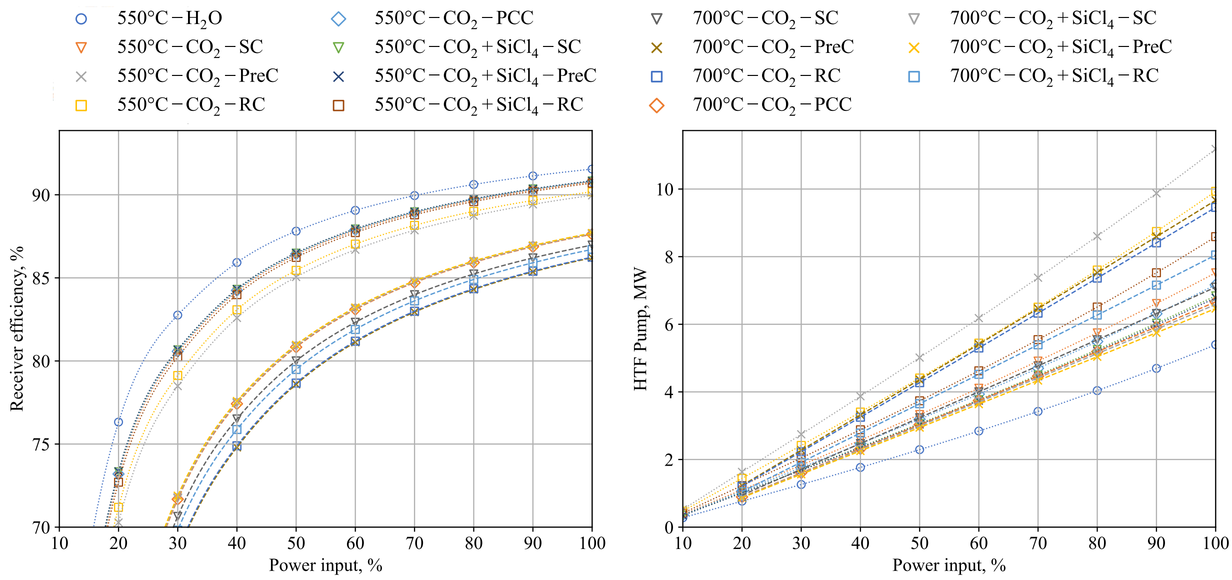

(a) *(b)*

Figure 7.8. Solar receiver efficiency (a) and HTF pump power (b) based on the receiver input power fraction

7.3.4. Comparison optimized CPS plants results

Since all the analyzed cycles have different TES temperature levels, efficiencies, and costs it is important to compare them under their optimal conditions (TES size and SM) to achieve the lowest possible LCOE. The results of sensitivity analysis for all cycles are shown in Supplementary materials C. The sCO_2, and CO_2+$SiCl_4$ mixture cycles (in partial cooling, simple and precompression configuration) which have the minimum LCOE are shown in Figure 7.9. Steam Rankine cycle sensitivity results obtained from the CSP plant model are shown in Figure 7.9a and show similar optimum LCOE, SM, and TES size to results of SAM shown in Figure 7.9b.

For all considered cycles and fluids, the minimum LCOE is reached at 3.2-3.5 SM and 14-15 hours of TES at both 550 and 700°C TIT. The 15 hours of thermal storage was already used in the Gemasolar CSP plant in Seville (Spain) commissioned in 2011 [53], while new solar tower CSPs have up to 17.5 hours of TES [59]. Optimum SM could be equal to 3 and above for both conventional and Gen3 plants [48,59–61] with values reaching almost 3.5 for Gen3 CSP plants with CO_2 mixture [62,63].

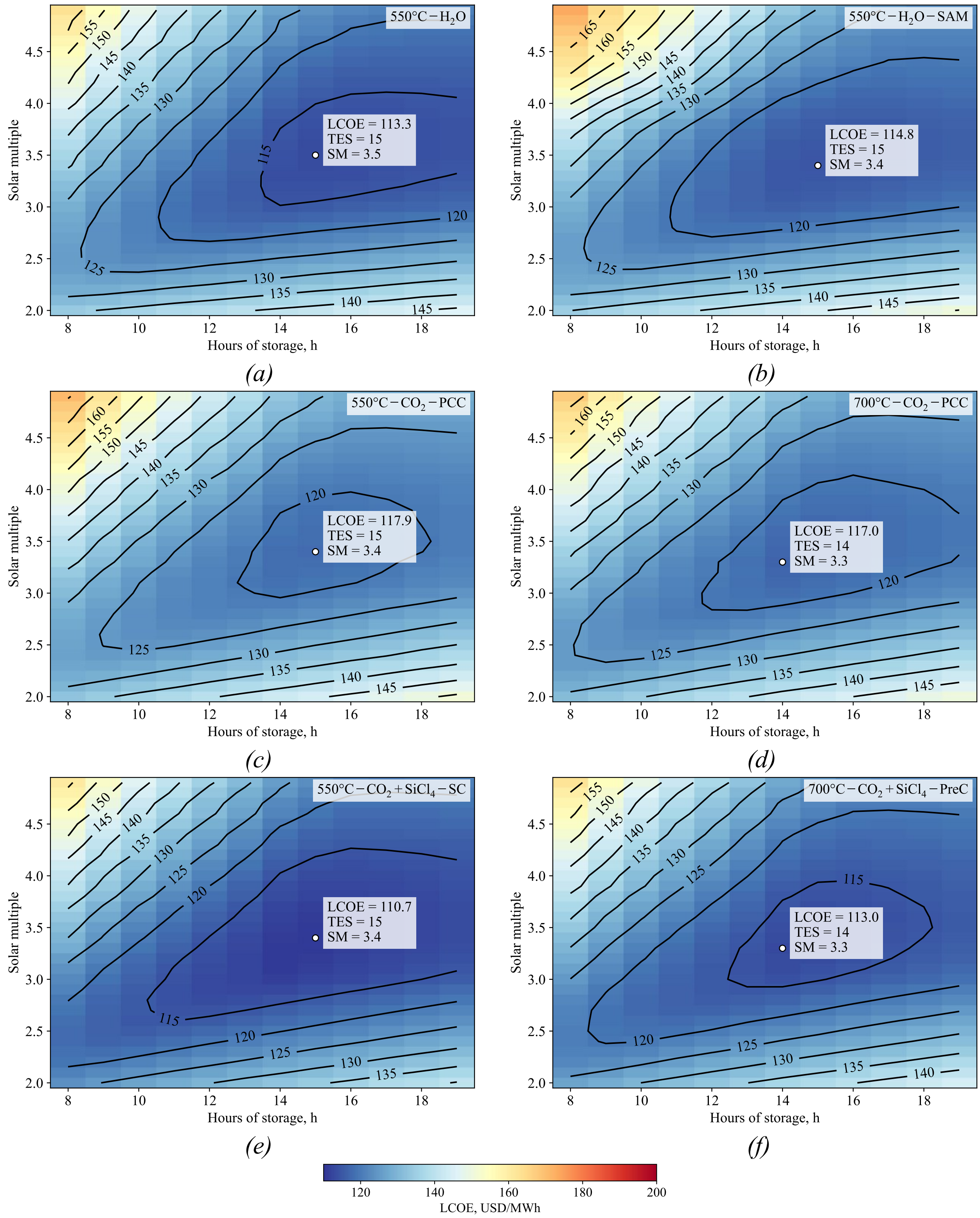

Figure 7.9. LCOE sensitivity for Rankine cycle using the CSP plant model (a) and SAM (b), sCO₂ partial cooling (c, d) and CO_2+$SiCl_4$ simple and precompression cycles (e, f) at 550 and 700°C TIT respectively

Due to higher SM, the power cycle size has decreased from 99-127 MWe to 77-95 MWe. This makes the specific cost of the power cycles 5-9% higher, as seen in Figure 10 (the detailed power cycles parameters can be seen in Supplementary materials C). The specific cost of PHE did not change due to a linear dependence on the UA. The specific cost of turbines, pumps, and compressors has increased by 12-19%, while recuperative and cooling systems by 6-9%, which means a higher influence of turbomachinery on the small power cycles costs. The specific cost of the sCO_2 precompression cycle at 700°C TIT becomes bigger than the Rankine one, which makes this cycle worse than currently used steam cycles in all aspects.

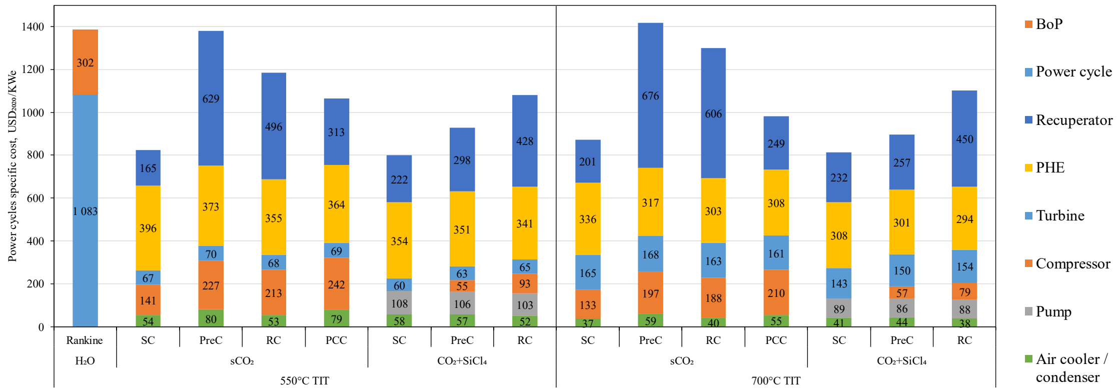

Figure 7.10. Power cycles specific cost distribution for the optimum case

The capacity factor varies for all cycles from 59.59 to 63%. The detailed results of optimized CSP plants are shown in Supplementary materials C. Simple and precompression sCO_2 cycles have lower optimum hours of storage and solar multiple compared to the mixture and the rest of the sCO_2 cycles, which is caused by their efficiency being lower than cycles at similar temperature rises across the PHE. Since the receiver efficiency is lower for sCO_2 and CO_2 mixtures cycles the solar to electric efficiency and electricity output are lower than in the Rankine cycle at 550°C TIT. In the case of CO_2+$SiCl_4$ recompression power cycle efficiency is higher than in the Rankine steam cycle but doesn't fully compensate for the lower efficiency of the receiver. At 700°C TIT solar to electric efficiency in sCO_2 precompression, partial cooling, and all CO_2+$SiCl_4$ cycles is higher than in the case of the steam Rankine cycle, which leads to higher electricity generation from a field of a similar output. Therefore, a transition from 550 to 700°C TIT can increase the electricity generation of the solar field of the same size. Comparing the sCO_2 and CO_2 mixtures cycles, at both 550 to 700°C TIT solar to electric efficiency is higher for all CO_2+$SiCl_4$ cycles, which is due to their higher efficiency and temperature rise across the PHE. The difference in CSP plants costs is mainly due to the thermal energy storage, which is determined by temperature rise across the PHE, and power cycle costs.

The heliostat field, receiver, and tower portions of the LCOE vary according to the electricity generation and are higher for sCO_2 and CO_2 mixtures at 550°C TIT as can be seen in Figure 2.5. The TES contribution to LCOE is also much higher for CO_2 cycles. The main advantage of sCO_2 and CO_2 mixtures is the cost of the power cycle, which is mainly influenced by the cost of PHE and recuperators. Since the simple CO_2+$SiCl_4$ cycle has the lowest cycle specific cost, low PHE inlet temperature, and good electric efficiency the resulting LCOE was the lowest among all considered cases. Compared to steam Rankine cycle CO_2+$SiCl_4$ SC has lower energy generation, but the much lower cycle cost outweighs the lower efficiency and higher cost of TES. The CO_2+$SiCl_4$ simple cycle is followed by the precompression one, which has a bigger specific cost, but also higher efficiency (electricity output) and TES size compared to the simple mixture cycle.

At 700°C TIT, the lowest LCOE has a CO_2+$SiCl_4$ precompression cycle, which has a higher specific cost than a simple cycle but also higher efficiency and therefore higher electricity output. Among sCO_2 cycles, the partial cooling cycle has the lowest LCOE which is in accordance with the results of [25]. The higher electricity output along with lower power cycle and TES cost lead to lower LCOE using the CO_2 mixture compared to sCO_2 cycles.

The resulting LCOE values are comparable to results in the literature: 110-150 USD/MWh [64,65] and 96-108 USD_{2020}/MWh [27] for CO_2 cycles, 116-121 USD_{2020}/MWh [62] and 95-105

USD2020/MWh [27] for CO_2 mixture cycles. Just like in the CSP plant with a particle receiver in [65] the lowest LCOE for CO_2 cycles is reached by simple and partial cooling cycles. However it should be noted that the reduced energy generation means bigger ecological impact of simple cycles compared to more complex recompression and partial cooling ones [12]. The main factors affecting the LCOE are electricity output, power cycle, and TES costs. Therefore, the main parameters to consider while choosing the fitting power cycle are efficiency, PHE inlet temperature, and UA of the recuperative system. Taking into account the uncertainty of cost correlations and financial parameters it is hard to clearly state the optimum cycle but obvious outsiders can be separated. In any case, it should be noted, that the increase of power cycle efficiency and TIT might be detrimental from the economical viewpoint, and CO_2 mixtures power cycles for CSP plants should be assessed taking into account the whole system.

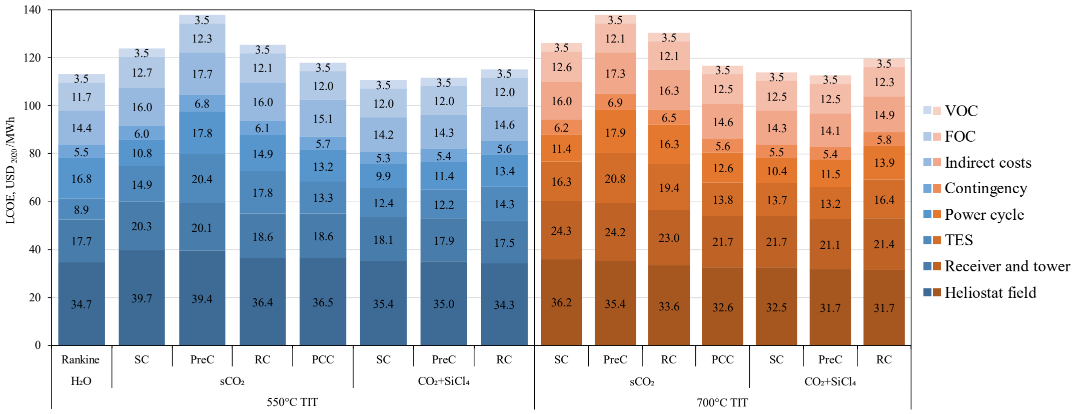

Figure 7.11. The LCOE distribution for at 550°C and 700°C TIT.

7.4. Conclusions

In the current paper simple, precompression, recompression, and partial cooling cycles using sCO_2 and CO_2+$SiCl_4$ mixture as a working fluid are optimized to reach maximum electric efficiency at 550 and 700°C turbine inlet temperature levels representative of Gen2 and Gen3 CSP technologies. A comparison of steam, sCO_2, and CO_2+$SiCl_4$ mixture CSP plants is carried out after optimizing the energy storage and power unit size to reach minimum LCOE for each case assuming the same receiver flux density within the same TIT.

A CSP plant model to calculate the annual electricity generation and LCOE was developed and showed a deviation below 3% in electricity output at 550°C TIT and below 5% for 700°C TIT compared to SAM and SolarTherm. The deviations for TCC and LCOE were within 1.5% and 2.5% for CSP plants with a steam cycle, 4.5% and 5% for the sCO2 cycle using a chloride salt receiver, and 2% and 3.5% using a sodium receiver.

At 550°C TIT the sCO_2 recompression and CO_2+$SiCl_4$ simple cycle have similar electrical efficiencies above 38.5%. The CO_2+$SiCl_4$ precompression cycle has an electrical efficiency of 39% followed by the recompression CO_2+$SiCl_4$ cycle having an electrical efficiency similar to the Rankine cycle of around 40%. At 700°C TIT, the CO_2+$SiCl_4$ recompression cycle has the highest electrical efficiency of 46.6%, followed by CO_2+$SiCl_4$ precompression and sCO_2 recompression cycles with electrical efficiency of around 45.3%. The CO_2+$SiCl_4$ simple cycle has an electrical efficiency of around 44.5% similar to the sCO_2 partial cooling one. In all cases, PHE inlet temperature is the lowest for the precompression mixture cycle, while specific cost is the lowest for the simple recuperated mixture cycle.

The solar to electric efficiency and electricity generation increases with the increase of TIT from 550°C to 700°C, however, the increase of CSP plant cost leads to the increase of LCOE for most of the cycles. The lowest LCOE at 550°C TIT is obtained by the simple CO_2+$SiCl_4$ mixture cycle (110.7 USD/MWh) due to the lower cost of the power cycle and TES, followed by the mixture precompression cycle (111.6 USD/MWh), Rankine cycle (113.3 USD/MWh), mixture recompression cycle (115.3 USD/MWh) and all the sCO_2 cycles. At 700°C TIT, the precompression CO_2+$SiCl_4$ mixture cycle has the lowest LCOE at 113.0 USD/MWh, followed by the simple mixture cycle at 114.1 USD/MWh. In all considered cases, CO_2 mixture power cycles have higher solar to electric efficiency than sCO_2 cycles while having lower power cycle and storage costs, leading to their lower LCOE. Among all the sCO_2 cycles partial cooling has the lowest LCOE at both TIT, followed by simple recuperated, recompression, and precompression ones. At the same time, the partial cooling sCO_2 cycle is the only one which has lower LCOE at 700°C and not at 550°C TIT. At 550°C TIT the CO_2+$SiCl_4$ mixture simple cycle LCOE is lower than state of the art steam Rankine cycle mainly due to the lower cost of the cycle. Therefore, it is clear that the performance of power cycles should be assessed within the whole CSP plant since the optimization of cycle efficiency alone might have a negative impact on the rest of the plant.

These results show that a CO_2+$SiCl_4$ mixture in the simple or precompression cycle layout is a promising working fluid, which performs better than sCO_2 at 550 and 700°C TIT. The CO_2+$SiCl_4$ mixture cycle might be interesting even for the 550°C TIT CSP plant. However, there is a big uncertainty in recuperator and primary heater cost assumptions which are the biggest part of cycle costs. Further research will be focused on equipment sizing to better assess the cost of the different cycles.

7.5. Bibliography

[1] Renewable power generation costs in 2021. Abu Dhabi: IRENA; 2022.

[2] Renewables 2020. Paris, France: IEA; 2020.

[3] Xie X, Zhu P, Ni M, Chai F, Li J, Xiao G. Design, simulation and on-sun experiments of a modified sliding-bed particle solar receiver for coupling with tower concentrating system. Renewable Energy 2024;235:121275. https://doi.org/10.1016/j.renene.2024.121275.

[4] Li Q, E E, Qiu Y, Wang J, Zhang Y. Conceptual design of novel He-SCO2 Brayton cycles for ultra-high-temperature concentrating solar power. Energy Conversion and Management 2022;260:115618. https://doi.org/10.1016/j.enconman.2022.115618.

[5] Zhang Y, Qiu Y, Li Q, Henry A. Optical-thermal-mechanical characteristics of an ultra-high-temperature graphite receiver designed for concentrating solar power. Applied Energy 2022;307:118228. https://doi.org/10.1016/j.apenergy.2021.118228.

[6] Dostal V, Driscoll MJ, Hejzlar P, Wang Y. Supercritical CO2 Cycle for Fast Gas-Cooled Reactors. Volume 7: Turbo Expo 2004, Vienna, Austria: ASMEDC; 2004, p. 683–92. https://doi.org/10.1115/GT2004-54242.

[7] Zhao B, Yao J, Su Y. Performance response to operating-load fluctuations for Sub-megawatt-scale recuperated supercritical CO2 Brayton cycles: Characteristics and improvement. Renewable Energy 2023;206:686–93. https://doi.org/10.1016/j.renene.2023.02.082.

[8] Dekhtyarev V. On the creation of a carbon dioxide power plant with high power and high efficiency. Electric stations 1962:2–6. https://doi.org/10.5281/zenodo.12191690.

[9] Angelino G. Real Gas Effects in Carbon Dioxide Cycles. ASME 1969 Gas Turbine Conference and Products Show, Cleveland, Ohio, USA: American Society of Mechanical Engineers; 1969, p. V001T01A071. https://doi.org/10.1115/69-GT-102.

[10] Dostal V, Driscoll MJ, Hejzlar P. A Supercritical Carbon Dioxide Cycle for Next Generation Nuclear Reactors. MIT; 2004.

[11] Delsoto GS, Battisti FG, Da Silva AK. Dynamic modeling and control of a solar-powered Brayton cycle using supercritical CO2 and optimization of its thermal energy storage. Renewable Energy 2023;206:336–56. https://doi.org/10.1016/j.renene.2023.01.088.

[12] Ma N, Meng F, Hong W, Li H, Niu X. Thermodynamic assessment of the dry-cooling supercritical Brayton cycle in a direct-heated solar power tower plant enabled by CO2-propane mixture. Renewable Energy 2023;203:649–63. https://doi.org/10.1016/j.renene.2022.12.084.

[13] Rodríguez-deArriba P, Crespi F, Sánchez D, Muñoz A, Sánchez T. The potential of transcritical cycles based on CO 2 mixtures: An exergy-based analysis. Renewable Energy 2022;199:1606–28. https://doi.org/10.1016/j.renene.2022.09.041.
[14] Manzolini G, Binotti M, Bonalumi D, Invernizzi C, Iora P. CO2 mixtures as innovative working fluid in power cycles applied to solar plants. Techno-economic assessment. Solar Energy 2019;181:530–44. https://doi.org/10.1016/j.solener.2019.01.015.
[15] Di Marcoberardino G, Morosini E, Di Bona D, Chiesa P, Invernizzi C, Iora P, et al. Experimental characterisation of CO2 + C6F6 mixture: Thermal stability and vapour liquid equilibrium test for its application in transcritical power cycle. Applied Thermal Engineering 2022;212:118520. https://doi.org/10.1016/j.applthermaleng.2022.118520.
[16] Binotti M, Invernizzi CM, Iora P, Manzolini G. Dinitrogen tetroxide and carbon dioxide mixtures as working fluids in solar tower plants. Solar Energy 2019;181:203–13. https://doi.org/10.1016/j.solener.2019.01.079.
[17] Crespi F, Rodríguez De Arriba P, Sánchez D, Ayub A, Di Marcoberardino G, Invernizzi CM, et al. Thermal efficiency gains enabled by using CO2 mixtures in supercritical power cycles. Energy 2022;238:121899. https://doi.org/10.1016/j.energy.2021.121899.
[18] Bonalumi D, Lasala S, Macchi E. CO2-TiCl4 working fluid for high-temperature heat source power cycles and solar application. Renewable Energy 2020;147:2842–54. https://doi.org/10.1016/j.renene.2018.10.018.
[19] Putelli L, Di Marcoberardino G, Gelfi M, Invernizzi CM, Iora PG, Manzolini G. Preliminary Analysis of High-Temperature Corrosion of Metallic Alloys With CO2 and CO2-Based Working Mixtures for Power Plants Applications, American Society of Mechanical Engineers Digital Collection; 2022. https://doi.org/10.1115/GT2022-84197.
[20] Scarabeusproject 2024. https://www.scarabeusproject.eu/ (accessed September 27, 2024).
[21] Desolination – Desolination n.d. https://desolination.eu/ (accessed September 27, 2024).
[22] Nakayama M, Miyamoto S, Ogawa T, Osae S, Tomono K, Sumimoto M, et al. Thermal decomposition of tetrabromosilane and deposition of crystalline silicon. Materials Science in Semiconductor Processing 2014;23:93–7. https://doi.org/10.1016/j.mssp.2014.02.045.
[23] Doninelli M, Morosini E, Di Marcoberardino G, Invernizzi CM, Iora P, Riva M, et al. Experimental investigation of the CO2+SiCl4 mixture as innovative working fluid for power cycles: Bubble points and liquid density measurements. Energy 2024:131197. https://doi.org/10.1016/j.energy.2024.131197.
[24] Doninelli M, Di Marcoberardino G, Iora P, Gelfi M, Invernizzi CM, Manzolini G. Silicon Tetrachloride as innovative working fluid for high temperature Rankine cycles: Thermal Stability, material compatibility, and energy analysis. Applied Thermal Engineering 2024;249:123239. https://doi.org/10.1016/j.applthermaleng.2024.123239.
[25] Neises T, Turchi C. Supercritical carbon dioxide power cycle design and configuration optimization to minimize levelized cost of energy of molten salt power towers operating at 650 °C. Solar Energy 2019;181:27–36. https://doi.org/10.1016/j.solener.2019.01.078.
[26] Manzolini G, Binotti M, Morosini E, Sanchez D, Crespi F, Marcoberdino GD, et al. Adoption of CO2 blended with C6F6 as working fluid in CSP plants. SOLARPACES 2020, Freiburg, Germany: 2022, p. 090005. https://doi.org/10.1063/5.0086520.
[27] Morosini E, Villa E, Quadrio G, Binotti M, Manzolini G. Solar tower CSP plants with transcritical cycles based on CO2 mixtures: A sensitivity on storage and power block layouts. Solar Energy 2023;262:111777. https://doi.org/10.1016/j.solener.2023.05.054.
[28] Aspen Plus | Leading Process Simulation Software | AspenTech n.d. https://www.aspentech.com/en/products/engineering/aspen-plus (accessed June 28, 2023).
[29] Mehos M, Turchi C, Vidal J, Wagner M, Ma Z, Ho C, et al. Concentrating Solar Power Gen3 Demonstration Roadmap. NREL, SNL; 2017. https://doi.org/10.2172/1338899.
[30] Wagner MJ, Wendelin T. SolarPILOT: A power tower solar field layout and characterization tool. Solar Energy 2018;171:185–96. https://doi.org/10.1016/j.solener.2018.06.063.
[31] Hamilton WT, Wagner MJ, Zolan AJ. Demonstrating SolarPILOT's Python API Through Heliostat Optimal Aimpoint Strategy Use Case. vol. ASME 2021 15th International Conference on Energy Sustainability, 2021, p. 6. https://doi.org/10.1115/ES2021-60502.
[32] Wang S, Asselineau C-A, Fontalvo A, Wang Y, Logie W, Pye J, et al. Co-optimisation of the heliostat field and receiver for concentrated solar power plants. Applied Energy 2023;348:121513. https://doi.org/10.1016/j.apenergy.2023.121513.
[33] Virtanen P, Gommers R, Oliphant TE, Haberland M, Reddy T, Cournapeau D, et al. SciPy 1.0: Fundamental Algorithms for Scientific Computing in Python. Nature Methods 2020;17:261–72. https://doi.org/10.1038/s41592-019-0686-2.
[34] Reda I, Andreas A. Solar position algorithm for solar radiation applications. Solar Energy 2004;76:577–89. https://doi.org/10.1016/j.solener.2003.12.003.
[35] Asselineau C-A, Pye J, Coventry J. Exploring efficiency limits for molten-salt and sodium external cylindrical receivers for third-generation concentrating solar power. Solar Energy 2022;240:354–75. https://doi.org/10.1016/j.solener.2022.05.001.
[36] Manzolini G, Lucca G, Binotti M, Lozza G. A two-step procedure for the selection of innovative high temperature heat transfer fluids in solar tower power plants. Renewable Energy 2021;177:807–22. https://doi.org/10.1016/j.renene.2021.05.153.

[37] Binotti M, Astolfi M, Campanari S, Manzolini G, Silva P. Preliminary assessment of sCO2 cycles for power generation in CSP solar tower plants. Applied Energy 2017;204:1007–17. https://doi.org/10.1016/j.apenergy.2017.05.121.
[38] Polimeni S, Binotti M, Moretti L, Manzolini G. Comparison of sodium and KCl-MgCl2 as heat transfer fluids in CSP solar tower with sCO2 power cycles. Solar Energy 2018;162:510–24. https://doi.org/10.1016/j.solener.2018.01.046.
[39] Idel′chik IE. Handbook of Hydraulic Resistance. 4th ed. Begell House; 2008.
[40] National Renewable Energy Laboratory. System Advisor Model Version 2022.11.21 (SAM 2022.11.21). NREL SAM 2022. https://https://sam.nrel.gov (accessed February 22, 2024).
[41] Kaltschmitt M, Streicher W, Wiese A, editors. Renewable Energy: Technology, Economics and Environment. 2007th edition. Berlin ; New York: Springer; 2007.
[42] Tang Z, Tao W-Q. Strength analysis of molten salt tanks for concentrating solar power plants. Energy Storage and Saving 2023:S2772683523000407. https://doi.org/10.1016/j.enss.2023.08.003.
[43] Weiland N, Thimsen D. A practical look at assumptions and constraints for steady state modeling of sCO2 Brayton power cycles, San Antonio, Texas: National Energy Technology Laboratory (NETL), Pittsburgh, PA, Morgantown, WV …; 2016.
[44] Lopes T, Fasquelle T, Silva HG. Pressure drops, heat transfer coefficient, costs and power block design for direct storage parabolic trough power plants running molten salts. Renewable Energy 2021;163:530–43. https://doi.org/10.1016/j.renene.2020.07.110.
[45] Span R, Wagner W. A New Equation of State for Carbon Dioxide Covering the Fluid Region from the Triple-Point Temperature to 1100 K at Pressures up to 800 MPa. J Phys Chem Ref Data 1996;25:1509–96. https://doi.org/10.1063/1.555991.
[46] Peng D-Y, Robinson DB. A New Two-Constant Equation of State. Ind Eng Chem Fund 1976;15:59–64. https://doi.org/10.1021/i160057a011.
[47] Weiland NT, Lance BW, Pidaparti SR. sCO2 Power Cycle Component Cost Correlations From DOE Data Spanning Multiple Scales and Applications. Volume 9: Oil and Gas Applications; Supercritical CO2 Power Cycles; Wind Energy, Phoenix, Arizona, USA: American Society of Mechanical Engineers; 2019, p. V009T38A008. https://doi.org/10.1115/GT2019-90493.
[48] Fontalvo A, Guccione S, Wang Y, Wang S, Kee Z, Asselineau C-A, et al. System-level comparison of sodium and salt systems in support of the Gen3 liquids pathway, Freiburg, Germany: 2022, p. 030007. https://doi.org/10.1063/5.0087911.
[49] Turchi C, Gage S, Martinek J, Jape S, Armijo K, Coventry J, et al. CSP Gen3: Liquid-Phase Pathway to SunShot. 2021. https://doi.org/10.2172/1807668.
[50] Kelly BD. Advanced Thermal Storage for Central Receivers with Supercritical Coolants. Lakewood, USA: ABENGOA SOLAR; 2010. https://doi.org/10.2172/981926.
[51] Carlson MD, Middleton BM, Ho CK. Techno-Economic Comparison of Solar-Driven SCO2 Brayton Cycles Using Component Cost Models Baselined With Vendor Data and Estimates. ASME 2017 11th International Conference on Energy Sustainability, Charlotte, North Carolina, USA: American Society of Mechanical Engineers; 2017, p. V001T05A009. https://doi.org/10.1115/ES2017-3590.
[52] Reference and discount rates - European Commission n.d. https://competition-policy.ec.europa.eu/state-aid/legislation/reference-discount-rates-and-recovery-interest-rates/reference-and-discount-rates_en (accessed April 15, 2024).
[53] System advisor model (SAM) case study: Gemasolar. NREL 2013:6.
[54] Wagner M. SAM Webinars 2017: Modeling Molten Salt Power Tower Systems in SAM 2017.1.17 n.d.
[55] Bell KJ. Heat Exchanger Design Handbook: Thermal and Hydraulic Design of Heat Exchangers. VDI-Verlag Gmbh; 1983.
[56] Liao Z, Li X, Xu C, Chang C, Wang Z. Allowable flux density on a solar central receiver. Renewable Energy 2014;62:747–53. https://doi.org/10.1016/j.renene.2013.08.044.
[57] Conroy T, Collins MN, Grimes R. Integrated optical-thermal-mechanical model for investigations into high temperature sodium receiver operation. Solar Energy 2019;194:751–65. https://doi.org/10.1016/j.solener.2019.10.089.
[58] Conroy T, Collins MN, Grimes R. Sodium receiver designs for integration with high temperature power cycles. Energy 2019;187:115994. https://doi.org/10.1016/j.energy.2019.115994.
[59] Khan MI, Gutiérrez-Alvarez R, Asfand F, Bicer Y, Sgouridis S, Al-Ghamdi SG, et al. The economics of concentrating solar power (CSP): Assessing cost competitiveness and deployment potential. Renewable and Sustainable Energy Reviews 2024;200:114551. https://doi.org/10.1016/j.rser.2024.114551.
[60] González-Gómez PA, Gómez-Hernández J, Briongos JV, Santana D. Thermo-economic optimization of molten salt steam generators. Energy Conversion and Management 2017;146:228–43. https://doi.org/10.1016/j.enconman.2017.05.027.
[61] Moser M, Trieb F, Fichter T, Kern J, Maier H, Schicktanz P. Techno-economic Analysis of Enhanced Dry Cooling for CSP. Energy Procedia 2014;49:1177–86. https://doi.org/10.1016/j.egypro.2014.03.127.
[62] Morosini E, Rodriguez De Arriba P, Salah SI, Illyés V, Guerif X, Ruggiero M, et al. Transcritical Cycles With CO2-based Mixtures for CSP Applications: An Overview of the SCARABEUS Findings. SolarPACES Conf Proc 2024;2. https://doi.org/10.52825/solarpaces.v2i.788.

[63] Rodríguez-deArriba P, Crespi F, Pace S, Sánchez D. Mapping the techno-economic potential of next-generation CSP plants running on transcritical CO 2 -based power cycles. Energy 2024:133142. https://doi.org/10.1016/j.energy.2024.133142.
[64] Heller L, Glos S, Buck R. sCO2 power cycle design without heat source limitations: Solar thermal particle technology in the CARBOSOLA project. Conference Proceedings of the European sCO2 Conference4th European sCO2 Conference for Energy Systems: March 23-24 2021;2021:177. https://doi.org/10.17185/DUEPUBLICO/73961.
[65] Heller L, Glos S, Buck R. Techno-economic selection and initial evaluation of supercritical CO2 cycles for particle technology-based concentrating solar power plants. Renewable Energy 2022;181:833–42. https://doi.org/10.1016/j.renene.2021.09.007.
[66] Doninelli M, Morosini E, Gentile G, Putelli L, Di Marcoberardino G, Binotti M, et al. Thermal desalination from rejected heat of power cycles working with CO2-based working fluids in CSP application: A focus on the MED technology. Sustainable Energy Technologies and Assessments 2023;60:103481. https://doi.org/10.1016/j.seta.2023.103481.
[67] Bradshaw R, Dawson D, De La Rosa W, Gilbert R, Goods S, Hale M, et al. Final Test and Evaluation Results from the Solar Two Project. 2002. https://doi.org/10.2172/793226.

Supplementary materials A: Validation

During the validation different input assumptions were chosen in each case based on reference used. First, the modified receiver model was compared against other models and experimental results. The location, solar field, receiver geometry, and wind speed were chosen according to reference unless they were not available, in which case they were taken from Table 1 in the manuscript. As can be seen from Table 7.9 there is good agreement both in receiver efficiency and pressure drop in design and off-design conditions. The HTF pump off-design power also showed good agreement with results in [1].

Table 7.9. Receiver validation results

Source	[2]		[3]				[4]	
	Ref.	Calc.	Ref.	Calc.	Ref.	Calc.	Ref.	Calc.
HTF	Solar salt						Sodium	
Power input, MWth	1000		42.2		34.6		385	
Power input as % of design	100		100		82		100	
Efficiency, %	89	89.9	88.8	88.6	87.4	86.9	89.1	89
Efficiency difference, %	1.0		-0.25		-0.57		-0.11	
HTF pump head, bar	-		24	25.8	-		14.3	13
Head difference, %	-		7.5		-		-9.1	

The developed CSP plant model was compared to the default SAM CSP plant [5] located in Sevilla, Spain with a 115 MW power cycle, solar multiple equal (SM) to 2.4 and 10 h of storage with assumptions set according to Table 1 and Table 2 in the manuscript. There is a good agreement in Figure 7.12 of hourly incident power, power flow in TES, and power output to the grid. After that, the SM and size of TES were varied by changing the hours of energy stored and power cycle capacity. The developed model showed deviations with SAM below 3% for all the considered conditions apart from 1 hour of storage.

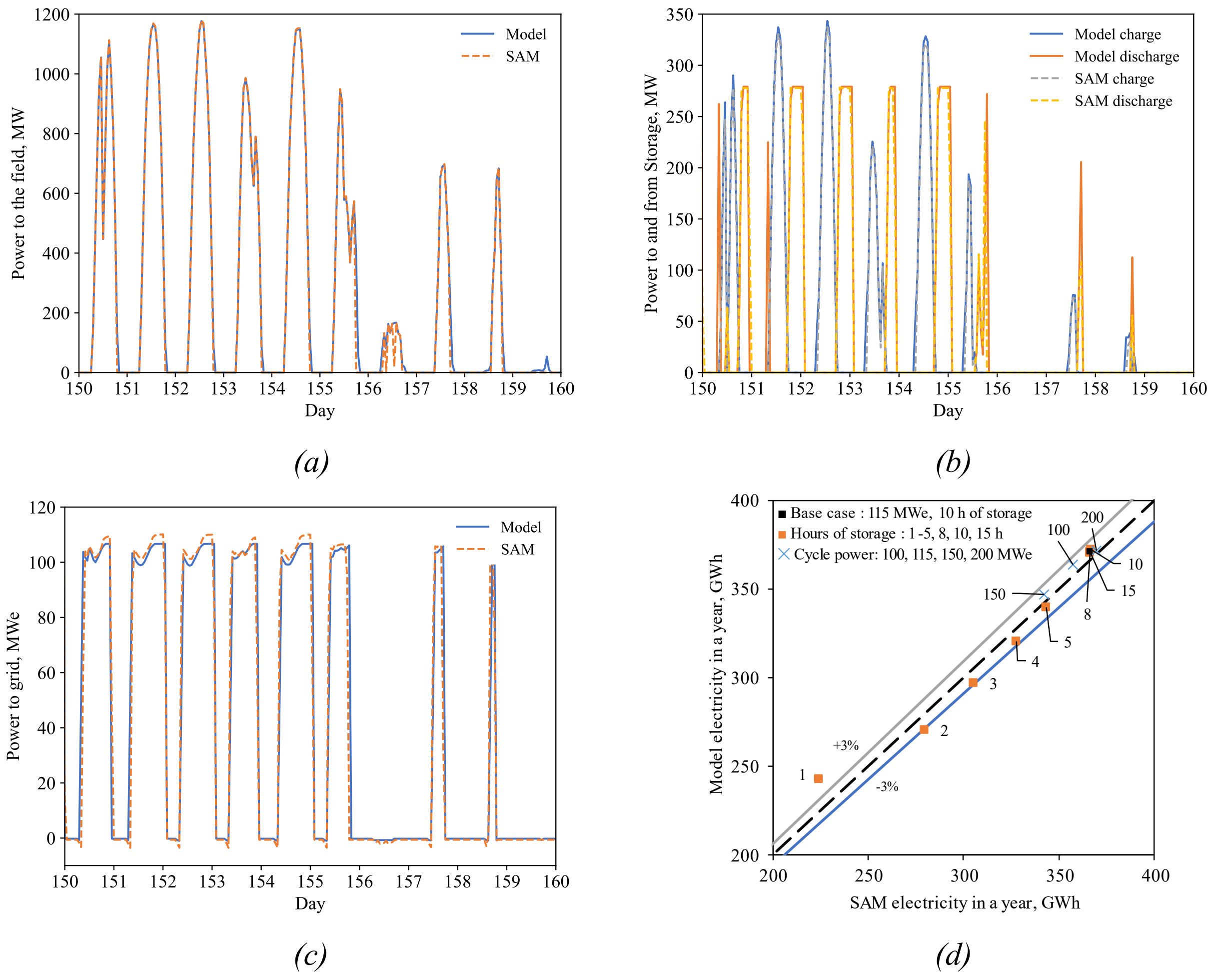

Figure 7.12. CSP plant model validation against SAM for steam cycle: power incident to the field (a), power flows in TES (b), power supplied to grid (c), comparison at different conditions (d)

The CSP plant model showed deviations in electricity output per year below 5% compared to the SolarTherm and SAM for sCO_2 cycles with high-temperature receivers using sodium and chloride salts as HTF as can be seen from Table 7.10 [6,7]. The deviations for TCC and LCOE were within 1.5% and 2.5% for CSP plants with a steam cycle, within 4.5% and 5% for the sCO_2 cycle using a chloride salt receiver, and within 2% and 3.5% using a sodium receiver.

The comparison of CSP plant model results with literature data is shown in Table 7.10. For SAM a real discount rate of 8% was assumed.

Table 7.10. CSP plant model comparison with literature

	Solar Salt [6]			Chloride Salt Receiver [7]					Sodium receiver [7]					
Parameter	**SAM**	**Model**	**Diff., %**	**SAM**	**SolarTherm**	**Model**	**Diff., %**	**Diff., %**	**Base case**	**Model**	**Diff., %**	**Improved case**	**Model**	**Diff., %**
Solar multiple	2.4	2.4	0.0	2.6	2.6	2.6	0.4	0.4	2.4	2.5	3.3	3.0	3.0	-0.4
Annual solar to thermal efficiency, %	44.1	43.7	-1.0	38.4	38.1	40.4	5.2	6.0	44.6	45.2	1.4	42.4	41.8	-1.5
Annual solar to electric efficiency, %	15.7	15.4	-1.9	16.8	17.2	18.2	8.3	5.8	20.4	20.3	-0.4	19.4	18.8	-2.9
Capacity factor, %	41.3	40.4	-2.2	63.0	63.9	62.8	-0.4	-1.8	64.2	61.9	-3.6	74.2	69.1	-6.9
Electricity per year, GWhe/year	366.7	372.0	1.6	551.6	559.1	559.4	1.4	0.0	562.0	555.6	-1.1	540.2	515.4	-4.6
Heliostat field cost, MUSD	196.4	195.9	-0.3	-	99.8	97.8	-	-2.0	83.0	87.1	4.9	83.0	87.1	4.9
Heat exchanger cost, MUSD	-	-	-	-	-	-	-	-	17.2	17.5	1.6	17.2	17.5	1.6
TES cost, MUSD	61.4	54.1	-11.9	-	104.5	110.8	-	6.0	104.5	110.8	6.0	86.9	94.6	8.8
Power cycle cost, MUSD	153.0	153.0	0.0	-	99.9	99.9	-	0.0	99.9	99.9	0.0	83.1	83.1	0.0
Receiver and tower cost, MUSD	105.6	105.6	0.0	-	206.0	179.7	-	-12.8	165.9	154.3	-7.0	165.9	146.2	-11.9
Direct capital cost subtotal, MUSD	516.3	508.6	-1.5		510.2	488.2	-	-4.3	470.5	469.6	-0.2	436.1	428.4	-1.8
Contingency cost, MUSD	36.1	35.6	-1.5		51.0	48.8	-	-4.3	47.1	47.0	-0.3	43.6	42.8	-1.7
Total direct capital cost, MUSD	552.5	544.2	-1.5	-	561.2	537.0	-	-4.3	517.6	516.5	-0.2	479.7	471.2	-1.8
EPC and owner costs, MUSD	71.8	70.7	-1.5	-	50.5	48.3	-	-4.3	46.6	46.5	-0.2	43.2	42.4	-1.8
Total capital (installed cost), MUSD	645.5	636.2	-1.5	-	630.1	603.5	-	-4.2	579.6	578.4	-0.2	538.3	529.1	-1.7
LCOE, USD/MWh	165.0	161.1	-2.4	79.3	78.6	75.7	-4.5	-3.6	72.7	73.5	1.2	69.6	72.0	3.4

Supplementary materials B: Initial CSP plant parameters

The electric power and specific cost of different power cycles in initial CSP plants are presented in Table 7.11.

Table 7.11. Power cycle parameters for initial CSP plants

Parameter	**Value**														
TIT, °C	**550**								**700**						
Cycle fluid	**H_2O**	**sCO_2**				**CO_2+$SiCl_4$**			**sCO2**				**CO_2+$SiCl_4$**		
Cycle	**Rankine**	**SC**	**PreC**	**RC**	**PCC**	**SC**	**PreC**	**RC**	**SC**	**PreC**	**RC**	**PCC**	**SC**	**PreC**	**RC**
Optimised CO_2 fraction, mol%	-	-	-	-	-	80	80	91	-	-	-	-	75	80	92
PHE duty, MWth	288.5	286.1	283.5	284.2	286.2	286.3	286.3	285.8	273.6	271.1	271.2	275.6	275.7	275.8	272.7
Turbine power, MW	-	153.0	175.0	179.5	178.1	149.0	161.6	179.5	170.7	183.5	189.0	193.3	156.3	176.2	184.9
Main compressor or pump power, MW	-	46.2	35.0	25.9	18.4	31.0	10.8	30.7	50.4	29.7	31.8	15.9	26.5	15.9	26.9
Recompressor or precompressor/partial compressor power, MW	-	-	26.5	34.3	19.8/22.6	-	30.8	24.6	-	26.9	24.7	19.6/25.1	-	26.2	21.6
HTR or recuperator UA, MW/K	-	16.8	39.1	29.3	15.1	28.2	15.1	14.0	16.1	32.3	31.1	15.3	26.6	14.2	22.8
LTR UA, MW/K	-	-	43.5	35.5	19.1	-	19.1	19.8	-	26.9	27.7	15.0	-	18.4	30.4
Power electrical, MWe	114.1	98.8	104.1	109.7	107.8	110.7	111.8	114.8	111.4	117.3	122.7	122.5	122.5	125.3	127.0
Power cycles specific cost, USD_{2020}/kWe	1385	787	1285	1104	1016	757	871	1008	821	1303	1195	935	766	849	1022

The parameters of initial CSP plants are shown in Table 7.12.

Table 7.12. CSP plants initial results

Parameter	**Value**														
TIT, °C	**550**								**700**						
Cycle fluid	**H_2O**	**sCO_2**				**CO_2+$SiCl_4$**			**sCO_2**				**CO_2+$SiCl_4$**		
Cycle type	**Rankine**	**SC**	**PreC**	**RC**	**PCC**	**SC**	**PreC**	**RC**	**SC**	**PreC**	**RC**	**PCC**	**SC**	**PreC**	**RC**
Solar multiple	2.5														
TES, h	15														
Annual solar to thermal efficiency, %	43.9	43.3	42.8	43.0	43.4	43.4	43.4	43.3	40.6	40.1	40.1	41.0	41.0	41.0	40.4
Annual solar to electric efficiency, %	15.7	13.3	13.7	14.7	14.7	15.2	15.3	15.6	14.7	15.2	16.0	16.4	16.4	16.8	16.8
Capacity factor, %	47.4	46.8	46.3	46.5	46.9	47.0	47.0	46.8	45.7	45.2	45.4	46.1	46.1	46.2	45.7
Electricity per year, GWh/yr	451.2	384.3	395.0	423.0	423.0	436.8	441.4	449.5	426.3	440.0	464.0	475.7	475.9	488.3	488.0
Heliostat field cost, MUSD	233.5								235.2						
Receiver and tower cost, MUSD	119.3								157.4	160.8	160.6	156.8	156.7	156.5	158.6
TES cost, MUSD	80.2	115.5	168.2	149.2	111.3	107.4	106.7	127.4	141.2	182.2	179.0	133.0	131.8	129.9	156.3
Power cycle cost, MUSD	158.1	77.8	133.7	121.2	109.5	83.8	97.3	115.8	91.4	152.8	146.7	114.5	93.9	106.4	129.9
Total capital (installed cost), MUSD	738.6	684.2	815.6	777.5	717.6	681.8	697.2	744.5	780.1	908.1	896.5	797.5	770.9	783.5	846.4
LCOE, USD_{2020}/MWh	125.9	135.4	154.1	139.3	129.9	121.1	122.3	127.4	139.0	154.4	145.8	128.9	125.2	124.2	132.8

Supplementary materials C: CSP plant optimization results

The sensitivity analysis of LCOE from solar multiple and hours of TES for different power cycles and TIT is shown in Figure 7.13.

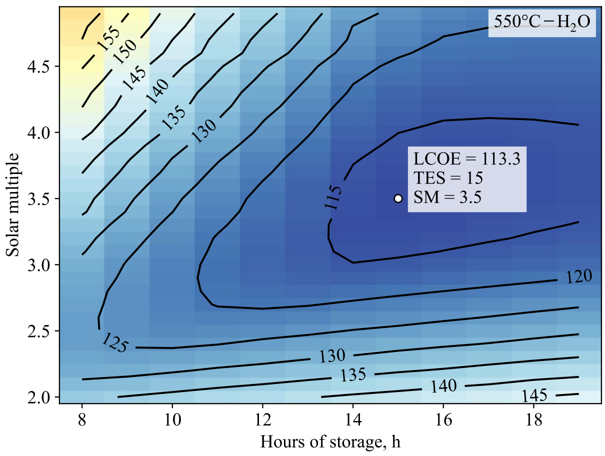

(a)

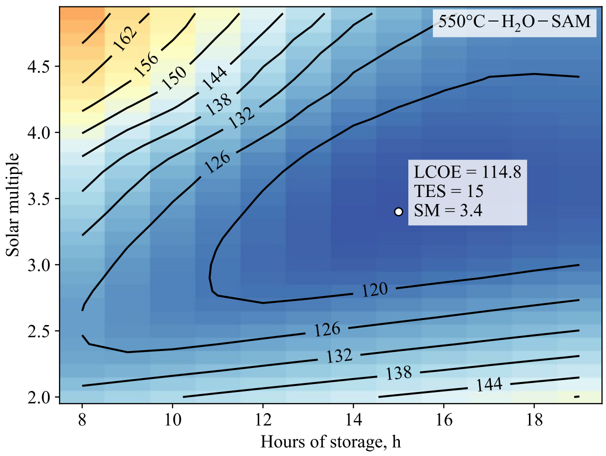

(b)

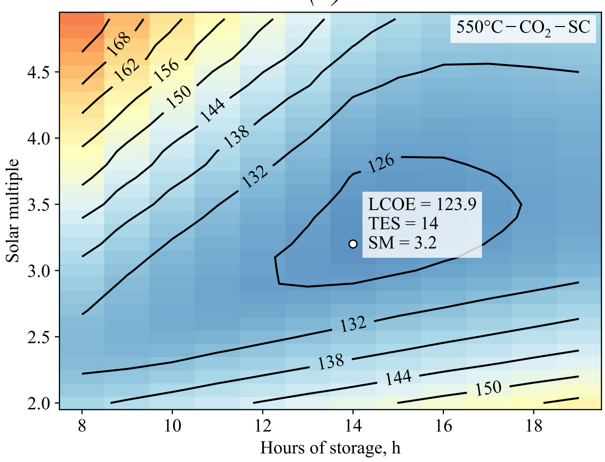

(c)

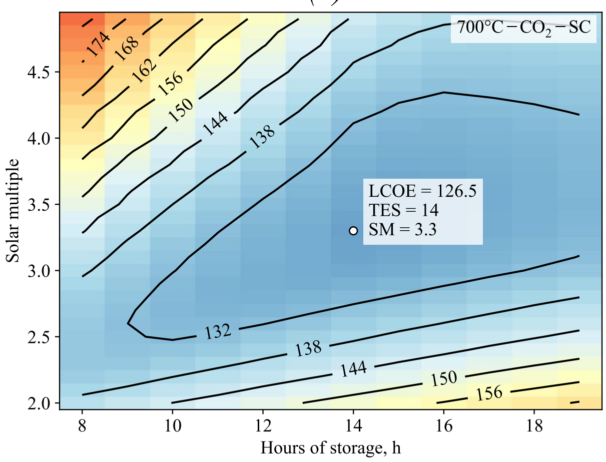

(d)

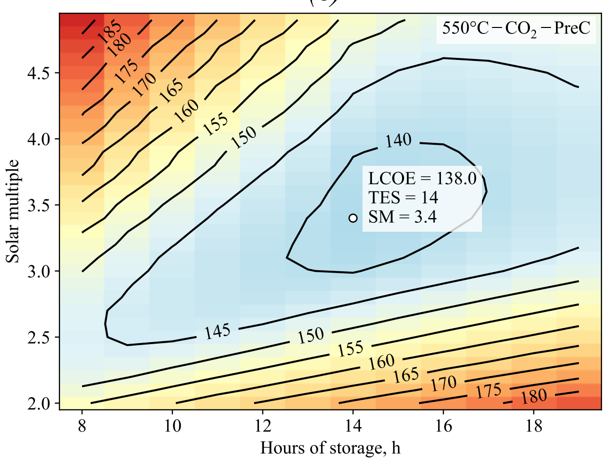

(e)

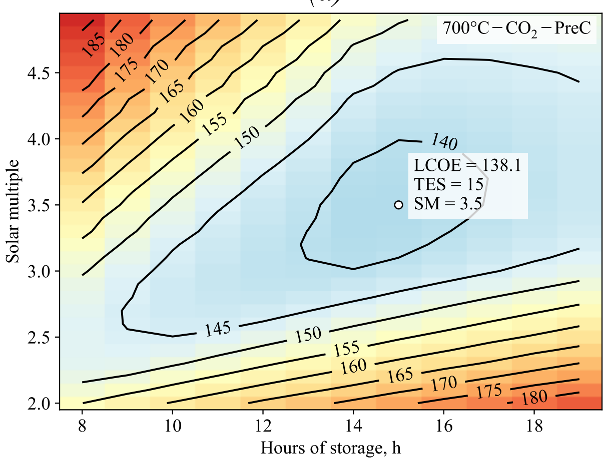

(f)

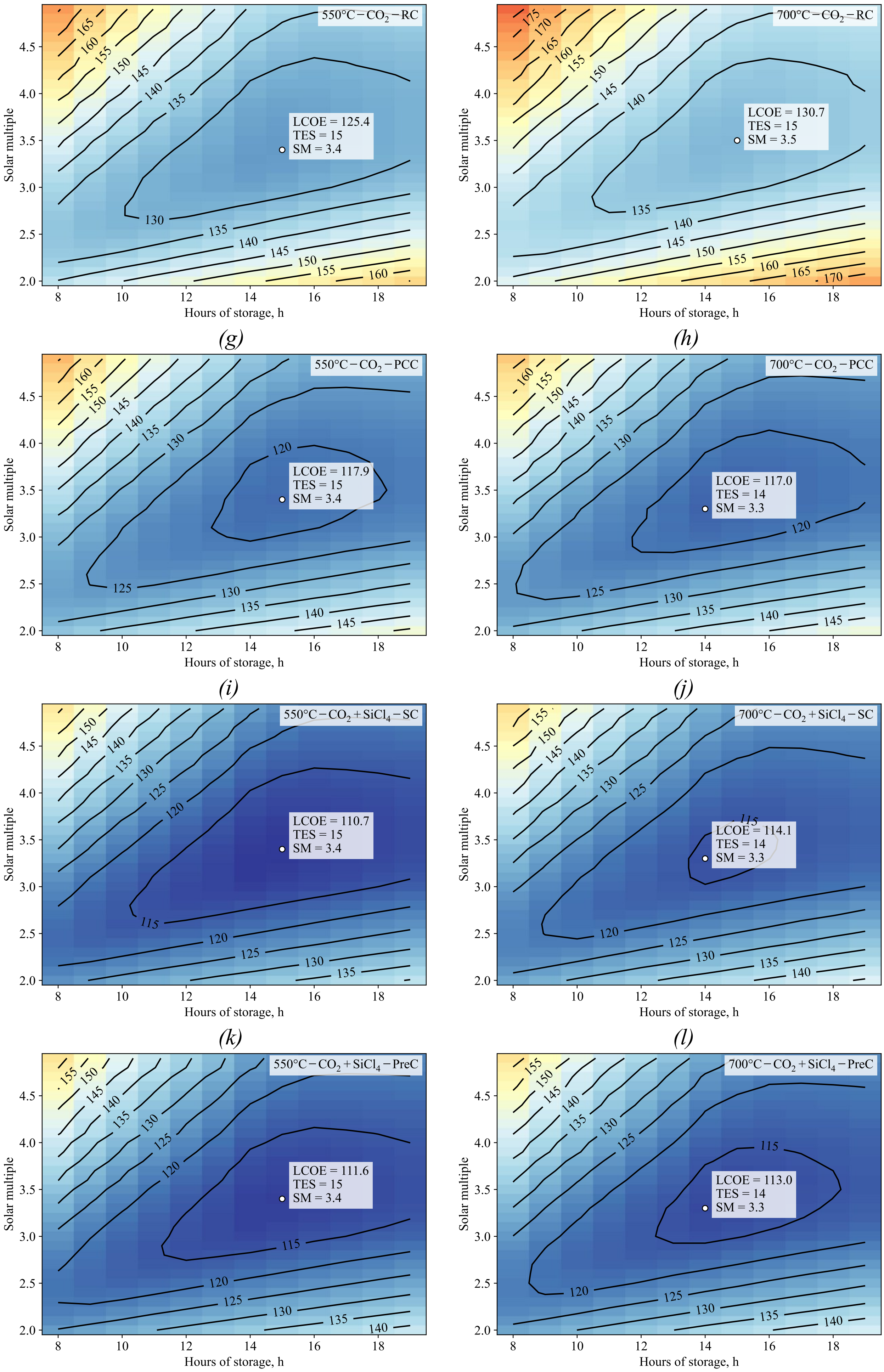
550°C − CO2 − RC
LCOE = 125.4
TES = 15
SM = 3.4
700°C − CO2 − RC
LCOE = 130.7
TES = 15
SM = 3.5
550°C − CO2 − PCC
LCOE = 117.9
TES = 15
SM = 3.4
700°C − CO2 − PCC
LCOE = 117.0
TES = 14
SM = 3.3
550°C − CO2 + SiCl4 − SC
LCOE = 110.7
TES = 15
SM = 3.4
700°C − CO2 + SiCl4 − SC
LCOE = 114.1
TES = 14
SM = 3.3
550°C − CO2 + SiCl4 − PreC
LCOE = 111.6
TES = 15
SM = 3.4
700°C − CO2 + SiCl4 − PreC
LCOE = 113.0
TES = 14
SM = 3.3
Solar multiple
Hours of storage, h

(g) *(h)*

(i) *(j)*

(k) *(l)*

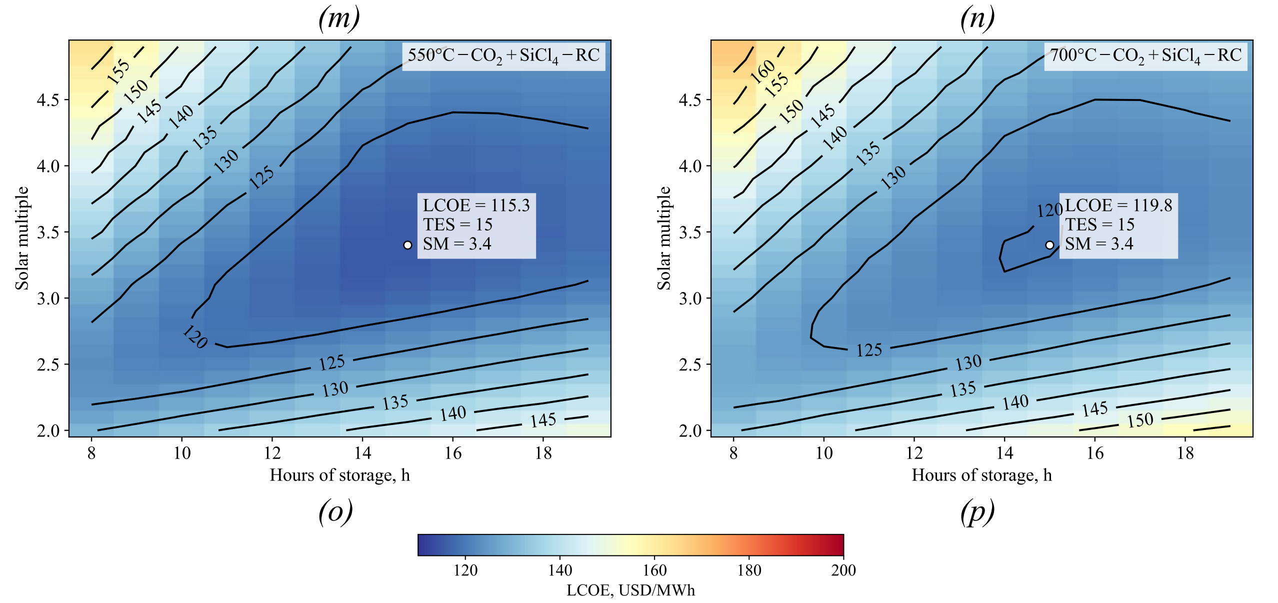

Figure 7.13. LCOE sensitivity for Rankine cycle (a) and Rankine cycle using SAM (b), sCO_2 simple cycle at (c, d), sCO_2 precompression cycle (e, f), sCO_2 recompression cycle (g, h), sCO_2 partial cooling cycle (i, j), CO_2+$SiCl_4$ simple cycle (k, l), CO_2+$SiCl_4$ precompression cycle (m, n), CO_2+$SiCl_4$ recompression cycle (o, p) at 550 and 700°C TIT respectively

The electric power and specific cost of different power cycles in optimum CSP plants are presented Table 7.13.

Table 7.13. Power cycle parameters for optimum CSP plants

Parameter	**Value**														
TIT, °C	**550**								**700**						
Cycle fluid	**H_2O**	**sCO_2**				**CO_2+$SiCl_4$**			**sCO2**				**CO_2+$SiCl_4$**		
Cycle	**Rankine**	**SC**	**PreC**	**RC**	**PCC**	**SC**	**PreC**	**RC**	**SC**	**PreC**	**RC**	**PCC**	**SC**	**PreC**	**RC**
Optimised CO_2 fraction, mol%	-	-	-	-	-	80	80	91	-	-	-	-	75	80	92
PHE duty, MWth	206.1	223.5	208.5	209.0	210.4	210.5	210.5	210.2	207.2	193.6	193.7	208.8	208.9	208.9	200.5
Turbine power, MW	-	119.5	128.7	132.0	130.9	109.5	118.8	132.0	129.3	131.1	135.0	146.5	118.4	133.4	135.9
Main compressor or pump power, MW	-	36.1	25.8	19.0	13.5	22.8	8.0	22.6	38.2	21.2	22.7	12.1	20.1	12.1	19.8
Recompressor or precompressor/partial compressor power, MW	-	-	19.5	25.2	14.6/16.6	-	22.7	18.1	-	19.2	17.6	14.8/19	-	19.9	15.9
HTR or recuperator UA, MW/K	-	13.1	28.7	21.6	11.1	20.7	11.1	10.3	12.2	23.1	22.2	11.6	20.1	10.8	16.8
LTR UA, MW/K	-	-	32.0	26.1	14.1	-	14.1	14.6	-	19.2	19.7	11.3	-	14.0	22.4
Power electrical, MWe	114.1	77.2	76.5	80.7	79.2	81.4	82.2	84.4	84.4	83.8	87.6	92.8	92.8	94.9	93.4
Power cycles specific cost, USD_{2020}/kWe	1385	824	1379	1184	1066	801	929	1081	873	1416	1300	982	813	896	1102

The parameters of optimized CSP plants are shown in Table 7.14.

Table 7.14. CSP plants optimum results

Parameter	Value														
TIT, °C	**550**								**700**						
Cycle fluid	**H_2O**	**sCO_2**				**CO_2+$SiCl_4$**			**sCO_2**				**CO_2+$SiCl_4$**		
Cycle type	**Rankine**	**SC**	**PreC**	**RC**	**PCC**	**SC**	**PreC**	**RC**	**SC**	**PreC**	**RC**	**PCC**	**SC**	**PreC**	**RC**
Solar multiple	3.5	3.2	3.4						3.3	3.5		3.3			3.4
TES, h	15	14		15					14	15		14			15
Annual solar to thermal efficiency, %	41.7	42.4	40.9	41.4	41.8	41.8	41.8	41.8	39.3	38.3	38.3	39.7	39.7	39.7	39.0
Annual solar to electric efficiency, %	15.2	13.3	13.4	14.5	14.5	14.9	15.1	15.4	14.6	14.9	15.7	16.2	16.2	16.6	16.6
Capacity factor, %	64.3	59.5	61.4	62.3	62.8	62.8	62.9	62.7	59.8	62.1	62.2	60.1	60.1	60.1	61.5
Electricity per year, GWh/yr	437	382	385	417	416	429	434	444	422	432	455	470	470	482	482
Heliostat field cost, MUSD	233.5								235.2						
Receiver and tower cost, MUSD	119.3								157	161	161	157	157	157	159
TES cost, MUSD	60	87	121	114	85	82	81	97	106	138	136	100	99	98	121
Power cycle cost, MUSD	113	62	106	96	86	65	76	91	74	119	114	92	75	85	103
Total capital (installed cost), MUSD	659	633	724	704	657	629	641	670	716	813	804	731	709	719	771
LCOE, USD_{2020}/MWh	113.3	123.9	138.0	125.4	117.9	110.7	111.6	115.3	126.5	138.1	130.7	117.0	114.1	113.0	119.8

Supplementary materials bibliography

[1] Doninelli M, Morosini E, Gentile G, Putelli L, Di Marcoberardino G, Binotti M, et al. Thermal desalination from rejected heat of power cycles working with CO2-based working fluids in CSP application: A focus on the MED technology. Sustainable Energy Technologies and Assessments 2023;60:103481. https://doi.org/10.1016/j.seta.2023.103481.

[2] Asselineau C-A, Pye J, Coventry J. Exploring efficiency limits for molten-salt and sodium external cylindrical receivers for third-generation concentrating solar power. Solar Energy 2022;240:354–75. https://doi.org/10.1016/j.solener.2022.05.001.

[3] Bradshaw R, Dawson D, De La Rosa W, Gilbert R, Goods S, Hale M, et al. Final Test and Evaluation Results from the Solar Two Project. 2002. https://doi.org/10.2172/793226.

[4] Turchi C, Gage S, Martinek J, Jape S, Armijo K, Coventry J, et al. CSP Gen3: Liquid-Phase Pathway to SunShot. 2021. https://doi.org/10.2172/1807668.

[5] System advisor model (SAM) case study: Gemasolar. NREL 2013:6.

[6] National Renewable Energy Laboratory. System Advisor Model Version 2022.11.21 (SAM 2022.11.21). NREL SAM 2022. https://https://sam.nrel.gov (accessed February 22, 2024).

[7] Fontalvo A, Guccione S, Wang Y, Wang S, Kee Z, Asselineau C-A, et al. System-level comparison of sodium and salt systems in support of the Gen3 liquids pathway, Freiburg, Germany: 2022, p. 030007. https://doi.org/10.1063/5.0087911.

8. Impact of air-cooled heat rejection unit design on the CSP plant with sCO_2 and CO_2 mixture power cycles

This chapter is based on the article: *"Techno-economic impact of air-cooled heat rejection unit design on solar tower power plant with sCO_2 and CO_2 mixture power cycles", published in Energy Conversion and Management Journal, July 2026, 121524, https://doi.org/10.1016/j.enconman.2026.121524*

Abstract

The next generation of concentrated solar power plants is expected to utilize supercritical CO_2 cycles as power block. These systems can be further enhanced by using dopants to increase the critical temperature and move towards transcritical cycles, allowing for higher power cycle efficiency and lower cost. Air-cooled condensers, usually used in new plants, have significant impact on power cycle and plant performance. This work aims at investigating the influence of air-cooled cooler/condenser design parameters on the technoeconomic performance of solar tower plant with sCO_2 and CO_2 mixture power cycles. Simple recuperated cycles using sCO_2 and CO_2 mixture with silicon tetrachloride ($SiCl_4$) are modeled at design and off-design conditions and integrated in the solar tower power plant model. The optimum cooler/condenser design parameters are determined for Seville, Spain by varying minimum cycle temperature, cooler/condenser approach temperature, solar multiple, and thermal energy storage size. Results show that CO_2 mixture cycles at the design point have on average 3.9 and 4 percentage points higher thermal and electric efficiency than an sCO_2 one. Moving to the annual overall analysis, the optimum ambient air design temperature, for both the solutions, is 35°C (a value 5°C below the maximum and not exceeded 96.8% of hours during the year), while the optimum cooler/condenser approach temperature is the minimum considered, equal to 5°C. At the same time, CO_2 mixture cycle has 8.4% lower levelized cost of electricity compared to the sCO_2 one at both the base and optimum solar multiple, lower thermal energy storage size and is less sensitive to the ambient air design temperature changes.

Nomenclature

Acronyms		*Symbols*	
ACC	air cooled cooler/condenser	Δh	pump head rise
COMP	compressor	mol%	mole fraction
COND	air cooled condenser	N	rotational speed
COOL	air cooled cooler	P	pressure
CRF	capital recovery factor	Q	thermal power, MW
CSP	concentrated solar power	W	power, MW
CFD	computational fluid dynamics	wt%	mass fraction
DNI	direct normal irradiance	η	efficiency
EoS	equation of state	ρ	density
FOC	fixed operating costs	*Subscripts*	
HTF	heat transfer fluid	$_{boil}$	boiling point
ITD	internal temperature difference	$_{c}$	compressor
LCOE	levelized cost of electricity	$_{cond}$	air-cooled condenser
M	motor	$_{cool}$	air-cooled cooler
MITA	minimum internal temperature difference	$_{cr}$	critical point
PHE	primary heat exchanger	$_{des}$	design point parameter
PUMP	pump	$_{el}$	electrical

REC	recuperator	fan	air cooler/condenser fan
RPM	Revolutions per minute	HTF	heat transfer fluid
sCO_2	supercritical CO_2	i	value characteristic for a single air temperature
SM	solar multiple	limit	thermal limit
TCC	total capital cost	max	maximum
TES	thermal energy storage	mech	mechanical
TIT	turbine inlet temperature	melt	melting point
TURB	turbine	min	minimum
UA	heat exchanger conductance	net	net electrical value
VF	volume flow	off	off-design parameter
VFD	variable frequency drive	out	outlet from PHE
VOC	variable operating costs	p	pump
		PHE	primary heat exchanger in power cycle
		rec	receiver
		REC	recuperator
		t	turbine
		wf	working fluid

8.1. Introduction

Solar energy is a renewable resource with significant potential for energy transition. Currently, two main technologies convert solar energy to electricity: photovoltaic solar panels and concentrating solar power (CSP) plants. CSP plants have a higher levelized cost of electricity (LCOE) compared to both PV and wind power plants [1]. However, the use of CSP plants can be beneficial to the electric grid because of the dispatchability provided by the low-cost thermal energy storage technology (TES). The primary advantages of tower CSP plants over other CSP technologies are high power and high solar concentration, which can lead to a more compact balance of plant, lower specific costs, higher turbine inlet temperature (TIT), and higher electric efficiency.

Most new large-scale CSP projects use a central receiver tower with molten salt as HTF and TES with an installed capacity around 100 MW, while TES is 8-16 hours, making them very flexible throughout the day [2]. At the moment, commercial CSP plants use direct TES systems with solar salt and the steam Rankine cycle to generate electricity. At high TIT, closed carbon dioxide (CO_2) cycles are more thermally efficient than traditional steam Rankine ones and can reach more than 50% cycle efficiency at 800°C TIT [3]. Multiple CO_2 cycle layouts have been extensively studied in the past, starting with precompression and recompression in 1962 [4], simple recuperated, recompression, partial cooling, and partial cooling with improved regeneration cycles in 1969 [5], and different cycles with intercooling and reheating for nuclear application in 2004 [6]. New CSP plants use dry cooling systems; therefore, the cycle minimum temperature will be above the critical temperature of the CO_2, leading to non-condensing and fully supercritical CO_2 (sCO_2) cycles. This leads to (i) technical problems due to compression of sCO_2 near the critical point with varying ambient temperature (large variations in thermophysical properties, possible two-phase flow in the intake [7]) and (ii) efficiency penalty due to the high compression power.

The efficiency of closed sCO_2 cycles can be improved by using dopants with high critical parameters, moving from supercritical to transcritical cycles at the same minimum cycle temperature [8]. Thermal efficiency gains derived from the adoption of CO_2-based mixtures have been extensively investigated for N_2O_4 [9], SO_2 [10], $SiCl_4$ [11], C_6F_6, and $TiCl_4$ [12]. But at such high-temperature applications, only a few dopants meet the criteria of thermochemical stability and material compatibility. The $TiCl_4$ is highly reactive and is proven to be thermally stable only up to 500°C [13]. In the case of C_6F_6, N_2O_4, and SO_2, there are material compatibility issues that would require a more thorough analysis of alloys being used and their influence on the cost of equipment. For example, C_6F_6 reacts with stainless steel in the CO_2 mixture even at 500°C [14] and causes cracks in Inconel alloys' heat-affected zone [15], while N_2O_4 is very corrosive and decomposes in NO_2, NO, and O_2 [16]. Since stainless steels are the main material for primary heat exchanger (PHE) and recuperative systems using printed circuit heat exchanger (PCHE) at 550°C TIT, such dopants require deeper analysis of the costs of equipment. On the other hand, a silicon tetrachloride ($SiCl_4$) dopant has been experimentally investigated [11] and showed both good thermal stability and material compatibility [17] and techno-economic performance [18].

The operation of both sCO_2 and CO_2 mixture power cycles is significantly influenced by the minimum temperature. Air-cooled condensers (ACC), which are standard in modern designs and are planned for the next generation of CSP plants, have a significant influence on the power cycle and plant performance. Therefore, their design requires careful trade-off analysis to balance power cycle efficiency gains against capital costs. The approach temperature in the cooler/condenser in sCO_2 and CO_2 mixture cycles is usually assumed to be 15°C, the same as the internal temperature difference (ITD) in steam cycles, with an air design temperature that is not exceeded 94-96% of annual operating hours in the location [19]. Nevertheless, lower values may be preferable [20,21] due to the low cost of the condenser in the overall power cycle and its high influence on the power cycle efficiency. To capture the impact of design point assumptions on overall plant economics, a power cycle model sensitive to changes in ambient air temperature during operation is required.

Several papers have addressed sCO_2 and CO_2 mixture power cycles off-design performance. De La Calle et al. [22] focused on the off-design operation of the recompression cycle. The design point minimum cycle temperature was optimized with respect to the objective function, which was defined as a product of design point cycle electrical efficiency, annual cycle efficiency, and annual electrical energy generation drop factor. Results obtained for different locations showed that for Seville and Alice Springs the optimum cycle minimum temperature is around 36°C, while for Daggett around 39°C.

Neises [23] has described the recompression sCO_2 cycle off-design performance varying both ambient air temperature and HTF mass flow. He used simplified primary heat exchanger and recuperator models based on heat transfer coefficient ratios from [24,25], a cooler model considering only the changes in air-side heat exchange and pressure drop, along with Dyreby et al. [26,27] turbomachinery models. During off-design operation, the HTF outlet temperature was kept as close as possible to its design value to avoid exceeding material temperature limits, HTF system thermal fluctuation, over-design mass flow rates, and decreasing the TES capacity. Power cycle operation was considered with fixed and optimized compressor shaft speed using a variable frequency drive (VFD). In 2023, Neises [20] investigated the influence of design parameters (recuperator conductance, ambient design temperature, air cooler approach temperature, and air cooler fan power) on the LCOE. It was found that the lowest cost of electricity (as low as 79 USD/MWh) is obtained with the lowest ambient air design temperature, air cooler approach, and recuperator conductance, while cooler fan power has a lower effect. The storage capacity was fixed at 10 hours, with a solar multiple of 2.4 with a cycle output of 50 MWe. The authors mention that adding TES capacity, especially to the cold ambient temperature designs, could be beneficial and make use of the higher cycle efficiency.

Ma et al. [28] presented an off-design model for an improved recompression power sCO_2 cycle using a simplified heat exchangers modeling approach and the Dyreby [27] compressor model. They investigated the influence of molten salt flow rate and temperature along with the main compressor inlet temperature on the cycle performance.

Chen et al. [29] used the same approach to modeling heat exchangers and turbomachinery to compare different sCO_2 cycle configurations' on-design and off-design performances in a particle based CSP plant. In 2023, Chen et al. [30] found that for different locations and minimum cycle temperatures, the lowest LCOE for the simple sCO_2 cycle is reached at the lowest TIT among 650, 750, and 850°C.

For two locations with the average annual temperature of around 20°C, the lowest LCOE is reached at a cycle minimum temperature of 40°C and ambient air design temperature of 35°C. At the same time, their results suggest that for the locations with 14°C and 5°C average annual temperatures, the optimal minimum temperature is 33°C and the ambient air design temperature is 25°C. Therefore, for all locations, the smallest cooler approach considered (5°C and 8°C respectively) yields the best LCOE (68-88 USD/MWh), while the cycle minimum temperature correlates with the location's average ambient air temperature. At the same time, the increase in solar resource from 6.4 to 9.1 kWh/m^2 decreases the minimum LCOE from 88.5 to 68.2 EUR/MWh, while the optimum cycle design conditions remain the same.

Yang et al. [31] investigated the simple sCO_2 cycle with varying compressor inlet temperatures and various power demand curves together with different optimization criteria. The power cycle off-design performance was optimized to reach maximum efficiency using a genetic algorithm. The minimum LCOE was found at the minimum compressor inlet temperature of 35°C. At stable power demand, the corresponding optimum solar multiple and TES were 2.89 and 14.4 hours for Daggett (128 USD/MWh), 3.4 and 11.6 for Delingha (140 USD/MWh), and 3.09 and 15.1 for Rajhastan (167 USD/MWh).

Heller et al. [32] have investigated the conventional steam cycle and ten different sCO_2 cycle layouts with multi tower particle receiver system at different TIT and found that the lowest LCOE (around 105 USD/MWh) among the sCO_2 cycles is obtained by the simple recuperated cycles without reheat and intercooling. In 2026 Heller et al. [33] expanded the investigation with updated primary heat exchanger and solar system cost correlations, equipment cost sensitivity, and power cycle off-design operation at an ambient air design temperature of 19°C. Both SM and TES size were optimized to minimize LCOE, with the steam Rankine cycle showing the best performance. Among the sCO_2 cycles, the basic ones, including the simple recuperated, were found to have the lowest LCOE at 550°C TIT (around 75 USD/MWh).

Unlike sCO_2 cycles, CO_2 mixtures undergo condensation in the recuperator and condenser, introducing two-phase heat transfer mechanisms that require more detailed heat exchanger modeling. Furthermore, they utilize a pump instead of a compressor, reducing their sensitivity to ambient conditions. Therefore, CO_2 mixture cycles require distinct design and off-design modeling approaches compared to sCO_2 power cycles.

Morosini et al. [34] investigated the performance of a simple recuperated cycle using a CO_2 + C_6F_6 mixture under varying ambient air temperature and input power. They used results of CFD analysis to model the turbine performance, while for the pump, proprietary characteristics were used. The recuperator and condenser were modeled in detail, while for PHE a simplified approach was developed. The results indicate maximum efficiency at ambient air temperature around 0°C and 100% input power while keeping the HTF outlet temperature as close as possible to the design point.

Rodríguez-de Arriba et al. [35] studied a recompression cycle using an 80% CO_2 and 20% SO_2 mixture at different net output power levels with different air-cooled condenser (without VFD, with 1 VFD, and all fans with VFD) and power cycle (constant TIT, TOT and HTF outlet temperature) operation strategies. They also used simplified recuperator and primary heat exchanger models along with a detailed condenser model, pump, and recompressor performance maps supplied by the manufacturer, and a turbine performance model based on CFD analysis. Crespi et al. in 2024 [36] further examined the same CO_2/SO_2 mixture cycle, varying the air temperature with various condenser and power cycle operation strategies. The best efficiency and NPV were obtained by using VFD for all condenser fans while keeping HTF outlet temperature constant at air temperatures above the design point.

This paper aims to use detailed validated models for both sCO_2 and CO_2 mixture cycle components to characterize their design and off-design performance. The simple recuperated power cycle layout is chosen for analysis due to its simplicity and ability to reach the lowest or second lowest LCOE both with sCO_2 and CO_2 mixture according to the following works [18,33,37–39]. The control strategy chosen allows the CSP plant to operate within design conditions for both the HTF pump and receiver while keeping the power cycle parameters within bounds with the aim of maintaining high electrical efficiency. During off-design operation, the compressor/pump rotational speed is optimized for both cycles, as is the minimum cycle pressure for the sCO_2 cycle. The techno-economic analysis is carried out using models for capital cost and annual CSP plant performance, which are based on previous validated work to determine energy generation, capital cost, and LCOE.

The main contribution of this paper is the study of how ambient air design temperature and cooler/condenser approach temperature influence the levelized cost of electricity (LCOE) for both the sCO_2 and CO_2 mixture cycles using detailed models of recuperator and cooler/condenser with the most promising tube layout. For the recuperator and cooler/condenser, detailed sizing is performed since the condensation of working fluid limits the use of simplified models, which consider only convective heat transfer. Simultaneously, the solar multiple and TES sizes are optimized, and the results are compared to constant SM and TES. This enables the economic optimization of the cooler/condenser design point for both the most economically effective CO_2 mixture cycle and the second-best sCO_2 cycle at constant and optimum SM and TES sizes.

The remainder of this paper is organized as follows. The Methods section presents the location data, the power cycle modeling at design conditions, and the design and off-design modeling of recuperator, heat rejection unit, primary heat exchanger, and turbomachinery, followed by the off-design modeling of the power cycle and the overall CSP plant model. The Results section then discusses the power cycle performance at both design and off-design conditions, the behavior of individual CSP plant components, and a comprehensive techno-economic analysis of the system. Finally, the paper concludes with the main findings and their implications, outlining potential directions for future investigation and improvement.

8.2. Methods

The overall modeling flow implemented in the paper is presented in the Figure 8.1. First, the power cycle modeling and optimization is done in Aspen Plus [40]. The PHE working fluid outlet temperature and thermal power is then used to design the solar field, receiver, and thermal energy storage in the CSP plant. The sCO_2 properties are calculated in Aspen Plus using REFPROP [41] and in MATLAB [42] using CoolProp [43] with the same correlations. For CO_2 mixture, property tables are generated in Aspen Plus and then used in MATLAB for interpolation during calculations. In MATLAB, the design of a recuperator using a printed circuit heat exchanger and air-cooled cooler/condenser is done. After that, the off-design performance of the cycle is calculated at different air temperatures to obtain the efficiency, net power, HTF flow, and PHE HTF outlet temperature curves. The off-design curves are first used to calculate the receiver and HTF pump off-design performance maps and then to calculate the annual CSP plant performance. The power cycles design parameters from Aspen Plus together with the results of recuperator and cooler/condenser designs from MATLAB are used to calculate the power cycle cost. The whole CSP plant cost is then calculated within the CSP plant model, followed by LCOE. The SM and TES size are optimized for each power cycle, and the optimum air design temperature together with the optimum cooler/condenser approach temperature is determined. Current analysis is limited to LCOE as the main economic indicator. While CSP plants offer distinct advantages in dispatchability that are not fully captured by the LCOE, the primary objective of this study is to identify optimal design parameters. Metrics such as net present value and internal rate of return are dependent on highly variable electricity price profiles. On the other hand, employing a standard price profile yields a results in a distribution consistent with that of LCOE [20].

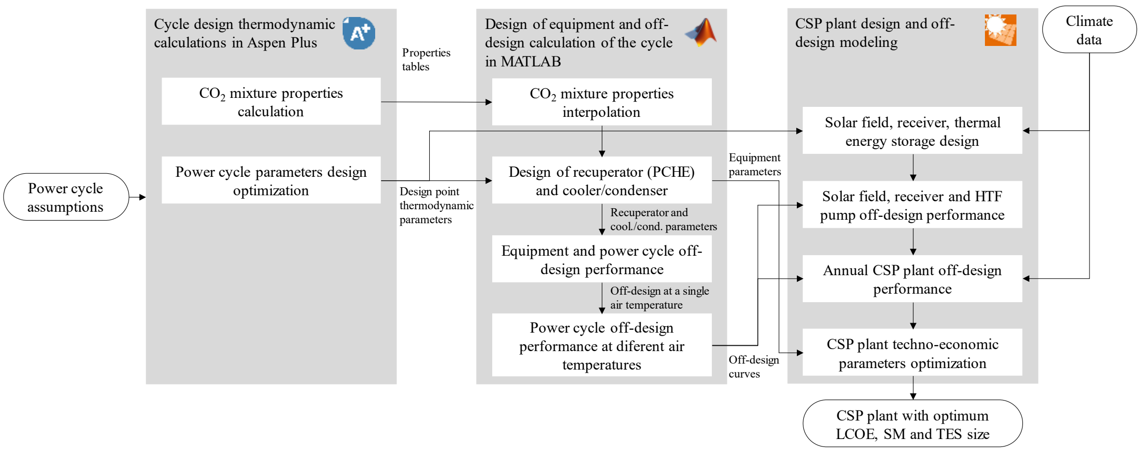

Figure 8.1. Overall paper framework

8.2.1. Location data

The CSP plant is placed in Seville, Spain: typical meteorological year data was taken from PVGIS-SARAH3 2005-2023 [44] for 37.40°N, 6.01°W following the paper [45]. As shown in Figure 8.2, the maximum direct normal irradiance (DNI) in the location is 984 W/m^2, while the temperature varies between 0.65°C and 40.19°C. The mean daily value of DNI is 6.2 kWh/m² with 95% DNI at 880 W/m², an average ambient temperature of 19°C, and wind velocity at 2.3 m/s. These values are quite consistent with the average DNI in the location, which was 5.68 kWh/m² based on the data from 2000-2012 [45], while NASA SSE (1983-1993) gave a value of 6.18 kWh/m^2. These two values, however, are both higher than 4.86 kWh/m², characteristic of the data usually used for the location from typical meteorological year data available in System Advisor Model (SAM) [46].

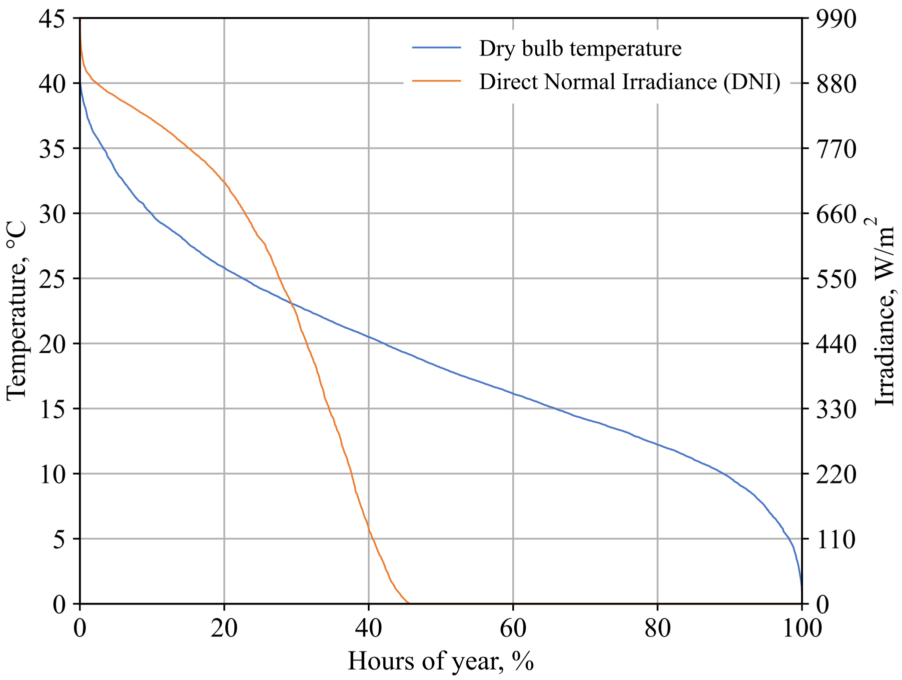

Figure 8.2. Duration curves of dry bulb temperature and DNI in the location.

8.2.2. Power cycle design point modeling

Both sCO_2 and CO_2 mixture power cycles were first modeled at the design point to establish a consistent basis for performance comparison. The main parameters of the considered fluids are shown in Table 8.1 [17,47]. The sCO_2 cycle is calculated using the Span-Wagner EoS [48] with transport properties calculated using REFPROP [41]. The binary interaction parameter for the CO_2+$SiCl_4$ mixture using the Peng-Robinson EoS [49] is equal to 0.06098 [11], while for transport properties, the TRAPP model is used [50]. Both cycles at the design point were modeled using Aspen Plus V14 [40], using previously validated models [51].

Table 8.1. Parameters of considered working fluids

CAS	Formula	T_{melt}, °C	T_{boil}, °C	T_{cr}, °C	P_{cr}, bar	GWP	ODP	NFPA 704			T_{limit}, °C
								H	F	R	
124-38-9	CO_2	-57	-78	31	73.8	1	0	2	0	0	>700
10026-04-7	$SiCl_4$	-69	58	233.9	35.9	0	0	3	0	2-w	>650

H - health hazard; F – flammability hazard; R – instability/reactivity hazard.

The simple recuperated power cycles layouts are shown in Figure 8.3 using sCO_2 (a) and CO_2+$SiCl_4$ mixture (b) as working fluids. Both cycles are shown on the T-s diagram in Figure 8.3c with a 50°C cycle minimum temperature. Due to the transcritical nature, the CO_2 mixture cycle has compression in the liquid phase, significantly reducing the work, as can be seen in the T-s diagram.

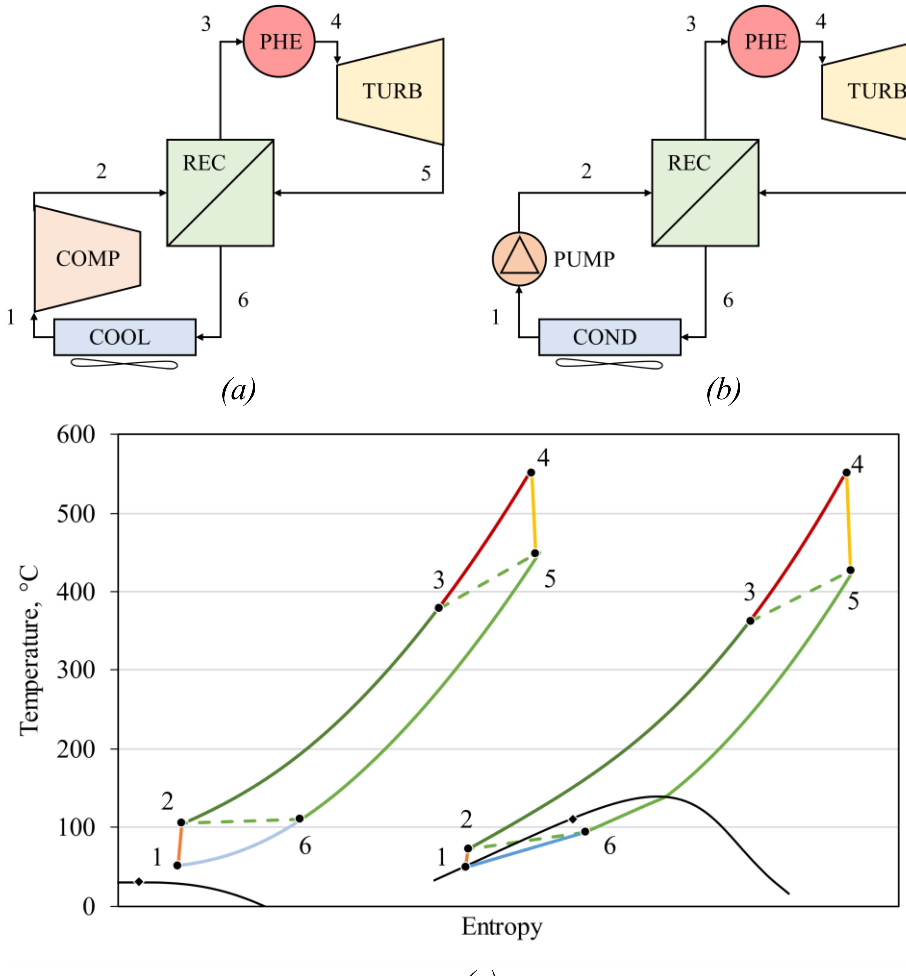

Figure 8.3. Layout of recuperated simple supercritical (a) and transcritical (b) cycles considered in the analysis. T-s diagram (c) of the cycles: black lines are saturation domes with diamonds showing critical points. PHE – primary heat exchanger; TURB – turbine; REC – recuperator; COMP – compressor; PUMP – pump; COOL – air-cooled cooler; COND – air-cooled condenser.

All power cycles are modeled according to assumptions presented in Table 8.2 [12,37]. The recuperator relative pressure drop is assumed to be 3%/0.6% for the hot/cold side, which gives an absolute pressure drop of 1.5 bar for the cold and around 3 bar for the hot side, similar to the optimum values proposed in literature [52,53].

Table 8.2. Power cycles design point assumptions

Parameter	Value
TIT, °C	550
Max pressure in the cycle P_{max}, bar	250
Cycle minimum temperature T_{min}, °C	35/40/45/50
Cooler/condenser approach temperature $\Delta T_{cool/cond}$, °C	5/10/15
Recuperators MITA, °C	5
Cooler/condenser, PHE working fluid Δp, %	2
Recuperators hot/cold side Δp, %	3/0.6
Turbine isentropic efficiency, %	92
Pump/compressor isentropic efficiency, %	88
Motor/generator electrical efficiency, %	97
Turbomachines mechanical efficiency, %	99

Since the cooler/condenser fan power can vary based on its design point, the electrical efficiency of the cycle (calculated according to equation (8.4)) is used for comparison of different power cycles and optimization purposes. It assumes separate shafts for the turbine, pumps, and compressors and neglects the cooler/condenser fan power.

$$\eta_{cycle,el} = \frac{W_{cycle,el}}{Q_{PHE}} = \frac{W_t \cdot \eta_{mech} \cdot \eta_{el} - (W_p + W_c)/(\eta_{mech} \cdot \eta_{el})}{Q_{PHE}} \tag{8.4}$$

where $W_{cycle,el}$ – cycle electrical power, MWe; Q_{PHE} – primary heat exchanger thermal power, MWth; W_t – turbine power, MW; W_p – pump power, MW; W_c – compressor power, MW; η_{mech} – mechanical efficiency, %; η_{el} – generator/motor electrical efficiency, %.

For both sCO_2 and CO_2+$SiCl_4$ mixture cycles, the design point electrical efficiency is optimized by varying minimum cycle pressure and the mixture composition, respectively.

8.2.3. Power cycle equipment: design and off-design modeling

All sizing and off-design modeling of power cycle equipment was carried out using MATLAB R2023b [42]. The air and sCO_2 properties were calculated using CoolProp [43], which uses the same correlations as REFPROP [41]. For each CO_2 mixture composition, tables of properties are made in Aspen Plus based on a pressure and temperature grid with the 2 bar/2°C step below and 20 bar/20°C above cricondenbar and cricondentherm. The interpolation errors are assessed using the 80%CO_2+20%$SiCl_4$ molar mixture with the average absolute deviation for pressure-temperature envelope interpolation around 1% and for supercritical density and transport properties below 0.6% (more information is available in Supplementary materials A). It should be noted that since the minimum and maximum pressures of the cycle are quite far from the critical point both at design and off-design conditions, the influence of interpolation accuracy in the critical point vicinity will not influence the calculation results.

The results of power cycles design point calculations are used for equipment design. For each minimum cycle temperature, three cooler/condenser approach temperatures are assumed (15, 10, and 5°C), which brings the total number of design points to 27. For the PHE, turbine, compressor, and pump, simplified approaches are used to describe the off-design performance. For the recuperator, cooler, and condenser, detailed sizing is performed, since the condensation of working fluid limits the use of simplified models that consider only convective heat transfer. The equipment design and off-design models are then used in off-design power cycle calculations.

8.2.3.1. Recuperator

For recuperator, the printed circuit heat exchanger is chosen, since it is the most promising design for sCO_2 and CO_2 mixture power cycles [54,55]. The single-phase heat transfer coefficient is calculated using the Gnielinski correlation [56], while for two phases the Cavallini model is used [57] with the Bell and Ghaly correction [58]. Friction pressure drops are calculated using Chen explicit correlation [59] for single-phase flows and Del Col model [60] for two-phase flows (Supplementary materials D). Total pressure drops included friction, acceleration, and local losses. Local losses coefficients for simplicity are assumed to be 0.5 for the tubesheet inlet/outlet, 0.2 for the header outlet, and 0.8 for the header inlet [61].

For the design point, a pure counter-flow central section is modeled with 500 segments, followed by cross-flow inlet and outlet 90° segments with headers [62]. All the exchanged heat is split into segments, and then, for each segment, the length is determined using the LMTD method and the overall heat transfer coefficient. For cross-flow sections, the length of segments is adjusted by the efficiency of cross-flow compared to counter-flow. The recuperator is made of SS316 with properties from [63] (Supplementary materials B). Single block size is assumed within 1.5 m × 0.6 m × 0.6 m with mechanical design done according to [64]. Design pressure and temperature for mechanical calculations are chosen to be 10% and 40°C [35] above the conditions from thermodynamic design point calculations. Fouling is assumed to be $8.8 \cdot 10^{-5}$ $m^2 \cdot K/W$ for both sides [65]. After a sensitivity analysis, the number of segments for off-design calculations is chosen to be 10 for counterflow sections, while each cross-flow is treated as a single segment. The examples of PCHE convergence progress can be seen in Supplementary materials D.

Regarding the economics, one of the ways to calculate the cost of PCHE is through its mass [66,67]. However, the cost per kg varies significantly from 19.8 to 80.4 USD/kg [67]. Based on average cost and calculated mass, the resulting PCHE costs are found to be just 35-64% of Weiland et al. [68] for PCHEs with straight channels. Therefore, to be more conservative, in this work correlations from Weiland et al. [68] are used to determine the cost of recuperators.

8.2.3.2. Heat rejection unit (cooler/condenser)

A direct air-cooled heat rejection unit is considered in this work because it allows better efficiency and lower cost [69]. The air-side heat transfer coefficient is calculated using Briggs&Young's correlations, while for the pressure drop the Robinson&Briggs correlation is used [70]. On the hot side the same correlations are implemented as in the recuperator. Fouling is assumed to be $8.8 \cdot 10^{-5}$ $m^2 \cdot K/W$ for the hot side [65] and $8.8 \cdot 10^{-4}$ $m^2 \cdot K/W$ for the cold side [71]. Fan efficiency is assumed to be 65%, including the motor and VFD losses: this is consistent with the range found in literature, which is between 68% in [72] and 60% in [23]. The calculated air-side tube bank pressure drop is increased by 20% to account for other friction losses [70,72].

For the pure sCO_2, the Krasnoshchekov-Protopopov [73] correlation provides more accurate results for supercritical conditions close to the critical point [74,75] compared to the widespread Gnielinski [56] one. Therefore, it is recommended for sCO_2 coolers [72,76]. However, the average change in the Nusselt number is around 4-6% on the hot side (Supplementary materials F), which doesn't have a significant effect on the performance, since the main limiting factor for heat exchange in air-cooled coolers is the air-side heat transfer. Due to this, in some literature, only air-side heat transfer is considered for off-design power cycle models [23]. This effect leads to a small difference between the wall and bulk temperature of the working fluid, thus minimizing the effect of property changes and effectively reducing the Krasnoshchekov-Protopopov to Gnielinski correlation. To reduce model complexity and execution time, the Gnielinski correlation is chosen in this work.

The cooler/condenser is modeled as parallel banks of tubes, each divided into 20 segments. The tube internal diameter is assumed to be 20.76 mm, and the external one is 26.8 mm in a staggered arrangement with 66.7 mm transversal and 57.7 mm longitudinal pitches with aluminum fins with 65% efficiency, 15.9 mm height, 0.12 mm thickness, and 2.52 mm spacing [72]. The layout chosen in this work is 7 tubes in 3 rows in 3-3-1 tubes per pass configuration, which proved to be more beneficial for pressure drops [77], while air velocity is assumed to be 3 m/s at the design point [72]. Validation of the developed model is carried out against results from [34,72,77] and is presented in the Supplementary materials F. The cost of the air-cooled condenser is calculated according to Weiland et al. [68].

8.2.3.3. Primary heat exchanger

The primary heat exchanger is assumed to be of shell and tube type. During the design phase heat exchanged in PHE is split into segments with design point conductance (UA) and the portion of total pressure drop determined for each segment. A comparison of the main models used in literature for the PHE off-design modeling is shown in Figure 8.4 with correlations from Hamilton et al. [78], Morosini et al. [34] and Neises [23] which is based on the approach proposed by Hoopes [24]. For comparison, two different baffle designs are simulated in a rigorous commercial program at equal fractions of mass flow [79,80]. A simplified correlation is used for calculating the normalized overall HTC, similar to the method used in [34]:

$$\frac{U_{off}}{U_{des}} = \left(\frac{\dot{m}_{HTF,off} \cdot \dot{m}_{wf,off}}{\dot{m}_{HTF,des} \cdot \dot{m}_{wf,des}}\right)^{0.25653} \tag{8.5}$$

where $\dot{m}$ – mass flow; U – overall heat transfer coefficient; $_{des}$ and $_{off}$ subscripts indicate design and off-design point parameter respectively.

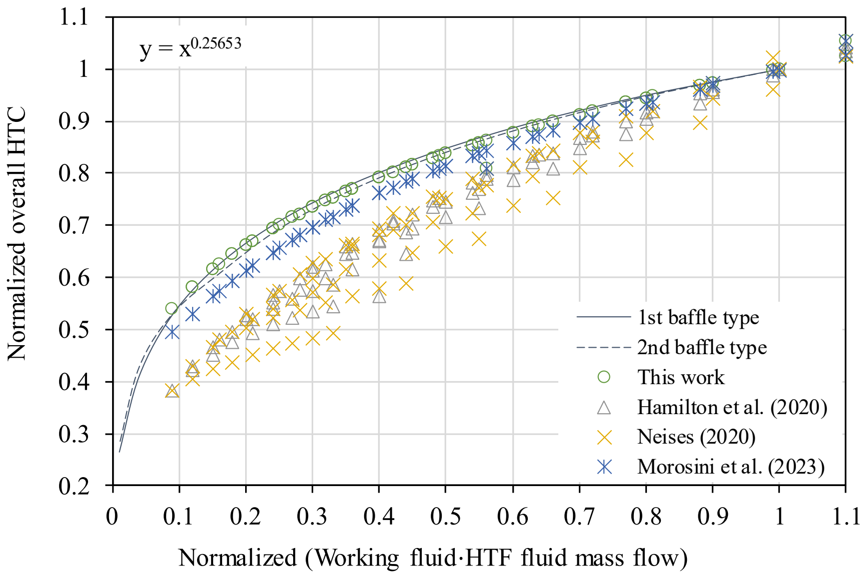

Figure 8.4. Overall HTC sensitivity to mass flow rate

The off-design pressure drop is calculated for each segment based on the ratios of mass flows and densities as in [23] according to the equation:

$$\Delta P_{off} = \Delta P_{des} \left(\frac{\dot{m}_{off}}{\dot{m}_{des}}\right)^2 \frac{\rho_{des}}{\rho_{off}} \tag{8.6}$$

where ΔP – pressure drop; $\dot{m}$ – mass flow; ρ – density.

During off-design modeling, all segments in PHE are iteratively converged. The number of segments was chosen to be 8 based on the sensitivity study carried out (more details are available in the Supplementary materials C).

8.2.3.4. Turbine, compressor and pump

In this paper, simplified approaches based on dimensionless numbers are adopted for the off-design performance characterization of turbomachines. They do not require extensive equipment design, which is outside of this paper scope, and allow for fast preliminary cycle screening.

To model the off-design turbine performance, a comparison of both steam and sCO_2 off-design turbine correlations [23,81–84] was carried out against the CO_2 mixture multistage axial turbine CFD results [34,85]. The comparison of efficiency and pressure ratio curves is shown in Figure 8.5 (a detailed analysis is available in the Supplementary materials E).The correlation as described by Neises [23], based on the Dyreby model [26,27] with a velocity ratio of 0.7476, is chosen in this work for being the closest to the CFD results. Moreover, the pressure-mass flow relationship is modeled using the Stodola formula [86].

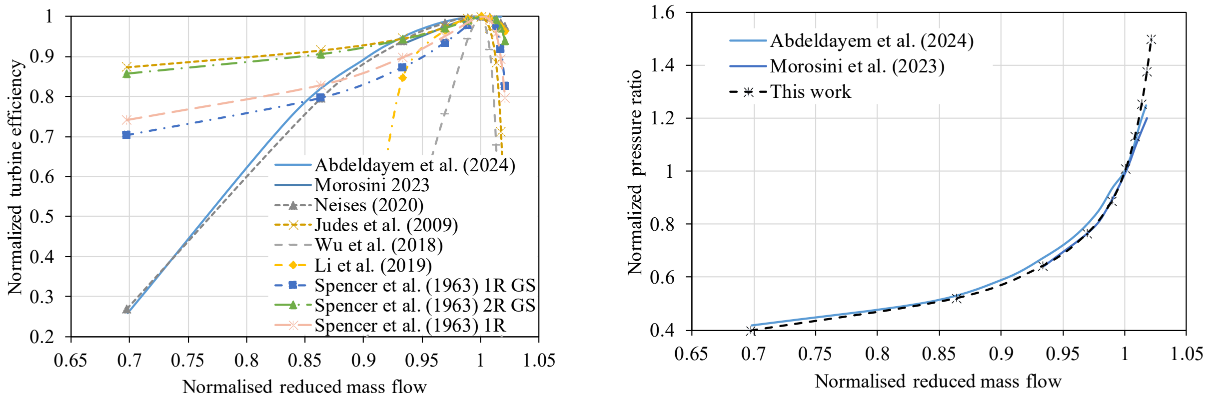

(a) *(b)*

Figure 8.5. Turbine off-design efficiency models (a) and pressure ratio (b) comparison

The compressor model is also taken from the same works [23,26,27] using an optimum isentropic head coefficient of 0.4618 [87]. The pump model is adapted from [88] (more details available in Supplementary materials E). The compressor and pump performance curves in dimensionless coordinates are shown in Figure 8.6.

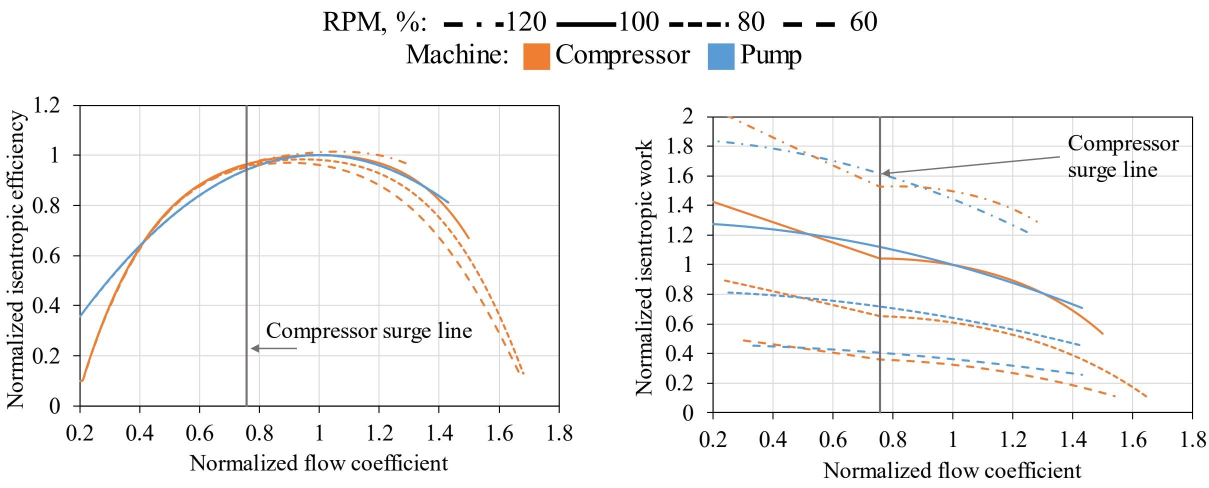

(a) *(b)*

Figure 8.6. Compressor and pump normalized isentropic efficiency (a) and normalized isentropic work (b) curves

8.2.4. Power cycle off-design modeling

In addition to the cycle electrical efficiency, the cycle electrical net efficiency is calculated according to (8.7) in order to account for the cooler/condenser fan power in design and off-design conditions:

$$\eta_{cycle,net} = \frac{W_{cycle,net}}{Q_{PHE}} = \frac{W_{cycle,el} - W_{fan}}{Q_{PHE}} = \frac{W_t \cdot \eta_{mech} \cdot \eta_{el} - (W_p + W_c)/(\eta_{mech} \cdot \eta_{el}) - W_{fan}}{Q_{PHE}} \tag{8.7}$$

where $\eta_{cycle,net}$ – cycle net electrical efficiency, %; $W_{cycle,net}$ – cycle net power, MWe; W_{fan} – condenser/cooler fan power, MW.

The power cycle layout with varied and controlled parameters is shown in Figure 8.7. An operation with maximum and minimum sliding pressure is considered. Therefore, the only two ways to control the cycle are the pump/compressor and the cooler/condenser fan rotation speeds. Pump/compressor rotation speed allows control of the flow rate of working fluid in the power cycle, while cooler/condenser fan speed control influences the cycle minimum temperature (Table 8.3).

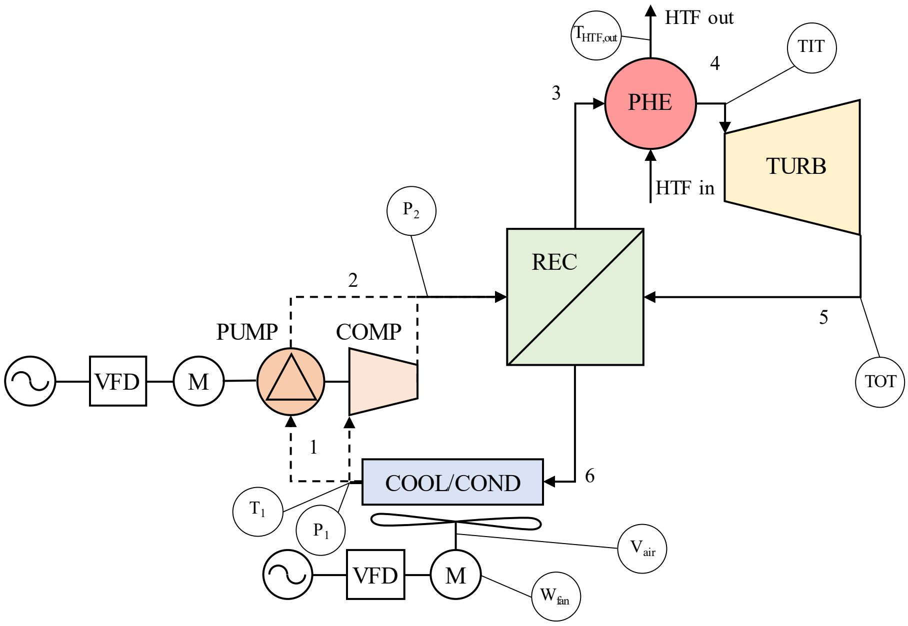

Figure 8.7. Power cycle layout with controlled and varied parameters. VFD – variable frequency drive; M – motor.

Table 8.3. Power cycle control organs

Control organ	Controlled variable
Condenser/cooler fan rotational speed	Cycle minimum temperature (T_1/T_{min})
Pump/compressor rotational speed	Working fluid mass flow rate

Limitations of the cycle main parameters are shown in Table 8.4. In most studies $T_{HTF,out}$ is kept constant [23]; however, already in existing plants, "during transient solar conditions, both the cold tank and the hot tank can receive salt at temperatures as much as 100°C above or below the bulk inventory temperature" [89]. Therefore, in the current study, $T_{HTF,out}$ is kept equal to or below the design point to keep the mass flow to the receiver within the design conditions, thus having no impact on the receiver and HTF pump operation. For the sCO_2 cycle, the minimum pressure is kept above 74 bar, while the minimum temperature is 32°C [23]. For the CO_2+$SiCl_4$ mixture cycle, the minimum temperature and pressure were not specified since the triple point of both CO_2 (-56.6°C) and $SiCl_4$ (-87.5°C) is significantly below the minimum air temperature in the location. All cooler/condenser fans are assumed to be equipped with VFD, which guarantees higher thermodynamic and economic performance [36]. The maximum fan power was limited to 105% [36], since VFD and fan motor are designed for continues power output and can produce up to 110% for limited amount of time [90]

Table 8.4. Boundary conditions for power cycles off-design performance

Parameter	Minimum	Design point	Maximum	Source
TIT	-	550°C	+0°C	-
TOT	-	calculated	+40°C	[35]
$T_{HTF,out}$	290°C	calculated	+0°C	-
P_{max} (P_2)	P_{crit} (for CO_2 mixture)	250 bar	+5%	[36]
P_{min} (P_1)	74 bar and $T_{min} \geq 32°C$ (for sCO_2)	optimised	-	[23]
W_{fan}	-	calculated	+5%	[36]

The off-design power cycle calculation algorithm done in MATLAB is shown in Figure 8.8. After loading power cycle component data and air temperature, the program iteratively calculates off-design conditions in the compressor/pump, PHE, and turbine until the mass flow rate is converged, after which recuperator (PCHE) and cooler/condenser off-design operation is calculated. After the cycle heat balance error is reduced below 0.01%, either the TIT or HTF outlet temperature is targeted by changing either the compressor rotation speed or HTF mass flow iteratively. Once both heat balance and cycle operation conditions are met, the off-design cycle parameters for the specific air temperature are obtained. The cooler/condenser air velocity and minimum cycle pressure optimization for sCO_2 cycle are done separately.

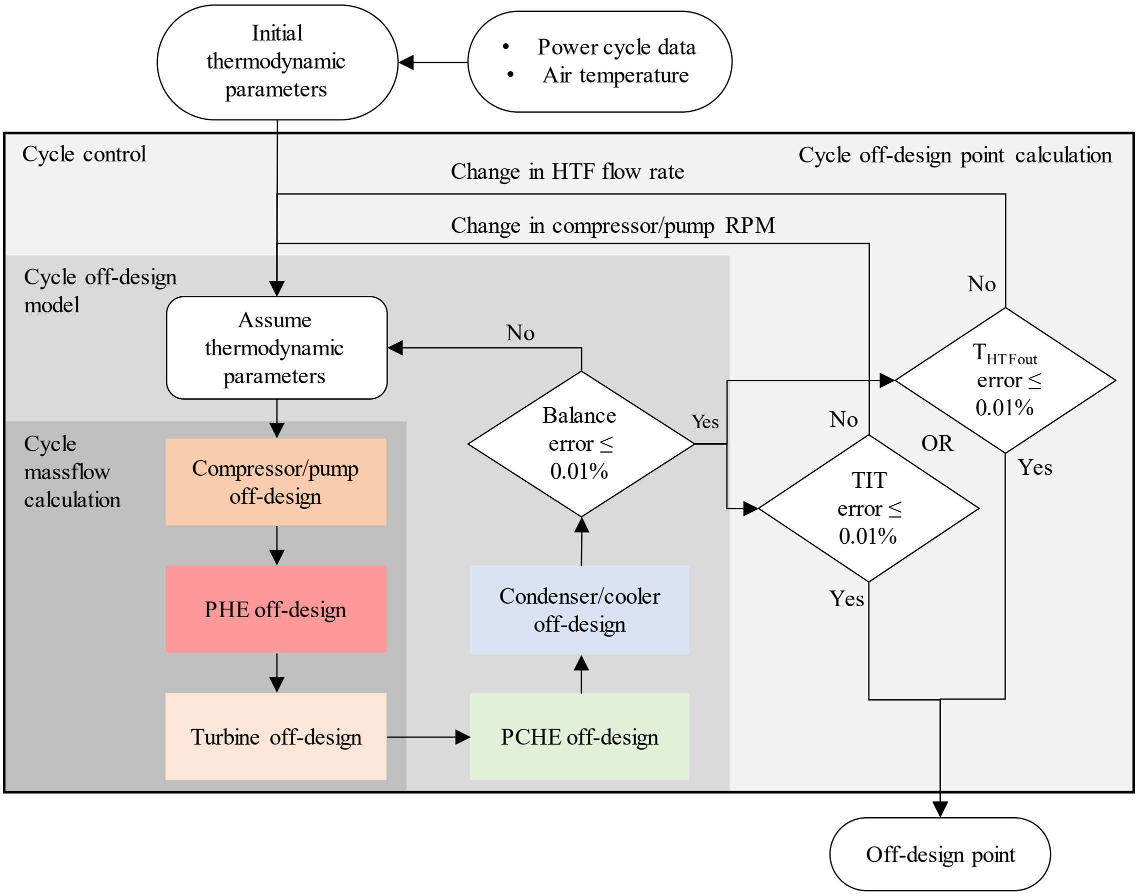

Figure 8.8. Power cycle off-design calculation procedure and control for a single air temperature

For the sCO_2 cycle, the minimum pressure should be optimized to reach maximum net cycle electrical efficiency. To reduce computational time for each cycle, minimum cycle pressure is first optimized while keeping the cooler fan air velocity constant to reach maximum net cycle electrical efficiency. From the results, the relationship between minimum cycle temperature and pressure is obtained and used for all off-design calculations.

To calculate the final power cycle operation curve at various air temperatures, the algorithm in Figure 8.9 is adapted to reduce the calculation time. At air temperatures below the design, TIT is kept constant to obtain higher power output and efficiency, while at air temperatures above the design, the HTF outlet temperature is kept constant. Therefore, for all air temperatures, TIT and $T_{HTF,out}$ remain equal to or below their design values, ensuring the safe operation of the power cycle and CSP plant. For air temperatures below the design point, a hybrid strategy is adapted for minimum cycle temperature/pressure and condenser/cooler control to ensure maximum performance [36]. Initially, for all considered air temperatures, power cycle operation is calculated with constant air cooler/condenser air velocity and TIT, after which all temperatures are divided into 3 groups: where fan power is above 105% of design ($T_{air,off,i}<T_{air,fan}$), where air temperature is above the design values ($T_{air,fan}>T_{air,des}$), and the rest. For the first and second groups the air cooler/condenser is assumed to work at maximum power, but in the first case, TIT is kept at design, while in the latter, the HTF outlet temperature is fixed at the design value by varying the HTF mass flow and keeping the compressor/pump RPM at the design point. The third group is calculated with air velocity in the cooler/condenser and TIT equal to the design value. These three control modes are summarized below:

1. If $T_{air,off,i}<T_{air,fan}$ then $W_{fan,off,i}$ is fixed at 105%$W_{fan,des}$ (or if $T_{min,off,i}<32°C$ for sCO_2 cycle then $T_{min,off,i}$ = 32°C) and TIT is fixed at design value.
2. If $T_{air,fan}>T_{air,des}$ then $W_{fan,off,i}$ is fixed at 105%$W_{fan,des}$ and T_{HTFout} is fixed at design value.
3. In the case of the rest of air temperatures $V_{air,off}$ (or if $T_{min,off,i}<32°C$ for sCO_2 cycle then $T_{min,off,i}$ = 32°C) and TIT are fixed at design value.

The maximum ambient air design temperature is 45°C since the location dry bulb temperatures can exceed 40°C.

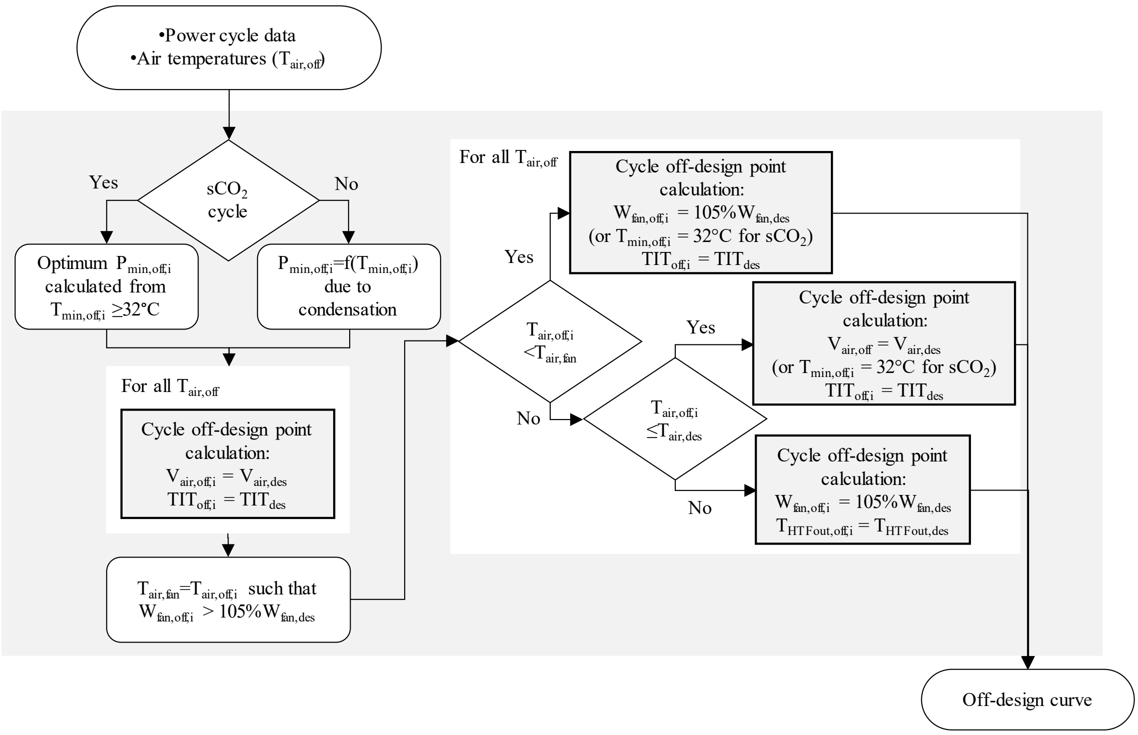

Figure 8.9. Algorithm for power cycle off-design calculation at different air temperatures

It is worth mentioning that in the case of the sCO_2 power cycle, the cycle minimum pressure will be changed by changing the amount of CO_2 in the circuit. In the case of CO_2 mixture at design conditions, around 80% of the cycle working fluid is present in the condenser, while with variation of both air and minimum cycle temperature, fluid inventory will change by around 20%, mainly due to a change in the amount stored in the condenser [91]. Therefore, for both cycles to accommodate the changes in the ambient air and cycle minimum temperatures, an inventory system is needed to vary the amount of fluid circulated. The inventory system will require additional vessels and compressors/pumps, but it will not significantly affect the capital cost since the vessels will be quite small and done from carbon steel. For example, for a 10 MWe recompression cycle around a 5 m^3 vessel with operating parameters varying in the 40-100°C and 80-180 bar range is required [92]. Therefore, this system will have minimal impact on the cost, power output, and operability limits and was considered out of scope for this article. It must, however, be taken into consideration when the basic design of CO_2 and CO_2 mixture power cycles is being done.

Another important aspect is the working fluid composition change during operation. According to Illyés et al. [93], mixture composition changes of up to 2% were observed in the experimental CO_2 mixture facility due to gas and liquid separation and liquid holdup. In the current simple recuperated CO_2+$SiCl_4$ mixture cycle, such a change will not significantly affect the operation and performance since the optimal compositions have critical points far from the cycle minimum temperature. This leads to small changes in condensation pressure and liquid density and therefore a small effect on the components operation and overall efficiency of the power cycle, as can be seen in Figure 8.10. Furthermore, the design of the equipment, specifically the recuperator, condenser, and pump, must prevent phase separation and fluid holdup.

8.2.5. Concentrated solar power plant model

The CSP plant model employed in this study was previously presented in [18], including validation of both the receiver and the overall plant performance. The main CSP plant assumptions are presented in Table 8.5, while for a complete list of assumptions, readers are referred to aforementioned work and its supplementary material. In the following analysis, the same assumptions are applied unless explicitly stated otherwise. The main changes that have been implemented to the model are:

4. The PHE cost model was updated based on [54], while the cost of other power cycle equipment is calculated based on Weiland et al. [68] (correlations are available in Supplementary materials H).
5. Cold tank temperature was allowed to vary due to the changes in the HTF outlet temperature from the cycle PHE, but it was assumed to be equal to the design condition at the beginning of the year.
6. Receiver and HTF pump operation maps are made based on both receiver input power and HTF inlet temperature to account for changes in the cold storage tank temperature.
7. Cycle power output, HTF flow to the PHE, and HTF outlet temperature are determined by the power cycle off-design model results.

An initial solar multiple (SM) of 2.8 and TES size of 13 hours is assumed based on results of previous works for similar locations, configurations, and mixtures [37,94]. The initial PHE thermal power is assumed to be 280 MWth to get the net power around 100 MWe [95], which leads to receiver power of 784 MWth at the design point.

Table 8.5. Concentrated solar power plant model design assumptions

Parameter	Value
CSP plant location	Sevilla, Spain
Design point DNI, W/m^2	880
Average dry bulb temperature, °C	19.0
Average wind speed, m/s	2.3
Solar field design power, MWth	784
Tower height, m	220
Receiver dimensions Diameter x Height, m	19.2x22.1
HTF/TES fluid	Solar salt
Sun design point location	Noon at summer solstice
Heliostat dimensions, m	12.2x12.2
Heliostat reflectivity and solar field availability, %	95
Receiver tube absorptivity and emissivity, %	94 and 84
ΔT between HTF/TES and TES/power cycle fluid, °C	20
Initial solar multiple (SM)	2.8
Initial TES size, h	13

The receiver dimensions are scaled from [95] to maintain the same maximum flux density. The number of flow paths, panels, and tube diameters of each receiver was chosen to maximize fictitious power [18,96]:

$$Q_{fictitious} = Q_{rec,output} - \frac{W_{p,HTF}}{\eta_{cycle,el}} \tag{8.8}$$

where $Q_{fictitious}$ – receiver fictitious power, MWth; $Q_{rec,output}$ – receiver output power, MWth; $W_{p,HTF}$ – receiver HTF pump power, MWe; $\eta_{cycle,el}$ – cycle electrical efficiency according to (8.4), %.

For SM optimization, the size of the solar field and receiver is kept constant while the PHE thermal power is varied. The TES size is optimized, changing the hours of storage needed for the power cycle nominal thermal input. The nominal CSP plant power was calculated considering the net power of the cycle and HTF pumps power according to equation (8.9), while the capacity factor was calculated using equation (8.10):

$$W_{CSP,nominal} = W_{cycle,net} - W_{p,HTF} - W_{p,HTF,PHE} \tag{8.9}$$

$$CF = \frac{EE}{W_{CSP,nominal} \cdot 8760} \tag{8.10}$$

where $W_{cycle,net}$ – cycle net power, MWe; $W_{p,HTF,PHE}$ – power of the pump used to transfer HTF through the cycle PHE, MWe; EE – electric energy output per year, MWh/yr.

The 30 years of service with a 6.5% CRF are assumed to calculate LCOE according to the equation [46]:

$$LCOE = \frac{TCC \cdot CRF + FOC}{EE} + VOC \tag{8.11}$$

where $LCOE$ – levelized cost of electricity, USD_{2020}/MWh; TCC – total capital cost, USD_{2020}; CRF – capital recovery factor; FOC – fixed operating costs, USD_{2020}; VOC – variable operating costs, USD_{2020}/MWh.

8.3. Results

During the analysis two main types of calculations were done: design point and off-design point. First, design point calculations of the power cycles were carried out, after which the obtained results were used to perform off-design power cycles calculations and CSP plant sizing, including receiver design. After that off-design performance of the solar field, the receiver and HTF pump are calculated, and finally the whole CSP plant annual operation is modeled. Additional optimization is carried out by varying both TES size and SM by changing the power cycle input power, assuming that the efficiency of the power cycle does not depend on its size and therefore linear scaling of cycle power output with thermal input. This assumption is valid since the capacity of power cycles changes between 85 and 130 MWe depending on the SM, and at this large scale the efficiency of turbomachinery is almost independent of size [97–99].

8.3.1. Power cycle design point

For both cycles, minimum pressure is optimized. For the CO_2 mixture cycle, the CO_2 molar fraction is varied to reach the maximum electrical efficiency, as shown in Figure 8.10. Due to the condensation, the cycle minimum pressure also changes. As the CO_2 molar fraction increases, the minimum cycle pressure rises while the dew point temperature decreases due to changes in working fluid composition. At the same time, the turbine outlet pressure increases, resulting in a higher turbine outlet temperature. Since the dew point is reached within the recuperator, it determines the hot side temperature at which the minimum temperature differences between the flows occurs. Therefore, increasing the CO_2 fraction reduces the amount of heat exchanged in the recuperator and lowers the working fluid temperature at the PHE inlet, thereby increasing the required heat input. At the same time, the turbine work increases. These two opposing effects lead to the existence of the optimum point.

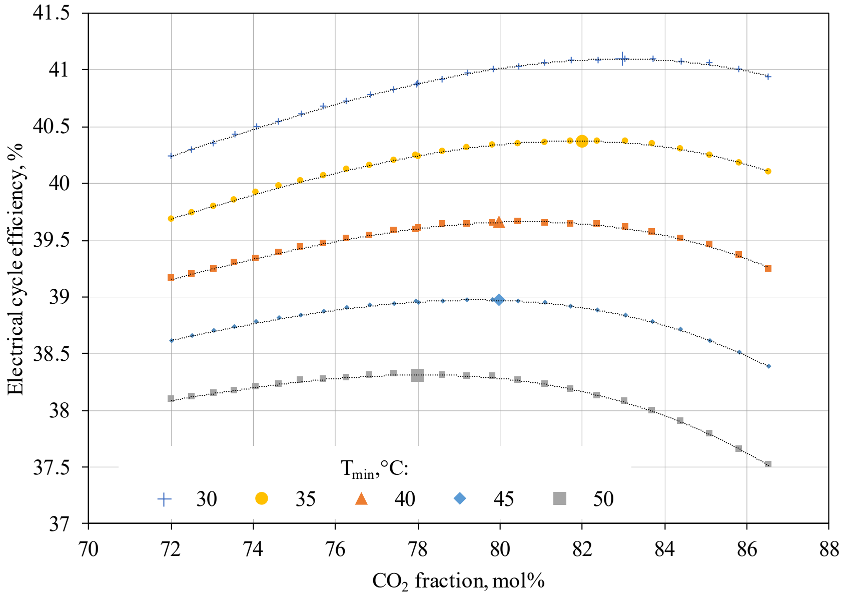

Figure 8.10. Power cycle electrical efficiency dependence on the CO_2 molar fraction

Power cycles optimization results are shown in Table 8.6. As expected with the reduction of cycle minimum temperature, the optimum cycle minimum pressure also decreases, leading to the increase of CO_2 molar fraction in the case of CO_2 mixture cycles. The results of power cycle design, together with three cooler/condenser approach temperatures, are then used for equipment design and off-design modeling.

Table 8.6. Power cycles design point parameters

Cycle fluid	sCO_2	CO_2 mix.	sCO_2	CO_2 mix.	sCO_2	CO_2 mix.	sCO_2	CO_2 mix.	
T_1 (T_{min}), °C	50		45		40		35		30
CO_2, mol%	100	78	100	80	100	80	100	82	83
P_1 (P_{min}), bar	101.0	70.4	96.0	67.2	89.0	62.1	82.0	58.5	54.2
T_3 ($T_{PHE,in}$), °C	398.6	382.7	385.8	372.5	369.2	362.5	348.4	351.0	339.3
T_6 ($T_{cool/cond,in}$), °C	109.8	93.9	101.7	87.9	95.2	82.9	82.0	76.1	70.1
P_t/Q_{PHE}, %	52.7	51.7	51.7	51.8	51.1	52.0	49.8	52.2	52.5
P_p or P_c/Q_{PHE}, %	15.9	10.9	14.2	10.4	12.9	9.9	10.7	9.4	8.9
UA_{REC}/Q_{PHE}, 1000/K	6.0	9.9	5.3	9.1	4.6	8.4	4.1	7.8	7.2

Cycle fluid	sCO_2	CO_2 mix.	sCO_2	CO_2 mix.	sCO_2	CO_2 mix.	sCO_2	CO_2 mix.	
$\eta_{cycle,th}$, %	36.72	40.81	37.50	41.45	38.25	42.14	39.14	42.83	43.55
$\eta_{cycle,el}$, %	33.97	38.31	34.73	38.97	35.69	39.66	36.72	40.37	41.10
Specific power, kJ/kg	72.80	71.80	80.00	78.15	89.63	83.76	101.88	91.54	99.15

8.3.2. Power cycle off-design

For the sCO_2 cycle, minimum cycle pressure is first optimized while keeping the cooler fan air velocity constant to reach maximum net cycle electrical efficiency. Results of the minimum cycle temperature-pressure relations for some of the power cycles are shown in Figure 8.11 with all the data available in Supplementary materials G. The big markers refer to the design point parameters, while small markers are the results of the off-design calculations with lines showing interpolation using the Piecewise Cubic Hermite Interpolating Polynomial (PCHIP) interpolator from SciPy [100]. The lowest pressure seen in operation is 75 bar, with lower pressure appearing only below 32°C. At the design point minimum temperature, the optimum minimum pressure is below the design one. This happens due to the compressor off-design performance. Specifically, as can be seen in Figure 8.6a, compressor efficiency increases above the design one when RPM and volume flow are above the design values. This leads to minimum cycle pressure lower and RPM higher than the design point to maintain almost the design point mass flow and TIT but at higher compressor efficiency.

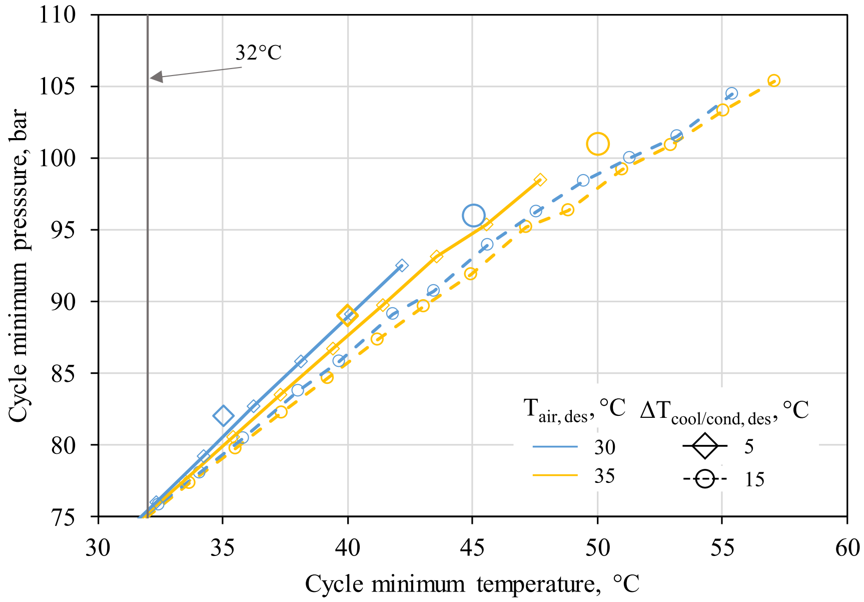

Figure 8.11. Some sCO_2 cycles minimum pressure dependence on the minimum temperature: big markers stand for design point, lines with smaller markers for off-design

In Figure 8.12 are shown some of the off-design parameters for the sCO_2 cycle with an air design temperature of 35°C and a cooler/condenser approach temperature of 15°C. All the air temperatures are split into four ranges (shown with arrows) according to the control modes used:

1. At an air temperature equal to 15°C ($T_{air,fan}$) the fan power reaches 105% of the design; therefore, from 12.5 to 15°C, $V_{air,off,i}$ is varied to obtain $W_{fan,off,i} = 105\% W_{fan,des}$ (dashed lines with arrows). At lower air temperatures, T_{min} reaches the minimum allowable value; therefore, below 12.5°C, $T_{min,off,i}$ is kept at 32°C (dashed dotted lines with arrows). For both cases, TIT is fixed at the design value, as can be seen from Figure 8.12.

2. At air temperatures above the design (dotted arrows), the fan power is kept at 105% of design, while HTF mass flow is varied to maintain constant HTF outlet temperature.
3. For air temperatures below the design point but above the $T_{air,fan}$ (solid lines with arrows), the cooler/condenser air velocity and TIT are kept at the design value.

One can see that at the first air temperature above the design, the minimum cycle temperature remains almost constant, which is due to an increase in cooler air velocity and therefore fan power. This leads to a reduction of efficiency drop at higher than design air temperatures, as can be seen from the efficiency curve slope change. With the air temperature reduction below the design, the cycle minimum temperature is also reduced due to the constant cooler fan air velocity. This increases the cycle thermal and net efficiency, even though the cooler fan power increases. At low air temperatures when the minimum cycle temperature is fixed, other parameters in the cycle remain fixed as well, as can be seen from the HTF outlet temperature curve. This fixes the power cycle thermal efficiency, but the net efficiency still increases with the decrease due to the reduction of cooler fan power.

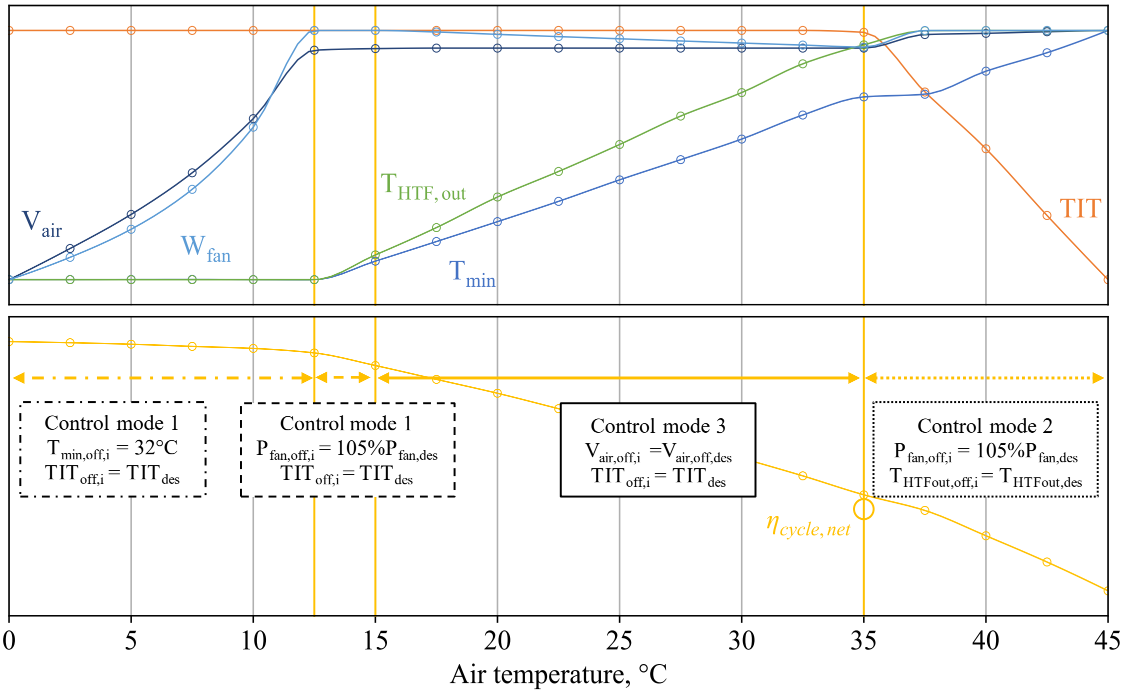

Figure 8.12. Power cycle off-design parameters with vertical lines showing the changes of control modes for sCO_2 cycle with $T_{air,des}$ = 35°C and $\Delta T_{cool/cond}$ = 15°C

The comparison of multiple power cycles off-design results is shown in Figure 8.13. In Figure 8.13a one can see the efficiencies of sCO_2 cycles in the bottom and CO_2 mixture cycles in the top, with vertical lines indicating the ranges of control modes. One can see that for CO_2 mixture cycles there is no limit for minimum cycle temperature, which influences the efficiency curves at low air temperatures (Control mode 1). In the case of the sCO_2 power cycle with $T_{air,des}$ = 20°C, the operation below the design point air temperature happens straight with the minimum cycle temperature limit, since the $T_{min,des}$ is only 35°C. It is also important to note that at air temperatures above the design, the efficiency of the sCO_2 cycle decreases faster than in the case of the CO_2 mixture one.

Comparing two cycles with different air design temperatures, cycle with higher $T_{air,des}$ has higher efficiency at high air temperatures, while at low air temperature the cycle with lower $T_{air,des}$ is more efficient. For sCO_2 cycle, the design point efficiency is lower than the one observed during off-design simulations due to lower off-design minimum pressure, which is favored by compressor operation. In the case of CO_2 mixture, the design point efficiencies are practically equal to the off-design model results. The power output of the cycle, considering the cooler/condenser fan power, is shown in Figure

8.13b. For the sCO_2 cycle, one can see a significant drop of power at temperature above the design, mainly due to the minimum cycle temperature increase as well as the increase in cooler fan power. For CO_2 mixture cycle, the reduction is less dramatic due to the compression of working fluid in the liquid zone.

HTF temperatures at the primary heat exchanger outlet at variable air temperature are shown in Figure 8.13c, while Figure 8.13d shows the HTF mass flow variation. For all cycles at temperatures below the design point, HTF mass flow is kept constant, while for air temperatures above the design condition, the flow is reduced to maintain the HTF outlet temperature equal to the design point, as shown in Figure 8.13d. As in the case for net power, the sCO_2 cycle is more affected by the high air temperature and has a significant reduction of HTF flow rate at air temperatures above the design.

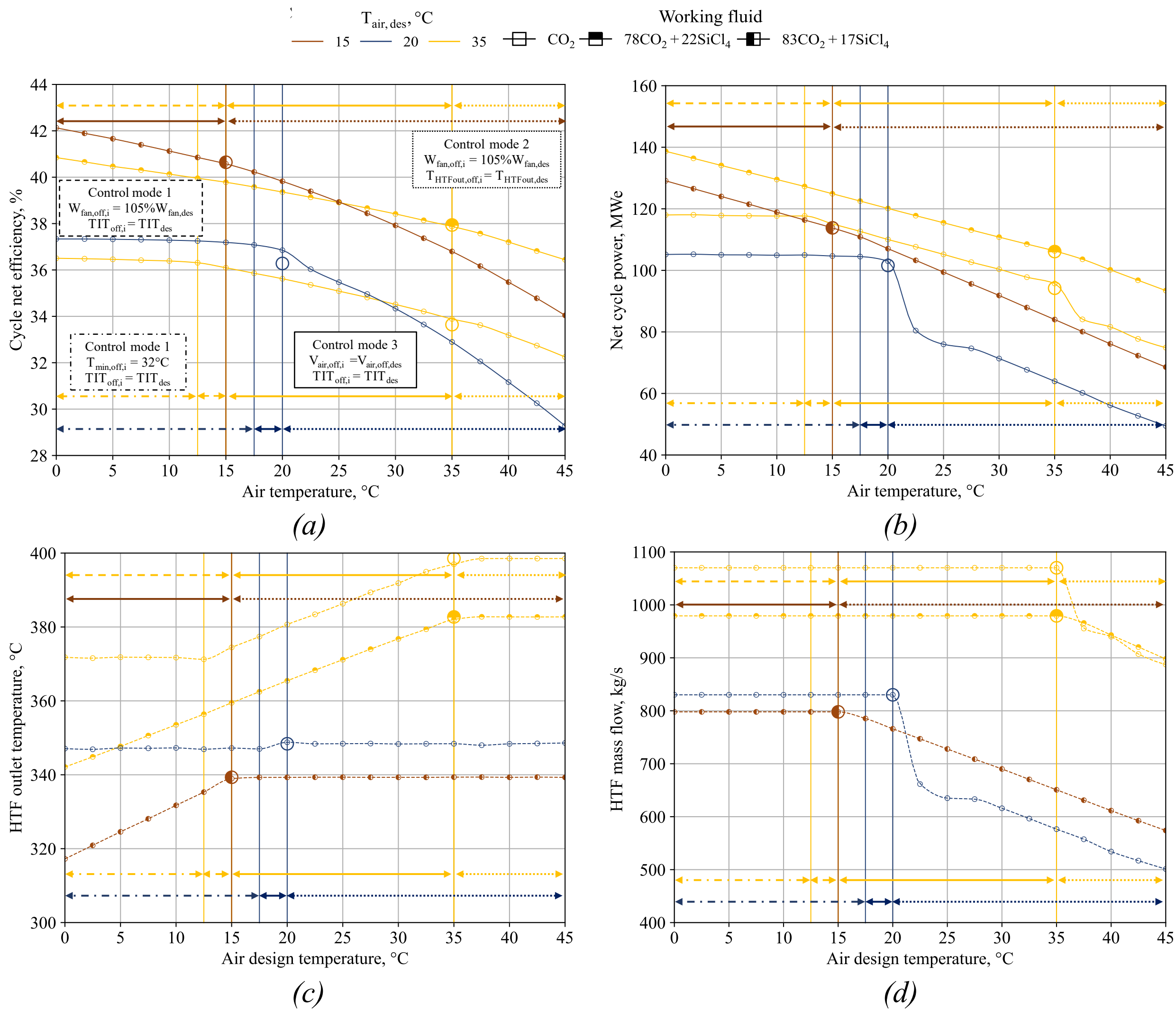

Figure 8.13. Off-design net efficiency (a), net power (b)and HTF outlet temperature (c) and mass flow (d) of some power cycles with cooler/condenser approach temperature $\Delta T_{cool/cond}$ =15°C and lines showing the changes of control modes

Fan power limit of 120% was also additionally assessed with results available in Supplementary materials G. The net cycle efficiency and power almost didn't change. Since increases in fan power result in progressively smaller gains in air flow rate [101], further increases in the fan power limit yield only marginal improvements in net efficiency and power output.

8.3.3. Concentrated solar power plant components performance

The solar field is designed with SolarPilot [102] and has 12010 heliostats with the layout shown in Figure 8.14a, with the highest annual total optical efficiency of 72.2% and the lowest of 36.3%. The design point flux map is shown in Figure 8.14b with a minimum density of 119 kW/m^2 and a maximum of 951 kW/m^2, which is within the limits of solar salt receivers.

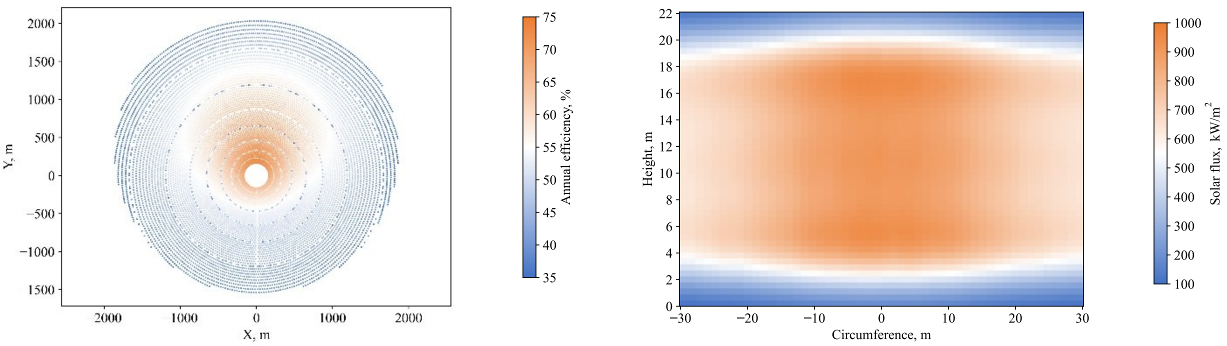

(a) *(b)*

Figure 8.14. Solar field (a) and flux map of receiver (b)

Receiver designs obtained from fictitious power optimization (8.8) are shown in Table 8.7 using the flux map from Figure 8.14b. Higher temperature rise across the receiver leads to slightly higher receiver efficiency and lower mass flow, tube diameter, and HTF pump power.

Table 8.7. Receivers design point parameters

Cycle fluid	sCO_2	**CO_2 mix.**	**sCO_2**	**CO_2 mix.**	**sCO_2**	**CO_2 mix.**	**sCO_2**	**CO_2 mix.**	
T_1 (T_{min}), °C	50		45		40		35		30
$\Delta T_{HTF,rec}$, °C	151	167	164	177	181	188	202	199	211
Panels per flow path	3								
Tube outer diameter, mm	34			32					25
Receiver pressure drop, bar	45.3	44.6	44.7	46.2	46.1	45.8	45.3	45.4	48.2
HTF pump power, MW	8.77	7.88	8.04	7.74	7.58	7.28	6.72	6.82	6.86
Receiver efficiency, %	90.6	90.7	90.6	90.8	90.8	90.8	90.9	90.9	91.1

For both the solar field and the receiver, off-design maps were made to replace direct calculation, as was done previously [18], using bivariate spline from SciPy [100] for interpolation. The solar field optical efficiency map is shown in Fig. 8.15a, with efficiency ranging from 39 to 57.4%. Receiver efficiency and HTF pump power maps were done for all the cases shown in Table 8.7. In Fig. 8.15b a receiver efficiency map is shown for the sCO_2 cycle with a minimum temperature of 45°C and an air design temperature of 30°C as an example. In this case, receiver efficiency varies between 49.8 and 91.1%. While reducing HTF inlet temperature does improve efficiency, the main influence is due to the reduced power input.

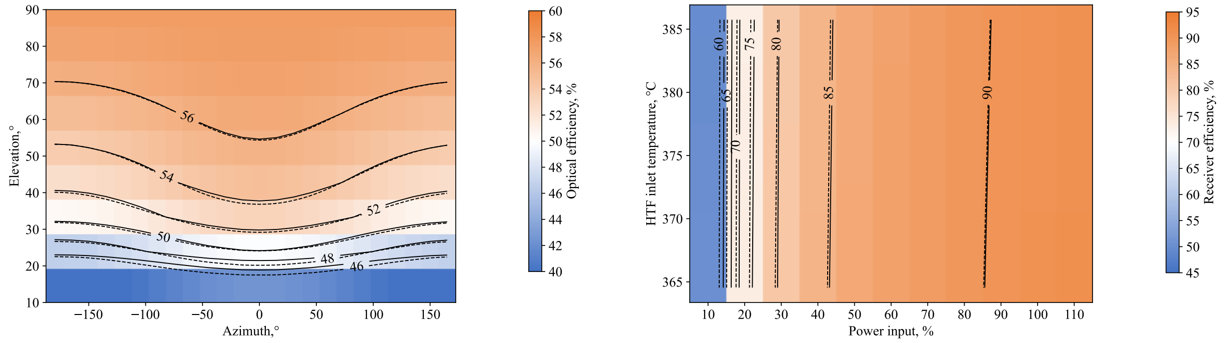

(a) *(b)*

Fig. 8.15. Solar field optical efficiency map (a) and receiver efficiency map (b) with colormap representing the calculated values, solid lines (—) for original efficiency levels and dashed lines (---) for interpolated

8.3.4. Concentrated solar power plant techno-economic analysis

The CSP plant model results are shown for two cases: the base case with SM = 2.8 and TES = 13 hours and optimized values of SM and TES size (more details available in Supplementary materials I). The base SM is also optimal for the CO_2 mixture cycle with a $T_{air,des}$ = 25°C and sCO_2 cycle with $T_{air,des}$ = 30°C and a 40 and 45°C cycle minimum temperatures, as can be seen in Figure 8.16a. For sCO_2 cycle, optimum SM changes from 2.3 at $T_{air,des}$ = 20°C to 3.2 at $T_{air,des}$ = 45°C, while for CO_2 mixture, the change is from 2.5 at $T_{air,des}$ = 15°C to 3.1. Therefore, design point air temperature has a higher influence on optimum SM for sCO_2 than for CO_2 mixture power cycle. Bigger capacities are favored for sCO_2 power cycles compared to CO_2 mixture ones. This can be explained by the operation in the supercritical phase and the use of a compressor in the sCO_2 cycle, which leads to a significant power output reduction at air temperatures above the design point. Optimal TES size is 12 hours for most cycles, as shown in Figure 8.16b. The exceptions are the CO_2 mixture cycle with $T_{air,des}$ = 15°C and the sCO_2 cycle with $T_{air,des}$ = 20°C, $T_{min,des}$ = 35°C and $T_{air,des}$ = 25°C, $T_{min,des}$ = 35°C which are the minimum air and cycle design temperatures for the corresponding cycles.

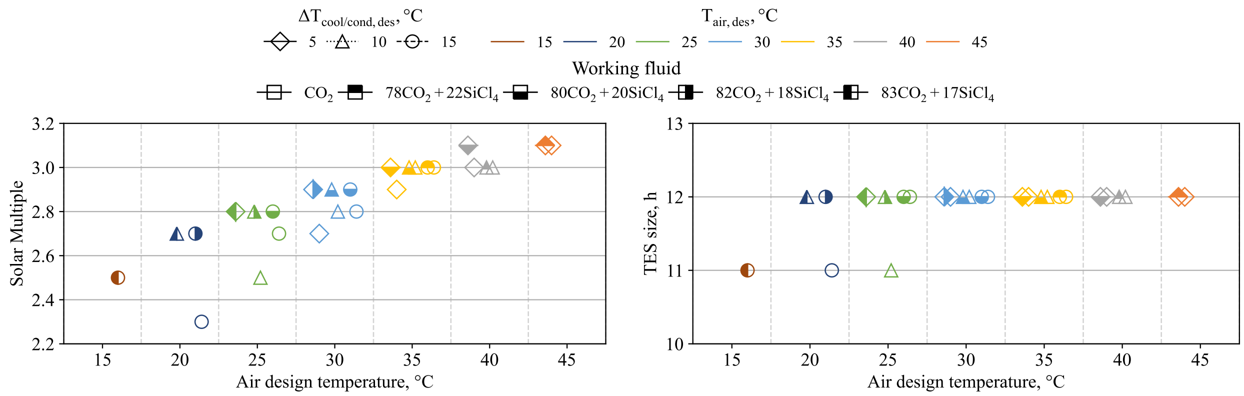

(a) *(b)*

Figure 8.16. Optimum Solar Multiple (a) and TES size (b)

The CSP plant nominal power for base and optimized SM and TES sizes is shown in Figure 8.17. In the base case, lower minimum temperature as well as using a CO_2 mixture leads to the increase of nominal power due to the higher power cycle efficiency. For the optimum conditions, the nominal power distribution follows the inverse of SM (Figure 8.16a), since the solar field and receiver capacities are fixed, leading to lower values at higher $T_{air,des}$. Therefore, it is important to properly size the power cycle depending on the design point air temperature, since this can have a significant effect on its cost.

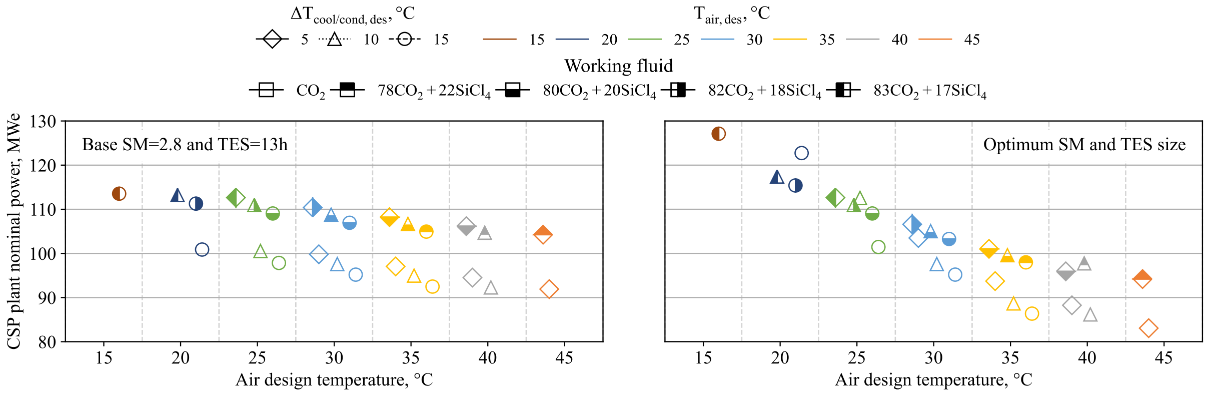

(a) *(b)*

Figure 8.17. CSP plant nominal power cost for base (a) and optimum (b) SM and TES size

The air cooler/condenser fan powers for base SM and TES size are shown in Figure 8.18a. The decrease of cooler/condenser approach temperature significantly increases the fan power since the heat exchange area also increases. The same can be seen also for optimum SM and TES size in Figure 8.18b, although the absolute values vary due to the change in the power cycle size. The footprint of cooler/condenser heat exchanger alone varies from 1600 m^2 to 4350 m^2, the latter number characteristic for the sCO_2 cycle with $T_{air,des}$ = 30°C and $T_{min,des}$ = 35°C. This parameter is linearly correlated with the fan power, since the number of rows is kept constant and pressure drop doesn't vary significantly.

It should be noted that in the case of CO_2 and CO_2 mixture cycles, the temperature of the hot fluid in the cooler/condenser is changing during the cooling, while in steam Rankine cycle condensers the heat rejection happens at almost constant hot flow temperature, while air temperature is increasing. This leads to ITD (cold end ΔT) in steam air-cooled condenser being higher than hot end ΔT (between steam entrance and air exit). In the case of sCO_2 and CO_2 mixture cooler/condenser, the cold end ΔT (approach temperature) is lower than hot end ΔT since the working fluid enters at around 100°C and exits at 35-50°C, while air heats up by around 30-40°C only. Therefore, for the same amount of heat rejected, the sCO_2 and CO_2 mixture cooler/condenser will be smaller than the steam ACC because of the bigger hot end ΔT (the overall heat transfer coefficient depends mainly on the air velocity). This allows to reduce the approach temperature compared to steam ACC, without significant penalty in heat exchange area and fan power. For comparison, the existing steam Rankine cycle in the 100 MW solar tower plant in Dunhuang employs a V-shaped air-cooled condenser consisting of two sections, each with a footprint of around 60 m × 30 m; the Jinta Zhongguang 100 MW plant uses a single A-shaped ACC with a footprint of around 45 m × 50 m; and the Noor Energy 1 (DEWA IV) 100 MW tower features an A-shaped ACC with an approximate footprint of 80 m × 50 m. Therefore, the assumed approach temperature is considered feasible, as the resulting footprints fall within the range of ACC dimensions observed in existing CSP plants.

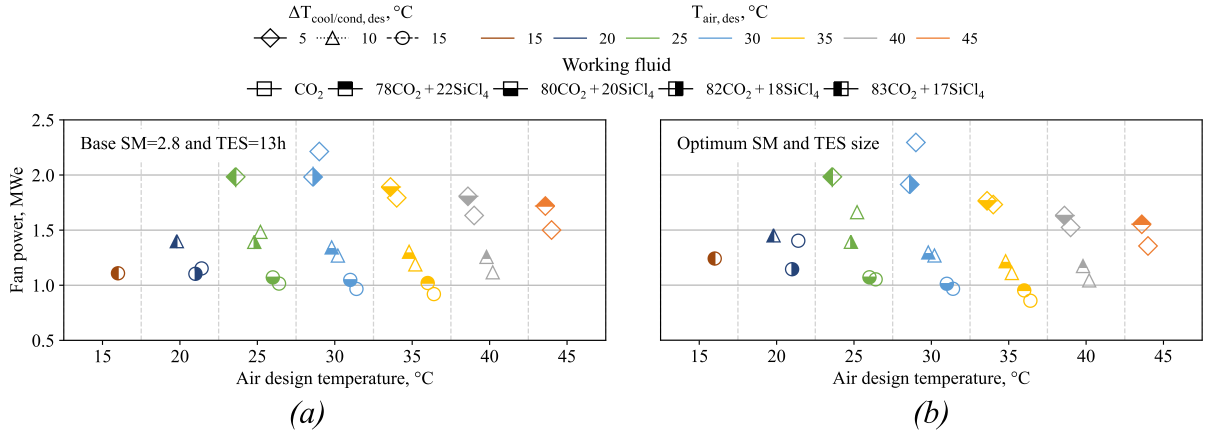

Figure 8.18. Cooler/condenser fan power for base (a) and optimum (b) SM and TES size

Electric energy generation for the base case is shown in Figure 8.19a. There is a peak of electricity produced at 30-35°C air design temperatures for all considered cases due to two effects taking place. First, with higher air design temperatures, the power cycle operates at air temperatures above the design point for a shorter period of the year and with higher efficiency, resulting in a higher capacity factor and more electricity generated. On the other hand, increasing the air design temperature also decreases the design point efficiency and leads to lower efficiencies at air temperatures below the design. A decrease of cooler/condenser approach temperature also increases electricity generation, since the power cycle efficiency increases with the decrease of minimum cycle temperature. For optimum SM and TES size, the electricity output slightly decreases with the increase of ambient air design temperature for the same cooler/condenser approach temperatures as shown in Figure 8.19b.

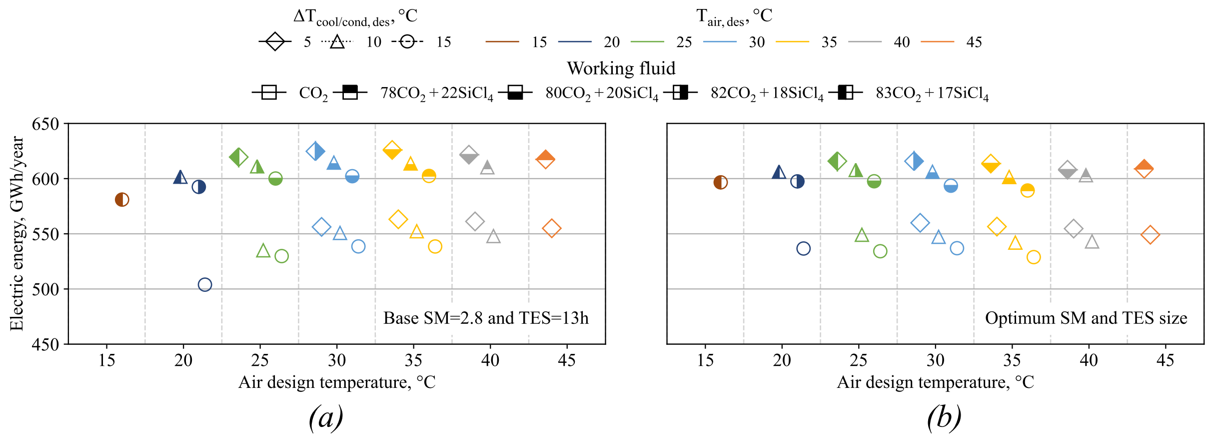

Figure 8.19. Annual electricity output for base (a) and optimum (b) SM and TES size

The influence of air design temperature on the capacity factor in the base case is shown in Figure 8.20a. With the increase in air design temperature, the capacity factor also increases since the cycle operates at its design output power or higher for longer periods. In Figure 8.20b the distribution of capacity factors with optimum SM and TES size is shown, which mimics the optimum solar multiple distribution from Figure 8.16a. Even if the electricity generation remains almost the same (Figure 8.19b), since the nominal power decreases significantly (Figure 8.17b), the resulting capacity factor increases.

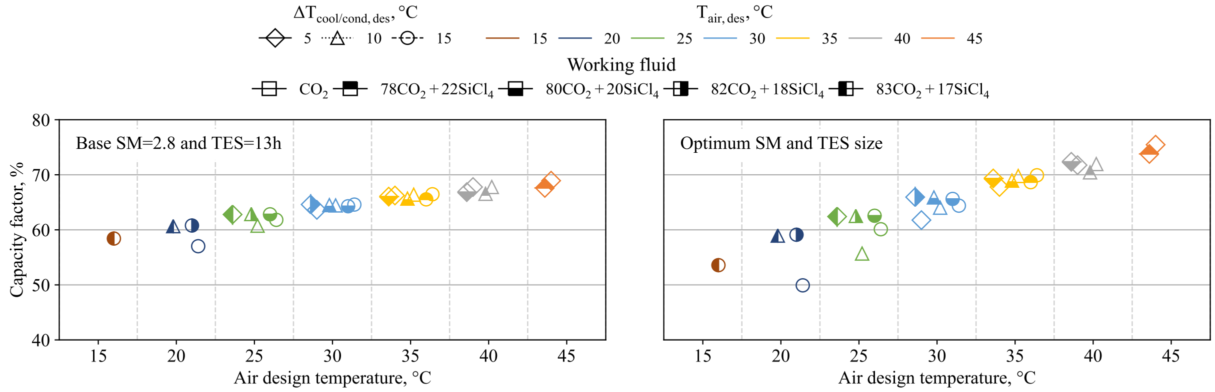

(a) *(b)*

Figure 8.20. Capacity factor for base (a) and optimum (b) SM and TES size

Next, the results of the capital expenditure estimates are presented, which depend strongly on the cost correlations used. Thermal energy storage costs for base and optimized SM and TES sizes are shown in Figure 8.21. In the current work, the correlation from Manzolini [103] is used for the TES cost calculation, which has an almost linear dependence on the amount of salt stored. Therefore, it is important to note that storage costs for the base case are in line with the results of Neises et al. [20], accounting for the 2.4 SM, 10 hours of TES, and 50 MWe power output in the reference. For optimum conditions, the TES cost is lower for almost all cases and reaches a minimum at $T_{air,des}$ = 25°C for both cycles. For both cases, lower cooler/condenser approach temperatures lead to reduced storage costs. This is because a lower cycle minimum temperature results in a lower PHE working fluid inlet temperature, which decreases both the PHE HTF outlet temperature and TES cold tank temperature. This increases the temperature difference between storage tanks, reducing the mass of solar salt required to provide the same hours of storage.

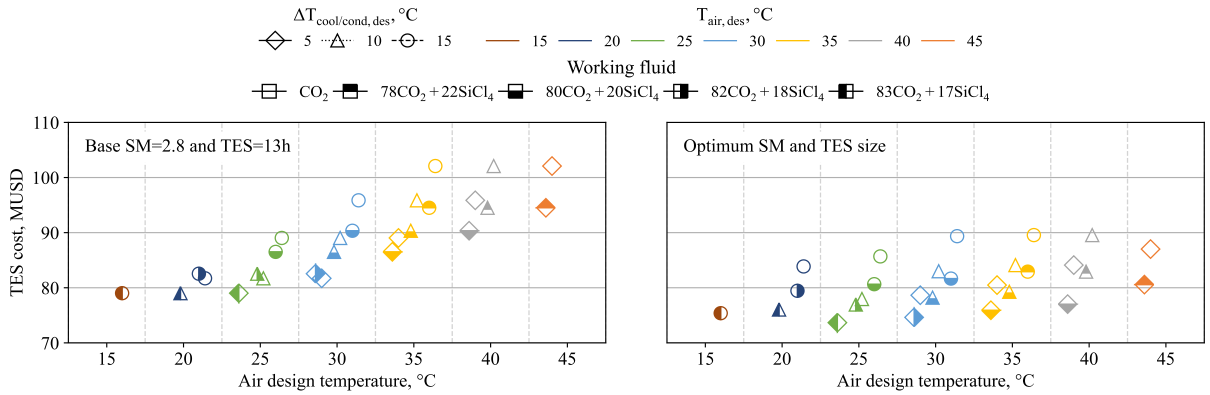

(a) *(b)*

Figure 8.21. TES cost for base (a) and optimum (b) SM and TES size

Power cycle costs for the base case are shown in Figure 8.22a and have the same linear increasing trend as in Neises [20] but lower absolute values. Part of the difference is due to the use of simple recuperated power cycles in this work compared with the recompression cycle used in the reference, which has a higher specific cycle cost [18,38]. Another reason is the significant PHE cost reduction (around 5 times) due to the use of a different cost correlation. In the case of Neises [20], a correlation from Carlson et al. [104] is used, which in turn used a "naïve" model derived from the ESDU dataset and does not depend on cold side pressure drop. In Morosini et al. [37], a correlation for PHE made from Inconel 617 is proposed for 700°C TIT, which gives around 2.5 times lower cost than Carlson et al. [104] at a 5 bar tube side pressure drop. While in this paper, a correlation developed for CO_2

and sCO_2 mixture to solar salt PHE from [54] is used, which has both 5 bar tube side pressure drop and uses cheaper 347 stainless steel for 550°C TIT.

The cost of an air cooler/condenser increases quadratically by around 25% and 70-90% moving from $\Delta T_{cool/cond}$ =15°C to 10 and 5°C, which can also be seen for steam air-cooled condensers [105], while the cost of a recuperator decreases. This leads to a minimum power cycle cost with 10°C cooler/condenser approach temperatures in some cases. For the optimal case, power cycle costs are shown in Figure 8.22b. With higher air design temperatures, lower power cycle costs are favored due to higher optimum SM, and the trend is more pronounced in the case of sCO_2.

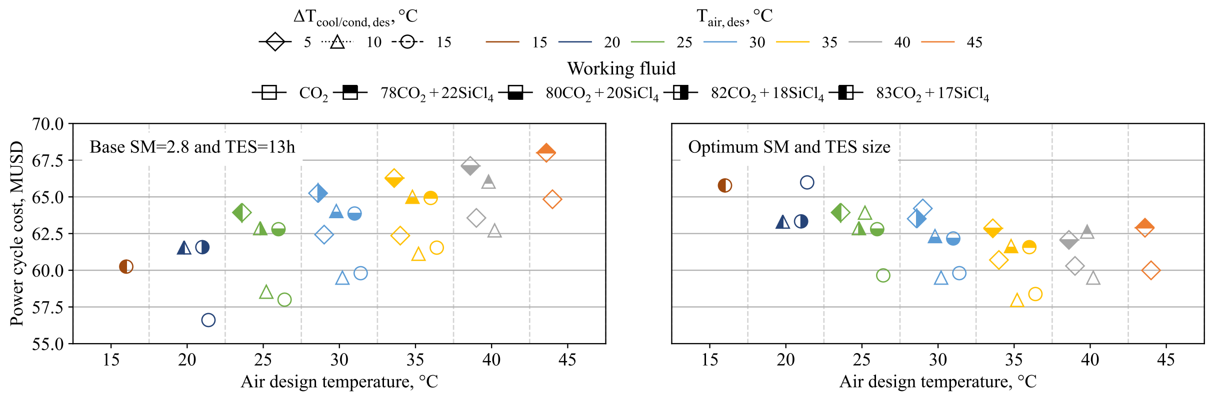

(a) (b)

Figure 8.22. Power cycle capital cost for base (a) and optimum (b) SM and TES size

Total CSP plant capital costs for the base case shown in Figure 8.23a have the same trend as in Neises [20] and similar absolute values, accounting for the size difference. For the optimal case, total capital costs are shown in Figure 8.23b and are mostly lower than the base. Only at low air design temperatures (25°C and below for sCO_2 and 15°C for CO_2 mixture) is the TCC increased compared to the base. For the same cooler/condenser approach temperatures, the lower TCC corresponds with the lower air design temperature for the CO_2 mixture cycle, while for sCO_2 there is a minimum within the 25-35°C air temperature range.

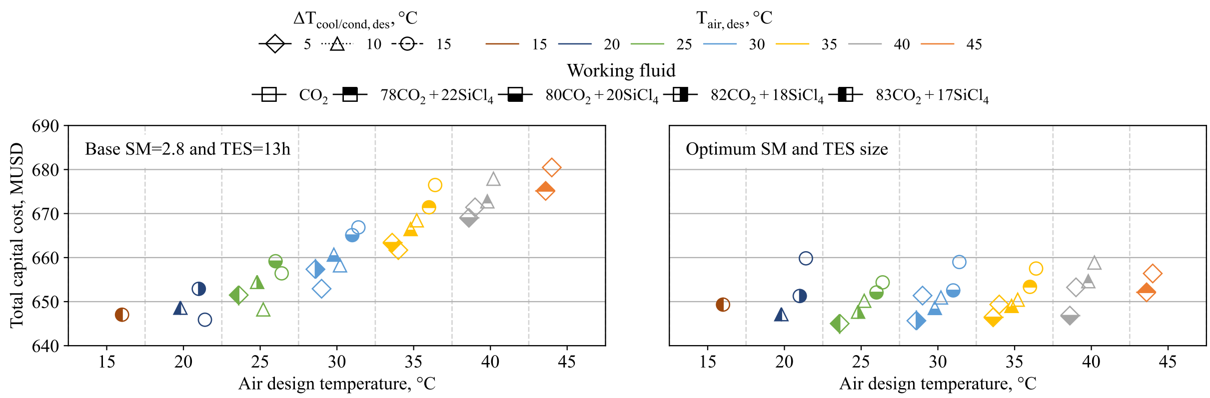

(a) (b)

Figure 8.23. Total plant capital cost for base (a) and optimum (b) SM and TES size

The LCOE distribution for the base case (SM = 2.8 and TES = 13 h) is shown in Figure 8.24a. The lowest LCOE is reached by the CO_2 mixture cycle at $T_{air,des}$ = 30°C and $T_{min,des}$ = 35°C, closely followed by $T_{air,des}$ = 25 and 35°C with $\Delta T_{cool/cond}$ = 5°C. For the sCO_2 cycle the lowest LCOE is reached at $T_{air,des}$ = 35°C with $T_{min,des}$ = 40°C and $T_{air,des}$ = 30°C with $T_{min,des}$ = 35°C being the close second. These optimum $T_{air,des}$ correspond to ambient air temperatures not exceeded 90.2 and 96.8%

of the year for CO_2 mixture and sCO_2 cycles respectively. This distribution of LCOE mimics the distribution of electricity generated shown in Figure 8.19a, since the electricity generation changes more than the total capital cost (Figure 8.23a) for different cases.

Therefore, for both cycles and all design ambient air temperatures, the optimum cooler/condenser approach temperature is the minimum one considered (5°C for most cases in this study), which is consistent with Neises [20]. On the other hand, the minimum LCOE $T_{air,des}$ is higher than the $T_{air,des}$ = 30°C and $T_{min,des}$ = 34°C obtained in [20] for SM = 2.4 and 10 hours of storage. This could be explained by the location with a lower average annual dry bulb temperature (around 16°C vs 20°C in Seville), the use of a recompression cycle with dispatch optimization, and a different control strategy used. However, these results are in line with work performed by Chen et al. [30] for the simple sCO_2 cycle at 650°C TIT, where the best performance for two locations with the average annual temperature of around 20°C is obtained at $T_{min,des}$ = 40°C and $T_{air,des}$ = 35°C. At the same time, their results suggest that for the locations with 14 and 5°C average annual temperatures, the optimal conditions are $T_{min,des}$ = 33°C and $T_{air,des}$ = 25°C (the smallest $\Delta T_{cool/cond}$ considered) which is in line with the results of Neises [20].

Results with optimum SM and TES size are shown in Figure 8.24b. For CO_2 mixture cycle the lowest LCOE is reached at $T_{air,des}$ = 35°C and $T_{min,des}$ = 40°C (SM = 3, TES = 12 h) closely followed by $T_{air,des}$ = 30 and 40°C with $\Delta T_{cool/cond}$ = 5°C. For the sCO_2 cycle, minimum LCOE is reached at $T_{air,des}$ = 35°C and $T_{min,des}$ = 40°C (SM = 2.9, TES = 12 h), followed by $T_{air,des}$ = 40°C and $T_{min,des}$ = 45°C. With optimized SM and TES sizes, the optimum cooler/condenser approach temperature remains the same, but the design ambient air temperature is 35°C for both CO_2 mixture and sCO_2 cycles (not exceeded 96.8% of hours in the location). Overall, the difference between the optimum LCOE before and after optimization is small (91.31 vs 90.52 USD/MWh for sCO_2 cycle and 83.61 vs 82.90 USD/MWh), which could be attributed to the base SM and TES being close to optimal values. Another important note is that in the case with the optimum SM and TES, the LCOE values almost plateau for the same cooler/condenser approach temperature when the air design temperature is above 30°C, especially in the case of CO_2 mixture cycle.

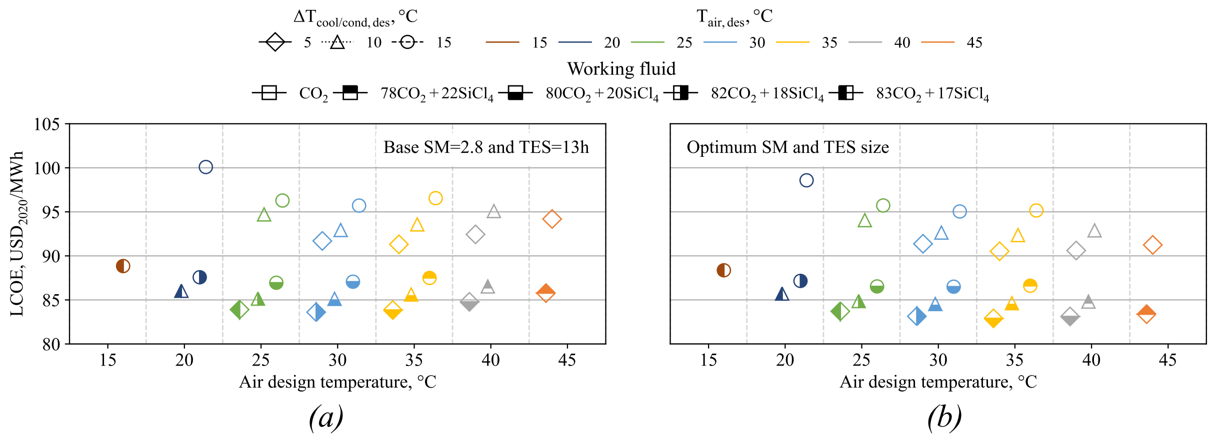

Figure 8.24. LCOE for base (a) and optimum (b) SM and TES size

Additional analysis was carried out using the climate data for Seville from SAM [46] with more results available in the Supplementary materials J. The main difference in the climate data from PVGIS and SAM is the amount of solar energy available, while dry bulb temperature duration curves are very close. The optimum LCOE, SM, and TES sizes were found to be higher for SAM climate data due to lower solar resource available, while optimum air design temperature and cooler/condenser approach temperature remain the same.

8.4. Conclusions

In this paper, simple recuperated cycles with sCO_2 and CO_2+$SiCl_4$ mixture as working fluids are analyzed in design and off-design conditions. At the design point, the power cycle electrical efficiency is optimized for both cycles at different minimum cycle temperatures by varying the sCO_2 minimum pressure and mixture composition, respectively. Results confirm that the decrease of the cycle minimum temperature from 50 to 35°C reduces the optimum cycle minimum pressure (from 101 to 82 bar for sCO_2 and from 70.4 to 58.5 bar for CO_2 mixture cycle) and, in the case of CO_2 mixture cycle, increases the CO_2 molar fraction in the working fluid (from 78 to 82%). On average, the CO_2 mixture cycle has 3.9 and 4 percentage points higher thermal and electric efficiency than an sCO_2 one, with a higher difference at higher minimum cycle temperatures (38.3% vs 34.0% at 50°C and 40.4% vs 36.7% at 35°C electric efficiency). This is due to the transcritical CO_2 mixture cycle having compression in the liquid phase.

For design and off-design analysis of power cycles, detailed PCHE and cooler/condenser models are implemented to accurately represent the condensation of the working fluid. Simplified models were adopted for the compressor, pump, turbine, and PHE, with the turbine and PHE models validated using literature CFD data and results from rigorous commercial software, respectively. The hybrid off-design control algorithm is adapted to maximize the power cycle efficiency at different ambient air temperatures. It also includes a simplified sCO_2 minimum cycle pressure optimization method to reduce computational time. Using the developed models and methods, off-design performance curves with different condenser/cooler approach temperatures ($\Delta T_{cool/cond}$ = 5, 10, 15°C) and cycle minimum temperatures (35-50°C for sCO_2 and 30-50°C for CO_2 mixture power cycles) are obtained. The results indicate the possibility of operation at all ambient air temperatures present in the location while maintaining the TIT, HTF outlet temperature, and HTF mass flow below or equal to the design condition. This allows for safe operation of power cycle and CSP plant equipment within design temperatures and flow rates.

The off-design curves are then used in the CSP plant model, located in Seville, Spain where the average ambient temperature is 19 °C, to calculate the annual electricity production and techno-economic performance. Starting from a base case with a fixed SM of 2.8 and TES equal to 12 h, lower minimum temperature as well as using a CO_2 mixture leads to the increase of nominal power due to the higher power cycle efficiency. For the optimum conditions, the nominal power distribution follows the inverse of optimum SM, since the capacity of the solar field and receiver were fixed. In the base case there is a peak of electricity production at 30-35°C air design temperatures, while for optimum SM and TES size, the electricity output only slightly decreases with the increase of ambient air design temperature ($T_{air,des}$) for the same $\Delta T_{cool/cond}$. Total plant cost for the base case increases with the increase of $T_{air,des}$ and $\Delta T_{cool/cond}$, while for optimum SM and TES size the costs have a minimum and are mostly lower. For the base case the minimum LCOE is reached at air design temperatures equal to 35°C and 30°C for the sCO_2 and CO_2 mixture cycles, corresponding to ambient temperatures not exceeded 90.2% and 96.8% of the year, respectively. The distribution mimics that of electricity generated, since it changes more than the total plant cost for different cases. At optimum solar multiple and TES size for both CO_2 mixture and sCO_2 cycles, the minimum LCOE is reached at $T_{air,des}$ = 35°C (12 hours TES, SM = 3 and 2.9, respectively). At the same time, for all conditions and cycles, the reduction of cooler/condenser approach temperature also reduces the LCOE, with a minimum considered $\Delta T_{cool/cond}$ = 5°C being the best. The $\Delta T_{cool/cond}$ also has a bigger effect on the LCOE than $T_{air,des}$, if the latter is in the 30-40°C range (not exceeded 90.2-99.9% of the year). For both base and optimized SM and TES sizes, the CO_2 mixture cycle has 8.4% lower LCOE compared to the sCO_2 one and is less sensitive to the ambient air design temperature changes.

Therefore, this paper confirms the results of previous studies focused on sCO_2 cycles off-design performance and the air cooler design impact on CSP plant techno-economic performance and expands on them by investigating the CO_2 mixture cycle and optimizing the CSP plant SM and TES size. The results of this study could be used as a starting point for the design of CSP plants with CO_2 mixture power cycles for locations with similar average annual ambient temperatures. it should be noted that operational experience with sCO_2 power cycles remains limited, while for CO_2 mixture cycles only experimental circuits exist and require further investigation of composition shifts, two-phase heat transfer, and related phenomena. Furthermore, additional material requirements could arise after compatibility tests depending on the dopant used, increasing the cost of equipment. Since most dopants stable at high temperatures have negative health effects, additional safety procedures will be needed, which would increase the cost of the plant. Finally, based on the specific case, the current study methodology could be further improved by considering the dispatch optimization to match the local electricity price/demand profile, wet or hybrid cooling technology, and improved equipment cost estimates.

8.5. Bibliography

[1] Renewable power generation costs in 2021. Abu Dhabi: IRENA; 2022.

[2] Renewables 2020. Paris, France: IEA; 2020.

[3] Dostal V, Driscoll MJ, Hejzlar P, Wang Y. Supercritical CO2 Cycle for Fast Gas-Cooled Reactors. Volume 7: Turbo Expo 2004, Vienna, Austria: ASMEDC; 2004, p. 683–92. https://doi.org/10.1115/GT2004-54242.

[4] Dekhtyarev V. On the creation of a carbon dioxide power plant with high power and high efficiency. Electric stations 1962:2–6. https://doi.org/10.5281/zenodo.12191690.

[5] Angelino G. Real Gas Effects in Carbon Dioxide Cycles. ASME 1969 Gas Turbine Conference and Products Show, Cleveland, Ohio, USA: American Society of Mechanical Engineers; 1969, p. V001T01A071. https://doi.org/10.1115/69-GT-102.

[6] Dostal V, Driscoll MJ, Hejzlar P. A Supercritical Carbon Dioxide Cycle for Next Generation Nuclear Reactors. MIT; 2004.

[7] Romei A, Gaetani P, Persico G. On sCO2 Compressor Performance Maps at Variable Intake Thermodynamic Conditions. Volume 10: Supercritical CO2, Virtual, Online: American Society of Mechanical Engineers; 2021, p. V010T30A028. https://doi.org/10.1115/GT2021-60252.

[8] Zheng N, Li Z, Fang J, Wei J. Supercritical CO2 mixture Brayton cycle with floating critical points for concentrating solar power application: Concept and thermodynamic analysis. Energy Conversion and Management 2023;284:116989. https://doi.org/10.1016/j.enconman.2023.116989.

[9] Manzolini G, Binotti M, Bonalumi D, Invernizzi C, Iora P. CO2 mixtures as innovative working fluid in power cycles applied to solar plants. Techno-economic assessment. Solar Energy 2019;181:530–44. https://doi.org/10.1016/j.solener.2019.01.015.

[10] Morosini E, Ayub A, Di Marcoberardino G, Invernizzi CM, Iora P, Manzolini G. Adoption of the CO2 + SO2 mixture as working fluid for transcritical cycles: A thermodynamic assessment with optimized equation of state. Energy Conversion and Management 2022;255:115263. https://doi.org/10.1016/j.enconman.2022.115263.

[11] Doninelli M, Morosini E, Di Marcoberardino G, Invernizzi CM, Iora P, Riva M, et al. Experimental investigation of the CO2+SiCl4 mixture as innovative working fluid for power cycles: Bubble points and liquid density measurements. Energy 2024:131197. https://doi.org/10.1016/j.energy.2024.131197.

[12] Crespi F, Rodríguez De Arriba P, Sánchez D, Ayub A, Di Marcoberardino G, Invernizzi CM, et al. Thermal efficiency gains enabled by using CO2 mixtures in supercritical power cycles. Energy 2022;238:121899. https://doi.org/10.1016/j.energy.2021.121899.

[13] Invernizzi CM, Iora P, Bonalumi D, Macchi E, Roberto R, Caldera M. Titanium tetrachloride as novel working fluid for high temperature Rankine Cycles: Thermodynamic analysis and experimental assessment of the thermal stability. Applied Thermal Engineering 2016;107:21–7. https://doi.org/10.1016/j.applthermaleng.2016.06.136.

[14] Di Marcoberardino G, Morosini E, Di Bona D, Chiesa P, Invernizzi C, Iora P, et al. Experimental characterisation of CO2 + C6F6 mixture: Thermal stability and vapour liquid equilibrium test for its application in transcritical power cycle. Applied Thermal Engineering 2022;212:118520. https://doi.org/10.1016/j.applthermaleng.2022.118520.

[15] Putelli L, Di Marcoberardino G, Gelfi M, Invernizzi CM, Iora PG, Manzolini G. Preliminary Analysis of High-Temperature Corrosion of Metallic Alloys With CO2 and CO2-Based Working Mixtures for Power Plants Applications, American Society of Mechanical Engineers Digital Collection; 2022. https://doi.org/10.1115/GT2022-84197.

[16] Binotti M, Invernizzi CM, Iora P, Manzolini G. Dinitrogen tetroxide and carbon dioxide mixtures as working fluids in solar tower plants. Solar Energy 2019;181:203–13. https://doi.org/10.1016/j.solener.2019.01.079.

[17] Doninelli M, Di Marcoberardino G, Iora P, Gelfi M, Invernizzi CM, Manzolini G. Silicon Tetrachloride as innovative working fluid for high temperature Rankine cycles: Thermal Stability, material compatibility, and energy analysis. Applied Thermal Engineering 2024;249:123239. https://doi.org/10.1016/j.applthermaleng.2024.123239.

[18] Naumov V, Doninelli M, Di Marcoberardino G, Iora P. Solar tower power plants with CO2 +SiCl4 mixtures transcritical cycles. Renewable Energy 2025:122518. https://doi.org/10.1016/j.renene.2025.122518.

[19] Schlünder EU, Bell KJ, Chisholm D, Hewitt GF, Schmidt FW, Spalding DB, et al. Heat Exchanger Design Handbook. Hemisphere Publishing Corporation; 1983.
[20] Neises T. Influence of the air-cooled supercritical carbon dioxide recompression cycle design-point on molten salt power tower techno-economic performance. Solar Energy 2023;264:112073. https://doi.org/10.1016/j.solener.2023.112073.
[21] Monjurul Ehsan M, Guan Z, Gurgenci H, Klimenko A. Novel design measures for optimizing the yearlong performance of a concentrating solar thermal power plant using thermal storage and a dry-cooled supercritical CO2 power block. Energy Conversion and Management 2020;216:112980. https://doi.org/10.1016/j.enconman.2020.112980.
[22] De La Calle A, Bayon A, Soo Too YC. Impact of ambient temperature on supercritical CO2 recompression Brayton cycle in arid locations: Finding the optimal design conditions. Energy 2018;153:1016–27. https://doi.org/10.1016/j.energy.2018.04.019.
[23] Neises T. Steady-state off-design modeling of the supercritical carbon dioxide recompression cycle for concentrating solar power applications with two-tank sensible-heat storage. Solar Energy 2020;212:19–33. https://doi.org/10.1016/j.solener.2020.10.041.
[24] Hoopes K, Sánchez D, Crespi F. A New Method for Modelling Off-design Performance of sCO2 Heat Exchangers Without Specifying Detailed Geometry. 2016.
[25] Crespi F, Sánchez D, Hoopes K, Choi B, Kuek N. The Conductance Ratio Method for Off-Design Heat Exchanger Modeling and its Impact on an sCO2 Recompression Cycle. Volume 9: Oil and Gas Applications; Supercritical CO2 Power Cycles; Wind Energy, Charlotte, North Carolina, USA: American Society of Mechanical Engineers; 2017, p. V009T38A025. https://doi.org/10.1115/GT2017-64908.
[26] Dyreby JJ, Klein SA, Nellis GF, Reindl DT. Modeling Off-Design and Part-Load Performance of Supercritical Carbon Dioxide Power Cycles. Volume 8: Supercritical CO2 Power Cycles; Wind Energy; Honors and Awards, San Antonio, Texas, USA: American Society of Mechanical Engineers; 2013, p. V008T34A014. https://doi.org/10.1115/GT2013-95824.
[27] Dyreby JJ. Modeling the supercritical carbon dioxide Brayton cycle with recompression. PhD Thesis. The University of Wisconsin-Madison, 2014.
[28] Ma Y, Morosuk T, Liu M, Liu J. Investigation of off-design characteristics of an improved recompression supercritical carbon dioxide cycle for concentrated solar power application. International Journal of Energy Research 2021;45:1818–35.
[29] Chen R, Romero M, González-Aguilar J, Rovense F, Rao Z, Liao S. Design and off-design performance comparison of supercritical carbon dioxide Brayton cycles for particle-based high temperature concentrating solar power plants. Energy Conversion and Management 2021;232:113870. https://doi.org/10.1016/j.enconman.2021.113870.
[30] Chen R, Barreto G, Romero M, González-Aguilar J. Impact of Site-related Solar Resource and ambient Temperature Condition of Optimizing Particle-based CSP Plant Using Supercritical CO2 Brayton Cycle. SolarPACES Conference Proceedings, poster presentation, Rome, Italy: 2024.
[31] Yang J, Yang Z, Duan Y. Novel design optimization of concentrated solar power plant with S-CO2 Brayton cycle based on annual off-design performance. Applied Thermal Engineering 2021;192:116924. https://doi.org/10.1016/j.applthermaleng.2021.116924.
[32] Heller L, Glos S, Buck R. Techno-economic selection and initial evaluation of supercritical CO2 cycles for particle technology-based concentrating solar power plants. Renewable Energy 2022;181:833–42. https://doi.org/10.1016/j.renene.2021.09.007.
[33] Heller L, Glos S, Buck R. Cost benefit analysis of supercritical CO2 cycles in next-generation solar thermal power plants. Renewable Energy 2026;256:123613. https://doi.org/10.1016/j.renene.2025.123613.
[34] Morosini E, Alfani D, Salah SI, Abdeldayem A, Crespi F, Di Marcoberardino G, et al. Off-design of a CO2-based mixture transcritical cycle for CSP applications: analysis at part load and variable ambient temperature. Applied Thermal Engineering 2023:121735. https://doi.org/10.1016/j.applthermaleng.2023.121735.
[35] Rodríguez-de Arriba P, Crespi F, Sánchez Martínez D, García Rodríguez L. Assessment of Part-Load Operation Strategies of Supercritical Power Cycles Using Carbon Dioxide Mixtures in CSP Plants, Including Air-Cooled Condenser Optimisation. Volume 12: Supercritical CO2, Boston, Massachusetts, USA: American Society of Mechanical Engineers; 2023, p. V012T28A026. https://doi.org/10.1115/GT2023-103665.
[36] Crespi F, Arriba PR, Sánchez D, García-Rodríguez L. Principles of operational optimization of CSP plants based on carbon dioxide mixtures. Applied Thermal Engineering 2024:124871. https://doi.org/10.1016/j.applthermaleng.2024.124871.
[37] Morosini E, Villa E, Quadrio G, Binotti M, Manzolini G. Solar tower CSP plants with transcritical cycles based on CO2 mixtures: A sensitivity on storage and power block layouts. Solar Energy 2023;262:111777. https://doi.org/10.1016/j.solener.2023.05.054.
[38] Neises T, Turchi C. Supercritical carbon dioxide power cycle design and configuration optimization to minimize levelized cost of energy of molten salt power towers operating at 650 °C. Solar Energy 2019;181:27–36. https://doi.org/10.1016/j.solener.2019.01.078.
[39] Brown T, Neises T, Hamilton W, Martinek J. Techno-economic comparison of sCO2 cycles for particle-based CSP at design-point conditions. Solar Energy 2025;302:114034. https://doi.org/10.1016/j.solener.2025.114034.
[40] Aspen Plus | Leading Process Simulation Software | AspenTech n.d. https://www.aspentech.com/en/products/engineering/aspen-plus (accessed June 28, 2023).

[41] Lemmon EW, Bell IH, Huber ML, McLinden MO. NIST Standard Reference Database 23: Reference Fluid Thermodynamic and Transport Properties-REFPROP, Version 10.0, National Institute of Standards and Technology 2018. https://doi.org/10.18434/T4/1502528.
[42] Inc TM. MATLAB version: R2023b 2023.
[43] Bell IH, Wronski J, Quoilin S, Lemort V. Pure and Pseudo-pure Fluid Thermophysical Property Evaluation and the Open-Source Thermophysical Property Library CoolProp. Industrial & Engineering Chemistry Research 2014;53:2498–508. https://doi.org/10.1021/ie4033999.
[44] JRC Photovoltaic Geographical Information System (PVGIS) - European Commission n.d. https://re.jrc.ec.europa.eu/pvg_tools/en/ (accessed May 28, 2025).
[45] Moreno-Tejera S, Silva-Pérez MA, Lillo-Bravo I, Ramírez-Santigosa L. Solar resource assessment in Seville, Spain. Statistical characterisation of solar radiation at different time resolutions. Solar Energy 2016;132:430–41. https://doi.org/10.1016/j.solener.2016.03.032.
[46] National Renewable Energy Laboratory. System Advisor Model Version 2022.11.21 (SAM 2022.11.21). NREL SAM 2022. https://https://sam.nrel.gov (accessed February 22, 2024).
[47] NIST Standard Reference Database 103b. NIST 2010.
[48] Span R, Wagner W. A New Equation of State for Carbon Dioxide Covering the Fluid Region from the Triple-Point Temperature to 1100 K at Pressures up to 800 MPa. J Phys Chem Ref Data 1996;25:1509–96. https://doi.org/10.1063/1.555991.
[49] Peng D-Y, Robinson DB. A New Two-Constant Equation of State. Ind Eng Chem Fund 1976;15:59–64. https://doi.org/10.1021/i160057a011.
[50] Ely JF, Hanley HJ. A computer program for the prediction of viscosity and thermal conductivity in hydrocarbon mixtures. vol. 13. US Department of Commerce, National Bureau of Standards; 1981.
[51] Naumov V, Doninelli M, Di Marcoberardino G, Iora P, Invernizzi C. High temperature Cesium-sCO2 combined cycle for concentrating solar power applications. Solar Energy 2024;275:112599. https://doi.org/10.1016/j.solener.2024.112599.
[52] Weiland N, Thimsen D. A practical look at assumptions and constraints for steady state modeling of sCO2 Brayton power cycles, San Antonio, Texas: National Energy Technology Laboratory (NETL), Pittsburgh, PA, Morgantown, WV …; 2016.
[53] Doninelli M, Di Marcoberardino G. On the Design of Recuperator for Transcritical Cycle Adopting CO2-Based Mixture as Working Fluid: A Focus on Transport Properties Prediction. Energy Technology 2024;12:2300677. https://doi.org/10.1002/ente.202300677.
[54] Naumov V, Gedik E, Petersen N, Di Marcoberardino G, Iora P, Wirsum M. Comparison of sCO2, CO2 mixture, and steam Rankine cycles for CSP with components sizing: implications for cost and flexibility. 6th Edition of the European Conference on Supercritical CO2 (sCO2) for Energy Systems, Conference Proceedings of the European sCO2 Conference, Delft, Netherlands: DuEPublico: Duisburg-Essen Publications Online; 2025, p. 244--254. https://doi.org/10.17185/DUEPUBLICO/83332.
[55] Lariviere B, Marion J, Macadam S, McDowell M, Lesemann M, McClung A, et al. sCO2 power cycle development and STEP Demo pilot project. Conference Proceedings of the European sCO2 Conference4th European sCO2 Conference for Energy Systems: March 23-24 2021;2021:352. https://doi.org/10.17185/DUEPUBLICO/73979.
[56] Gnielinski V. New equations for heat and mass transfer in turbulent pipe and channel flow. International Chemical Engineering 1976;16:359–67.
[57] Cavallini A, Col DD, Doretti L, Matkovic M, Rossetto L, Zilio C, et al. Condensation in Horizontal Smooth Tubes: A New Heat Transfer Model for Heat Exchanger Design. Heat Transfer Engineering 2006;27:31–8. https://doi.org/10.1080/01457630600793970.
[58] Bell KJ, Ghaly MA. An approximate generalized design method for multicomponent/partial condensers. AIChE Symp. Ser., vol. 69, 1973, p. 72–9.
[59] Chen NH. An Explicit Equation for Friction Factor in Pipe. Ind Eng Chem Fund 1979;18:296–7. https://doi.org/10.1021/i160071a019.
[60] Del Col D, Bisetto A, Bortolato M, Torresin D, Rossetto L. Experiments and updated model for two phase frictional pressure drop inside minichannels. International Journal of Heat and Mass Transfer 2013;67:326–37. https://doi.org/10.1016/j.ijheatmasstransfer.2013.07.093.
[61] Idelʹchik IE. Handbook of Hydraulic Resistance. 4th ed. Begell House; 2008.
[62] Shiferaw D, Carrero JM. Economic analysis of SCO2 cycles with PCHE Recuperator design optimisation 2016.
[63] Schappel D, Terrani K. Key Material Properties for Thermo-Structural Analysis of Transformational Challenge Reactor Core Components. 2019. https://doi.org/10.2172/1558508.
[64] Le Pierres R, Southall D, Osborne S. Impact of mechanical design issues on printed circuit heat exchangers. Proceedings of SCO2 power cycle symposium, vol. 2011, University of Colorado Bolder; 2011.
[65] Investigation of thermal storage and steam generator issues. 1993. https://doi.org/10.2172/10189397.
[66] Crespi F, Sánchez D, Sánchez T, Martínez GS. Capital Cost Assessment of Concentrated Solar Power Plants Based on Supercritical Carbon Dioxide Power Cycles. Journal of Engineering for Gas Turbines and Power 2019;141:071011. https://doi.org/10.1115/1.4042304.
[67] Lee SW, Kwon JG, Kim MH, Jo H. Cycle analysis and economic evaluation for seawater-LNG Organic Rankine Cycles. Energy 2021;234:121259. https://doi.org/10.1016/j.energy.2021.121259.

[68] Weiland NT, Lance BW, Pidaparti SR. sCO2 Power Cycle Component Cost Correlations From DOE Data Spanning Multiple Scales and Applications. Volume 9: Oil and Gas Applications; Supercritical CO2 Power Cycles; Wind Energy, Phoenix, Arizona, USA: American Society of Mechanical Engineers; 2019, p. V009T38A008. https://doi.org/10.1115/GT2019-90493.
[69] Monjurul Ehsan M, Guan Z, Klimenko AY, Wang X. Design and comparison of direct and indirect cooling system for 25 MW solar power plant operated with supercritical CO2 cycle. Energy Conversion and Management 2018;168:611–28. https://doi.org/10.1016/j.enconman.2018.04.072.
[70] Shah RK, Sekulić DP. Fundamentals of heat exchanger design. Hoboken, NJ: John Wiley & Sons; 2003. https://doi.org/10.1002/9780470172605.
[71] Swan WP, Fernandes DP, Khade A, Chen DH. Abnormal Situation Management: Detection of Fouling and Longitudinal Bypass in Heat Exchangers. IJCEA 2018;9:9–15. https://doi.org/10.18178/ijcea.2018.9.1.691.
[72] Rodríguez-de Arriba P, Crespi F, Sánchez D, Muñoz A. A methodology to design air-cooled condensers for supercritical power cycles using carbon dioxide and carbon dioxide mixtures. Conference Proceedings of the European sCO2 Conference5th European sCO2 Conference for Energy Systems: March 14-16 2023;2023:283. https://doi.org/10.17185/DUEPUBLICO/77329.
[73] Krasnoshchekov E, Protopopov V. Experimental study of heat exchange in carbon dioxide in the supercritical range at high temperature drops. Teplofizika Vysokikh Temperatur 1966;4:389–98.
[74] Olson DA, Allen D. Heat transfer in turbulent supercritical carbon dioxide flowing in a heated horizontal tube. Gaithersburg, MD: National Institute of Standards and Technology; 1998. https://doi.org/10.6028/NIST.IR.6234.
[75] Olson DA. Heat transfer of supercritical carbon dioxide flowing in a cooled horizontal tube. Gaithersburg, MD: National Institute of Standards and Technology; 2000. https://doi.org/10.6028/NIST.IR.6496.
[76] White MT, Bianchi G, Chai L, Tassou SA, Sayma AI. Review of supercritical CO2 technologies and systems for power generation. Applied Thermal Engineering 2021;185:116447.
[77] Illyés V, Morosini E, Doninelli M, David P-L, Guerif X, Werner A, et al. Design of an Air-Cooled Condenser for CO2-Based Mixtures: Model Development, Validation and Heat Exchange Gain with Internal Microfins. Volume 9: Supercritical CO2, Rotterdam, Netherlands: American Society of Mechanical Engineers; 2022, p. V009T28A016. https://doi.org/10.1115/GT2022-82438.
[78] Hamilton WT, Newman AM, Wagner MJ, Braun RJ. Off-design performance of molten salt-driven Rankine cycles and its impact on the optimal dispatch of concentrating solar power systems. Energy Conversion and Management 2020;220:113025. https://doi.org/10.1016/j.enconman.2020.113025.
[79] Naumov V, Di Marcoberardino G, Iora P. sCO2 and CO2 mixture cycles off-design operation in CSP plants. Book of abstracts. EU-Solaris 2nd Doctoral Colloquium 2025, Almería, Spain: 2025.
[80] Naumov V, Mantegazza M, Doninelli M, Di Marcoberardino G, Iora P, Rottoli M. Comparison of Shell and Tube Heat Exchangers for CO2 and CO2+SiCl4 Mixtures Transcritical Cycles. SolarPACES Conf Proc 2025;3. https://doi.org/10.52825/solarpaces.v3i.2331.
[81] Jüdes M, Vigerske S, Tsatsaronis G. Optimization of the Design and Partial-Load Operation of Power Plants Using Mixed-Integer Nonlinear Programming. In: Kallrath J, Pardalos PM, Rebennack S, Scheidt M, editors. Optimization in the Energy Industry, Berlin, Heidelberg: Springer Berlin Heidelberg; 2009, p. 193–220. https://doi.org/10.1007/978-3-540-88965-6_9.
[82] Spencer RC, Cotton KC, Cannon CN. A Method for Predicting the Performance of Steam Turbine-Generators, 16,500 kW and Larger. Journal of Engineering for Power 1963;85:249–98. https://doi.org/10.1115/1.3677341.
[83] Li X, Shu G, Tian H. Integrating off-design performance in designing CO2 power cycle systems for engine waste heat recovery. Energy Conversion and Management 2019;201:112146. https://doi.org/10.1016/j.enconman.2019.112146.
[84] Wu C, Wang S, Li J. Parametric study on the effects of a recuperator on the design and off-design performances for a CO2 transcritical power cycle for low temperature geothermal plants. Applied Thermal Engineering 2018;137:644–58. https://doi.org/10.1016/j.applthermaleng.2018.04.029.
[85] Abdeldayem AS, Salah SI, Aqel OA, White MT, Sayma AI. Design of a 130 MW Axial Turbine Operating with a Supercritical Carbon Dioxide Mixture for the SCARABEUS Project. IJTPP 2024;9:5. https://doi.org/10.3390/ijtpp9010005.
[86] Turbines - OffDesign - Stodola n.d. https://help.ebsilon.com/EN/Part_load_Steam_Turbine.html (accessed August 12, 2025).
[87] Sato T, Oh JM, Engeda A. Experimental and Numerical Investigation of the Flow in a Vaneless Diffuser of a Centrifugal Compressor Stage. Part 1: Experimental Investigation. Proceedings of the Institution of Mechanical Engineers, Part C: Journal of Mechanical Engineering Science 2005;219:1053–9. https://doi.org/10.1243/095440605X31904.
[88] Manente G, Toffolo A, Lazzaretto A, Paci M. An Organic Rankine Cycle off-design model for the search of the optimal control strategy. Energy 2013;58:97–106. https://doi.org/10.1016/j.energy.2012.12.035.
[89] Mehos M, Price H, Cable R, Kearney D, Kelly B, Kolb G, et al. Concentrating Solar Power Best Practices Study. National Renewable Energy Laboratory; 2020. https://doi.org/10.2172/1665767.
[90] Fonstad K. Sizing VFDs for HVAC Applications, Based on the National Electrical Code. New Berlin, USA: ABB Inc.; 2017.

[91] Morosini E, Astolfi M, Doninelli M, Iora P, Serret D, Hugo J-M, et al. Preliminary Characterization of the Desolination Project Demo Plant: Design and Off-Design Operability. Volume 11: Supercritical CO2, London, United Kingdom: American Society of Mechanical Engineers; 2024, p. V011T28A023. https://doi.org/10.1115/GT2024-127246.
[92] Tom B, Smith J, Day Towler M. Inventory management operational strategies for a 10 MWe sCO2 power block. Proceedings of the 7th International sCO2 Power Cycles Symposium, San Antonio, TX, USA, San Antonio, Texas, USA: 2022, p. 13.
[93] Illyés VC, Di Marcoberardino G, Werner A, Haider M, Manzolini G. Experimental evaluation of the CO2-based mixture CO2/C6F6 in a recuperated transcritical cycle. Energy 2024:133713. https://doi.org/10.1016/j.energy.2024.133713.
[94] Naumov V, Di Marcoberardino G, Iora P. Preliminary analysis of CO2+GeCl4 and CO2+Cl3FSi mixtures for CSP application. SolarPACES Conf Proc in press.
[95] System advisor model (SAM) case study: Gemasolar. NREL 2013:6.
[96] Morosini E, Gentile G, Binotti M, Manzolini G. Techno-economic assessment of small-scale solar tower plants with modular billboard receivers and innovative power cycles. J Phys: Conf Ser 2022;2385:012109. https://doi.org/10.1088/1742-6596/2385/1/012109.
[97] Glos S, Musch C, Stueer C, Schlehuber D, Wechsung M. Design of an axial sCO2 turbine for a demo plant in an industrial environment. Conference Proceedings of the European sCO2 Conference5th European sCO2 Conference for Energy Systems: March 14-16 2023;2023:162. https://doi.org/10.17185/DUEPUBLICO/77286.
[98] Glos S, Lippe P, Schlehuber D, Kobler S, Wechsung M. Design considerations of sCO2 turbines developed within the CARBOSOLA project. Conference Proceedings of the European sCO2 Conference4th European sCO2 Conference for Energy Systems: March 23-24 2021;2021:106. https://doi.org/10.17185/DUEPUBLICO/73952.
[99] Allison TC, Moore J, Pelton R, Wilkes J, Ertas B. Turbomachinery. Fundamentals and Applications of Supercritical Carbon Dioxide (SCO2) Based Power Cycles, Elsevier; 2017, p. 147–215. https://doi.org/10.1016/B978-0-08-100804-1.00007-4.
[100] Virtanen P, Gommers R, Oliphant TE, Haberland M, Reddy T, Cournapeau D, et al. SciPy 1.0: Fundamental Algorithms for Scientific Computing in Python. Nature Methods 2020;17:261–72. https://doi.org/10.1038/s41592-019-0686-2.
[101] Alfani D, Astolfi M, Binotti M, Silva P, Macchi E. Off-design performance of CSP plant based on supercritical CO2 cycles, Daegu, South Korea: 2020, p. 130001. https://doi.org/10.1063/5.0029801.
[102] Wagner MJ, Wendelin T. SolarPILOT: A power tower solar field layout and characterization tool. Solar Energy 2018;171:185–96. https://doi.org/10.1016/j.solener.2018.06.063.
[103] Manzolini G, Lucca G, Binotti M, Lozza G. A two-step procedure for the selection of innovative high temperature heat transfer fluids in solar tower power plants. Renewable Energy 2021;177:807–22. https://doi.org/10.1016/j.renene.2021.05.153.
[104] Carlson MD, Middleton BM, Ho CK. Techno-Economic Comparison of Solar-Driven SCO2 Brayton Cycles Using Component Cost Models Baselined With Vendor Data and Estimates. ASME 2017 11th International Conference on Energy Sustainability, Charlotte, North Carolina, USA: American Society of Mechanical Engineers; 2017, p. V001T05A009. https://doi.org/10.1115/ES2017-3590.
[105] Davis G, Selkowitz S, Brook M. Comparison of Alternate Cooling Technologies for California Power Plants Economic, Environmental and Other Tradeoffs. Public Interest Energy Research California Energy Commission 2004.

Supplementary materials A: Assessment of working fluid properties interpolation accuracy

To characterize the deviation between original Aspen data and results of interpolation in MATLAB, an 80%CO_2+20%$SiCl_4$ molar mixture is used as an example with a 105°C critical temperature and 113 bar critical pressure, 113.6 bar cricondenbar, and 133.3°C cricondentherm. In Table 8.8 are shown the grid used to interpolate the data for modeling (main grid) and the grid used for consistency check (check grid). Using the main grid data, properties are calculated in MATLAB for points in the check grid and compared with properties obtained in Aspen. The check grid is chosen such that its points would be in the middle of the main grid and to have more points in the supercritical region close to the critical point.

Table 8.8. Grids used for interpolation and check for 80%CO_2+20%$SiCl_4$ molar mixture

Main grid					**Check grid**					
Temperature, °C			**Pressure, bar**		**Temperature, °C**			**Pressure, bar**		
0	60	120	10	70	31	91	350	11	71	131
2	62	122	12	72	33	93	370	13	73	133
4	64	124	14	74	35	95	390	15	75	135
6	66	126	16	76	37	97	410	17	77	137
8	68	128	18	78	39	99	430	19	79	139
10	70	130	20	80	41	101	450	21	81	141
12	72	132	22	82	43	103	470	23	83	143
14	74	134	24	84	45	105	490	25	85	145
16	76	155	26	86	47	107	510	27	87	147
18	78	175	28	88	49	109	530	29	89	149
20	80	195	30	90	51	111	550	31	91	151
22	82	215	32	92	53	113	570	33	93	153
24	84	235	34	94	55	115		35	95	155
26	86	255	36	96	57	117		37	97	175
28	88	275	38	98	59	119		39	99	195
30	90	295	40	100	61	121		41	101	215
32	92	315	42	102	63	123		43	103	235
34	94	335	44	104	65	125		45	105	255
36	96	355	46	106	67	127		47	107	
38	98	375	48	108	69	129		49	109	
40	100	395	50	110	71	150		51	111	
42	102	415	52	112	73	170		53	113	
44	104	435	54	114	75	190		55	115	
46	106	455	56	135	77	210		57	117	
48	108	475	58	155	79	230		59	119	
50	110	495	60	175	81	250		61	121	
52	112	515	62	195	83	270		63	123	
54	114	535	64	215	85	290		65	125	
56	116	555	66	235	87	310		67	127	
58	118	575	68	255	89	330		69	129	

In Figure 8.25 is shown the difference between total enthalpy interpolated in MATLAB and calculated in Aspen Plus. Maximum deviations can be seen on the pressure-temperature envelope (PT) at low pressure/temperature and are equal to around 3.2 kJ/kg, which is mainly due to the rapid change from single-phase to two-phase. This will not significantly affect calculations, since during modeling vapor fraction is used as an input and enthalpy change in components is much larger (pump specific work is around 50 kJ/kg, in condenser working fluid loses around 200kJ/kg). At supercritical temperature, the maximum deviation is within 0.5 kJ/kg, at supercritical pressure close to critical point, it is within 0.9 kJ/kg and at lower temperatures within 1.5 kJ/kg (turbine specific work is around 200 kJ/kg).

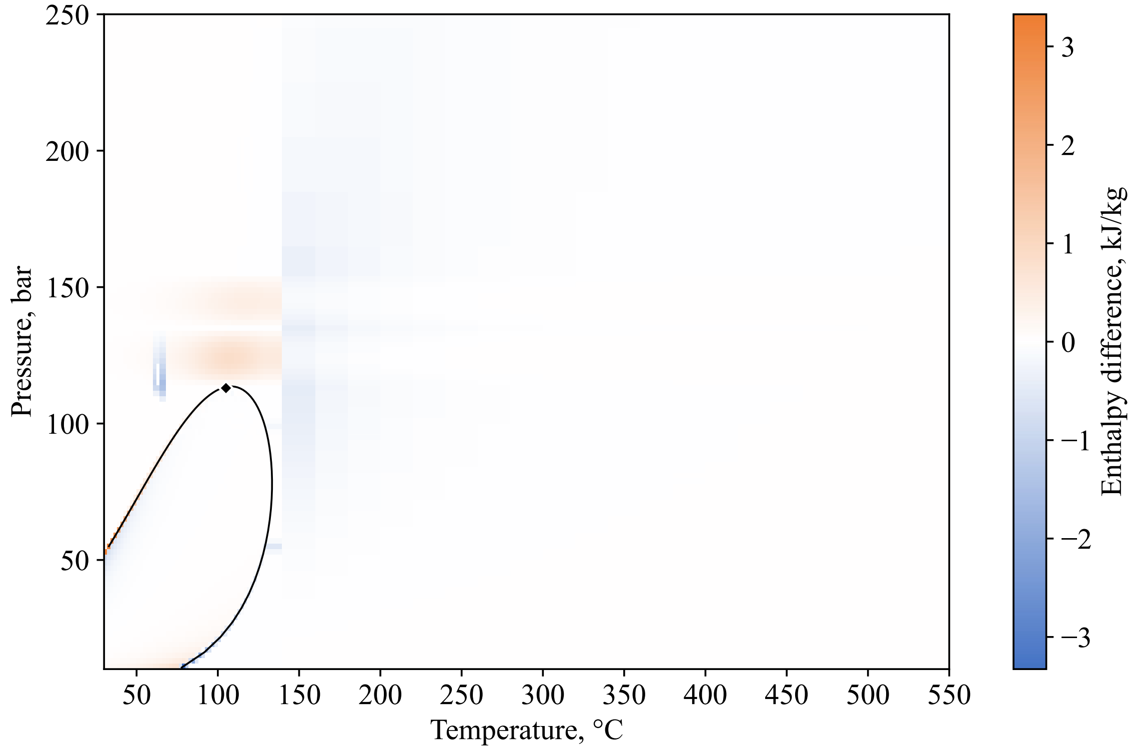

Figure 8.25. Total enthalpy difference between MATLAB and Aspen Plus with line showing PT envelope and diamond for critical point

In Figure 8.26 is presented the PT envelope of the mixture with temperature and vapor fraction used as input in Figure 8.26a and pressure and vapor fraction used in Figure 8.26b. Some of the points could not be interpolated correctly in MATLAB, especially near the critical point and the cricodentherm/cricodenbar due to the existence of multiple points with the same input pressure/temperature and vapor fraction. To quantify the difference between MATLAB interpolation and Aspen results, the average deviation (AAD) calculated according to equation (8.12) is used. For the 53 points present in Figure 8.26a the ADD is 1.07%, while for 59 points in Figure 8.26b the ADD is 0.81%. It should be noted that for power cycle off-design modeling, more importance has the calculation of saturation temperature from the pressure (Figure 8.26b), since the heat transfer processes happen at almost constant pressure.

$$AAD = \frac{100}{n}\sum_{i=1}^{n}\left|\frac{X_i^{inter} - X_i^{ref}}{X_i^{ref}}\right| \tag{8.12}$$

where X_i^{calc} – the interpolated value of the parameter from MATLAB; X_i^{ref} – reference value of the parameter from Aspen Plus; n – number of points.

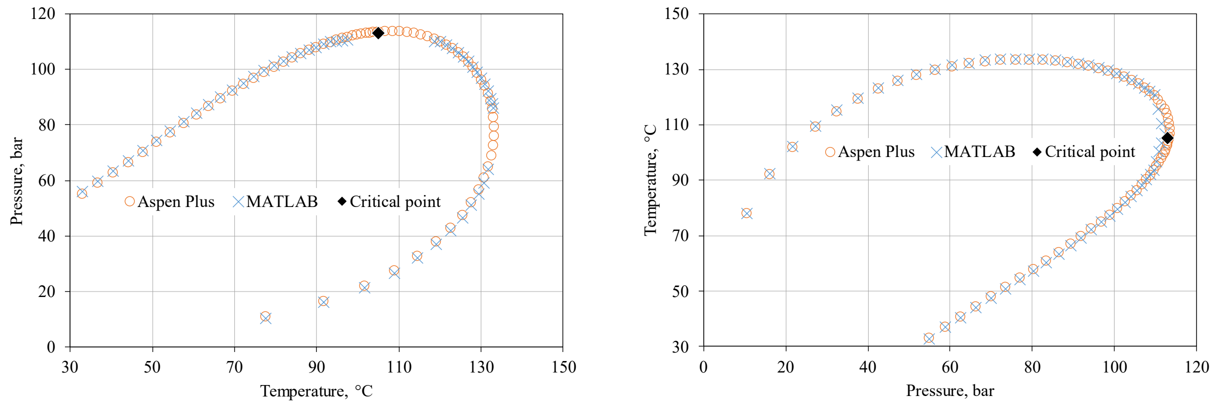

(a) *(b)*

Figure 8.26. PT envelopes using data from Aspen and calculating pressure based on vapor fraction and temperature (a) and temperature based on vapor fraction and pressure (b) of 80%CO_2+20%$SiCl_4$ molar mixture

The supercritical transport properties are compared between Aspen Plus and MATLAB in Figure 8.27. The pressures 115, 125, 135, and 145 are chosen to represent the region close to the critical point (105°C and 113 bar) while not repeating the pressures in the main grid, while 235 bar represents design and off-design operation happening at 220-250 bar (Supplementary materials G: Off-design power cycle results). The deviations are available in Table 8.9 and are below 0.5%. For the temperature between 72°C and 94°C, the Aspen Plus could not converge the transport property model with values belonging to liquid phase at lower temperatures and vapor phase at higher temperatures. Therefore, this data is not considered in both grids and not used in MATLAB.

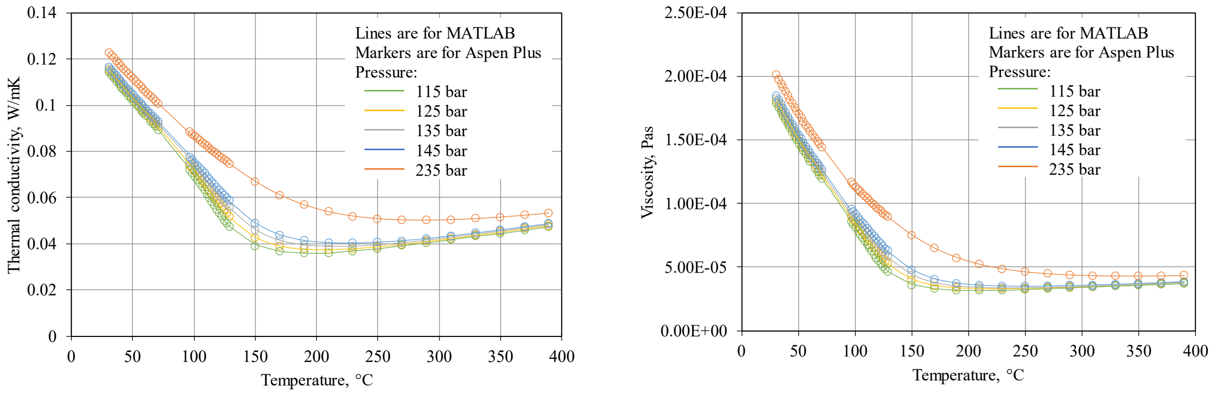

(a) *(b)*

Figure 8.27. Thermal conductivity (a) and viscosity (b) of 80%CO_2+20%$SiCl_4$ molar mixture. Lines correspond to MATLAB interpolation results, markers to Aspen Plus results

The density is compared between Aspen Plus and MATLAB in Figure 8.28. For 114 bar, there is a spice around the critical temperature, while the rest of the data is consistent. At 130 and 250 bar the density dependence on temperature has a monotonous character with deviation between the Aspen Plus and MATLAB below 0.6% (Table 8.9). Therefore, the current MATLAB model can accurately interpolate properties from the tables generated in Aspen Plus both at subcritical and supercritical pressures.

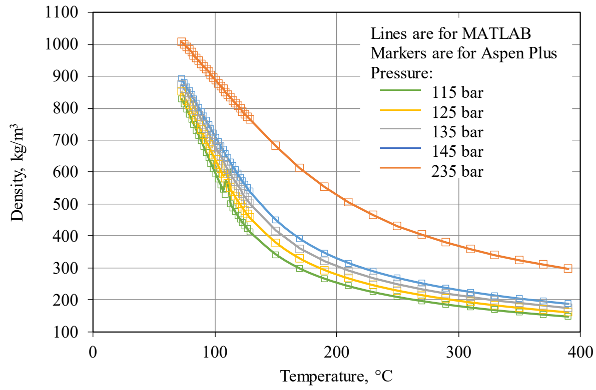

Figure 8.28. Density of supercritical 80%CO_2+20%$SiCl_4$ molar mixture. Lines correspond to MATLAB interpolation results, markers to Aspen Plus results

Table 8.9. Deviations of properties in supercritical region between MATLAB and Aspen Plus

Pressure, bar	Viscosity		Thermal conductivity		Density	
	Points	AAD, %	Points	AAD, %	Points	AAD, %
115	50	0.46	50	0.20		0.47
125	51	0.57	51	0.38		0.51
135	51	0.21	51	0.20	42	0.12
145	51	0.34	51	0.20		0.22
235	51	0.33	51	0.10		0.03

Supplementary materials B: SS316 Allowable stress

The 316 stainless steel allowable stress is shown in Table 8.10.with properties from [1].

Table 8.10. Allowable stress of SS316

T, °C	40	65	100	125	150	200	250	300	325	350	375	400	425	450	475
P, MPa	138	128	118	112	107	99.2	92.8	88.1	86.1	84.1	82.9	82	81.4	80.6	79.8
T, °C	500	525	550	575	600	625	650	675	700	725	750	775	800	825	-
P, MPa	79.2	78.7	77.8	77.1	75	65.5	50.4	38.6	29.6	23	17.7	13.4	10.4	8.05	-

Supplementary materials C: PHE model segments determination and validation

The influence of the number of segments on the power exchanged and pressure drop is carried out varying cold and hot flows and comparing the values obtained with the results of 20 segments. While the power exchanged error has remained below 1% for all segments considered, for pressure drop 8 segments and above should be used as shown in Figure 8.29a. The resulting pressure drop for the whole PHE is compared with the results for two different baffle designs from a rigorous commercial program at equal fractions of mass flow [2] in Figure 8.29b.

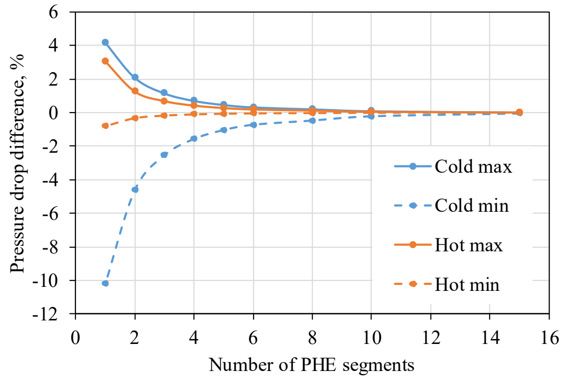

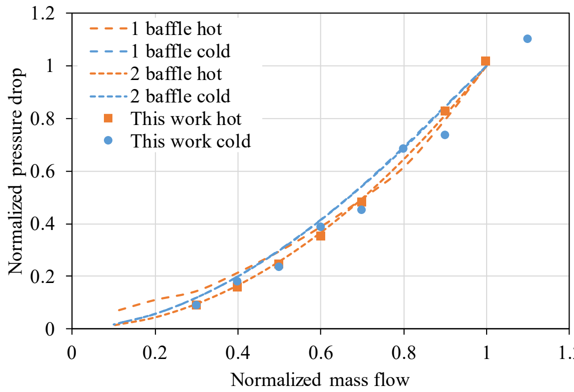

(c) *(d)*

Figure 8.29. Pressure drop sensitivity to number of segments (a) and pressure drop sensitivity to mass flow (b)

Supplementary materials D: PCHE correlations and convergence

Single-phase heat transfer coefficient is calculated according to Gnielinski [3] based on Petukhov and Kirilov equation [4] and Filonenko friction factor [5]:

$$f = (1.82\, log_{10} Re - 1.64)^{-2} \tag{8.13}$$

$$Nu = \frac{f/8(Re - 1000)Pr}{1 + 12.7(\,Pr^{2/3} - 1)\sqrt{f/8}} \tag{8.14}$$

where f – Darcy friction factor; $Re = \frac{GD}{\mu}$ – Reynolds number with D – internal tube diameter, μ – dynamic viscosity and G – mass velocity; Pr – Prandtl number; $Nu = \frac{\alpha D}{\lambda}$ – Nusselt number with α – heat transfer coefficient and λ – thermal conductivity.

Single-phase friction pressure drop is calculated according to Chen explicit correlation [6]:

$$RR = \frac{roughness}{D} \tag{8.15}$$

$$f = \left[-2log_{10}\left(\frac{RR}{3.7065} - \frac{5.0452}{Re} log_{10}\left(\frac{RR^{1.1098}}{2.8257} + \frac{5.8506}{Re^{0.8981}}\right)\right)\right]^{-2} \tag{8.16}$$

where RR – relative roughness; $roughness$ – channel roughness (0.005 mm);

Two phases heat transfer coefficient is calculated according to the Cavallini [7] with Bell and Ghaly correction [8] for zeotropic mixtures:

$$Re_{LO} = \frac{GD}{\mu_L} \tag{8.17}$$

$$X_{tt} = (\frac{\mu_L}{\mu_V})^{0.1}(\frac{\rho_V}{\rho_L})^{0.5}(\frac{1-x}{x})^{0.9} \quad (8.18)$$

$$J_G = \frac{xG}{gD\rho_V(\rho_L - \rho_V)^{0.5}} \quad (8.19)$$

$$J_G^T = \left[(\frac{7.5}{4.3X_{tt}^{1.111}+1})^{-3} + C_T^{-3}\right]^{-1/3} \quad (8.20)$$

$$\alpha_{LO} = 0.023Re_{LO}^{0.8}Pr_L^{0.4}\frac{\lambda_L}{D} \quad (8.21)$$

$$\alpha_{STRAT} = \frac{0.725}{(1+0.741(\frac{1-x}{x})^{0.3321}}\left[\frac{\lambda_L^3\rho_L(\rho_L-\rho_V)g\Delta h_{LV}}{\mu_L D\Delta T}\right]^{0.25} + (1-x^{0.087})\alpha_{LO} \quad (8.22)$$

$$\alpha = \begin{cases} \alpha_A = \alpha_{LO}\left[1+1.128x^{0.817}\left(\frac{\rho_L}{\rho_V}\right)^{0.3685}\left(\frac{\mu_L}{\mu_V}\right)^{0.2363}\left(1-\frac{\mu_V}{\mu_L}\right)^{2.144}Pr_L^{-0.1}\right], if\ J_G > J_G^T \\ \alpha_D = \left[\alpha_A\left(\frac{J_G^T}{J_G}\right)^{0.8} - \alpha_{STRAT}\right]\left(\frac{J_G}{J_G^T}\right) + \alpha_{STRAT}, if\ J_G \le J_G^T \end{cases} \quad (8.23)$$

$$Re_V = \frac{xGD}{\mu_V} \quad (8.24)$$

$$\alpha_V = 0.023Re_V^{0.8}Pr_V^{0.4}\frac{\lambda_V}{D} \quad (8.25)$$

$$\alpha_{corrected} = (\frac{1}{\alpha} + \frac{xCp_V\Delta T_{glide}}{\Delta h_{LV}\alpha_V})^{-1} \quad (8.26)$$

where C_T = 1.6 for hydrocarbons and 2.6 for other refrigerants (this work); g – gravitational acceleration; $_V$ and $_L$ subscripts indicate vapor or liquid property used respectively; Δh_{LV} – latent heat of vaporization/condensation; ΔT – saturation temperature minus wall temperature; Cp – heat capacity; ΔT_{glide}– temperature range over which zeotropic mixture boils or condenses.

Two-phase flows friction pressure drops are calculated according to Del Col [9]:

$$Z = (1-x)^2 + x^2\frac{\rho_L}{\rho_V}(\frac{\mu_V}{\mu_L})^{0.2} \quad (8.27)$$

$$W = 1.398p_r \quad (8.28)$$

$$F = x^{0.9525}(1-x)^{0.414} \quad (8.29)$$

$$H = (\frac{\rho_L}{\rho_V})^{1.132}(\frac{\mu_V}{\mu_L})^{0.44}(1-\frac{\mu_V}{\mu_L})^{3.542} \quad (8.30)$$

$$j_G = \frac{xG_V}{\rho_V} \quad (8.31)$$

$$J_G = \frac{xG_V}{gD_h\rho_V(\rho_L-\rho_V)^{0.5}} \quad (8.32)$$

$$E = \begin{cases} 0.015 + 0.44log\left[(\frac{\rho_{GC}}{\rho_L})(\frac{\mu_L j_G}{\sigma})^2 10^4\right] \\ 0, if\ E \le 0 \\ 0.95, if\ E \ge 0.95 \end{cases} \quad (8.33)$$

$$\rho_{GC} = (\frac{x+(1-x)E}{\frac{x}{\rho_V} + \frac{(1-x)E}{\rho_L}}) \quad (8.34)$$

$$\Phi_{LO}^2 = Z + 3.595 \cdot F \cdot H \cdot (1-E)^W \quad (8.35)$$

$$A = 8.9938Z \cdot 10^{-3} \quad (8.36)$$

$$RR = \frac{2Ra}{D_h} \tag{8.37}$$

$$Re_{LO}^{+} = (\frac{A + 0.7 \cdot RR}{0.046})^{-5} \tag{8.38}$$

$$Re_{LO} = \frac{GD_h}{\mu_L} \tag{8.39}$$

$$X = \begin{cases} 0, if\ Re_{LO} < Re_{LO}^{+} \\ 1, if\ Re_{LO} \geq 3500 \\ 1 + \frac{A - 0.046(Re_{LO})^{-0.2}}{0.7 \cdot RR}, if\ E \geq 0.95 \end{cases} \tag{8.40}$$

$$f_{LO} = \begin{cases} 0.046(Re_{LO})^{-0.2} + 0.7 \cdot RR \cdot X, \quad if\ J_G \geq 2.5 \\ 0.046(\frac{GD_h}{\mu_L})^{-0.2}, if\ Re_{LO} > 2000\ and\ J_G < 2.5 \\ C(\frac{GD_h}{\mu_L})^{-1}, if\ Re_{LO} \leq 2000\ and\ J_G < 2.5 \end{cases} \tag{8.41}$$

$$(\frac{dp}{dz})_f = \Phi_{LO}^2 \frac{2f_{LO}G^2}{D_h \rho_L} \tag{8.42}$$

where $(\frac{dp}{dz})_f$ – frictional pressure gradient; C = 16 for circular cross section (this work) and 14.3 for square cross one; x – vapor mass fraction; p_r – reduced pressure; Ra – roughness; σ – surface tension.

The acceleration pressure drop is calculated as follows:

$$Re_L = \frac{GD(1-x)(1-E)}{\mu_L} \tag{8.43}$$

$$\delta^+ = \begin{cases} (\frac{Re_L}{2})^{0.5}, if\ Re_L < 1145 \\ 0.0504 Re_L^{7/8}, if\ Re_L > 1145 \end{cases} \tag{8.44}$$

$$\delta = \frac{\delta^+ {\rho_L}^{-0.5}}{\left[(\frac{dp}{dz})_f \frac{D}{4}\right]^{0.5}} \tag{8.45}$$

$$\varepsilon = 1 - (\frac{D - 2\delta}{D})^2 \tag{8.46}$$

$$(\frac{dp}{dz})_{acc} = G^2 \frac{d}{dz}\left[\frac{(1-x)^2(1-E)^2}{\varepsilon \rho_L} + \frac{(x + (1-x)E)^2}{(1-\varepsilon)\rho_{GC}}\right] \tag{8.47}$$

where $(\frac{dp}{dz})_{acc}$ – acceleration pressure gradient.

An example of iterative PCHE convergence process for two cycles and two mass flows is shown in Figure 8.30. The thin lines show the intermediate iteration results with the thick line showing the final iteration.

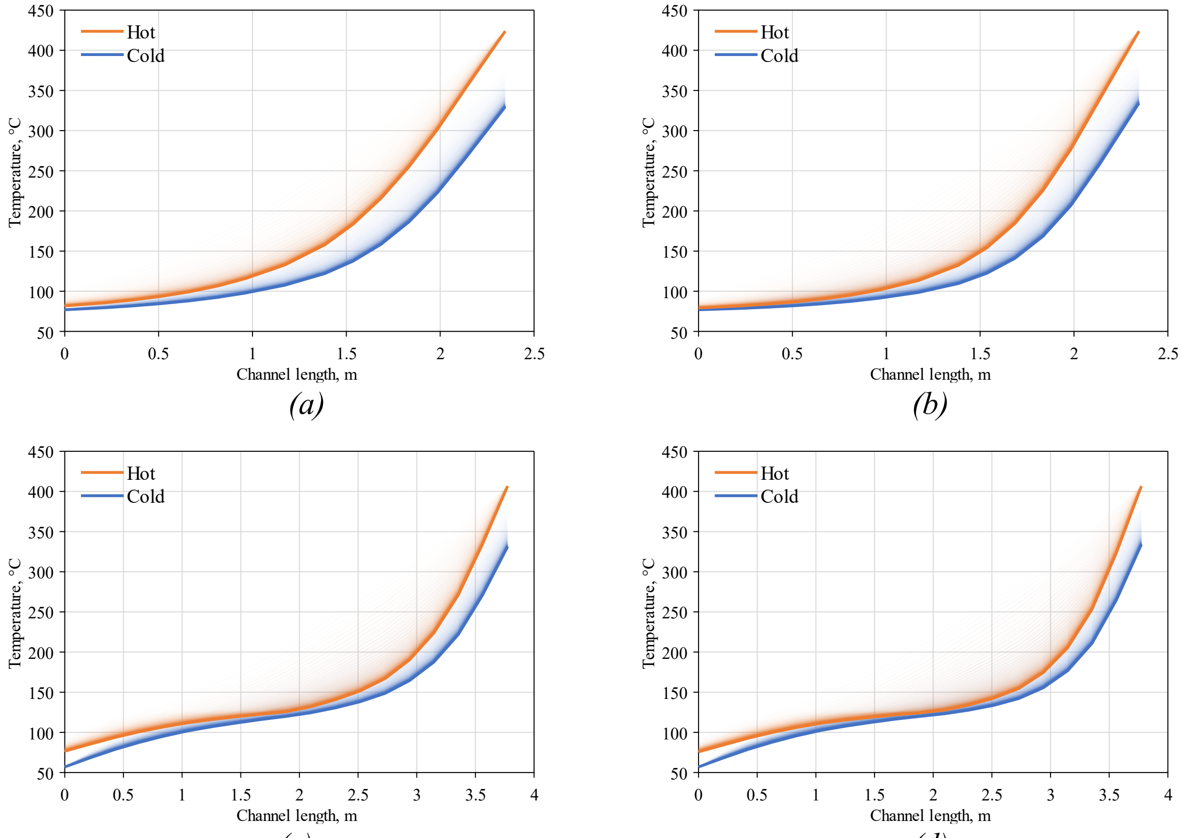

(a) (b)
(c) (d)

Figure 8.30. Temperature distribution along the PCHE length during iterations at 100 and 50% mass flow rates and nominal input temperature and pressures for sCO_2 (a and b) and CO_2 mixture (c and d) cycles with 35°C minimum temperature

Supplementary materials E: Turbomachines off-design models

A comparison of simplified correlations for off-design performance of the turbine is carried out using correlations following sources: Judes et al. (2009) [10], Neises (2020) [11] based on Dyreby correlations [12,13], Spencer et al. (1963) [14], Li et al. (2019) [15], Wu et al. (2018) [16]. As a benchmark, results from Abdeldayem et al. (2024) for 14 stages turbine [17] and Morosini et al. (2023) [18] for 9 stages turbine are considered. Also off-design curves are available in Illyes et al. (2024) [19], however there are no numbers to compare to. The turbines with pressure ratios closest to the benchmarks are chosen for both sCO_2 and CO_2 mixture (Table 8.11). The results of efficiency and are shown in Figure 8.31. It should be noted that the reduced normalized mass flow of around 70% corresponds to the mass flow fraction of around 30%, which is close to minimum levels to be found during normal operation of the plant. The reduced normalized mass flow is calculated according to [17]:

$$m_{red} = \frac{\dot{m}\sqrt{\gamma R T_{01}}}{D_h^2 \cdot P_{01}} \tag{8.48}$$

where $\dot{m}$ – mass flow; γ – is the specific heat ratio; R – ideal gas constant; D_h – hub diameter; P_1 – turbine inlet pressure; T_1 – turbine inlet temperature.

The turbine off-design efficiency model used in this work as described by Neises [11] is shown below:

$$C_{s,des} = \sqrt{2\Delta h_{is,des}} \tag{8.49}$$

$$C_{s,off} = \sqrt{2\Delta h_{is,off}} \tag{8.50}$$

$$U = \nu_{opt} C_{s,des} \tag{8.51}$$

$$\nu_{off} = U / C_{s,off} \tag{8.52}$$

$$\eta_{is,off} = \eta_{is,des}(1.0626\nu_{off}{}^{4} - 3.0874\nu_{off}{}^{3} + 1.3668\nu_{off}{}^{2} + 1.3567\nu_{off} + 0.17992) \tag{8.53}$$

where Δh_{is} – isentropic enthalpy change; C_s – spouting velocity; ν – velocity ratio ($\nu_{opt} = 0.7476$); U – tip speed; *des* and *off* subscripts indicate property calculated at design and off-design point respectively.

The Stodola formula [20] used for the pressure-mass flow relationship in calculated according to equation:

$$\dot{m}_{off} = \dot{m}_{des} \sqrt{\frac{P_{1,off}^2 - P_{2,off}^2}{P_{1,des}^2 - P_{2,des}^2}} \sqrt{\frac{P_{1,des} V_{1,des}}{P_{1,off} V_{1,off}}} \tag{8.54}$$

where P_2 – turbine outlet pressure; V – specific volume.

Table 8.11. Turbines design point parameters

Turbine	1	2
Cycle fluid	sCO_2	CO_2 mix.
CO_2, mol%	100	78
TIP, bar	250	
TIT, °C	550	
TOP, bar	85	75
Efficiency, %	92	
Mass flow, kg/s	1700	1500
Frequency, Hz	50	

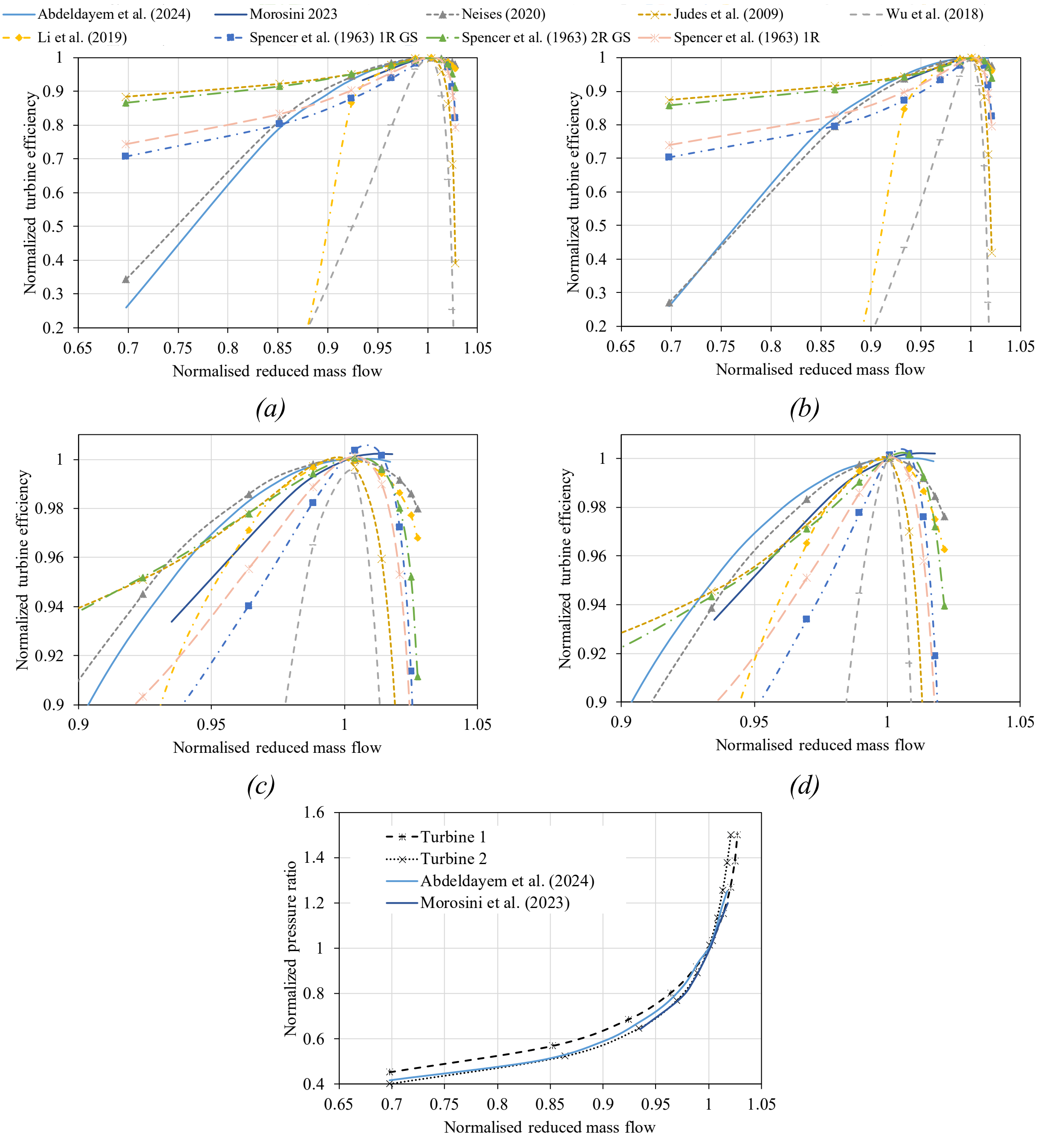

(e)

Figure 8.31. Efficiency vs the normalized reduced mass flow all normalized mass flows (a) and (b) and high values (c) and (d) for Turbine 1 and 2, respectively, and pressure ratio vs mass flow relation (e)

The compressor model as described by Neises [11], based on works of Dyreby [13] and Peng [21] is calculated according to the equations below:

$$U_{des} = \sqrt{\frac{\Delta h_{is,des}}{\psi_{opt}}} \tag{8.55}$$

$$D = \sqrt{\frac{\dot{m}_{des}}{\rho_{in,des} U \phi_{opt}}} \tag{8.56}$$

$$U_{off} = \frac{D}{2} N_{off} \quad (8.57)$$

$$\phi_{off} = \frac{\dot{m}_{off}}{\rho_{in,off} U_{off} D^2} (\frac{N_{off}}{N_{des}})^{1/5} \quad (8.58)$$

$$\psi_{off} = \begin{cases} -4.987 \cdot 10^5 {\phi_{off}}^4 + 5.322 \cdot 10^4 {\phi_{off}}^3 - 2505 {\phi_{off}}^3 + 54.6\phi_{off} + 4.049 \cdot 10^{-2}, if\ \phi_{off} \geq 0.0225 \\ 0.4815 \left[1 + \frac{0.5(0.0225 - \phi_{off})}{0.0225}\right], if\ \phi_{off} < 0.0225 \end{cases} \quad (8.59)$$

$$\Delta h_{is,off} = \psi_{off} {U_{off}}^2 (\frac{N_{off}}{N_{des}})^{(20\phi_{off})^3} \quad (8.60)$$

$$\eta_{is,off} = \frac{\eta_{is,des}}{0.6778} (\frac{N_{off}}{N_{des}})^{(20\phi_{off})^5} (-1.638 \cdot 10^6 {\phi_{off}}^4 + 1.828 \cdot 10^5 {\phi_{off}}^3 - 8089 {\phi_{off}}^3 + 168.8\phi_{off} - 0.7069) \quad (8.61)$$

where ψ – isentropic head coefficient ($\psi_{opt} = 0.4618$ [22]); ϕ – flow coefficient ($\phi_{opt} = 0.02971$); ρ – density; D – compressor impeller diameter ; N – rotational speed.

The pump model is adapted from [23] and consists of two equations that correlate normalized efficiency and head pump rise to normalized volume flow (8.62) using coefficients from Table 8.12 and two correlations that describe the operation at off-design frequency (8.63),(8.64).

$$Y = A(\frac{VF_{in,off}}{VF_{in,des}})^2 + B\frac{VF_{in,off}}{VF_{in,des}} + C \quad (8.62)$$

$$\dot{m}_{off} = \dot{m}_{des}(\frac{\rho_{in,off}}{\rho_{in,des}})(\frac{N_{off}}{N_{des}}) \quad (8.63)$$

$$\Delta h_{is,off} = \Delta h_{is,des}(\frac{N_{off}}{N_{des}})^2 \quad (8.64)$$

where VF – volume flow.

Table 8.12. Pump efficiency and head curve parameters

Resulting parameter (Y)	A	B	C
Normalized efficiency	-1.0108	2.0164	-0.0056
Normalized head	-0.2704	-0.0182	1.2885

Supplementary materials F: Condenser correlations comparison and validation

The Krasnoshchekov-Protopopov [24] correlation is shown below:

$$\overline{Cp} = \frac{h_W - h_B}{T_W - T_B} \quad (8.65)$$

$$n = \begin{cases} 0.4, if\ \frac{T_W}{T_M} < 1\ or\ \frac{T_B}{T_M} \geq 1.25 \\ 0.4 + 0.18\left(\frac{T_W}{T_M} - 1\right), if\ \frac{T_B}{T_M} < 1 \leq \frac{T_W}{T_M} < 1 \\ 0.4 + 0.18\left(\frac{T_W}{T_M} - 1\right)\left[1 - 5\left(\frac{T_B}{T_M} - 1\right)\right], if\ \frac{T_W}{T_M} \geq 1\ and\ 1 < \frac{T_B}{T_M} < 1.2 \end{cases} \quad (8.66)$$

$$Nu_{KP} = Nu_G (\frac{\rho_W}{\rho_B})^{0.3} (\frac{\overline{Cp}}{Cp_B})^{0.3} \quad (8.67)$$

where Nu_G – Nusselt number calculated according to Gnielinski correlation (8.14); T – temperature; h – enthalpy; $_W$ and $_B$ subscripts indicate property calculated at wall or bulk temperature respectively T_M – temperature at which the Cp is maximum at the operating pressure (pseudocritical pressure).

The differences between Gnielinski and Krasnoshchekov-Protopopov correlations are shown in Figure 8.32. Coolers are calculated for different working fluid outlet parameters. The darker lines correspond to the lower rows with lower temperatures, closer to the exit of the cooler and the entrance of air. There is a clear difference between the cases further away from the pseudocritical line (Figure 8.32a and Figure 8.32b) and closer (Figure 8.32c and Figure 8.32d). When the conditions in the segment are close to the pseudocritical line, the difference between two correlations becomes bigger, but it always remains within 10% due to the small differences in wall and bulk temperatures of the fluid. The average deviation is 4.3-5.5% with minimum and maximum being -2.2 and 9.7%, which is within the limits of heart transfer correlation error.

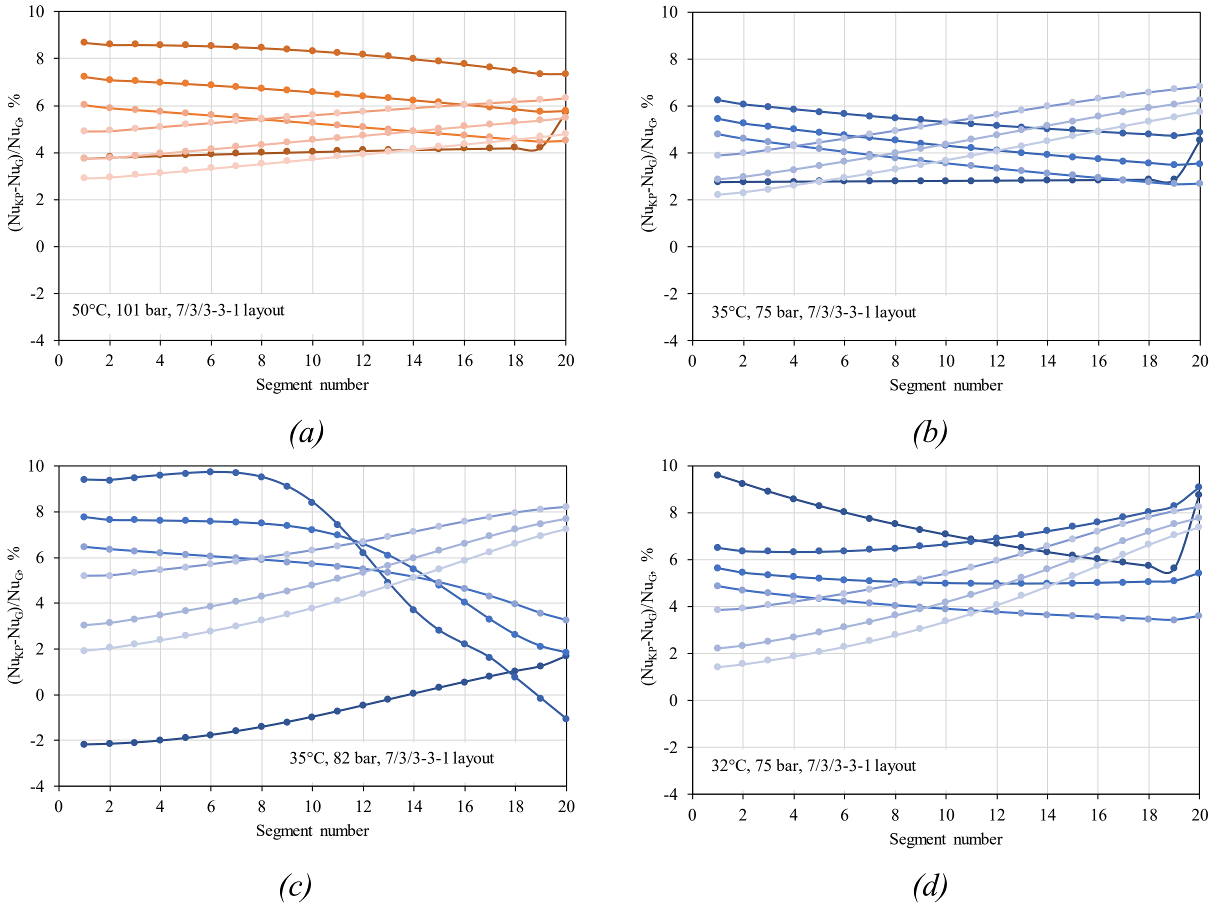

Figure 8.32. Difference between Gnielinski and Krasnoshchekov-Protopopov for different segments and rows of the cooler in 7/3/3-3-1 layout for (a) 50°C and 101 bar, (b) 35°C and 75 bar, (c) 35°C and 82 bar and (d) 32°C and 75 bar outlet parameters

Condenser model validation is carried out against the results available in the literature [18,25,26] and is shown in Table 8.13. In the case of comparison with [18] the calculated air-side tube bank pressure drop is divided by 1.2 to not take into account other friction losses. The difference in the air heat up is -4.2–3.0% with an average of -0.6%, in number of tubes it is -8.9–9.9% with average of 3.3%, in external area it is -7.8–2.5% with an average of -3.0%, in overall HTC it is -4.6–11.3% with an average of 0.8%, in pass length it is -12.2–6.7% with an average of -2.0%. Therefore, the geometric results of the model are close to the literature. On the other hand, the air side pressure drop and, as a result, the fan power are less consistent. The fan power results compared to literature are within -13.7–19.2% with an average of 4.5%, which could be the result of different pressure drop equations being used and inconsistency in the calculation methodologies implementations. On average, the results appear to be within a 5% deviation, which is a good agreement, considering the three different references used.

Table 8.13. Condenser model validation results

Parameter	Source																					
	[18]									[25]							[26]					
Fluid, %mol.	$87CO_2+13C_6F_6$									$92CO_2+8C_6F_6$							CO_2			$85CO_2+15C_6F_6$		
Layout	7/7/1									7/3/ 3-3-1												
$\dot{m}_{wf}$, kg/s	1202.3									1200							752			880		
$T_{wf\ in}$, °C	80.5									114							107			87.1		
$T_{wf\ out}$, °C	51									51							50					
ΔP_{wf}, bar	0.5			1			2			0.46							0.81			0.51		
$T_{air,in}$, °C	36																					
V_{air}, m/s	2.6									3.23							3					
Fan eff., %	43									-							0.681			0.687		
Fouling wf, m²K/W	0.00176																					
Fouling air, m²K/W	0.00176																					
Source	Ref.	Calc.	%	Ref.	Calc.	%	Ref.	Calc.	%	MATLAB	Xace®	[26]	Calc.	%			Ref.	Calc.	%	Ref.	Calc.	%
ΔT_{air}, °C	22.1	21.2	-4.2	23.0	22.2	-3.6	23.9	23.1	-3.4	23.5	23.0	23.5	23.6	0.3	2.4	0.3	24.9	25.7	3.0	19.8	19.9	0.6
N_{tubes}	3830	3958	3.3	2759	2883	4.5	2034	2083	2.4	2030	2242	1858	2042	0.6	-8.9	9.9	990	1088	9.9	1246	1308	5.0
A_{ex}, m²	392029	377960	-3.6	370924	358970	-3.2	354256	341290	-3.7	487800	499500	481135	475700	-2.5	-4.8	-1.1	222480	205090	-7.8	278160	285040	2.5
U, W/m²/K	22.9	22.2	-3.3	24.9	23.8	-4.2	26.6	25.4	-4.6	23.0	21.6	21.9	22.4	-2.5	3.8	2.3	23.6	26.3	11.3	21.5	22.2	3.4
L_{pass}, m	8.2	8.0	-2.4	10.7	10.4	-2.5	14.0	13.7	-1.9	19.3	18.3	20.9	19.5	1.2	6.7	-6.4	18.0	15.8	-12.2	18.0	18.3	1.5
ΔP_{air}, bar	-	61.7	-	72.0	61.9	-14.0	-	61.9	-	-	-	-	-	-	-	-	-	-	-	-	-	
Fan power, kW	890.0	946.0	6.3	800.0	900.6	12.6	720.0	858.1	19.2	-	-	-	-	-	-	-	678.0	585.1	-13.7	812.0	796.8	-1.9

Layout – Tubes/ rows /tubes per pass; U – Overall HTC; A_{ex} – external area; L_{pass} – pass length; $\dot{m}_{wf}$ – working fluid mass flow.

Supplementary materials G: Off-design power cycle results

Results of minimum pressure optimization in sCO_2 cycles are shown in Figure 8.33, with big markers showing design points and lines showing off-design minimum pressure vs minimum cycle temperature relations. The points closely follow the CO_2 pseudocritical line.

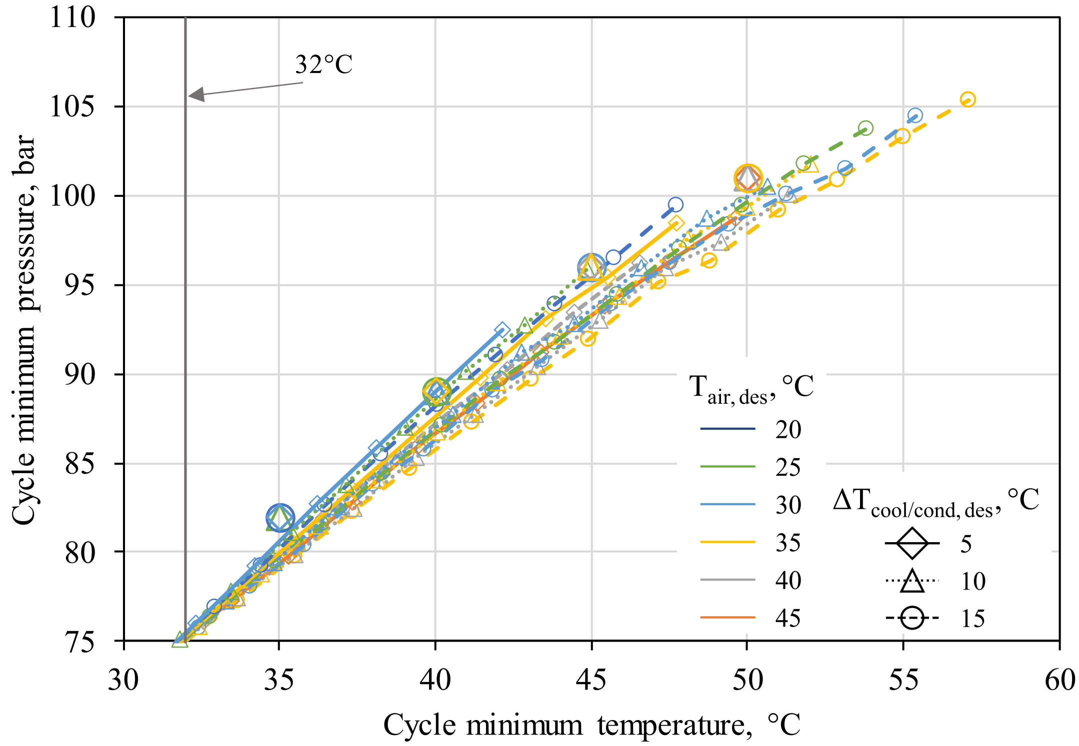

(a)

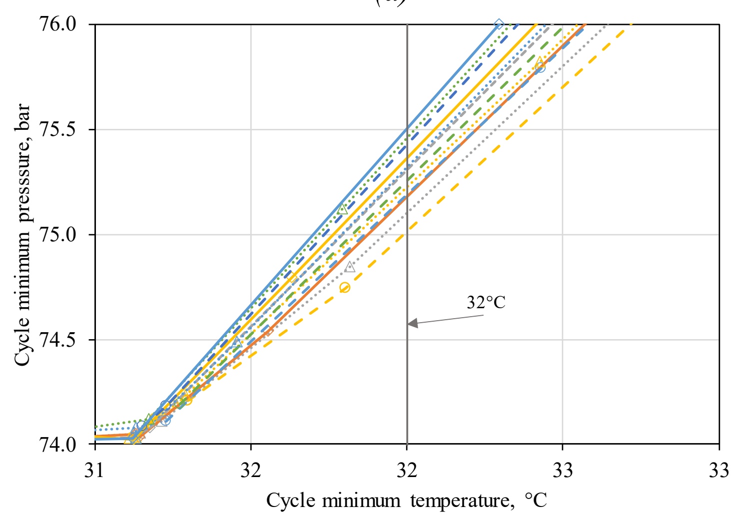

(b)

Figure 8.33. sCO_2 cycles minimum pressure dependence on the minimum temperature

Main off-design power cycle parameters are shown in Figure 8.34. The big markers signify the design point parameters, while small markers are the results of off-design calculations with lines showing interpolation results using the PCHIP interpolator from SciPy [27].

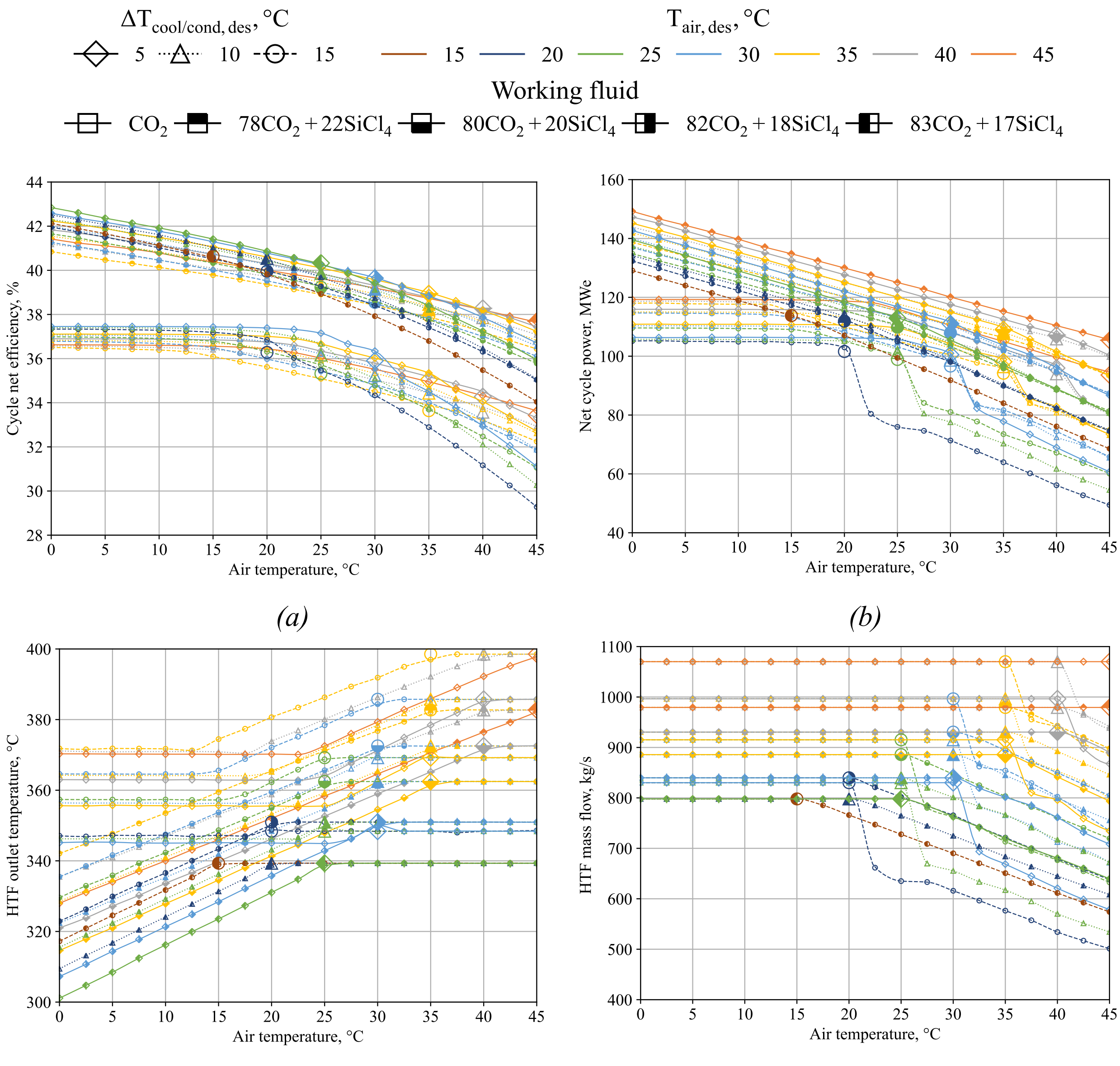

(a) *(b)*

(c) *(d)*

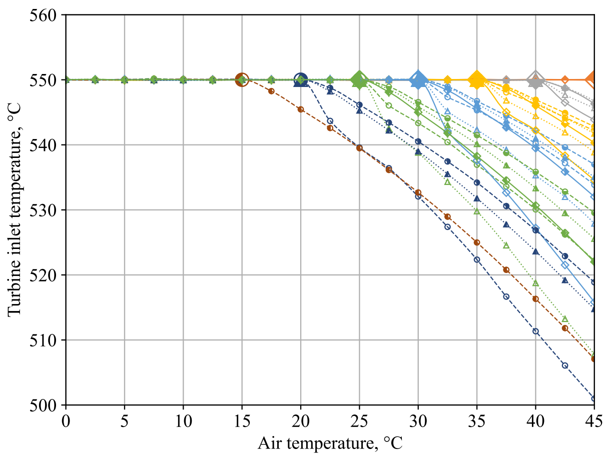
Turbine inlet temperature, °C
Air temperature, °C

(e)

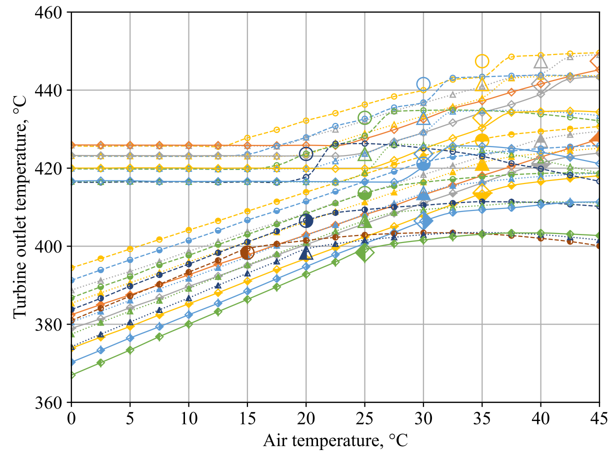
Turbine outlet temperature, °C
Air temperature, °C

(f)

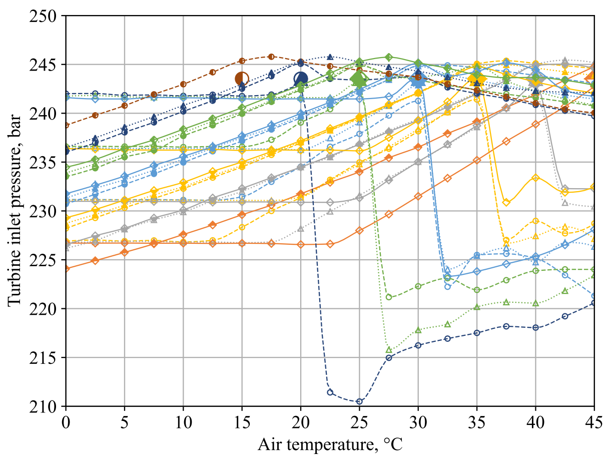
Turbine inlet pressure, bar
Air temperature, °C

(g)

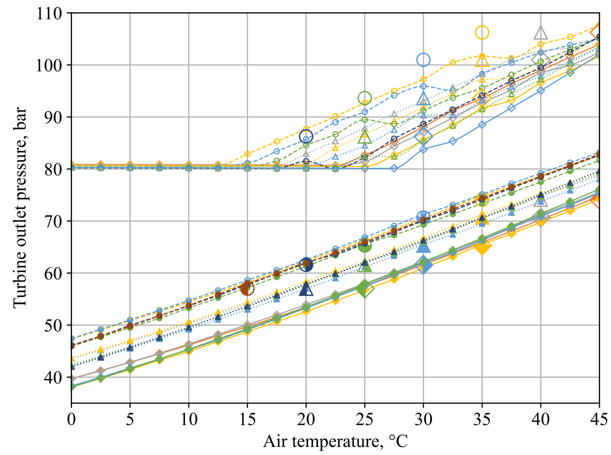
Turbine outlet pressure, bar
Air temperature, °C

(h)

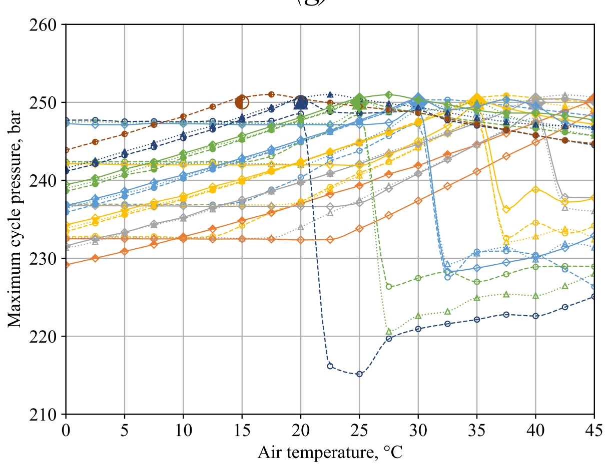
Maximum cycle pressure, bar
Air temperature, °C

(i)

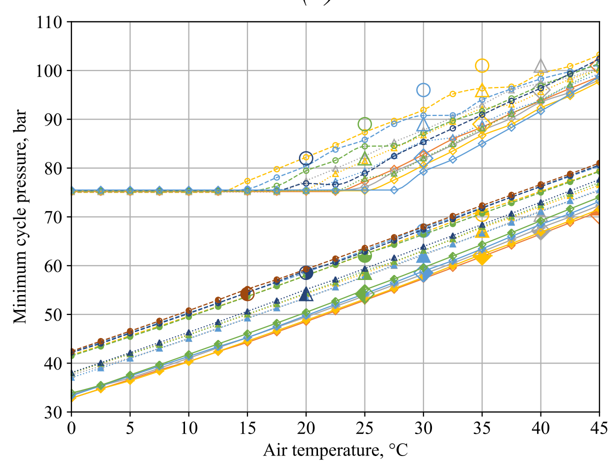
Minimum cycle pressure, bar
Air temperature, °C

(j)

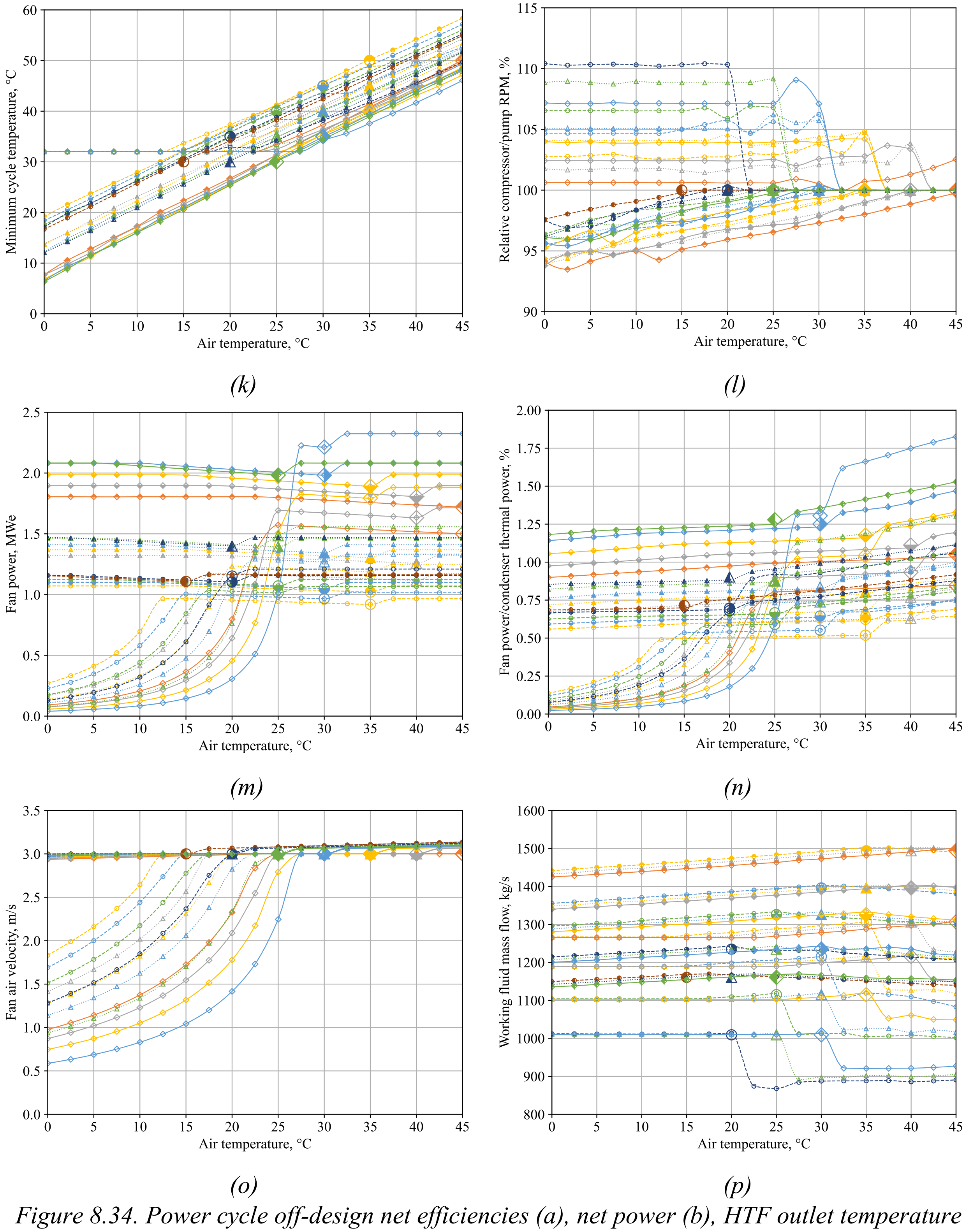

Figure 8.34. Power cycle off-design net efficiencies (a), net power (b), HTF outlet temperature (c), HTF mass flow (d), turbine inlet temperature (TIT) (e), turbine outlet temperature (TOT) (f), turbine inlet pressure (TIP) (g) and turbine outlet pressure (TOP) (h), maximum cycle pressure (i), minimum cycle pressure (j), minimum cycle temperature (k) and pump/compressor RPM fraction (l), fan power (m), fan power fraction of the cooler/condenser thermal power (n), fan air velocity (o) and working fluid mass flow (p)

To assess the influence of the cooler/condenser maximum fan power limitation, cycles off-design operation with a 120% fan power limit is calculated. Since the fan power increases nonlinearly with the volume flow [28], the air velocity at 120% power has increased by 7-10% depending on the air temperature compared to design. For brevity, only the results for the CO_2 cycle with a design air temperature of 20°C and a minimum cycle temperature of 35°C are presented in Figure 8.35. The results indicate that, since the air mass flow rate increase is quite low, further increases in the fan power limit yield only marginal improvements in net efficiency and power.

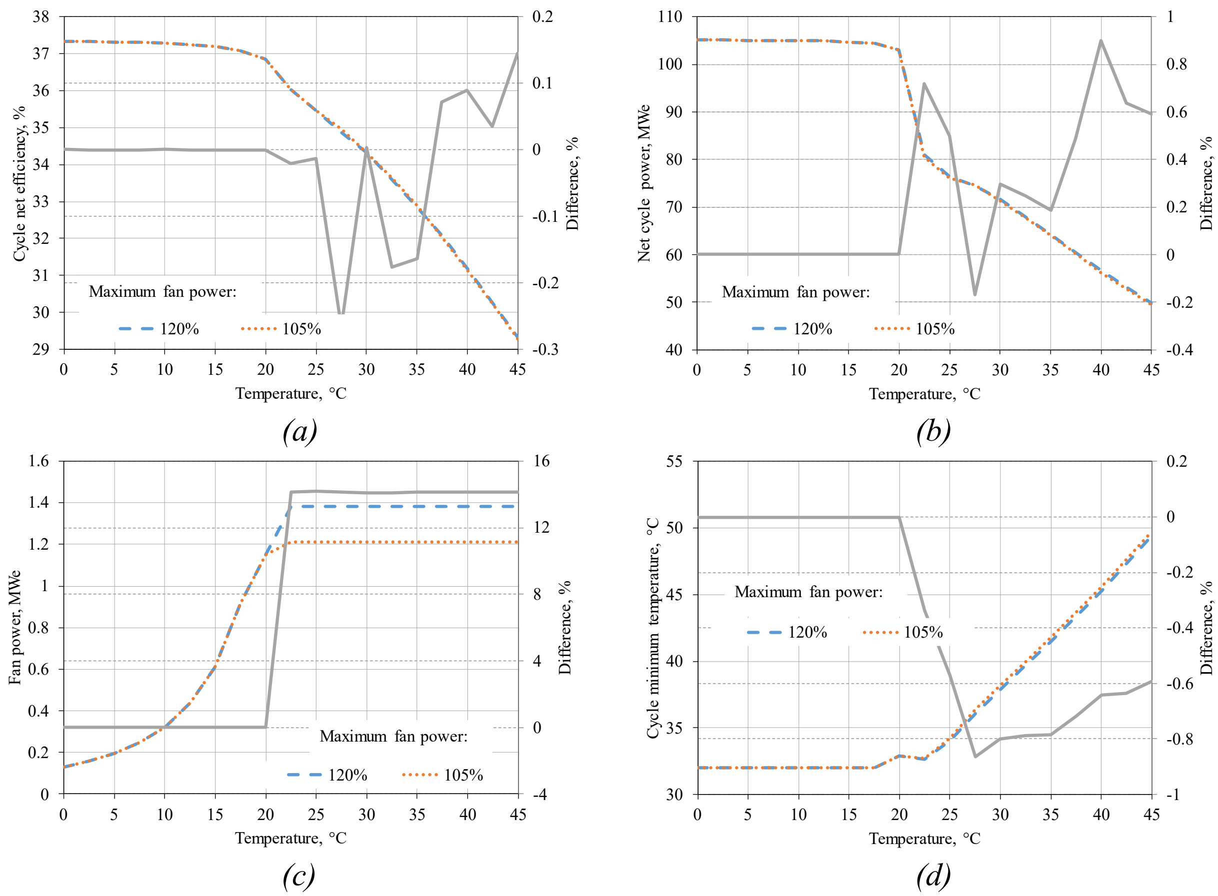

Figure 8.35. Power cycle off-design cycle net efficiency (a), net power (TOT) (b), cooler/condenser fan power (c) and minimum cycle temperature (d) using 105% and 120% fan power limit with deviation shown in grey on the right axis

Supplementary materials H: Power cycle components cost correlations

Costs correlation of the cycle components presented in Table 8.8 are homogenized to 2020 using the Chemical Engineering Plant Cost Index (CEPCI) [29]. The CO_2 mixture pumps costs are calculated as using the correlations for the compressor. Installation costs for the PHE, air cooler/condenser, turbine, compressor, pump, motor, and generator are assumed to be 20% while for the recuperator, 5% [30].

Table 8.14. Power cycle components cost correlations used, USD_{2020}

Component	Correlation	Input	Source
Primary heat exchanger (TIT=550°C)	$C_{PHE}^{2020} = 1.943 \cdot UA \cdot \Delta P_{tube}{}^{-0.2705}$	ΔP_{tube} – tube side pressure drop, bar	[31]
Air cooler/condenser	$C_{cooler/condenser}^{2020} = 34.54 \cdot UA^{0.75}$		[30]
Recuperator (T_{max}<550°C)	$C_{recuperator}^{2020} = 51.95 \cdot UA^{0.7544}$	UA – heat exchanger conductance, W/K	[30]
Turbine (TIT=550°C)	$C_{turbine}^{2020} = 191\,834 \cdot W_t{}^{0.5561}$	W_t – turbine shaft power, MW	[30]
Generator	$C_{generator}^{2020} = 114\,407 \cdot W_t{}^{0.5463}$		[30]
Compressor	$C_{compressor}^{2020} = 1\,292\,204 \cdot W_{c/p}{}^{0.3992}$	$W_{c/p}$ – compressor or pump shaft power, MW	[30]
Open drip-proof motor	$C_{motor}^{2020} = 419\,599 \cdot W_{c/p}{}^{0.6062}$		[30]

Supplementary materials I: CSP plant techno-economic results

Base CSP plant power cycle results with a solar multiple equal to 2.8 and 13 hours of TES are shown in Table 8.15, with the whole plant parameters shown in Table 8.16.The cooler/condenser total width represents all the length of heat exchanger needed with the specified depth (length of a single tube). In practice the cooler/condenser will probably be split in multiple parallel units (3 to 4) with dimensions of 20-40 meters each depending on the cycle.

Table 8.15. Base CSP plant power cycle results

Cycle fluid	sCO$_2$			CO$_2$ mix.			sCO$_2$			CO$_2$ mix.		
$T_{air,des}$, °C	35	40	45	35	40	45	30	35	40	30	35	40
$T_{min,des}$, °C	50						45					
$\Delta T_{cool/cond}$	15	10	5	15	10	5	15	10	5	15	10	5
TES size, h	13	13	13	13	13	13	13	13	13	13	13	13
Solar multiple	2.8	2.8	2.8	2.8	2.8	2.8	2.8	2.8	2.8	2.8	2.8	2.8
Power cycle cost, MUSD												
Turbine		3.72			3.68			3.68			3.69	
Compressor		7.09			-			6.78			-	
Pump		-			6.10			-			5.99	
Generator		2.11			2.09			2.09			2.10	
Motor		5.06			4.03			4.73			3.92	
Cooler/cond.	6.97	8.15	10.27	6.70	7.81	9.78	7.30	8.62	11.07	6.84	8.02	10.13
Recuperator		15.52			22.13			14.22			21.20	
PHE		21.06			20.20			21.01			20.14	
Total	61.54	62.72	64.84	64.93	66.04	68.00	59.80	61.12	63.57	63.87	65.01	67.11
Cycle net power, MWe	95.12	94.92	94.53	107.35	107.11	106.65	97.64	97.42	96.97	109.25	108.99	108.48
Power cycles specific cost, USD$_{2020}$/kWe	646.99	660.74	685.88	604.80	616.57	637.66	612.43	627.42	655.52	584.60	596.44	618.65
Cooler/condenser parameters (only heat exchanger considered)												
Height, m												
Depth, m	19.9	23.3	29.3	21.1	24.7	31.4	21.5	25.5	32.5	21.6	25.6	32.6
Total width, m	85.4	90.6	99.1	90.5	97.0	107.0	82.4	87.6	96.6	89.8	96.5	107.1
Design fan power, MW	0.92	1.12	1.50	1.02	1.26	1.72	0.97	1.19	1.63	1.05	1.30	1.81
Total UA, MW/K	9.20	11.32	15.41	8.71	10.68	14.41	9.77	12.20	17.02	8.94	11.06	15.09
Total footprint, m²	1700	2113	2906	1907	2401	3355	1772	2232	3139	1941	2467	3495

Cycle fluid	sCO$_2$			CO$_2$ mix.			sCO$_2$			CO$_2$ mix.					
$T_{air,des}$, °C	25	30	35	25	30	35	20	25	30	20	25	30	15	20	25
$T_{min,des}$, °C	40						35						30		
$\Delta T_{cool/cond}$	15	10	5	15	10	5	15	10	5	15	10	5	15	10	5
TES size, h	13	13	13	13	13	13	13	13	13	13	13	13	13	13	13
Solar multiple	2.8	2.8	2.8	2.8	2.8	2.8	2.8	2.8	2.8	2.8	2.8	2.8	2.8	2.8	2.8
Power cycle cost, MUSD															
Turbine		3.66			3.70			3.61			3.71			3.72	
Compressor		6.52			-			6.06				-			
Pump		-			5.87			-			5.75			5.65	
Generator		2.08			2.10			2.05			2.11			2.11	
Motor		4.46			3.80			3.99			3.69			3.58	
Cooler/cond.	7.61	9.11	11.97	6.86	8.10	10.35	8.56	10.48	14.37	6.97	8.26	10.64	6.95	8.26	10.63
Recuperator		12.73			20.50			11.57			19.50			18.53	
PHE		20.93			19.97			20.77			19.85			19.71	
Total	58.00	59.50	62.36	62.80	64.03	66.28	56.61	58.54	62.43	61.58	62.87	65.25	60.25	61.56	63.93
Cycle net power, MWe	100.11	99.86	99.33	111.25	110.97	110.42	102.94	102.61	101.87	113.37	113.07	112.48	115.54	115.24	114.65
Power cycles specific cost, USD$_{2020}$/kWe	579.31	595.82	627.83	564.49	577.03	600.27	549.90	570.51	612.84	543.15	556.00	580.11	521.46	534.17	557.65
Cooler/condenser parameters (only heat exchanger considered)															
Height, m		0.4													
Depth, m	23.0	27.5	35.9	21.2	25.3	32.8	26.8	32.8	44.3	21.1	25.1	32.2	21.2	25.4	33.1
Total width, m	80.2	86.0	95.4	92.4	99.4	110.4	77.6	83.8	94.8	95.1	103.2	117.0	94.0	101.1	112.5
Design fan power, MW	1.01	1.27	1.79	1.07	1.34	1.89	1.15	1.48	2.21	1.10	1.39	1.98	1.11	1.40	1.98
Total UA, MW/K	10.31	13.10	18.86	8.98	11.20	15.52	12.04	15.79	24.04	9.16	11.49	16.11	9.11	11.46	16.06
Total footprint, m²	1845	2363	3420	1964	2518	3626	2083	2747	4197	2004	2587	3764	1990	2571	3727

SM – solar multiple; $\eta_{sol.\ to\ th.}$ - annual solar to thermal efficiency; $\eta_{sol.\ to\ el.}$ - annual solar to electric efficiency; CF - capacity factor; EE – electricity generated per year; Heliostats – heliostat field cost; R&T – receiver and tower cost; TES – TES cost; Power cycle – power cycle cost; TCC – total capital cost (installed cost).

Table 8.16. Base CSP plant results

Cycle fluid	sCO₂			CO₂ mix.			sCO₂			CO₂ mix.			sCO₂			CO₂ mix.			sCO₂			CO₂ mix.					
$T_{air,des}$, °C	35	40	45	35	40	45	30	35	40	30	35	40	25	30	35	25	30	35	20	25	30	20	25	30	15	20	25
$T_{min,des}$, °C	50						45						40						35						30		
$\Delta T_{cool/cond}$	15	10	5	15	10	5	15	10	5	15	10	5	15	10	5	15	10	5	15	10	5	15	10	5	15	10	5
TES size, h														13													
SM														2.8													
$\eta_{sol. to th.}$, %	43.0	43.2	43.3	43.0	43.2	43.4	42.4	43.0	43.3	42.8	43.1	43.4	41.3	42.4	43.0	42.3	42.8	43.2	39.0	40.8	41.9	41.6	42.3	42.9	40.9	41.7	42.4
$\eta_{sol. to el.}$, %	14.2	14.4	14.6	15.8	16.0	16.2	14.2	14.5	14.8	15.8	16.1	16.3	13.9	14.5	14.8	15.8	16.2	16.5	13.3	14.1	14.6	15.6	16.1	16.4	15.3	15.8	16.3
CF, %	66.5	67.8	68.9	65.5	66.5	67.6	64.6	66.4	67.8	64.3	65.7	66.8	61.8	64.4	66.2	62.8	64.5	66.0	57.0	60.8	63.6	60.8	62.9	64.6	58.4	60.7	62.8
EE, GWh/year	538.5	548.0	555.0	602.5	610.3	617.4	538.6	552.3	561.2	602.2	613.7	621.7	529.8	550.8	563.1	600.1	614.5	626.0	503.9	535.1	556.3	592.5	611.2	624.7	581.0	601.7	619.6
Heliostats, MUSD														248.0													
R&T, MUSD														126.1													
TES, MUSD	102.1	102.1	102.1	94.5	94.5	94.5	95.9	95.9	95.9	90.3	90.3	90.3	89.0	89.0	89.0	86.5	86.5	86.5	81.7	81.7	81.7	82.6	82.6	82.6	79.0	79.0	79.0
Power cycle, MUSD	61.5	62.7	64.8	64.9	66.0	68.0	59.8	61.1	63.6	63.9	65.0	67.1	58.0	59.5	62.4	62.8	64.0	66.3	56.6	58.5	62.4	61.6	62.9	65.2	60.2	61.6	63.9
TCC, MUSD	676.5	677.9	680.5	671.4	672.8	675.1	666.9	668.5	671.4	665.1	666.5	669.0	656.4	658.2	661.7	659.2	660.7	663.4	645.9	648.2	652.9	652.9	654.5	657.4	647.0	648.6	651.5
LCOE, USD_{2020}/MWh	96.6	95.1	94.2	87.5	86.5	85.8	95.7	93.6	92.4	87.1	85.6	84.8	96.3	92.9	91.3	86.9	85.1	83.8	100.1	94.7	91.7	87.6	85.1	83.6	88.8	86.0	83.9

CSP plant power cycle results with optimized SM and TES size are shown in Table 8.17, with the whole plant parameters shown in Table 8.18.

Table 8.17. Optimum CSP plant power cycle results

Cycle fluid	sCO₂			CO₂ mix.			sCO₂			CO₂ mix.			sCO₂			CO₂ mix.			sCO₂			CO₂ mix.					
$T_{air,des}$, °C	35	40	45	35	40	45	30	35	40	30	35	40	25	30	35	25	30	35	20	25	30	20	25	30	15	20	25
$T_{min,des}$, °C	50						45						40						35						50		
$\Delta T_{cool/cond}$	15	10	5	15	10	5	15	10	5	15	10	5	15	10	5	15	10	5	15	10	5	15	10	5	15	10	5
TES size, h	12	12	12	12	12	12	12	12	12	12	12	12	12	12	12	12	12	12	11	11	12	12	12	12	11	12	12
Solar multiple	3	3	3.1	3	3	3.1	2.8	3	3	2.9	3	3.1	2.7	2.8	2.9	2.8	2.9	3	2.3	2.5	2.7	2.7	2.8	2.9	2.5	2.7	2.8
Power cycle cost, MUSD																											
Turbine	3.58	3.58	3.51	3.54	3.54	3.48	3.68	3.54	3.54	3.62	3.55	3.49	3.74	3.66	3.59	3.70	3.63	3.56	4.03	3.85	3.69	3.78	3.71	3.64	3.96	3.80	3.72
Compressor	6.90	6.90	6.81		-		6.78	6.59	6.59		-		6.61	6.52	6.43		-		6.55	6.34	6.15			-			
Pump			-	5.93	5.93	5.85		-		5.90	5.82	5.75		-		5.87	5.79	5.71		-		5.84	5.75	5.67	5.91	5.73	5.65
Generator	2.03	2.03	2.00	2.01	2.01	1.98	2.09	2.01	2.01	2.06	2.02	1.98	2.12	2.08	2.04	2.10	2.06	2.02	2.29	2.18	2.09	2.15	2.11	2.07	2.25	2.16	2.11
Motor	4.86	4.86	4.76	3.86	3.86	3.78	4.73	4.53	4.53	3.83	3.76	3.68	4.56	4.46	4.36	3.80	3.72	3.64	4.49	4.27	4.08	3.77	3.69	3.61	3.84	3.66	3.58
Cooler/cond.	6.62	7.74	9.52	6.36	7.42	9.06	7.30	8.19	10.51	6.66	7.62	9.38	7.82	9.11	11.66	6.86	7.89	9.83	9.92	11.41	14.77	7.16	8.26	10.37	7.57	8.49	10.63
Recuperator	14.73	14.73	14.37	21.01	21.01	20.49	14.22	13.49	13.49	20.65	20.08	19.59	13.09	12.73	12.40	20.50	19.96	19.46	13.43	12.61	11.90	20.04	19.50	18.99	20.18	19.04	18.53
PHE	19.66	19.66	19.02	18.85	18.85	18.24	21.01	19.61	19.61	19.44	18.79	18.19	21.71	20.93	20.21	19.97	19.28	18.64	25.28	23.26	21.54	20.59	19.85	19.17	22.07	20.44	19.71
Total	58.38	59.50	59.99	61.57	62.63	62.90	59.80	57.97	60.29	62.16	61.65	62.07	59.65	59.50	60.70	62.80	62.33	62.86	65.99	63.92	64.21	63.33	62.87	63.51	65.78	63.31	63.93
Cycle net power, MWe	88.78	88.59	85.38	100.20	99.97	96.33	97.64	90.93	90.51	105.48	101.72	97.98	103.82	99.86	95.90	111.25	107.15	103.06	125.32	114.92	105.64	117.57	113.07	108.60	129.40	119.51	114.65
Power cycles specific cost, USD_{2020}/kWe	657.59	671.59	702.63	614.53	626.50	652.95	612.43	637.59	666.18	589.34	606.02	633.43	574.53	595.82	632.94	564.49	581.70	609.92	526.52	556.24	607.81	538.68	556.00	584.81	508.31	529.77	557.65
Cooler/condenser parameters (only heat exchanger considered)																											
Height, m														0.4													
Depth, m	19.9	23.3	29.3	21.1	24.7	31.4	21.5	25.5	32.5	21.6	25.6	32.6	23.0	27.5	35.9	21.2	25.3	32.8	26.8	32.8	44.3	21.1	25.1	32.2	21.2	25.4	33.1
Total width, m	79.7	84.6	89.5	84.5	90.6	96.6	82.4	81.8	90.1	86.7	90.1	96.7	83.1	86.0	92.1	92.4	96.0	103.0	94.5	93.9	98.4	98.6	103.2	113.0	105.3	104.9	112.5
Design fan power, MW	0.86	1.04	1.36	0.95	1.17	1.55	0.97	1.11	1.52	1.01	1.22	1.63	1.05	1.27	1.73	1.07	1.30	1.77	1.40	1.66	2.30	1.14	1.39	1.91	1.24	1.45	1.98
Total UA, MW/K	8.58	10.57	13.92	8.13	9.97	13.02	9.77	11.39	15.88	8.63	10.32	13.63	10.69	13.10	18.21	8.98	10.81	14.49	14.65	17.68	24.93	9.50	11.49	15.55	10.20	11.89	16.06
Total footprint, m²	1586	1972	2625	1780	2241	3030	1772	2083	2930	1874	2303	3157	1914	2363	3302	1964	2431	3384	2536	3077	4353	2078	2587	3635	2229	2666	3727

Table 8.18. Optimum CSP plant results

Cycle fluid	sCO₂			CO₂ mix.			sCO₂			CO₂ mix.			sCO₂			CO₂ mix.			sCO₂			CO₂ mix.					
$T_{air,des}$	35	40	45	35	40	45	30	35	40	30	35	40	25	30	35	25	30	35	20	25	30	20	25	30	15	20	25
$T_{min,des}$	50						45						40						35						30		
$\Delta T_{cool/cond}$	15	10	5	15	10	5	15	10	5	15	10	5	15	10	5	15	10	5	15	10	5	15	10	5	15	10	5
TES size, h	12	12	12	12	12	12	12	12	12	12	12	12	12	12	12	12	12	12	11	11	12	12	12	12	11	12	12
SM	3	3	3.1	3	3	3.1	2.8	3	3	2.9	3	3.1	2.7	2.8	2.9	2.8	2.9	3	2.3	2.5	2.7	2.7	2.8	2.9	2.5	2.7	2.8
$\eta_{sol. to th.}$, %	42.0	42.6	42.5	42.0	42.5	42.5	42.3	42.0	42.6	42.1	42.1	42.1	41.7	42.2	42.4	42.2	42.2	42.2	42.0	42.2	42.4	42.1	42.2	42.2	42.5	42.2	42.3
$\eta_{sol. to el.}$, %	13.9	14.3	14.4	15.5	15.9	16.0	14.1	14.3	14.6	15.6	15.8	16.0	14.0	14.4	14.6	15.7	15.9	16.1	14.1	14.4	14.7	15.7	16.0	16.2	15.7	15.9	16.2
CF, %	69.9	71.9	75.5	68.7	70.4	73.8	64.4	69.8	71.8	65.6	68.9	72.4	60.1	64.0	67.8	62.6	65.9	69.3	49.9	55.7	61.8	59.1	62.5	65.9	53.6	58.9	62.4
EE, GWh/year	528.9	543.1	549.1	589.2	603.1	608.9	536.9	542.0	554.7	593.6	601.5	608.0	534.2	547.3	556.5	597.6	606.2	613.6	536.7	549.1	559.9	597.5	607.9	615.8	596.6	606.3	615.8
Heliostats, MUSD														248.0													
R&T, MUSD														126.1													
TES, MUSD	89.6	89.6	87.0	82.9	82.9	80.6	89.4	84.1	84.1	81.7	79.3	77.0	85.7	83.0	80.5	80.6	78.2	75.9	83.9	78.0	78.6	79.4	77.0	74.6	75.4	76.0	73.7
Power cycle, MUSD	58.4	59.5	60.0	61.6	62.6	62.9	59.8	58.0	60.3	62.2	61.6	62.1	59.6	59.5	60.7	62.8	62.3	62.9	66.0	63.9	64.2	63.3	62.9	63.5	65.8	63.3	63.9
TCC, MUSD	657.5	658.9	656.4	653.4	654.6	652.1	659.0	650.4	653.2	652.5	649.0	646.8	654.4	650.9	649.3	652.1	648.6	646.4	659.8	650.2	651.4	651.3	647.7	645.7	649.3	647.1	645.0
LCOE, USD_{2020}/MWh	95.2	92.9	91.2	86.6	84.8	83.4	95.0	92.4	90.6	86.5	84.6	83.1	95.7	92.6	90.5	86.5	84.5	82.9	98.6	94.1	91.4	87.2	84.9	83.1	88.4	85.7	83.7

Supplementary materials J: Influence of TMY data on the results

A comparison of typical meteorological year (TMY) data for Seville, Spain, from PVGIS-SARAH3 2005-2023 [32] and System Advisor Model (SAM) [33] is shown in Figure 8.36 with characteristic values in Table 8.19. The dry bulb temperature duration curves and average wind speeds are effectively the same, while the main difference lies in the solar resource.

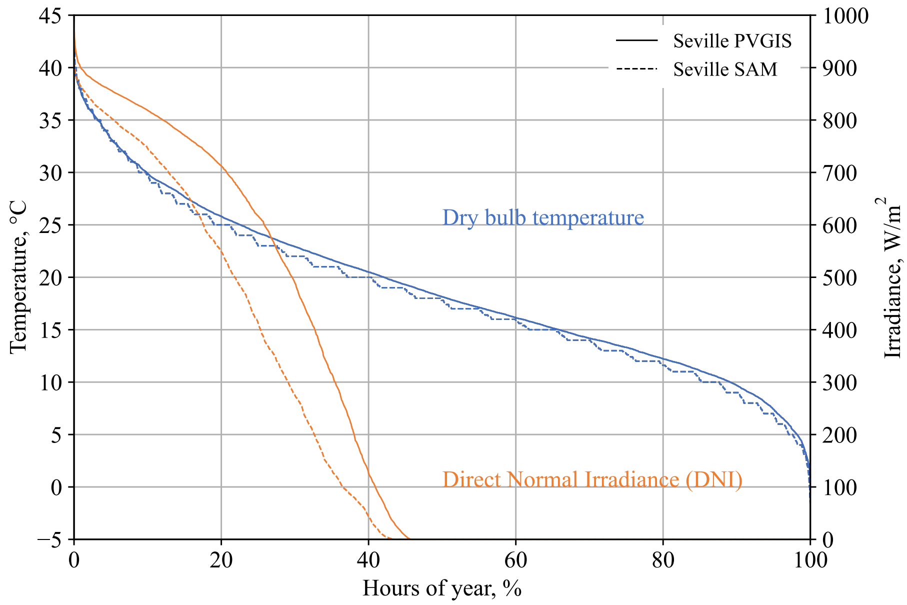

Figure 8.36. Comparison of climate parameters for Seville from PVGIS-SARAH3 2005-2023 [32] and SAM [33]

Table 8.19. CSP plant model assumptions for two temperature levels

Parameter	Value	
TMY source	PVGIS	SAM
Design point DNI, W/m^2	880	840
Average annual DNI, kWh/m²	6.196	4.857
Average dry bulb temperature, °C	19.0	18.4
Maximum dry bulb temperature, °C	0.65	-2.0
Minimum dry bulb temperature, °C	40.19	43.0
Average wind speed, m/s	2.3	2.7

To understand the influence of the TMY choice on the results for Seville SAM TMY data [33] are presented in Figure 8.37. Optimum SM are higher than from PVGIS data, since there is less solar irradiance available, and therefore the solar field of the same incidence power will capture less energy annually, and the power block can be smaller to convert it. The TES sizes are slightly higher moving from 12 to 13 hours, which is partially due to the reduction of the PHE power, so the absolute size of TES will remain almost the same. These results are in line with the values calculated previously for the same SAM TMY data and the same cycle, but without the power cycle off-design curves, assuming constant power cycle operation with $T_{air,des}$ = 35°C and $T_{min,des}$ = 50°C [34]. The optimum SM obtained is 3.4 with 15 hours of storage. The difference in TES size could be explained by the lower cold tank temperature when using power cycle off-design curves compared to fixed power cycle operation, which will effectively increase the TES storage capacity and reduce its design point size.

For the base SM and TES sizes, the optimum air design temperatures are quite low and reached at the minimum temperature available with the minimum cooler/condenser approach temperature

($\Delta T_{cool/cond}$ = 5°C, $T_{air,des}$ = 30°C and 25°C for sCO_2 and CO_2 mixture cycles, respectively). At the optimum SM and TES size, the minimum LCOE is reached for both sCO_2 and CO_2 mixture cycles at $T_{air,des}$ = 35°C. Therefore, the optimum SM and TES sizes vary based on the solar resource available, while optimum air design temperature and cooler/condenser approach temperature remain the same since both PVGIS and SAM have similar dry bulb temperature duration curves.

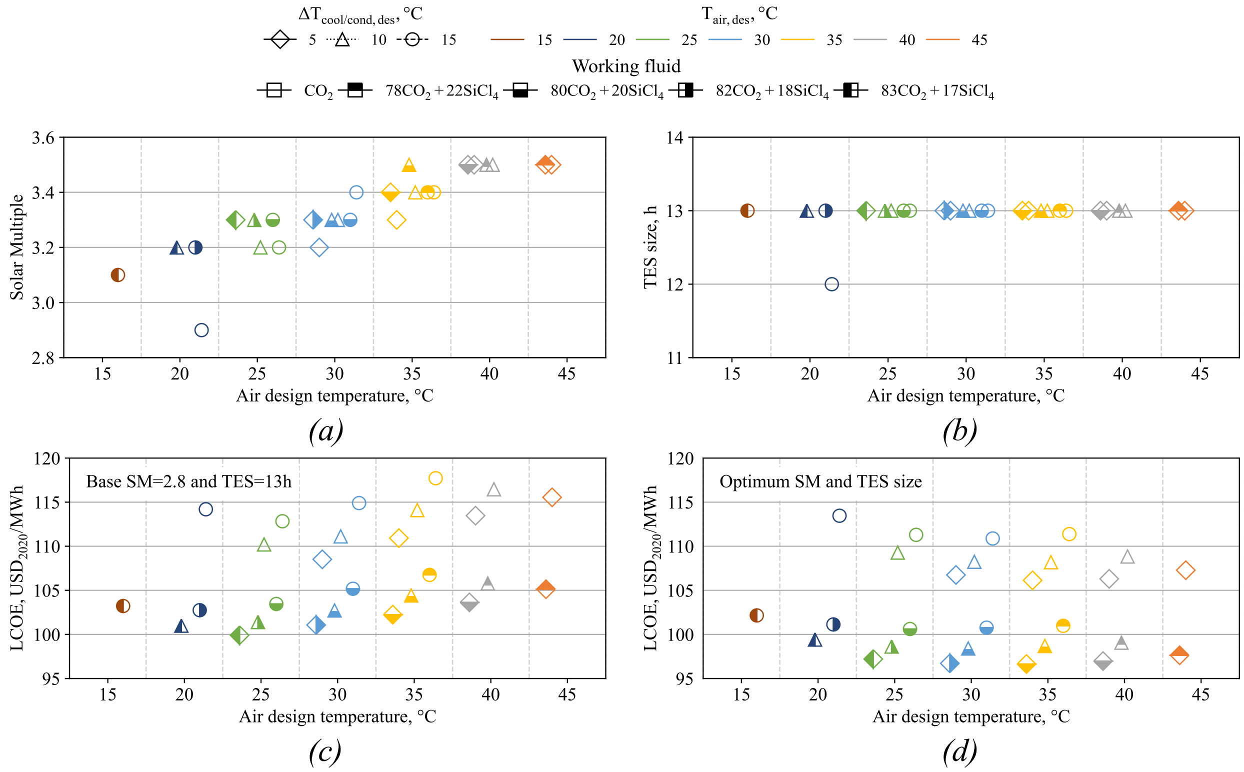

Figure 8.37. Optimum Solar Multiple (a), TES size (b), LCOE for base (c) and optimum (d) SM and TES size for Seville SAM TMY

Supplementary materials bibliography

[1] Schappel D, Terrani K. Key Material Properties for Thermo-Structural Analysis of Transformational Challenge Reactor Core Components. 2019. https://doi.org/10.2172/1558508.

[2] Naumov V, Di Marcoberardino G, Iora P. sCO2 and CO2 mixture cycles off-design operation in CSP plants. Book of abstracts. EU-Solaris 2nd Doctoral Colloquium 2025, Almería, Spain: 2025.

[3] Gnielinski V. New equations for heat and mass transfer in turbulent pipe and channel flow. International Chemical Engineering 1976;16:359–67.

[4] Petukhov B, Kirillov P. About heat transfer at turbulent fluid flow in tubes. Thermal Engineering 1958;4:63–8.

[5] Filonenko G. Hydraulic resistance in pipes. Thermal Engineering 1954;1:40–4.

[6] Chen NH. An Explicit Equation for Friction Factor in Pipe. Ind Eng Chem Fund 1979;18:296–7. https://doi.org/10.1021/i160071a019.

[7] Cavallini A, Col DD, Doretti L, Matkovic M, Rossetto L, Zilio C, et al. Condensation in Horizontal Smooth Tubes: A New Heat Transfer Model for Heat Exchanger Design. Heat Transfer Engineering 2006;27:31–8. https://doi.org/10.1080/01457630600793970.

[8] Bell KJ, Ghaly MA. An approximate generalized design method for multicomponent/partial condensers. AIChE Symp. Ser., vol. 69, 1973, p. 72–9.

[9] Del Col D, Bisetto A, Bortolato M, Torresin D, Rossetto L. Experiments and updated model for two phase frictional pressure drop inside minichannels. International Journal of Heat and Mass Transfer 2013;67:326–37. https://doi.org/10.1016/j.ijheatmasstransfer.2013.07.093.

[10] Jüdes M, Vigerske S, Tsatsaronis G. Optimization of the Design and Partial-Load Operation of Power Plants Using Mixed-Integer Nonlinear Programming. In: Kallrath J, Pardalos PM, Rebennack S, Scheidt M, editors. Optimization in the Energy Industry, Berlin, Heidelberg: Springer Berlin Heidelberg; 2009, p. 193–220. https://doi.org/10.1007/978-3-540-88965-6_9.

[11] Neises T. Steady-state off-design modeling of the supercritical carbon dioxide recompression cycle for concentrating solar power applications with two-tank sensible-heat storage. Solar Energy 2020;212:19–33. https://doi.org/10.1016/j.solener.2020.10.041.
[12] Dyreby JJ, Klein SA, Nellis GF, Reindl DT. Modeling Off-Design and Part-Load Performance of Supercritical Carbon Dioxide Power Cycles. Volume 8: Supercritical CO2 Power Cycles; Wind Energy; Honors and Awards, San Antonio, Texas, USA: American Society of Mechanical Engineers; 2013, p. V008T34A014. https://doi.org/10.1115/GT2013-95824.
[13] Dyreby JJ. Modeling the supercritical carbon dioxide Brayton cycle with recompression. PhD Thesis. The University of Wisconsin-Madison, 2014.
[14] Spencer RC, Cotton KC, Cannon CN. A Method for Predicting the Performance of Steam Turbine-Generators, 16,500 kW and Larger. Journal of Engineering for Power 1963;85:249–98. https://doi.org/10.1115/1.3677341.
[15] Li X, Shu G, Tian H. Integrating off-design performance in designing CO2 power cycle systems for engine waste heat recovery. Energy Conversion and Management 2019;201:112146. https://doi.org/10.1016/j.enconman.2019.112146.
[16] Wu C, Wang S, Li J. Parametric study on the effects of a recuperator on the design and off-design performances for a CO2 transcritical power cycle for low temperature geothermal plants. Applied Thermal Engineering 2018;137:644–58. https://doi.org/10.1016/j.applthermaleng.2018.04.029.
[17] Abdeldayem AS, Salah SI, Aqel OA, White MT, Sayma AI. Design of a 130 MW Axial Turbine Operating with a Supercritical Carbon Dioxide Mixture for the SCARABEUS Project. IJTPP 2024;9:5. https://doi.org/10.3390/ijtpp9010005.
[18] Morosini E, Alfani D, Salah SI, Abdeldayem A, Crespi F, Di Marcoberardino G, et al. Off-design of a CO2-based mixture transcritical cycle for CSP applications: analysis at part load and variable ambient temperature. Applied Thermal Engineering 2023:121735. https://doi.org/10.1016/j.applthermaleng.2023.121735.
[19] Illyés V, Salah S, Abdeldayem A, Werner A, Sayma A, Manzolini G, et al. Dry-Cooled Rankine Cycle Operated With Binary Carbon Dioxide Based Working Fluids. SolarPACES Conference Proceedings, vol. 1, 2024. https://doi.org/10.52825/solarpaces.v1i.625.
[20] Turbines - OffDesign - Stodola n.d. https://help.ebsilon.com/EN/Part_load_Steam_Turbine.html (accessed August 12, 2025).
[21] Peng WW. Fundamentals of turbomachinery. John Wiley & Sons; 2007.
[22] Sato T, Oh JM, Engeda A. Experimental and Numerical Investigation of the Flow in a Vaneless Diffuser of a Centrifugal Compressor Stage. Part 1: Experimental Investigation. Proceedings of the Institution of Mechanical Engineers, Part C: Journal of Mechanical Engineering Science 2005;219:1053–9. https://doi.org/10.1243/095440605X31904.
[23] Manente G, Toffolo A, Lazzaretto A, Paci M. An Organic Rankine Cycle off-design model for the search of the optimal control strategy. Energy 2013;58:97–106. https://doi.org/10.1016/j.energy.2012.12.035.
[24] Krasnoshchekov E, Protopopov V. Experimental study of heat exchange in carbon dioxide in the supercritical range at high temperature drops. Teplofizika Vysokikh Temperatur 1966;4:389–98.
[25] Illyés V, Morosini E, Doninelli M, David P-L, Guerif X, Werner A, et al. Design of an Air-Cooled Condenser for CO2-Based Mixtures: Model Development, Validation and Heat Exchange Gain with Internal Microfins. Volume 9: Supercritical CO2, Rotterdam, Netherlands: American Society of Mechanical Engineers; 2022, p. V009T28A016. https://doi.org/10.1115/GT2022-82438.
[26] Rodríguez-de Arriba P, Crespi F, Sánchez D, Muñoz A. A methodology to design air-cooled condensers for supercritical power cycles using carbon dioxide and carbon dioxide mixtures. Conference Proceedings of the European sCO2 Conference5th European sCO2 Conference for Energy Systems: March 14-16 2023;2023:283. https://doi.org/10.17185/DUEPUBLICO/77329.
[27] Virtanen P, Gommers R, Oliphant TE, Haberland M, Reddy T, Cournapeau D, et al. SciPy 1.0: Fundamental Algorithms for Scientific Computing in Python. Nature Methods 2020;17:261–72. https://doi.org/10.1038/s41592-019-0686-2.
[28] Alfani D, Astolfi M, Binotti M, Silva P, Macchi E. Off-design performance of CSP plant based on supercritical CO2 cycles, Daegu, South Korea: 2020, p. 130001. https://doi.org/10.1063/5.0029801.
[29] CEPCI n.d. https://www.training.itservices.manchester.ac.uk/public/gced/CEPCI.html?reactors/CEPCI/index.html (accessed March 26, 2026).
[30] Weiland NT, Lance BW, Pidaparti SR. sCO2 Power Cycle Component Cost Correlations From DOE Data Spanning Multiple Scales and Applications. Volume 9: Oil and Gas Applications; Supercritical CO2 Power Cycles; Wind Energy, Phoenix, Arizona, USA: American Society of Mechanical Engineers; 2019, p. V009T38A008. https://doi.org/10.1115/GT2019-90493.
[31] Naumov V, Gedik E, Petersen N, Di Marcoberardino G, Iora P, Wirsum M. Comparison of sCO2, CO2 mixture, and steam Rankine cycles for CSP with components sizing: implications for cost and flexibility. 6th Edition of the European Conference on Supercritical CO2 (sCO2) for Energy Systems, Conference Proceedings of the European sCO2 Conference, Delft, Netherlands: DuEPublico: Duisburg-Essen Publications Online; 2025, p. 244--254. https://doi.org/10.17185/DUEPUBLICO/83332.
[32] JRC Photovoltaic Geographical Information System (PVGIS) - European Commission n.d. https://re.jrc.ec.europa.eu/pvg_tools/en/ (accessed May 28, 2025).
[33] National Renewable Energy Laboratory. System Advisor Model Version 2022.11.21 (SAM 2022.11.21). NREL SAM 2022. https://https://sam.nrel.gov (accessed February 22, 2024).
[34] Naumov V, Doninelli M, Di Marcoberardino G, Iora P. Solar tower power plants with CO2 +SiCl4 mixtures transcritical cycles. Renewable Energy 2025:122518. https://doi.org/10.1016/j.renene.2025.122518.

Part 4: Combined power cycle for CSP

Part 4 focuses on the combined power cycle in CSP plants. This approach offers the advantage of using different cycles for different temperature levels, enabling higher overall efficiency while reducing demands on materials.

In Chapter 9, the combined cycle, consisting of a topping alkali metal power cycle and a bottoming sCO_2 power cycle, is investigated. The results are compared to the sCO_2 recompression power cycle.

9. High temperature combined cycle for CSP

This chapter is based on the article: *"High Temperature Cesium-sCO₂ Combined Cycle for Concentrating Solar Power Applications", published in Solar Energy Journal, 275, June 2024, 112599, https://doi.org/10.1016/j.solener.2024.112599.*

Abstract

The temperature potential of concentrating solar power plants is not fully utilized using existing steam cycles. The increase of turbine inlet temperature is limited by the materials used due to the high pressures, temperatures, and corrosion potential. The use of alkali metals with high-temperature boiling points allows for lower pressure in high-temperature parts of the cycle. A novel approach using standard SRK EoS with Twu alpha function and Rackett equation for calculating the thermodynamic properties of Cs, K, and Na is proposed and compared with experimental data and property tables showing maximum deviation of vapor pressure, heat of vaporization, and vapor specific heat capacity below 10%, vapor density below 15%, and saturated liquid density below 4% between 600 and 1000°C. The resulting conversion efficiency of the novel combined cycle comprised of the topping cesium Rankine cycle and bottoming recompression CO_2 cycle is 53.50% at 800°C, to be compared with 52.83% of the reference recompression cycle. Preliminary designs of cesium and sCO_2 turbines along with the Cs-sCO_2 heat exchanger were carried out according to the cycle assumptions. Based on the literature review it is possible to design a combined cycle with 900°C TIT using the same materials as the 800°C TIT sCO_2 recompression cycle and reach a thermal efficiency of 56.8%. After additional tests, it might be possible to significantly reduce the equipment cost by using advanced austenitic or even stainless steel in the high-temperature part of the cesium cycle.

Nomenclature

Acronyms	
AAD	Average absolute deviation
CSP	concentrating solar power
EoS	equation of state
HTF	Heat transfer fluid
ISM	Ihm-Song-Mason
MRK	modified Redlich-Kwong
PR	Peng-Robinson
PC-SAFT	perturbed chain statistical associating fluid theory
PV	Photovoltaic
UA	product of the overall heat transfer coefficient. and the heat transfer area, MW/K
SRK	Soave-Redlich-Kwong
sCO_2	supercritical CO_2
TIT	turbine inlet temperature
Symbols	
α	alpha function
c	heat capacity, J/mol K or kJ/kg K
ε	energy of dispersion interactions between segments, K
η	cycle efficiency, %
R	gas constant, 8.31 J/ mol K
S	entropy
σ	segment diameter, Å
T	temperature, K
V	density, kg/m3
W	work, kJ/kg
Z	critical compressibility
Subscripts	
0	supplied to the cycle
c	critical parameter
l	saturated liquid
MC	main compressor
P	pump
p	isobaric
r	reduced parameter
RC	Recompresing compressor
t	turbine
th	thermal
v	saturated vapor

H	enthalpy	$_{va}$	vaporization
$\dot{m}$	mass flow, kg/s.	*Superscripts*	
m	number of segments	^{ig}	ideal gas
P	power, kW	^{Ra}	Rackett equation
Q	thermal power, kW		

9.1. Introduction

Solar energy has great potential for energy transition. Two main technologies make use of solar energy today: photovoltaic (PV) solar panels and concentrating solar power (CSP) plants. The latter is characterized by the higher levelized cost of electricity with respect to both PV solar and wind power plants [1]. However, the use of CSP plants can help with electric grid balancing because it can be considered a dispatchable technology thanks to cheap thermal energy storage.

The main types of CSP technologies are parabolic troughs, linear Fresnel reflectors, parabolic dishes, and solar towers. Parabolic trough is the most mature and widespread CSP technology, however, there is little or no use of thermal storage currently, and often fossil fuel is used as a backup to keep the nominal capacity. Linear Fresnel reflectors are similar to parabolic trough systems in principle but use rows of flat mirrors to approximate parabolic shape [2]. Solar towers use hundreds and thousands of heliostats (sun-tracking mirrors) to concentrate light on the central receiver in the tower. In the receiver, heat transfer fluid (HTF) or working fluid is heated and then used in the power cycle. Due to higher solar concentration both high temperatures in the receiver and higher electric efficiencies can be achieved in solar tower CSPs. The technology is very flexible since one can choose from different types of heliostats, receivers, HTFs, heat storage systems, and power cycles. Because of that solar towers are the most promising CSP technology.

The power generated by CSP plants has steadily increased through the years and is projected to grow further from 15.6 TWh in 2019 to 53.8 TWh in 2025 and 183.8 TWh in 2030 due to the increasing need for sustainable energy production [3]. Newer plants usually have a bigger installed capacity and storage, which allows for improvement not only in the flexibility of power production but also in the economics, since the increase in the capacity factor brings down the LCOE [4]. Most new large-scale CSP projects use a central receiver tower with molten salt storage [5]. For new tower designs, the standard installed capacity is 100 MW, while heat storage is 8-16 hours, making them very flexible throughout the day. Most CSP systems use direct energy storage and steam Rankine cycle for power generation with turbine inlet temperatures (TIT) up to 560°C.

The materials needed to withstand high-temperature corrosion and creep limit the further increase in maximum temperature using the steam Rankine cycle. However, HTF temperatures up to 750°C have been achieved for particle receivers [6,7], and up to 1000°C could be attained for liquid metal HTF [8]. The final design of the CSP system highly depends on the materials and technology chosen and is subject to optimization based also on the heliostat control to reach safe levels of receiver material stress and fatigue [9–12]. However, the possibility of such receiver designs means that power cycles can use TIT from 700°C up to around 1000°C. Such high temperatures are currently present only in open gas turbine combustion cycles that use air as a working fluid without HTF. The combined plant with topping open air Brayton and bottoming water Rankine cycle have efficiency around 45% at 700°C TIT [13], 46% at 1050°C, and up to 50.7% at 1250°C TIT [14]. Closed gas cycles, such as the helium Brayton cycle, have around 40% efficiency at 800°C TIT, which is close to the existing state-of-the-art steam Rankine cycles with the 600°C TIT [14]. One can improve the Helium cycle efficiency by utilizing the low-temperature heat at around 220°C before the cooler to reach 48.3% efficiency at 816°C TIT [15]. The closed supercritical CO_2 cycles offer the efficiency advantage over both the steam Rankine and helium Brayton cycles at TIT > 600°C and can reach more than 50% at 800°C TIT, however, they also require high pressures (comparable to steam cycles ones) and complex regeneration systems [16]. The efficiency of closed sCO_2 cycles can be improved by using dopants with high critical parameters. A regenerated cycle with condensation can reach 46.7% using N_2O_4, and 51% using $TiCl_4$, precompression cycle using C_6F_6 can reach 50.3% at 700°C TIT [17–19]. However, C_6F_6 is not stable at temperatures above 600°C, N_2O_4 is usually mixed with nitric oxide to slow down corrosion and forms nitrous acid along with nitric acid upon contact with water, while $TiCl_4$ in contact with water forms hydrochloric acid [20]. Another way is to go towards alternative working fluids which could allow an increase in the maximum temperature or higher efficiencies at similar TIT by having lower pressures and less corrosion activity. Alkali metals present a possible alternative and were already tested in stainless steel experimental loops with TIT around 800°C [21]. To calculate thermodynamic properties of alkali metals within the temperature and pressure range of interest multiple unique correlations are currently used in literature based on the virial equation for vapor properties, the Antoine equation for vapor pressure, etc. [22,23]. Combined cycles using the topping metal Rankine cycle with bottoming water Rankine one were already used in power plants with mercury [24]. There were also multiple studies focused on using alkali metals in combined cycles topping part. For liquid metal nuclear reactor application combined cycle with Cs topping cycle was calculated to have 48, 51, and 51.7% efficiency at 621, 676, and 732°C TIT [25] while for molten salt nuclear reactor using sodium in topping cycle efficiency reached 54,6% at 838°C TIT [26]. Considering the CSP application alkali metal topping cycle with bottoming water Rankine cycle one can reach 55% at 700°C and 58% at 800°C TIT [14]. However, in those cases, the condensation was at lower than atmospheric pressures, which would magnify the problem of alkali metals reactions with water and air, as well as challenges related to the big volume flow at the turbine outlet.

In the present paper, a combined cycle is proposed to utilize high-temperature heat from the CSP. A more conservative approach is adopted by keeping the minimum pressure in the alkali metal cycle above the atmosphere and coupling the alkali cycle with the sCO_2 cycle to reduce the risk of metal reactions with bottoming cycle working fluid, however, some metal loss is unavoidable. A model is proposed for calculating the thermodynamic properties of Cs, K, and Na based on two widespread, standard equations, and compared to experimental data and multiple unique correlations currently used in literature for calculating alkali metal properties. The proposed cycle is compared to the sCO_2 recompression cycle at different TIT and its feasibility is assessed by the preliminary selection of materials and equipment design.

9.2. Overview of the working fluids for high-temperature CSP application

9.2.1. High-temperature boiling fluids

The proposed combined cycle utilizes the high-temperature heat in the topping cycle. The working fluids for the topping cycle should have high boiling temperatures and comparatively low maximum pressures in the cycle [14,24,27]. One can see that alkali and heavy metals such as mercury, cesium, etc. are good candidates [28]. An interesting alternative could be the use of sulfur with a normal boiling temperature of 444°C in the topping cycle [29], also because sulfur atoms form a mixture of different polyatomic molecules [30] and have a dry expansion like organic fluids [29,31]. However, sulfur reacts with both iron and nickel, special alumina coating to protect the steel from sulfur up to 750°C is easy to crush [32,33], and even the use of gold sheets to protect steel is not appropriate since it melts in liquid sulfur above 600°C [29].

The vapor pressure of heavy and alkali metals is shown in Figure 9.1. Thermodynamic parameters of metals with boiling temperatures up to 1000°C are presented in Table 9.1. One can see that all metals have very high critical temperatures. Heavy metals have overall higher critical pressures and densities due to the bigger molar mass. Mercury is an outlier in terms of its vapor pressure and critical parameters compared to other alkali and heavy metals. It can be observed that even at high temperatures cycles with metals will remain subcritical and with moderate maximum pressures. This was one of the reasons for using mercury in the binary cycle with the Rankine water bottoming cycle in the first half of the 20th century [24]. The use of mercury allowed to have high turbine inlet temperatures up to 540°C at 14 bar.

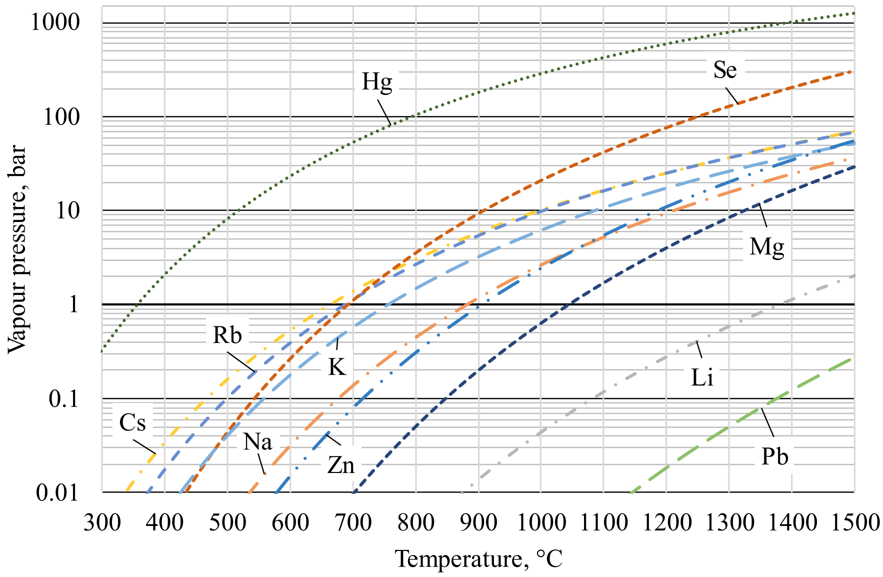

Figure 9.1. Vapor pressure of different metals [22]

Table 9.1. Thermodynamic parameters of metals with boiling temperature up to 1000°C

Metal	Molar mass, g/mol	Boiling temperatures, °C [34]	Triple point temperature, K	Critical temperature, K	Critical pressure, MPa	Critical density, kg/m3	Critical compressibility	Source
Mercury (Hg)	200.6	357	234.3	1764	167	5270	0.4334	[35]
Cesium (Cs)	132.9	671	363.2	1938	9.4	390	0.1988	[36]
Rubidium (Rb)	85.5	688	318.9	2017	12.45	290	0.2189	[37]
Selenium (Se)	79	700	-	1766	27.2	1235	0.1185	[38]
Potassium (K)	39.1	760	336.3	2178	14.8	170	0.1880	[39]
Cadmium (Cd)	112.4	767	594.3	-	-	-	-	-
Sodium (Na)	23	884	370.9	2500	25.6	220	0.1288	[40]
Zinc (Zn)	65.4	910	692.8	3261	356	2342	0.3667	[41]

However, mercury combined power plants were abandoned due to the toxicity of the working fluid. All heavy metals are very toxic and harmful (Appendix A), alkali metals on the other hand are highly flammable and corrosive. EU banned mercury-containing batteries, thermometers, barometers, and blood pressure monitors and is revising the current rules to further restrict the remaining uses of mercury in the EU [42]. Therefore, only alkali metals are considered further, specifically cesium, potassium, and sodium. Rubidium was not considered because of its relative rarity.

9.2.2. Overview of alkali metals thermodynamic properties modeling approaches

Over the last years, several equations of state (EoS) have been used to calculate the thermodynamic properties of alkali metals. Most of the existing models in the literature focus on predicting liquid properties, especially density in saturated liquid and compressed liquid conditions. This is due to the wide application of liquid alkali metals and their mixtures as heat transfer fluids in the nuclear sector [43]. Two widespread EoS for describing the alkali metals liquid density are Ihm-Song-Mason (ISM), and perturbed chain statistical associating fluid theory (PC-SAFT). Both of them are based on statistical equations.

In the case of ISM EoS, statistical-mechanical theory is used to reduce the entire PVT surface to a single curve proposing the new corresponding principle [44]. Three temperature-dependent functions are used: a virial coefficient, an effective van der Waals co-volume, and a scaling factor. However, ISM EoS cannot be applied to critical and two-phase region to predict the vapor pressure of fluids [45]. A combination of perturbation correction terms to change the attractive forces was added to ISM EoS by Tao and Mason to improve the phase boundaries (vapor pressure) prediction [46].

PC-SAFT EoS is based on Helmholtz's free energy contribution of different intermolecular interactions: the hard chain reference, dispersion, association, and electrostatic. The hard chain reference is based on the hard-sphere and chain references with the segment number parameter. Dispersion describes the attractive interactions between molecules, while association term is due to the hydrogen bonding between molecules [47]. For non-associating, neutral pure fluids PC-SAFT EoS requires three parameters: number of segments (m), segment diameter (σ), and energy of dispersion interactions between segments (ε). In this case, only hard chain and dispersion terms are used [48]. Similar equations used for alkali metals in the literature are the perturbated Lennard-Jones chain (PLJC) [49] and the perturbated hard-sphere chain (PHSC) [50]. In the case of PLJC Helmholtz free energy potential is separated into hard-sphere and attractive perturbation parts and has variable parameters similar to PC-SAFT EoS. PHSC is based on the hard-sphere chains with the van der Waals attraction term for perturbation [51]. Similar is the composition of Yukawa perturbated chain (Yukawa PC) EoS which is based on the Yukawa potential equation between segments [52]. The parameter used further for comparison of different EoS accuracy is an average absolute deviation (AAD):

$$AAD = \frac{100}{n}\sum_{i=1}^{n}\left|\frac{X_i^{calc} - X_i^{ref}}{X_i^{ref}}\right| \tag{9.1}$$

where X_i^{calc} – the calculated value of the parameter; X_i^{ref} – reference value of the parameter (experimental or table); n – number of points.

Among the presented EoS, ISM and TM EoS, which are a part of the same family of EoS, have the highest accuracy (AAD < 1% for pure fluids and <2% for mixtures) with the latter EoS being slightly better (Appendix B). The next group is PC-SAFT and SAFT-VR EoS which have an AAD of around 1.5-2%, followed by Yukawa PC EoS with an AAD in the range of 2-6%. This is due to the use of temperature-dependent coefficients by ISM and TM EoS which can be tuned better, than constant parameters used in the perturbated chain EoS family.

Cubic equations were also used in the literature to determine different alkali metal properties. The compressibility factor AAD of 4.2% for sodium, 2.9% for potassium, and 2.7% for cesium vapor were obtained in pressure and temperature range of 1-1000 kPa and 500-3000 K through the use of the Peng-Robinson (PR) equation of state with the new alpha function equation by Zhao et al. [53]. Morita and Fischer [54,55] modified the Redlich-Kwong (MRK) equation to take into account the effects of sodium dimerization on internal energy and specific heat. The new MRK equation was used for calculating vapor properties along with the separate equations for vapor pressure and saturated density. The new model showed adequate accuracy for saturated enthalpies and specific heat of vapor.

As in the case of Morita and Fischer [54,55], it is possible to use various equations for different properties and phases of alkali metals. Heimel et al. [56,57] calculated vapor properties from the virial equation using hard-sphere potentials to guess part of the coefficients and regressed the other part from PVT data. Ewing et al. [58–61] calculated vapor properties from a fitted virial equation with four coefficients for cesium and three for other metals, liquid specific volume and vapor pressure from correlations in the literature, and heat of vaporization from the Clapeyron equation. Enthalpy, entropy, and heat capacity were calculated through the ideal monomeric gas path (Table 9.6).

Since three alkali metals were investigated, the working fluid was modeled as a real gas because the monomer and dimer mixture approach of Morita and Fischer [54,55] did not give satisfactory results for potassium [57]. Peng-Robinson, Riedlich-Kwong, and PC-SAFT EoS were chosen for further analysis due to their good accuracy, ability to describe both the vapor and liquid phase, and simplicity. Vargaftik [62] and Reynolds [22] tables of thermodynamic properties were chosen as a benchmark for vapor pressure, heat of vaporization, saturated vapor and liquid heat capacity and density. Both tables use multiple equations to calculate the thermodynamic properties including unique virial EoS for the vapor phase.

9.3. Methodology

9.3.1. The equation of state to model alkali metals thermodynamic properties

Critical temperature and pressure, along with the acentric factor (which is calculated based on the vapor pressure curve and critical temperature) are the main parameters of cubic EoS. Therefore, it is important to have accurate data on the critical point. One should point out that the critical parameters of alkali metals are very high which led to discrepancies in experimental data. For cesium, both critical pressure and temperature data reported in the literature significantly changed by the end of the 20th century [36]. For potassium, the uncertainty is mostly in critical pressure [63,64]. Parameters used in further modeling are shown in Table 9.1 along with the acentric factors equal to -0.2170, -0.1684, and -0.1206 for cesium, potassium, and sodium calculated from vapor pressure correlation from Reynolds [22].

To reduce the complexity of the thermodynamic model one should use an EoS which could describe both liquid and vapor phase and be widespread. Initial estimates were done using cubic equations of state: Soave-Redlich-Kwong (SRK) and Peng-Robinson (PR). The further analysis considered SRK EoS due to lower deviations for vapor pressure and density of vapor, while deviations in the heat of vaporization, saturated liquid density, and specific heat capacities were similar.

For all alkali metals reduced saturated liquid and vapor density curves lie further apart compared to gases and mercury [39]. This leads to very high (20-50%) liquid density deviations of cubic and PC-SAFT equations of state. Because of that a separate Rackett equation was used for calculating liquid density [65]:

$$V_l = \frac{RT_c (Z_c^{Ra})^{1+(1-T_r)^{2/7}}}{P_c} \tag{9.2}$$

where V_l – saturated liquid density; R – gas constant; Z_c^{Ra} – critical compressibility for Rackett equation; T_r – reduced temperature.

The resulting deviations of calculated values from the Vargaftik and Reynolds tables can be seen in Figure 9.2. For cesium and potassium Rackett equation gives low deviations with critical compressibility from Table 9.1. However, as in the case of reduced liquid density, sodium is an outlier with a deviation of 60-67%. This could be due to the inaccuracies in the critical parameters of sodium due to their high values or the effects of dimerization. Therefore, to get the correct results the $Z_c^{Ra} = 0.169$ parameter was regressed for Na from liquid density data in NIST ThermoData Engine [66].

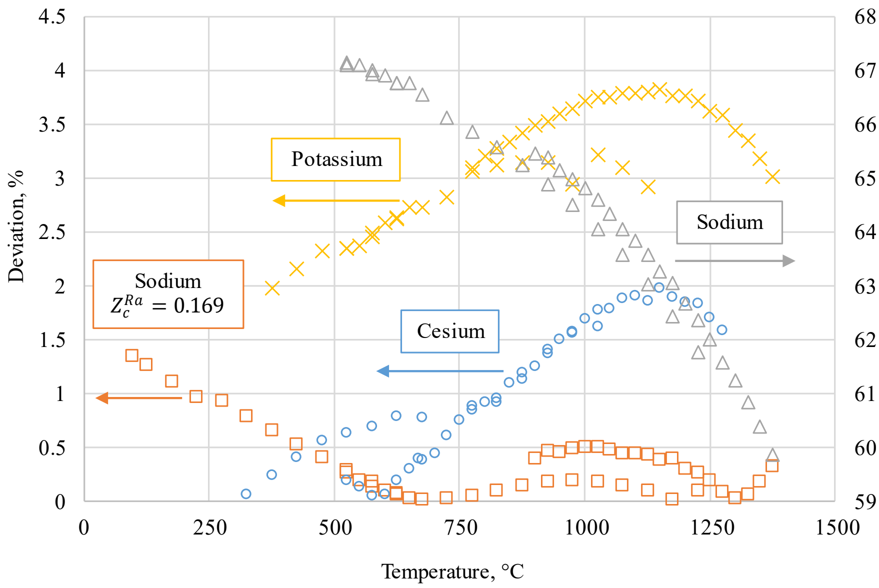

Figure 9.2. Saturated liquid density relative deviation for different alkali metals as a function of temperature

One of the reasons the standard SRK and PR EoS models have big deviations in vapor pressure is the equation of the acentric factor. It is calculated at a reduced temperature of 0.7 which is a very high temperature for alkali metals cycle application. Since it has good accuracy at subcritical temperatures the Twu alpha function (9.3) parameters were regressed from the vapor pressure [67].

$$\alpha(T) = T_r^{\,N(M-1)} e^{L(1-T_r^{\,NM})} \tag{9.3}$$

Another way is to regress the vapor pressure data using the PC-SAFT EoS (Table 9.2). Although the molecules of alkali metals are mostly monomers or dimers the regression gives the average number of segments (m) below one, which is not physical but shows good accuracy.

Table 9.2. Parameters for alkali metal EoS

Metal	**Twu alpha function parameters for SRK EoS**			**PC-SAFT EoS parameters**		
	L	**M**	**N**	**ε, K**	**m**	**σ, Å**
Cs	1.998	10.39	$1.507\ 10^{-2}$	1284.64	0.934	8.181
K	1.894	11.71	$2.008\ 10^{-2}$	1825.19	0.614	7.528
Na	1.951	14.23	$2.124\ 10^{-2}$	2246.4	0.556	6.407

For further analysis, SRK EoS with Twu alpha function was considered because of its better accuracy in determining the heat of vaporization (a more detailed comparison of final versions of both EoS is shown in Appendix C). Both EoS have high deviations in saturated liquid and vapor specific heat capacities (Cp). Specific heat capacities of saturated liquid and vapor are calculated as a sum of ideal gas heat capacity and residual component calculated from the EoS. Therefore, heat capacities are interconnected and one can adjust only the saturated liquid of vapor one. In our case, alkali metals are used in Rankine cycles, where fluid is pumped in a liquid state. The maximum pressure is set to reach the specified evaporation temperature, while the minimum pressure is determined by condensation temperature. The steep vapor pressure curve of alkali metals results in a small pump pressure difference. Pump work is calculated using liquid phase density and pressure increase, while liquid c_p determines the temperature increase in the pump. This all leads to negligible enthalpy and temperature increases in the pump in alkali metal cycles [23,68], therefore the saturated steam c_p was chosen as more important for power cycle application. The values of ideal monoatomic/diatomic gas, as well as ideal gas c_p from NIST [69] and Aspen databases, real gas c_p from Heimel [56], Reynolds [22], Vargaftik [62] and Ewing et al. [59–61] and values calculated through SRK EoS are shown in Figure 9.3. Saturated vapor Cp is at the monoatomic level for low temperatures and increases with the increase in temperature to its maximum. This behavior is mainly due to the additional heat being stored in the endothermic dimerization reaction. At higher temperatures, c_p should be closer to the diatomic gas because of the bigger dimer fraction and reduced reaction heat impact. Therefore, to accurately capture the real saturated vapor, c_p the working fluid should be calculated as a mixture of monomer and dimer with the heat of dimerization reaction influence on the system. In the presented study a single EoS was used to describe the whole system therefore an adjustment of the, c_p calculation method is required.

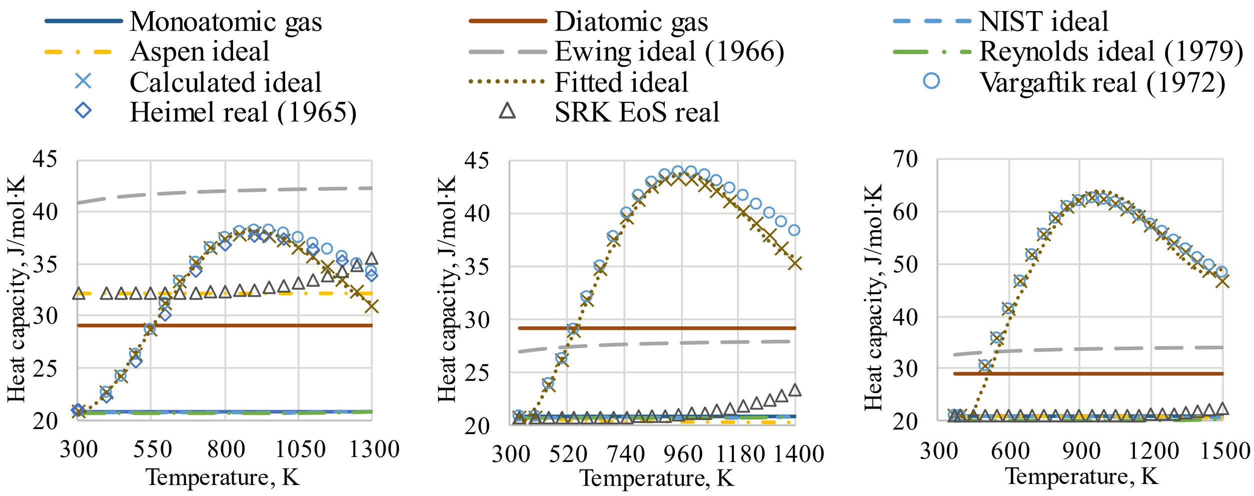

(e) Cesium *(f) Potassium* *(g) Sodium*

Figure 9.3. Specific heat capacity of saturated vapor for different alkali metals. Data from NIST [69], Aspen [66], Heimel [56], Reynolds [22], Vargaftik [62], and Ewing et al. [59–61]

To get the calculated SRK EoS saturated gas heat capacity as close to real gas as possible, a difference was calculated and fitted with a polynomial:

$$c_p^{ig} = a + bT^1 + cT^2 + dT^3 + eT^4, \tag{9.4}$$

where the c_p^{ig} is the ideal gas specific heat capacity in J/mol·K, T is the temperature in K, a, b, c, d, and e are coefficients from Table 9.3.

Table 9.3. Ideal gas specific heat capacity fitting parameters

Metal	Parameters				
	a	b	c	d	e
Cs	44.62	-0.2033	$5.466\ 10^{-4}$	$-4.977\ 10^{-7}$	$1.473\ 10^{-10}$
K	50.14	-0.2455	$6.276\ 10^{-4}$	$-5.398\ 10^{-7}$	$1.511\ 10^{-10}$
Na	32.62	-0.2369	$7.607\ 10^{-4}$	$-6.854\ 10^{-7}$	$1.921\ 10^{-10}$

Results of the comparison between literature data and SRK EoS with Twu alpha function are presented in Figure 9.4 (a more detailed comparison including experimental data on vapor pressure and saturated liquid density is shown in Appendix C). The deviations of liquid heat capacity, were 61%, 68%, and 133% for Cesium, Potassium, and Sodium and are not shown in the graph. Since the work of the pump will be calculated through the liquid density and pressure increase, cycle efficiency won't be affected by this deviation.

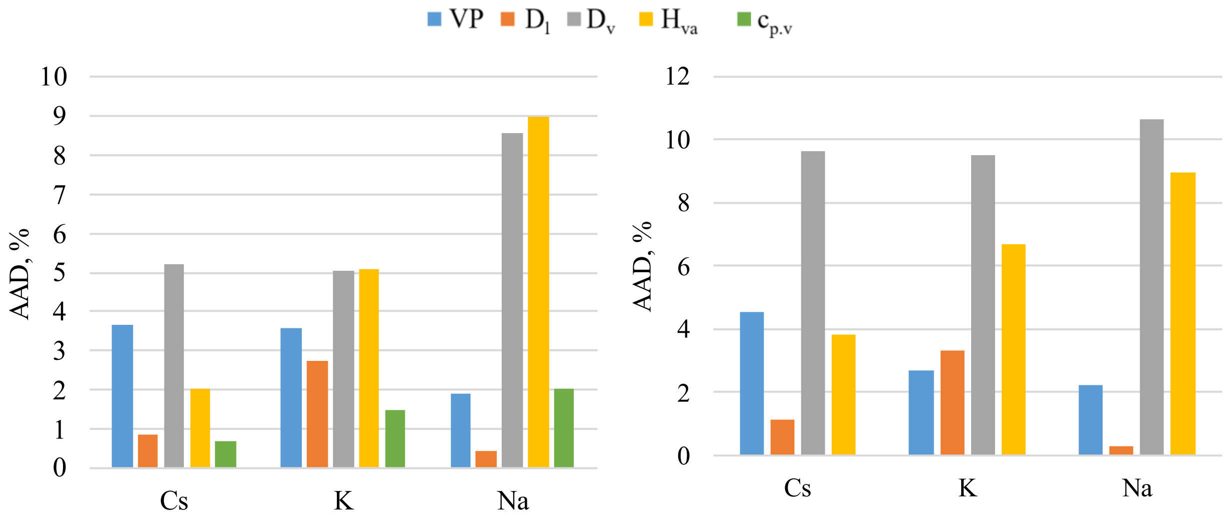

(a) Comparison with Vargaftik *(b) Comparison with Reynolds*

Figure 9.4. AAD of SRK EoS with Twu against literature

To validate the thermodynamic properties model a calculation was made based on cycles in the literature [23,68] where potassium is the working fluid. The analysis was made for a simple Rankine cycle with the feed pump driven by a separate turbine (Figure 9.5). The main cycle assumptions are listed in Table 9.4, while Table 9.5 compares the cycle results highlighting the deviation between this work and the references.

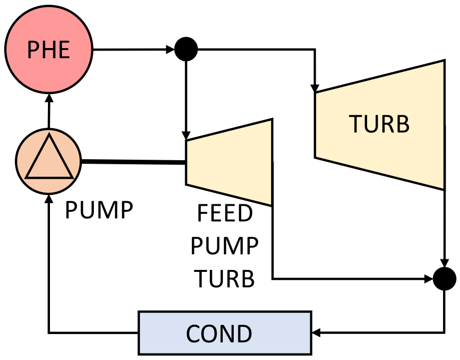

Figure 9.5. Rankine cycle with turbopump configuration in Aspen. PHE – primary heat exchanger; COND – condenser; TURB – cesium turbine; FEED PUMP TURB – feed pump driving cesium turbine;

Table 9.4. Assumptions for Rankine cycle with turbopump

Parameter	Value
Turbine efficiency, %	74
Main turbine mass flow, kg/s	0.2633
Feed pump turbine mass flow, kg/sec	0.00908
Main turbine outlet pressure, kPa	21.58
Feed pump turbine outlet pressure, kPa	211.2
Pump outlet pressure, kPa	968
Evaporator outlet temperature, K	1310

Table 9.5. Comparison of potassium cycle modeling with literature

Parameter	SRK with Twu	PC-SAFT	Yoder et al. [68]	Deviation, %		Sun et al. [23]	Deviation, %	
Turbine inlet pressure, kPa	745.8	792.0	774	-3.6	2.3	773	-3.5	2.5
Turbine outlet temperature, K	886.6	889.2	887	0.0	0.3	887	0.0	0.3
Feed turbine outlet temperature, K	1118.2	1115.6	-	-	-	1116	0.2	0.0
Evaporator heat, kW	684.2	689.6	631.8	8.3	9.2	631	8.4	9.3
Condenser heat, kW	540.8	545.3	504.8	7.1	8.0	499.5	8.3	9.2
Turbine power, kW	142.0	142.8	127	11.8	12.4	131.5	8.0	8.6
Thermal efficiency, %	20.7	20.6	20.1	2.8	2.6	20.8	-0.6	-0.8

One can see that temperatures and pressure deviations are within 4%, while condenser, evaporator, and turbine power have a deviation of around 8% (which is determined by the accuracy of the heat of vaporization calculation) for the SRK with Twu. It should be pointed out that the deviation in heat of vaporization for potassium between Reynolds [22] and Vargaftik [62] tables reaches 2% at 1000°C. In the case of Yoder et al. [68] and Sun et al. [23] the thermodynamic properties are the same as in Reynolds while for the proposed model both thermodynamic tables were used. The higher deviation in turbine power and efficiency compared to Yoder et al. is due to losses of working fluid through turbine seals which were not accounted for by Sun et al. and in the current calculation. The deviation of cycle efficiency is within 1% compared to Sun et al.

Therefore, models employed currently in the literature give higher accuracy, but they are based on multiple, usually uniquely formulated equations, which require multiple fitted coefficients for each equation (Table 9.6). While the proposed model employs 2 widespread, standard equations with 11 coefficients 3 of which are critical parameters.

Table 9.6. Comparison of thermodynamic models

Model	Property	Equation used	Number of coefficients	Number of coefficients for the model
Reynolds [30]	Vapor PVT	Virial	9	18
	Vapor pressure	Extended Antoine	3	
	Saturated liquid density	Polynomial	3	
	Ideal gas isochoric heat capacity	$c_v^{ig} = A + B\frac{e^{-C/T}}{T^2}$	3	
Ewing [54–56]	Vapor PVT	Virial	6-8	25-27
	Vapor pressure	Extended Antoine	3	
	Saturated liquid density	Polynomial	3	
	Ideal gas isobaric heat capacity	$c_p^{ig} = A + Be^{-C/T}$	3	
	Ideal gas Entropy	$S^{ig} = A + B\ln T + Ce^{-D/T}$	4	
	Ideal gas Enthalpy	$H^{ig} = A + B\ln T + Ce^{-D/T}$	4	
	Enthalpy of vaporization	Derived from Clapeyron	2	
Proposed model	Vapor and liquid PVT, except liquid density	SRK EoS with Twu alpha function	2+3	11 (3 being critical parameters)
	Ideal gas isobaric heat capacity	Polynomial	5	
	Saturated liquid density	Rackett	3	

9.3.2. Modeling the power cycles

The proposed combined cycle allows for the utilization of high-temperature heat by using an alkali metal in the topping cycle. The recompression sCO_2 cycle was chosen as the bottoming and as a reference cycle since it is widely accepted as the most efficient CO_2 cycle at TIT>600°C [16] and is widely investigated for high-temperature (650-750°C) CSP plants [70–74]. Using the proposed model for calculating thermodynamic properties, the two power cycles depicted in Figure 9.6 were compared: the sCO_2 recompression cycle and the combined cycle.

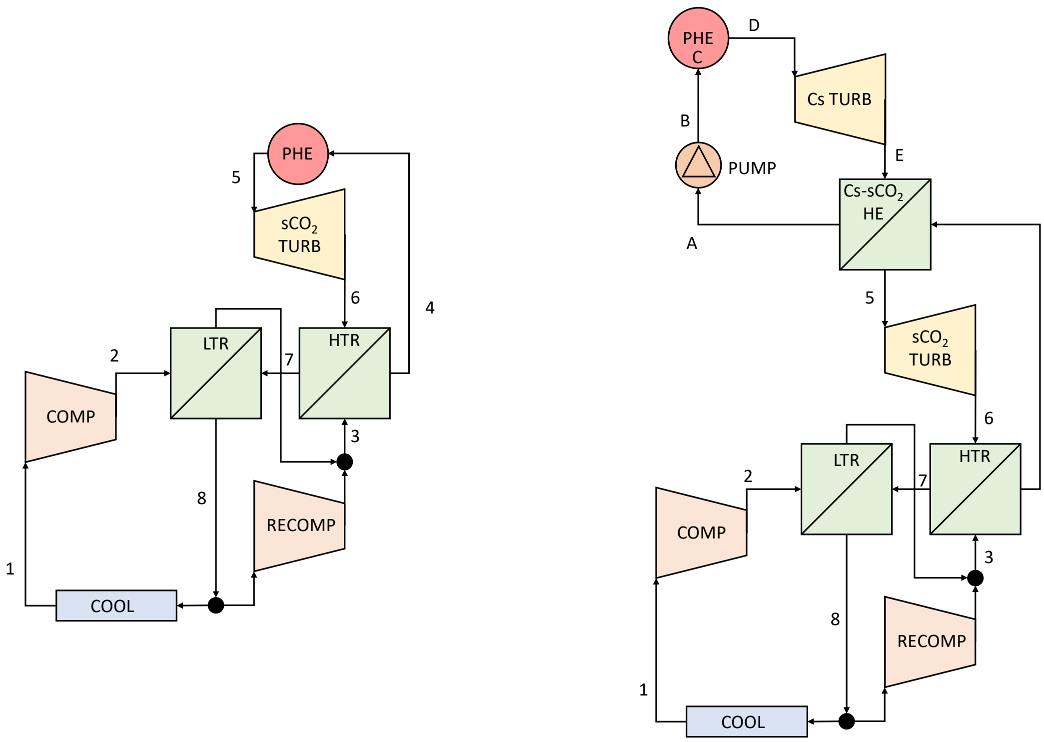

(a) Recompression cycle *(b) Combined cycle*

Figure 9.6. Layout of cycles considered in the analysis. LTR – low-temperature recuperator; HTR - high-temperature recuperator; COMP – main compressor; RECOMP – recompressing compressor; COOL – air cooler; TURB – turbine working with sCO_2 or Cs; HE – heat exchanger.

The combined cycle is made of a simple alkali metal topping Rankine cycle and recompressed sCO_2 bottoming cycle. The comparison of T-s diagrams is shown in Figure 9.7. The advantage of such an arrangement is the low maximum pressure in the equipment with the highest temperature, which should allow for lower stress in materials and thinner equipment walls.

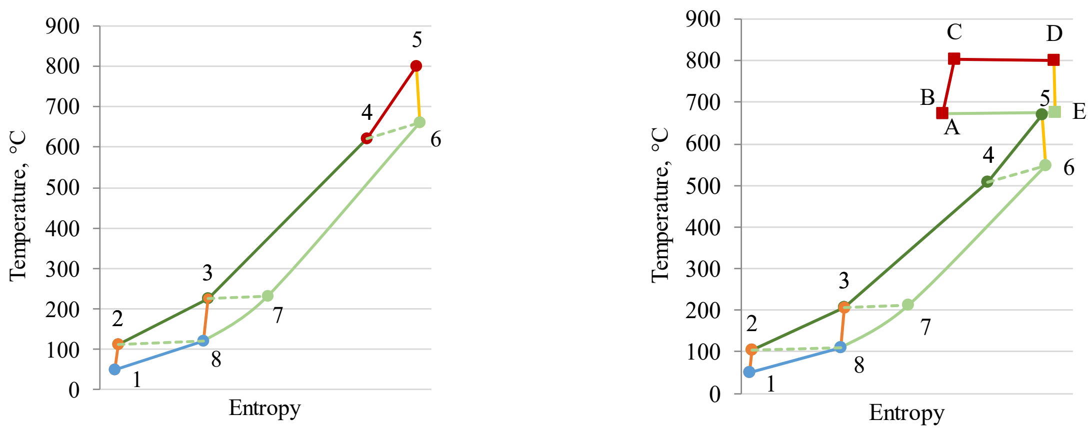

(a) Recompression cycle *(b) Combined cycle*

Figure 9.7. T-s diagram of cycles considered in the analysis

Since cesium has the lowest boiling point, it was chosen as a working fluid of the alkali metal Rankine cycle. Alkali metals are reactive with CO_2 [75], but the result of such a reaction will be a Cs_2CO_3 salt, which is thermally stable up to around 610°C [76], and at higher temperatures decomposes to CsO_2, CO_2, and cesium suboxides [77]. Both cycles were calculated based on the assumptions in Table 9.7, which are typical for sCO_2 cycles for CSP applications [18,78]. The design temperature for the air cooler was chosen to be 35°C with a 15°C air cooler approach temperature, which is close to optimum parameters [79]. A more detailed analysis is needed to assess the optimal minimum cycle temperature based on the air cooler optimization and CSP plant performance overall [80,81]. A 100 MWe class tower CSP plant was assumed according to the introduction and high-capacity turbomachinery efficiency was chosen. A minimum pressure of 1.05 bar in the alkali metal cycle was chosen to not let any air react with cesium in the cycle. For each calculation, minimum recompression cycle pressure was optimized with a 5 bar step. Maximum pressure in the sCO_2 cycles was chosen at 250 and 300 bar for current acceptable and prospective levels [82,83].

Table 9.7. Assumptions for modeling the cycles

Parameter	**Value**
Topping cycle fluid	Cs
Maximum cycle temperature range, °C	700 – 1000
Topping cycle minimum pressure, bar	1.05
CO_2 cycles maximum pressure, bar	250, 300
CO_2 cycles minimum temperature, °C	50
Approach temperature in heat exchangers, °C	5
Turbine efficiency, %	92
Pump/compressor efficiency, %	88
Condenser/cooler pressure drop, %	2
Heater pressure drop, %	2
Recuperator LP side pressure drop, %	1.5
Recuperator HP side pressure drop, %	0.3

The main performance indicators chosen were thermal efficiency and specific work. Latter was calculated based on the power produced in the turbine or multiple turbines in the case of a combined cycle, power used by the pump of the alkali metal cycle, in the main and recompressing compressors of sCO_2 cycles, and mass flow to the turbine:

$$W_s = \frac{\Sigma P_t - P_{MC} - P_{RC} - P_P}{\dot{m}} \tag{9.5}$$

where W_s – specific work, kJ/kg; P_t – turbine power, kW; P_{MC} – main compressor power, kW; P_{RC} – recompressing compressor power, kW; P_P – pump power if used, kW; $\dot{m}$ – mass flow at turbine inlet, kg/s.

Thermal efficiency was calculated based on the power supplied in the PHE:

$$\eta_{th} = \frac{\Sigma P_t - P_{MC} - P_{RC} - P_P}{Q_0} \tag{9.6}$$

where η_{th} – thermal cycle efficiency, %; Q_0 – power supplied to the cycle in the PHE, kW.

9.4. Results and Discussion

A sensitivity analysis was carried out to investigate the influence of minimum pressure on efficiency, temperature, and turbine outlet vapor quality. According to Figure 9.8 the combined cycle thermal efficiency and specific work increase from 53.50 to 53.86% and from 284 to 329 kJ/kg with the decrease of topping cycle minimum pressure from 1.05 to 0.1 bar. The condenser outlet temperature and vapor quality increase from 460°C to 670°C and from 86.7 to 95% with the increase of topping cycle minimum pressure. Therefore, the decrease of alkali metal cycle minimum pressure leads to negligible efficiency gain while amplifying the problem with cesium reactivity and turbine outlet vapor quality.

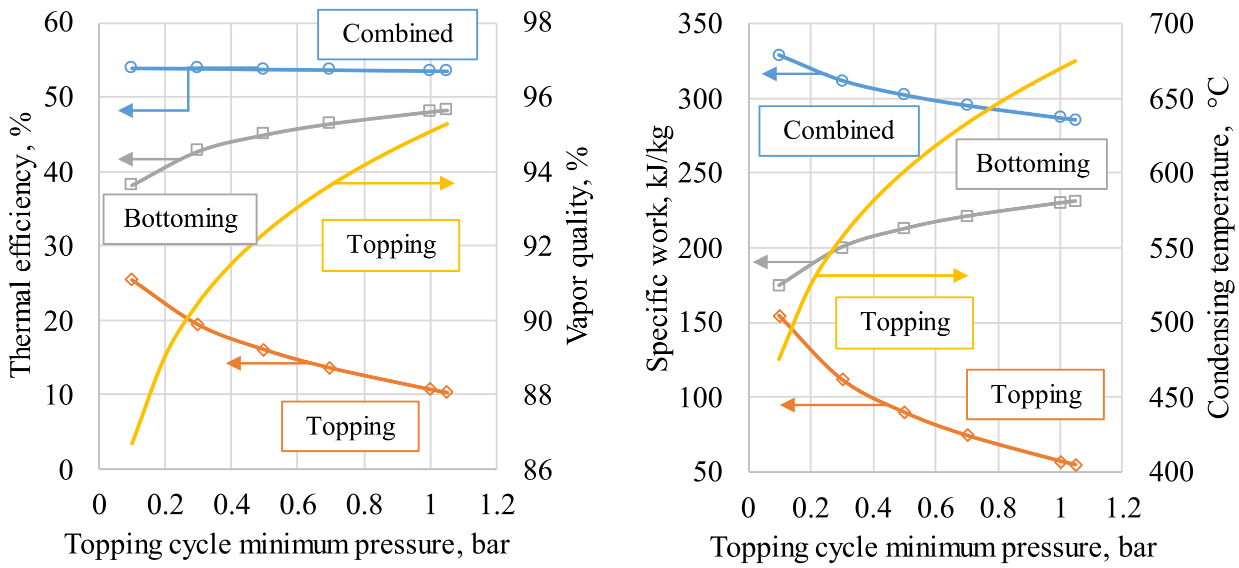

(a) Thermal efficiency and turbine exhaust vapor quality

(b) Specific work and condenser outlet temperature

Figure 9.8. Varying the topping cycle minimum pressure with 800°C TIT and bottoming cycle maximum pressure of 300 bar

The comparison between the combined and recompression cycles at different TIT is presented in Figure 9.9. For sCO_2 recompression cycle values for TIT above 800°C are shown with dashed lines due to the material constraints. At 900°C TIT alkali metal turbine exhaust vapor fraction decreases to 92.3% and at 1000°C – 89.8%. Combined cycle thermal efficiency with 300 bar maximum pressure is 53.50% at 800°C, 56.68% at 900°C and 59.19% at 1000°C TIT, while for the recompression cycle, it is 52.83% at 800°C, 56.01% at 900°C and 58.74% at 1000°C TIT. The increase of maximum pressure from 250 to 300 bar leads to an increase in thermal efficiency of 0.6%. At the same TIT and maximum pressure combined cycle has 0.7% higher thermal efficiency.

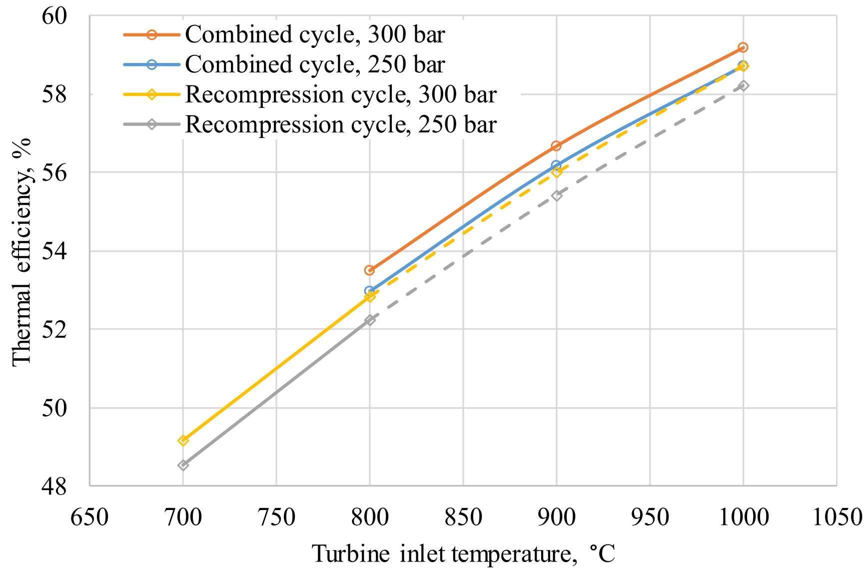

Figure 9.9. Influence of turbine inlet temperature and maximum pressure in the sCO_2 cycle on cycles thermal efficiency

Another advantage of the combined cycle is the possibility of using cesium not only for power generation but also as a heat transfer and/or storage fluid [84]. In this case, the heat transfer fluid can also be used as a working fluid in the topping cycle.

9.4.1. Materials selection for high-temperature power cycles

The choice of the material for the high-temperature section of the power cycle is strictly related to the adopted working fluid. Over the last few years, several studies investigated the material compatibility with pure CO_2 for the recompression cycle at high temperatures. According to [85], high-nickel, heat-resistant alloys have similar rates of oxidization in s-CO_2 and air and do not undergo internal carburization. This makes nickel-based alloys with 24% chromium and 20% cobalt (Alloy 740H) a suitable material up to 800°C and 30 MPa s-CO_2 application. For lower temperatures, relatively cheaper advanced austenitic alloys such as Alloy 709 (tested up to 650°C, but could probably work with higher temperatures), austenitic alloy 316H (up to 550°C), and martensitic alloy VM12 (up to 500°C) should be enough [83].

For alkali metal cycles a lot of experiments and studies were done for space energy applications [68,86]. There was no substantial corrosion after 1000 hours in liquid or vapor cesium up to a maximum test temperature of 870°C for stainless steel and nickel-based alloys, 1370°C for columbium alloys, 1800°C for molybdenum alloys, 1370°C for tantalum alloys [87]. Stainless steel such as AISI 316 is considered a good candidate for relatively low temperatures (up to 730°C) [68,88] and might be resistant enough even up to 830°C [68,86]. For temperatures up to 815°C nickel-based alloys with 15% chromium and 16-18 % cobalt (Udimet 700, Rene 77, Waspalloy) were tested in turbine blades and didn't show any substantial corrosion or erosion [24,88,89]. For higher temperatures alloys based on refractory materials can be used, specifically based on molybdenum (TZM and TZC) [24,89] and niobium (Nb-1%Zr) up to around 1080°C and tantalum (T-111) up to 1230°C [68]. However, the alkali metal corrosion is more present for refractory than for nickel-based alloys, even though in both cases it is minimal and is due to the liquid accumulation in selected areas. The main reason for the corrosion of the refractory metal is the oxygen impurity, followed by the use of stainless steel in the circuit which leads to the mass transfer of elements in the cycle and accelerates the corrosion [88,89]. The use of non-refractory materials in the power cycle should solve the problem of corrosion in the turbine. Overall, for the system operating at 800-900°C TIT most of the equipment (condenser, pump) could be made from stainless steel while the evaporator, steam headers, and high-temperature parts of the turbine from nickel-based alloys or even stainless steel depending on the stresses. For example, in the experimental loop in [88], stainless steel 316 was used in turbine casing, inlet, and outlet piping, gas-fired boiler, pumps, and valves. Therefore, at similar temperatures equipment for Cs and CO_2 cycles will have to use different materials.

The distribution of chosen alloys by power cycle equipment is shown in Table 9.8. They can be divided into nickel-based alloy (740H), advanced austenitic (709), austenitic (316 or 316H), and martensitic (VM12) steels. Nickel-based Alloy 740H will be used in high-temperature parts of both cycles: above 730°C for Cs and above 670°C for CO_2. Stainless steel will be used for low-temperature equipment of Cs cycle and CO_2 cycle equipment with working temperatures above 450°C and below 550°C. For CO_2 and temperatures between 550°C and 670°C Alloy 709 will be used. This distribution of alloys could make the sCO_2 equipment in the combined plant less expensive than the similar one in the recompression cycle due to the less use of nickel-based alloys and lower pressures in high-temperature parts of the sCO_2 cycles.

Table 9.8. Alloys chosen for cycles equipment [68,83,86,88]

Cycle	Equipment	Hot side			Cold side		
		Pres., bar	**Temp., °C**	**Alloy**	**Pres., bar**	**Temp., °C**	**Alloy**
Topping cycle	PHE	-	-	-	3	670/800	740H
	Turbine	3/1	800/670	740H	-	-	-
	Cs-sCO_2 HE	1	670	316	300	520/670	709
	Pump	1	670	316	-	-	-
Bottoming cycle	Turbine	300/120	670/550	709	-	-	-
	HTR	120	550/210	316H	300	210/520	316H
	LTR	120	210/110	VM12	300	110/210	VM12
Recompression cycle	PHE	-	-	-	300	620/800	740H
	Turbine	300/110	800/660	740H	-	-	-
	HTR	110	660/230	709	300	230/620	709
	LTR	110	230/110	VM12	300	110/230	VM12

9.4.2. Preliminary equipment design

Heat exchangers and fluid machines for sCO_2 cycles have already been developed and tested for low-powered applications. There are already CO_2 compressors available for pressures up to 580 bar [90]. The most of existing experimental setups are in several kilowatt-class and test benches for full recompression cycles already exist [91,92]. Designs of megawatt-class equipment do exist [82,93] with panned pilot facilities [94], but the only experimental facility has just reached mechanical completion as far as authors know [95].

The equipment needed for the alkali metal cycles was also developed and extensively tested [24]. The potassium axial turbines with powers up to 250 kW were tested with different exhaust vapor qualities, but all of them showed negligible erosion [86]. The highest liquid fraction was around 7% and after 5000 hours of testing a microscopic amount of erosion occurred on nickel-based blades with a tip speed of around 240 m/s [89]. Overall, the refractory materials showed lower erosion than nickel and steel alloys. The moisture extraction devices similar to steam turbine ones were tested and considered feasible. The transition from potassium to cesium should not be too difficult, since existing design studies and operating experience indicate that differences between the systems working with two fluids are due to their physical properties and have relatively little effect on the design of heat exchange equipment, but reduce the size of vapor manifolds and turbine [21]. However, the long-term endurance testing of equipment to prove the lifetime capabilities of the prospective power plants is of great interest.

A 100 MWe output power was chosen for both of the investigated cycles according to the overview in the beginning for new CSP plants with solar towers [96]. The comparison of the cycles' main parameters can be seen in Table 9.9.

Table 9.9. Comparison of cycles' main parameters

Parameter	Combined cycle	Recompression cycle
PHE power, MWth	186.9	189.2
Cs turbine power, MW	19.2	-
Pump power, MW	0.05	-
Cs-sCO_2 heat exchanger power, MWth	167.7	-
sCO_2 turbine power, MW	119.2	142.5
HTR power, MWth	323.4	422.9
LTR power, MWth	107.4	112.8
Compressor power, MW	23.6	26.1
Recompressor power, MW	14.7	16.4
Cooler power, MWth	86.9	89.3
Output power, MW	100.0	100.0

Turbines designs were obtained from the AxialOpt program, which implements a mean line model with the Kacker and Okapuu loss model and has been validated against experimental data and similar programs [97]. Since the sCO_2 turbines' capacity is too high for a gearbox, they were designed at 3000 rpm to work directly with the electric generator [82]. For alkali metal high-capacity turbines low rotation speeds are more beneficial [98]. This is due to the low enthalpy drop (around 50 kJ/kg) compared to steam and sCO_2 turbines and therefore lower blade speeds with optimum work coefficient [99]. For the cesium turbine, a rotation speed of 1500 rpm was chosen like in nuclear steam turbines. Because the cesium turbine works in a double-phase region it is important to keep the flow subsonic to reduce erosion effects. To account for the efficiency reduction due to the presence of liquid in the turbine the Bauman rule was used with mean Bauman factor $\alpha = 0.6$ [100]. A similar approach was used during the design and modeling of potassium turbines to estimate vapor quality losses [68,101].

Turbines with different designs were obtained and the ones with efficiency above 92 and the least number of stages were chosen. In the case of Cs turbine efficiencies obtained for 1, and 2 stage turbines were 91.8 and 92.5% with mean diameters 3.20 and 2.36m. For sCO_2 turbines mean diameter almost doesn’t change while efficiency increases in the bottoming cycle from 89.2 to 91.4 and 92.2% for the 4, 5, and 6 stages, in the recompression cycle from 91.1 to 91.9 and 92.4% for 5, 6 and 7 stages. The parameters of the chosen designs are shown in Table 9.10. In terms of pressure and volume ratio, all turbines are similar. Due to the higher volume flow cesium turbine has the biggest mean diameter and Mach number. In Figure 9.10 one can see that the CO_2 turbines designs are similar due to the close volume flows, however, in the combined cycle the carbon dioxide turbine has a smaller enthalpy drop and 2 less stages. The flaring angle for CO_2 turbines is much smaller than in the cesium turbine case because of the limited hub-to-tip ratio and more stages used.

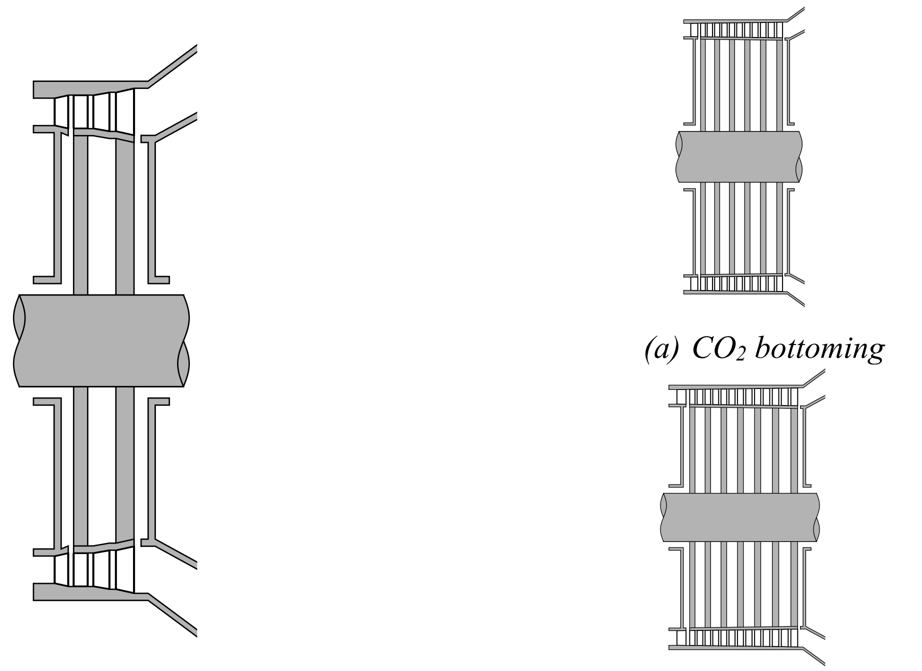

(a) CO_2 bottoming

(b) Topping (c) CO_2 recompression

Figure 9.10. Turbine flow path views in relative scale

Table 9.10. Turbines parameters

Parameter	Cycles					
	Cs		CO_2 bottoming		CO_2 recompression	
Design parameters						
Turbine inlet temperature, °C	800		670.52		800.0	
Turbine inlet pressure, bar	2.94		293.12		293.12	
Mass flow, kg/s	349.2		808.16		813.31	
Pressure ratio	2.73		2.53		2.63	
RPM	1500		3000		3000	
Number of stages	2		6		7	
Inlet volume flow, m^3/s	76.57		5.25		6.05	
Volume flow ratio	2.35		2.09		2.18	
Calculation results						
Number of stages	2		6		7	
Mean diameter, m	2.36		1.06		1.07	
Axial length, m	0.41		0.36		0.53	
Maximum Mach number	0.77		0.38		0.37	
Power output, MW	19.391		118.69		142.53	
Stage number	1^{st}	last	1^{st}	last	1^{st}	last
Tip diameter, m	2.71	2.81	1.17	1.19	1.20	1.23
Hub-to-tip ratio	0.89	0.84	0.9	0.88	0.89	0.86
Reaction degree	0.52	0.56	0.50	0.54	0.50	0.54
Total to static efficiency, %	92.49		92.16		92.39	

The design of the heat exchanger between cesium and sCO_2 was carried out adopting a shell and tube configuration. A low-pressure flow of Cesium will condense on the outside area of tubes, while high-pressure sCO_2 will be heated inside of tubes.

The design was carried out in Aspen Exchanger Design & Rating (EDR) [102] using the transport properties of saturated liquid and vapor from Vargaftik for Cesium [62], and NIST REFPROP for sCO_2 [103]. Shell and other parts on the hot side were made from SS 316, while tubes, tube sheets, and everything else on the cold side should be made from Alloy 709. Since alloy 709 is not present in EDR alloy 800 was chosen instead, because it has a similar chemical composition, which leads to similar cost, and similar but lower performance [104,105]. Like usual condensers Cs-sCO_2 heat exchanger was designed to be cross flow, but with a special high-pressure closure head in the front and a floating head in the rear.

As a result of optimization, the following design was obtained as reported in Table 9.11. Shell side film's average heat transfer coefficient was calculated to be 31 kW/m^2K with a heat flux ranging from 15 to 270 kW/m^2, which is consistent with 85 and 120 kW/m^2 for potassium and rubidium in [106] and authors' estimations of 41 kW/m^2K based on [107].

Table 9.11. Heat exchanger design parameters

Parameter	**Value**
Tube outside diameter, mm	13
Tube thickness, mm	0.6
Length, mm	4950
Pitch, mm	30
Number of tubes in the shell	3059
Tube side passes	2
Shell inside diameter, mm	1977
Shell outside diameter, mm	2005
Shells in parallel	3
Area per shell, m^2	539.1
The overall area, m^2	1617.4
Tube side pressure drop, bar	1.21
Shell side pressure drop, bar	0.019

A more optimized design, which uses different nozzles and custom head closures, could lead to smaller pressure drops and a cheaper heat exchanger overall. The heat exchange area could be reduced by using the flow intensification on the sCO_2 side, however, it is not clear, if this is needed and will reduce the cost of the exchanger.

The cost of the equipment is strongly related to material costs (the cost of alloys used and the amount of material needed). Nickel-based alloy 740 is around two times as expensive compared to alloy 709, four times compared to 316, and 10-15 times compared to VM12, which is mostly due to the composition [108–111]. The comparison of designs of equipment, which is substantially different between the power cycles is shown in Table 9.12. Since the sCO_2 turbines in the combined and recompression cycle will have similar flow path dimensions and pressure levels, one can expect similar material use, however, in the combined cycle the turbine can be done from alloys which are around two times cheaper. The same can be said about the HTR with similar UA in both cycles but different materials. Also, the use of cesium in the primary heater of the cycle instead of sCO_2 should increase the heat transfer coefficient and reduce the area of the high-temperature heat exchanger between the HTF and working fluid. However, in the combined cycle there is also the need for a high-temperature two stage turbine, which will be made from nickel-based alloy, and a cesium-sCO_2 heat exchanger, which will be made from both 709 alloy and stainless steel. The cesium pump was not considered because it will have low pressure, head, and volume flow, which will lead to its small dimensions, and will be made from stainless steel, which is much cheaper than alloy 740H and 709.

Table 9.12. Comparison of cycles equipment

Cycle	Parameter	Combined cycle	Recompression cycle
Cs turbine	Number of stages	2	-
	Mean diameter, m	2.36	-
	Axial length, m	0.41	-
	Alloy	740H	-
sCO_2 turbine	Number of stages	6	7
	Mean diameter, m	1.06	1.07
	Axial length, m	0.36	0.53
	Alloy	709	740H
Cs-sCO_2 heat exchanger	Area, m^2	1617.4	-
	Alloy	709/316H	-
HTR	UA, MW/K	20.55	19.73
	Alloy	316H	709
LTR	UA, MW/K	14.96	14.41
	Alloy	VM12	VM12

9.5. Conclusions

The present paper proposes a combined cycle to utilize high-temperature heat from the CSP using the alkali metal Rankine cycle as a topping one. A model is proposed for calculating the thermodynamic properties of Cs, K, and Na based on two standard, widespread equations. A more conservative approach is adopted by keeping the minimum pressure in the alkali metal cycle above the atmosphere and coupling the alkali cycle with the sCO_2 cycle to reduce the risk of metal reactions. The proposed cycle is compared to the sCO_2 recompression cycle at different TIT and its feasibility is assessed by the preliminary selection of materials and equipment design.

A comparison of fluids with high boiling points was carried out and three alkali metals were chosen: cesium, potassium, and sodium. A new model for calculating the thermodynamic properties of chosen alkali metals is proposed using two standard widespread equations instead of multiple, unique correlations used currently. It is based on the SRK EoS with the Twu alpha function and Rackett equation for determining the liquid density. The new model can be widely and easily applied, and has average absolute deviations below 10% for vapor pressure, the heat of vaporization, liquid density, and saturated vapor heat capacity. In the 600-1000°C temperature interval maximum deviation of vapor pressure, heat of vaporization, and vapor specific heat capacity are below 10%, vapor density below 15%, and saturated liquid density below 4%. The biggest deviations are present in liquid heat capacity, which is not a critical factor in Rankine cycles because pump work is calculated through pressure increase, density, and pump efficiency and is relatively small. The accuracy of the proposed model was demonstrated by comparing the cycle parameters with literature data, resulting in an efficiency difference of less than 1%.

A new combined power cycle comprising a topping cesium Rankine cycle and a bottoming sCO_2 recompression cycle was modeled and compared with the recompression sCO_2 cycle at various turbine inlet temperatures. Cesium was used to get a lower condensing temperature. The increase of maximum pressure in the sCO_2 cycle from 250 to 300 bar leads to an increase in thermal efficiency of 0.6%. At the same TIT and maximum pressure combined cycle has 0.7% higher thermal efficiency. Combined cycle thermal efficiency with 300 bar maximum pressure is 53.50% at 800°C, 56.68% at 900°C and 59.19% at 1000°C TIT, while for recompression cycle it is 52.83% at 800°C, 56.01% at 900°C and 58.74% at 1000°C TIT.

A review of materials, which can be used for Cs and sCO_2 was carried out and the main materials and their application temperature levels were determined. Based on this review cesium Rankine cycle equipment can be made from stainless steel for temperatures up to 730°C, from nickel-based alloys up to 880°C, molybdenum and niobium alloys up to 1080°C and tantalum alloys up to 1230°C. Meanwhile, for sCO_2, nickel-based alloys can be used up to 800°C, advanced austenitic steels up to 650°C, stainless steel up to 550°C and martensitic steel up to 450°C.

A comparison of the combined and recompression cycles was made at 800°C TIT and 300 bar maximum pressure and 100 MW power capacity. Preliminary designs of cesium and sCO_2 turbines along with the Cs-sCO_2 heat exchanger were obtained to estimate the efficiencies and feasibility. All the equipment designs were carried out according to the cycle assumptions. It was found that a combined cycle sCO_2 turbine has a higher volume and mass flow while having fewer stages. The HTR and LTR UA parameters were found to be the same in the bottoming and recompression cycles, which means that they will have a similar heat exchange area. The main difference between the two power cycle designs (apart from the use of the topping cesium cycle) is in the temperature levels and the materials used for equipment. The compressors and sCO_2 coolers will be almost the same due to the similar mass flows and almost the same temperatures and pressure. In a combined cycle Cs turbine and primary heater will be made from nickel-based alloys, the pump and hot side of the Cs-sCO_2 heat exchanger from stainless steel, while the sCO_2 turbine and cold side of the Cs-sCO_2 heat exchanger from advanced austenitic steel, HTR from stainless steel and LTR from martensitic steel. In the recompressed cycle, the primary heater and sCO_2 turbine will be made from nickel-based alloy, HTR from advanced austenitic steel, and LTR from martensitic steel. The combined cycle power plant uses more equipment, but its cost may still be comparable to that of the recompression cycle. This is due to the substantially higher cost of nickel-based alloys, which are approximately two times more expensive than advanced austenitic steel, four times the cost of stainless steel, and 10-15 times more costly than martensitic steel.

Another important consideration is the possibility of using higher TIT in the combined cycle compared to the recompression one. It is possible to design a combined cycle with 900°C TIT using the same materials (since nickel-based alloys can probably be used up to 900°C and the maximum pressure of the topping cycle is only several bar), which means similar cost and designs of equipment. At the same time recompression cycle nickel-based alloys have a limit of around 800°C due to sCO_2 corrosion, while high maximum pressures mean a more complex design and thicker walls of all equipment, which leads to higher material use and cost. This leads to the thermal efficiency of the recompression sCO_2 cycle at 52.8% at 800°C TIT and combined cycle one at 56.8% at 900°C TIT. Furthermore, it might be possible to use austenitic or even stainless steel alloys in the primary heater and turbine at 800 and 900°C TIT, which will significantly reduce the equipment cost.

The main drawbacks of the combined cycle come from the use of cesium. Since it is a reactive alkali metal, special attention has to be paid to the sealings and joints of the power cycle. Another point is the isothermal heat supply to the cycle due to the evaporation. It leads to a higher heat transfer coefficient on the cold side of the primary heat exchanger, but also to lower inlet and outlet temperature difference in the hot fluid which could negatively affect thermal energy storage and receiver efficiency and cost.

Future work will be focused on assessing the power cycle performance within the scope of the whole CSP plant, which should give a better understanding of the strengths and weaknesses of the proposed cycles and their influence on the overall system.

Appendix A: Metals hazard parameters

The hazard parameters of different metals are shown in Table 9.13 with corresponding phrases in Table 9.14 [112].

Table 9.13. Hazard parameters of different metals

Metal	Hazard code
Mercury (Hg)	H330-H360-H372
Cesium (Cs)	H260-H314
Rubidium (Rb)	H260-H314
Selenium (Se)	H301-H331-H373
Potassium (K)	H260-H314
Cadmium (Cd)	H330-H341-H350-H361-H372
Sodium (Na)	H260-H314
Zinc (Zn)	-

Table 9.14. Hazard Statements phrases

Code	Phrase
H260	In contact with water releases flammable gases which may ignite spontaneously
H301	Toxic if swallowed
H314	Causes severe skin burns and eye damage
H330	Fatal if inhaled
H331	Toxic if inhaled
H341	Suspected of causing genetic defects
H350	May cause cancer
H360	May damage fertility or the unborn child
H361	Suspected of damaging fertility or the unborn child
H372	Causes damage to organs through prolonged or repeated exposure
H373	May cause damage to organs through prolonged or repeated exposure

Appendix B: Metals liquid EoS comparison

A comparison of the different EoS predictions of alkali metals (Cs, K, Na) liquid density is shown in Table 9.15 and Figure 9.11.

Table 9.15. Comparison of equations of state for modeling liquid alkali metals in the literature

Type of EOS	Metals	N points	Range pressure, Pa	Range temperature, K	AAD, % Density*	Source
ISM	Na	109	$1–10^6$	1200–2700	0.372	[45]
	K	107	$1–10^6$	1300–2000	0.382	
	Cs	105	$1–8\cdot10^4$	600–1500	0.853	
ISM	Na	95	-	400-2000	1.07	[113]
	K	144	-	400-2000	1.18	
	Cs	132	-	400-2000	1.62	
TM	Na	20	-	250-1800	0.35	[114]
	K	20	-		0.35	
	Cs	23	-		0.35	
	Binary mixtures	Up to 25	-	350–1300	Up to 1.64	
PC-SAFT	Na	9	-	400–1200	2.03	[115]
	K	8	-	400–1100	1.45	
	Cs	9	-	400–1200	1.83	
	Binary mixtures	-	-	350-1200	Up to 4.51	

Type of EOS	Metals	N points	Range pressure, Pa	Range temperature, K	AAD, % Density*	Source
	0.1 Na + 0.4749 K + 0.4246 Cs	-	2.036–108700	450–1000	5.87	
PLJC	Na	22	-	371–2400	2.07	[49]
	K	28	-	371–2000	1.77	
	Cs	26	-	302–1900	2.12	
PHSC	Na	20	-	371–2200	1.89	[50]
	K	19	-	336,7–2100	1.97	
	Cs	17	-	301,6–1900	2.14	
Yukawa PC	Na	43	10^7- 10^8	400–1600	2.06	[52]
	K	16		600–1000	3.70	
	Cs	12		600–1000	6.22	
SAFT-VR	Na	-	-	300-2500	1.52	[116]
	K	-	-	300-2500	1.57	
	Cs	-	-	300-2500	2.45	
	Na	-	-	300-2500	1.52	

* - where pressure interval is present the density is of compressed liquid, otherwise of saturated

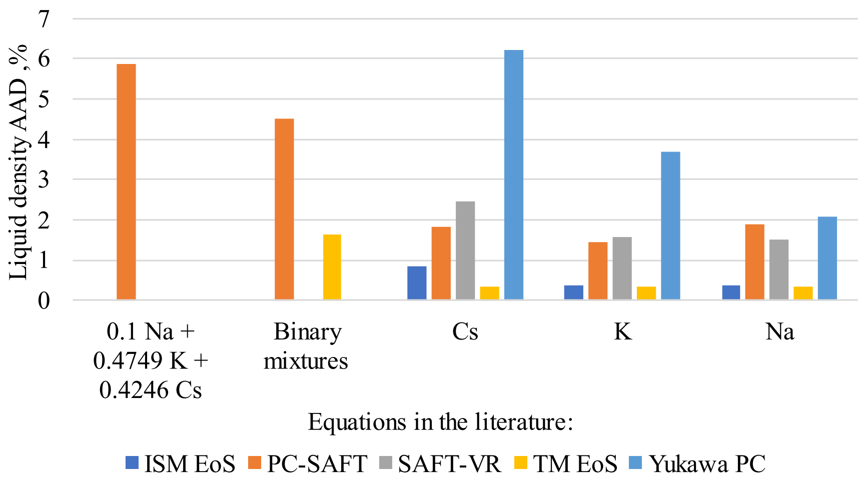

Figure 9.11. Liquid density AAD for different alkali metals and EoS (refer to Appendix B for more details)

Appendix C: Comparison of SRK EoS with Twu alpha and PC-SAFT with literature

Figure 9.12 shows the temperature based distribution of thermodynamic parameters deviation for different EoS from Reynolds [22] and Vargaftik [62] data. Saturated liquid density is not shown since it is the same between models and is calculated through the Rackett equation. In the temperature interval of interest deviations of vapor pressure, heat of vaporization, and vapor specific heat capacity are below 10% for SRK EoS. The density of vapor has a deviation of around 10% for both EoS, while liquid specific heat is consistently off by more than 50%, however, as noted above it is not critical for further analysis. One can see that the results are almost identical and thermodynamic models can be used interchangeably in the temperature interval of interest.

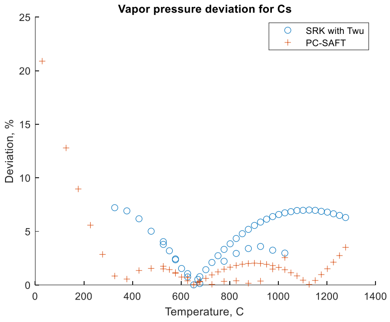

(a) Vapor pressure of cesium

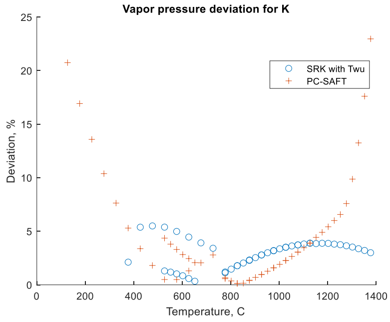

(b) Vapor pressure of potassium

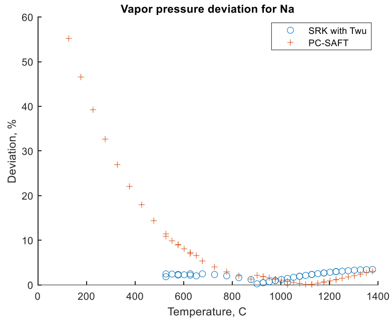

(c) Vapor pressure of sodium

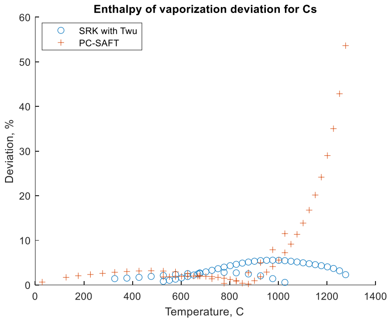

(d) Enthalpy of vaporization of cesium

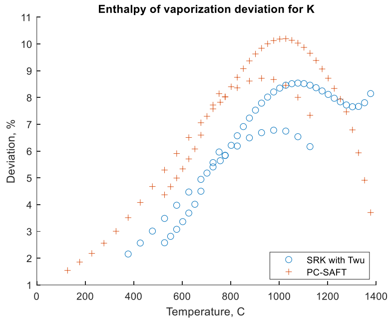

(e) Enthalpy of vaporization of potassium

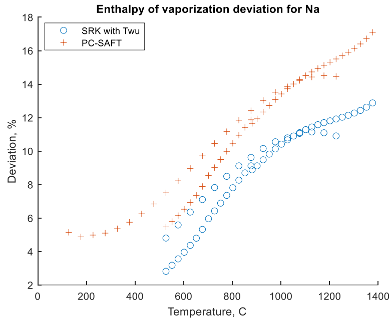

(f) Enthalpy of vaporization of sodium

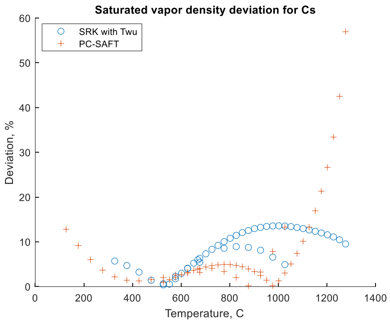

(g) Vapor density of cesium

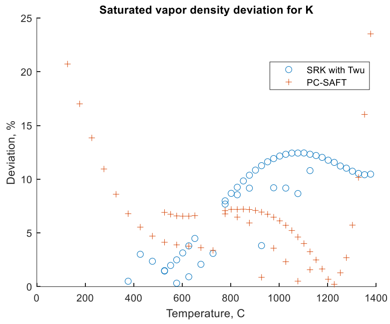

(h) Vapor density of potassium

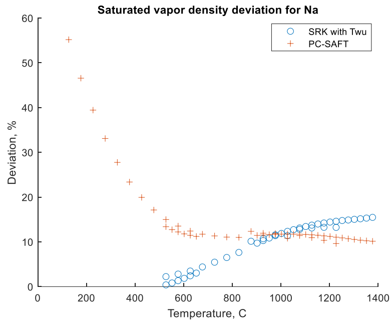

(i) Vapor density of sodium

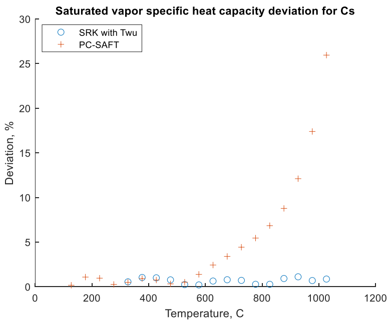

(j) Vapor specific heat capacity of cesium

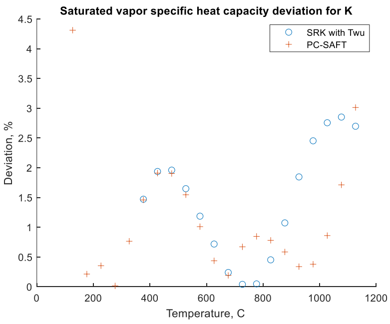

(k) Vapor specific heat capacity of potassium

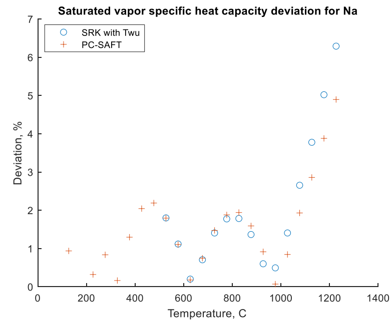

(l) Vapor specific heat capacity of sodium

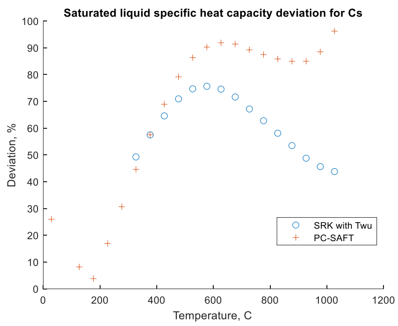

(m) Liquid specific heat capacity of cesium

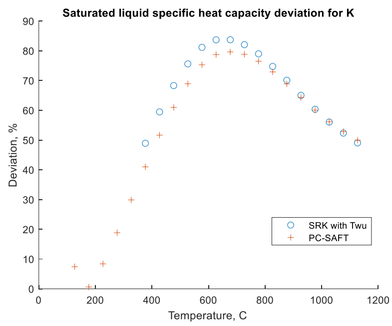

(n) Liquid specific heat capacity of potassium

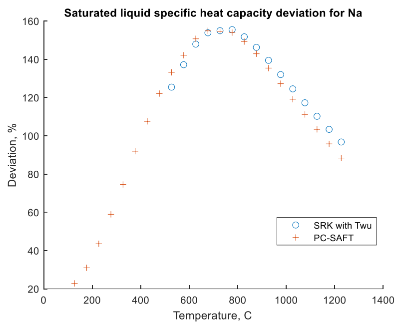

(o) Liquid specific heat capacity of sodium

Figure 9.12. Deviation in alkali metals properties modeling with SRK EoS with Twu alpha function and PC-SAFT EoS

A comparison of the vapor pressure and saturated liquid density calculated using SRK EoS with Twu alpha function against experimental data from NIST TDE in Aspen [66] is shown in Figure 9.13

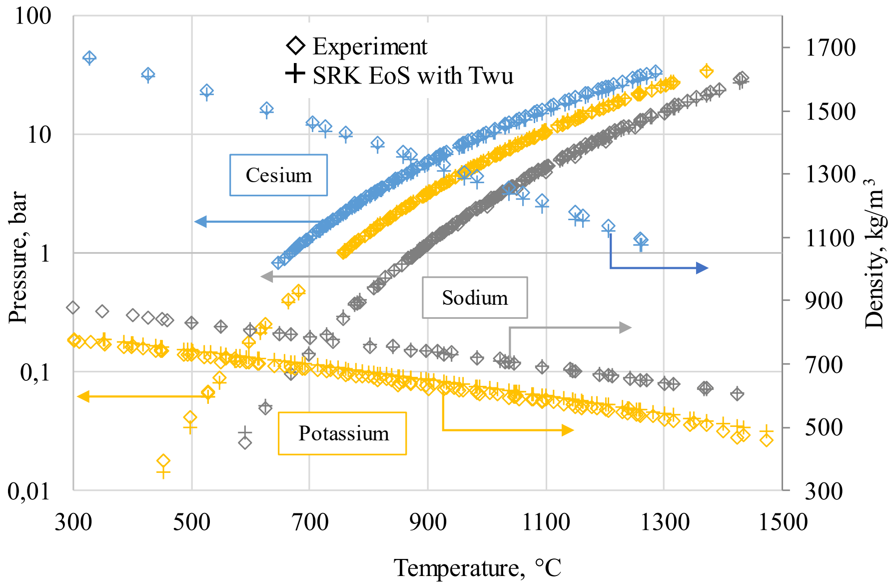

Figure 9.13. Comparison of vapor pressure and density between SRK EoS with Twu function and experimental data

9.6. Bibliography

[1] Renewable power generation costs in 2021. Abu Dhabi: IRENA; 2022.
[2] International Energy Agency. Technology Roadmap: Concentrating Solar Power. Paris, France: IEA; 2010. https://doi.org/10.1787/9789264088139-en.
[3] Concentrating solar power generation in the Sustainable Development Scenario, 2000-2030 – Charts – Data & Statistics. IEA n.d. https://www.iea.org/data-and-statistics/charts/concentrating-solar-power-generation-in-the-sustainable-development-scenario-2000-2030 (accessed July 20, 2023).
[4] Murphy C, Sun Y, Cole WJ, Maclaurin GJ, Mehos MS, Turchi CS. The Potential Role of Concentrating Solar Power within the Context of DOE's 2030 Solar Cost Targets. Golden, USA: NREL; 2019. https://doi.org/10.2172/1491726.
[5] Renewables 2020. Paris, France: IEA; 2020.
[6] Ho CK, Schroeder NR, Laubscher HF, Yue L, Mills B, Shaeffer R, et al. Receiver design and On-Sun testing for G3P3-USA, Freiburg, Germany: 2022, p. 110004. https://doi.org/10.1063/5.0086071.

[7] Alaqel S, Djajadiwinata E, Saeed RS, Saleh NS, Al-Ansary H, El-Leathy A, et al. Performance of the world's first integrated gas turbine–solar particle heating and energy storage system. Applied Thermal Engineering 2022;215:119049. https://doi.org/10.1016/j.applthermaleng.2022.119049.
[8] Wilk G, DeAngelis A, Henry A. Estimating the cost of high temperature liquid metal based concentrated solar power. Journal of Renewable and Sustainable Energy 2018;10:023705. https://doi.org/10.1063/1.5014054.
[9] Wang S, Asselineau C-A, Fontalvo A, Wang Y, Logie W, Pye J, et al. Co-optimisation of the heliostat field and receiver for concentrated solar power plants. Applied Energy 2023;348:121513. https://doi.org/10.1016/j.apenergy.2023.121513.
[10] Gentile G, Picotti G, Binotti M, Cholette ME, Manzolini G. Dynamic thermal analysis and creep-fatigue lifetime assessment of solar tower external receivers. Solar Energy 2022;247:408–31. https://doi.org/10.1016/j.solener.2022.10.010.
[11] Laporte-Azcué M, González-Gómez PA, Rodríguez-Sánchez MR, Santana D. A procedure to predict solar receiver damage during transient conditions. Renewable and Sustainable Energy Reviews 2022;154:111905. https://doi.org/10.1016/j.rser.2021.111905.
[12] Gentile G, Picotti G, Binotti M, Cholette ME, Manzolini G. A comprehensive methodology for the design of solar tower external receivers. Renewable and Sustainable Energy Reviews 2024;193:114153. https://doi.org/10.1016/j.rser.2023.114153.
[13] Zohuri B. Innovative open air Brayton combined cycle systems for the next generation nuclear power plants. The University of New Mexico, 2014.
[14] Angelino G, Invernizzi C. Binary conversion cycles for concentrating solar power technology. Solar Energy 2008;82:637–47. https://doi.org/10.1016/j.solener.2008.01.003.
[15] Markòczy G. Binary cycles for a high temperature gas cooled reactor with helium turbine. Annals of Nuclear Science and Engineering 1974;1:555–9. https://doi.org/10.1016/0302-2927(74)90078-6.
[16] Dostal V, Driscoll MJ, Hejzlar P, Wang Y. Supercritical CO2 Cycle for Fast Gas-Cooled Reactors. Volume 7: Turbo Expo 2004, Vienna, Austria: ASMEDC; 2004, p. 683–92. https://doi.org/10.1115/GT2004-54242.
[17] Binotti M, Invernizzi CM, Iora P, Manzolini G. Dinitrogen tetroxide and carbon dioxide mixtures as working fluids in solar tower plants. Solar Energy 2019;181:203–13. https://doi.org/10.1016/j.solener.2019.01.079.
[18] Crespi F, Rodríguez De Arriba P, Sánchez D, Ayub A, Di Marcoberardino G, Invernizzi CM, et al. Thermal efficiency gains enabled by using CO2 mixtures in supercritical power cycles. Energy 2022;238:121899. https://doi.org/10.1016/j.energy.2021.121899.
[19] Manzolini G, Binotti M, Bonalumi D, Invernizzi C, Iora P. CO2 mixtures as innovative working fluid in power cycles applied to solar plants. Techno-economic assessment. Solar Energy 2019;181:530–44. https://doi.org/10.1016/j.solener.2019.01.015.
[20] Di Marcoberardino G, Morosini E, Di Bona D, Chiesa P, Invernizzi C, Iora P, et al. Experimental characterisation of CO2 + C6F6 mixture: Thermal stability and vapour liquid equilibrium test for its application in transcritical power cycle. Applied Thermal Engineering 2022;212:118520. https://doi.org/10.1016/j.applthermaleng.2022.118520.
[21] Young HC, Grindell AG. Summary of design and test experience with cesium and potassium components and systems for space power plants. Oak Ridge, USA: ORNL; 1967. https://doi.org/10.2172/4361858.
[22] Reynolds WC. Thermodynamic properties in SI: graphs, tables, and computational equations for forty substances. Department of Mechanical Engineering, Stanford University Stanford, CA; 1979.
[23] Sun Q, Zhang H, Sun Z, Xia Y. Thermodynamic analysis of potassium Rankine cycle in space nuclear power by energy analysis and exergy analysis. Energy 2023;273:127241. https://doi.org/10.1016/j.energy.2023.127241.
[24] Gutstein M, Furman ER, Kaplan GM. Liquid-metal binary cycles for stationary power. Cleveland, USA: Lewis Research Center, NASA; 1975.
[25] Fraas A. Cesium vapor cycle for an advanced LMFBR. Oak Ridge National Lab., Tenn.(USA); 1975.
[26] Fraas AP. A Potassium-Steam Binary Vapor Cycle for a Molten-Salt Reactor Power Plant. Journal of Engineering for Power 1966;88:355–64. https://doi.org/10.1115/1.3678548.
[27] Angelino G, Invernizzi C. Combined binary cycles using combustion gases, alkali metal and steam as working fluids, Sardinia, Italy: 2005.
[28] Boiling Point of Chemical Elements. Material Properties n.d. https://material-properties.org/boiling-point-of-chemical-elements/ (accessed June 23, 2023).
[29] Goldstein S, Vrillon B. Confirmation of the advantages of a thermodynamic cycle using sulfur with the help of an experimental facility. Energy Conservation in Industry—Combustion, Heat Recovery and Rankine Cycle Machines: Proceedings of the Contractors' Meetings held in Brussels on 10 and 18 June, and 29 October 1982, Springer; 1983, p. 213–22.
[30] Steudel R, Steudel Y, Wong MW. Speciation and Thermodynamics of Sulfur Vapor. In: Steudel R, editor. Elemental Sulfur and Sulfur-Rich Compounds I, vol. 230, Berlin, Heidelberg: Springer Berlin Heidelberg; 2003, p. 117–34. https://doi.org/10.1007/b12405.
[31] West JR. Thermodynamic Properties of Sulfur. Ind Eng Chem 1950;42:713–8. https://doi.org/10.1021/ie50484a041.
[32] Foroulis ZA. Kinetics and mechanism of the reaction of iron with sulfur vapor in the temperature range of 250 to 500°C. Materials and Corrosion 1978;29:385–93. https://doi.org/10.1002/maco.19780290602.

[33] Dravnieks A. Kinetics of Nickel-Sulfur and Steel-Sulfur Reactions. J Electrochem Soc 1955;102:435. https://doi.org/10.1149/1.2430120.
[34] Metals - Boiling Temperatures n.d. https://www.engineeringtoolbox.com/boiling-temperature-metals-d_1267.html (accessed April 6, 2023).
[35] Morita K, Sobolev V, Flad M. Critical parameters and equation of state for heavy liquid metals. Journal of Nuclear Materials 2007;362:227–34. https://doi.org/10.1016/j.jnucmat.2007.01.048.
[36] Kozhevnikov V. Equation of state and sound speed of cesium at temperatures up to 2200 K and pressures up to 60 MPa. Journal of Experimental and Theoretical Physics 1990;70:298–310.
[37] Likalter AA, Hess H, Schneidenbach H. Critical Parameters of Alkali Metals: Deviation from Scaling. Phys Scr 2002;66:89–93. https://doi.org/10.1238/Physica.Regular.066a00089.
[38] Rau H. Vapour composition and critical constants of selenium. The Journal of Chemical Thermodynamics 1974;6:525–35.
[39] Hensel F, Hohl GF, Schaumlöffel D, Pilgrim W-C, Franck EU. Empirical Regularities in the Behaviour of the Critical Constants of Fluid Alkali Metals. Zeitschrift Für Physikalische Chemie 2000;214. https://doi.org/10.1524/zpch.2000.214.6.823.
[40] Sobolev V. Database of thermophysical properties of liquid metal coolants for GEN-IV. Boeretang, Belgium: SCK CEN; 2010.
[41] Khishchenko KV, Zhernokletov MV, Fortov VE, Kirshanov SI, Kovalev AE, Lomonosov IV, et al. Isentropic expansion of shock-compressed zinc at high pressures and temperatures. High Temperatures-High Pressures 2008;37:291–8.
[42] Mercury n.d. https://environment.ec.europa.eu/topics/chemicals/mercury_en (accessed June 23, 2023).
[43] Sabzi F, Eslami H, Boushehri A. Modified perturbed hard-sphere equation of state for alkali metal alloys. Journal of Non-Crystalline Solids 2006;352:3113–20. https://doi.org/10.1016/j.jnoncrysol.2006.02.093.
[44] Ihm G, Song Y, Mason EA. A new strong principle of corresponding states for nonpolar fluids. The Journal of Chemical Physics 1991;94:3839–48. https://doi.org/10.1063/1.460684.
[45] Haas L. Thermodynamic properties of alkali metals from a statistically-based equation of state. Review of Education, Pedagogy, and Cultural Studies 1995;17:1–6. https://doi.org/10.1080/1071441950170102.
[46] Tao F, Mason EA. Statistical-mechanical equation of state for nonpolar fluids: Prediction of phase boundaries. The Journal of Chemical Physics 1994;100:9075–87. https://doi.org/10.1063/1.466713.
[47] Kleiner M, Sadowski G. Modeling of Polar Systems Using PCP-SAFT: An Approach to Account for Induced-Association Interactions. J Phys Chem C 2007;111:15544–53. https://doi.org/10.1021/jp072640v.
[48] Al-fnaish H, Lue L. Modelling the solubility of H2S and CO2 in ionic liquids using PC-SAFT equation of state. Fluid Ph Equilib 2017;450:30–41. https://doi.org/10.1016/j.fluid.2017.07.008.
[49] Mousazadeh MH, Marageh MG. A perturbed Lennard-Jones chain equation of state for liquid metals. J Phys: Condens Matter 2006;18:4793–800. https://doi.org/10.1088/0953-8984/18/20/003.
[50] Eslami H. A perturbed hard-sphere-chain equation of state for liquid metals. Journal of Nuclear Materials 2005;336:135–9. https://doi.org/10.1016/j.jnucmat.2004.08.011.
[51] Lambert M, Prausnitz M. Diagrams for binary from a perturbed equation of state n.d.
[52] Mousazadeh MH, Diarmand H, Hakimelahi R. A perturbed Yukawa chain equation of state for liquid metals. Journal of Molecular Liquids 2012;170:41–4. https://doi.org/10.1016/j.molliq.2012.03.013.
[53] Zhao C, Li YF, Xu BQ, Yang B, Liu DC, Yang HW. Calculation of the second virial coefficients of alkali metals by modified Peng–Robinson equation. J Math Chem 2018;56:2768–84. https://doi.org/10.1007/s10910-018-0916-3.
[54] Morita K, Fischer EA. Thermodynamic properties and equations of state for fast reactor safety analysis Part I: Analytic equation-of-state model. Nuclear Engineering and Design 1998.
[55] Morita K, Fischer EA, Thurnay K. Thermodynamic properties and equations of state for fast reactor safety analysis Part II: Properties of fast reactor materials. Nuclear Engineering and Design 1998.
[56] Heimel S. Thermodynamic Properties of Cesium up to 1500 K. Cleveland, USA: Lewis Research Center; 1965.
[57] Heimel S, Ceater LR. Thermodynamic properties of potassium to 2100°K. Cleveland, USA: Lewis Research Center; 1967.
[58] Ewing C, Stone J, Spann J, Miller R. High Temperature Properties of Cesium. Journal of Chemical and Engineering Data 1966;11:473–80.
[59] Ewing CT, Stone JP, Spann JR, Miller RR. High Temperature Properties of Potassium. J Chem Eng Data 1966;11:460–8. https://doi.org/10.1021/je60031a004.
[60] Ewing C, Stone J, Spann J, Miller R. High Temperature Properties of Sodium. Journal of Chemical and Engineering Data 1966;11:468–73.
[61] Ewing CT, Spann R, Steinkuller EW, Williams DD, Miller RR. High Temperature PVT Properties of Sodium, Potassium, and Cesium. J Chem Eng Data 1966;11:309–14.
[62] Vargaftik N. Tables on the thermophysical properties of liquids and gases. 2nd ed. New York: Hemisphere Pub. Corp.; 1975.
[63] Alchagirov BB, Karamurzov BS, Kalazhokov KK, Kokov ZA, Kyasova OK. Estimation of the critical temperatures of alkaline metals on the basis of specified data on surface tension polytherms. J Phys: Conf Ser 2019;1147:012004. https://doi.org/10.1088/1742-6596/1147/1/012004.

[64] Khomkin AL, Shumikhin AS. Critical points of metal vapors. J Exp Theor Phys 2015;121:521–8. https://doi.org/10.1134/S1063776115090162.
[65] Rackett HG. Equation of state for saturated liquids. J Chem Eng Data 1970;15:514–7. https://doi.org/10.1021/je60047a012.
[66] Aspen Plus | Leading Process Simulation Software | AspenTech n.d. https://www.aspentech.com/en/products/engineering/aspen-plus (accessed June 28, 2023).
[67] Twu CH, Bluck D, Cunningham JR, Coon JE. A cubic equation of state with a new alpha function and a new mixing rule. Fluid Ph Equilib 1991;69:33–50. https://doi.org/10.1016/0378-3812(91)90024-2.
[68] Yoder GL. Technology Development Program for an Advanced Potassium Rankine Power Conversion System Compatible with Several Space Reactor Designs. Oak Ridge, USA: ORNL; 2005. https://doi.org/10.2172/885992.
[69] NIST Chemistry WebBook n.d. https://doi.org/10.18434/T4D303.
[70] Binotti M, Astolfi M, Campanari S, Manzolini G, Silva P. Preliminary assessment of sCO2 cycles for power generation in CSP solar tower plants. Applied Energy 2017;204:1007–17. https://doi.org/10.1016/j.apenergy.2017.05.121.
[71] Polimeni S, Binotti M, Moretti L, Manzolini G. Comparison of sodium and KCl-MgCl2 as heat transfer fluids in CSP solar tower with sCO2 power cycles. Solar Energy 2018;162:510–24. https://doi.org/10.1016/j.solener.2018.01.046.
[72] Neises T, Turchi C. Supercritical carbon dioxide power cycle design and configuration optimization to minimize levelized cost of energy of molten salt power towers operating at 650 °C. Solar Energy 2019;181:27–36. https://doi.org/10.1016/j.solener.2019.01.078.
[73] University of Adelaide, PROMES-CNRS, DLR, Bridgers & Paxton, Bohannan Huston, Solar Dynamics, et al. Gen 3 Particle Pilot Plant (G3P3) -- High-Temperature Particle System for Concentrating Solar Power (Phases 1 and 2). 2021. https://doi.org/10.2172/1832285.
[74] Turchi C, Gage S, Martinek J, Jape S, Armijo K, Coventry J, et al. CSP Gen3: Liquid-Phase Pathway to SunShot. 2021. https://doi.org/10.2172/1807668.
[75] Yuasa S, Isoda H. Ignition and combustion of metals in a carbon dioxide stream. vol. 22, 1989, p. 1635–41. https://doi.org/10.1016/S0082-0784(89)80175-4.
[76] Smirniotis PG. Development of Superior Sorbents for Separation of CO2 from Flue Gas at a Wide Temperature range during Coal Combustion. Cincinnati, USA: Univ. of Cincinnati; 2007.
[77] Huang J, Xu Z, Yang Y. Low-Work-Function Surface Formed by Solution-Processed and Thermally Deposited Nanoscale Layers of Cesium Carbonate. Adv Funct Mater 2007;17:1966–73. https://doi.org/10.1002/adfm.200700051.
[78] Morosini E, Alfani D, Salah SI, Abdeldayem A, Crespi F, Di Marcoberardino G, et al. Off-design of a CO2-based mixture transcritical cycle for CSP applications: analysis at part load and variable ambient temperature. Applied Thermal Engineering 2023:121735. https://doi.org/10.1016/j.applthermaleng.2023.121735.
[79] Neises T. Influence of the air-cooled supercritical carbon dioxide recompression cycle design-point on molten salt power tower techno-economic performance. Solar Energy 2023;264:112073. https://doi.org/10.1016/j.solener.2023.112073.
[80] Ehsan MM, Duniam S, Guan Z, Gurgenci H, Klimenko A. Seasonal variation on the performance of the dry cooled supercritical CO2 recompression cycle. Energy Conversion and Management 2019;197:111865. https://doi.org/10.1016/j.enconman.2019.111865.
[81] Ehsan MM, Duniam S, Li J, Guan Z, Gurgenci H, Klimenko A. Effect of cooling system design on the performance of the recompression CO2 cycle for concentrated solar power application. Energy 2019;180:480–94. https://doi.org/10.1016/j.energy.2019.05.108.
[82] Bidkar RA, Mann A, Singh R, Sevincer E, Cich S, Day M, et al. Conceptual designs of 50 MWe and 450 MWe supercritical CO2 turbomachinery trains for power generation from coal. Part 1: cycle and turbine. 5th International symposium-supercritical CO, vol. 2, 2016, p. 28–31.
[83] Pint BA, Su YF, Lance MJ, Pillai R, Keiser JR. Internal carburization and scale formation on austenitic steels in supercritical carbon dioxide. Materials at High Temperatures 2023;40:308–17. https://doi.org/10.1080/09603409.2023.2219875.
[84] Lorenzin N, Abánades A. A review on the application of liquid metals as heat transfer fluid in Concentrated Solar Power technologies. International Journal of Hydrogen Energy 2016;41:6990–5. https://doi.org/10.1016/j.ijhydene.2016.01.030.
[85] Olivares RI, Young DJ, Nguyen TD, Marvig P. Resistance of High-Nickel, Heat-Resisting Alloys to Air and to Supercritical CO2 at High Temperatures. Oxid Met 2018;90:1–25. https://doi.org/10.1007/s11085-017-9820-7.
[86] Bevard BB. Technology Development Program for an Advanced Potassium Rankine Power Conversion System Compatible with Several Space Reactor Designs. AIP Conference Proceedings, vol. 654, Albuquerque, New Mexico (USA): AIP; 2003, p. 629–34. https://doi.org/10.1063/1.1541348.
[87] Stang JH, Simons E, DeMastry JA, Genco J. Compatibility of liquid and vapor alkali metals with construction materials. vol. 227. Defense Metals Information Center, Battelle Memorial Institute; 1966.
[88] Zimmerman WF, Rossbach RJ. Metallurgical and Fluid Dynamic Results of a 2000-Hour Endurance Test on a Two-Stage, 200-Horsepower Turbine in Wet Potassium Vapor. ASME 1967 Gas Turbine Conference and Products Show, Houston, Texas, USA: American Society of Mechanical Engineers; 1967, p. V001T01A009. https://doi.org/10.1115/67-GT-9.
[89] Moor BL, Schnetzer E. Three-stage potassium vapor turbine test. Cincinnati, USA: GE; 1971.

[90] Antonio S. Novel concepts for the compression of large volumes of carbon dioxide. USA: SwRI; 2007.
[91] Pasch J, Conboy T, Fleming D, Rochau G. Supercritical CO2 recompression Brayton cycle : completed assembly description. 2012. https://doi.org/10.2172/1057248.
[92] Shin H, Cho J, Baik Y-J, Cho J, Roh C, Ra H-S, et al. Partial Admission, Axial Impulse Type Turbine Design and Partial Admission Radial Turbine Test for SCO2 Cycle. Volume 9: Oil and Gas Applications; Supercritical CO2 Power Cycles; Wind Energy, Charlotte, North Carolina, USA: American Society of Mechanical Engineers; 2017, p. V009T38A019. https://doi.org/10.1115/GT2017-64349.
[93] Zhang H, Zhao H, Deng Q, Feng Z. Aerothermodynamic Design and Numerical Investigation of Supercritical Carbon Dioxide Turbine. Volume 9: Oil and Gas Applications; Supercritical CO2 Power Cycles; Wind Energy, Montreal, Quebec, Canada: American Society of Mechanical Engineers; 2015, p. V009T36A007. https://doi.org/10.1115/GT2015-42619.
[94] Ehsan MM, Awais M, Lee S, Salehin S, Guan Z, Gurgenci H. Potential prospects of supercritical CO2 power cycles for commercialisation: Applicability, research status, and advancement. Renewable and Sustainable Energy Reviews 2023;172:113044. https://doi.org/10.1016/j.rser.2022.113044.
[95] SwRI, GTI Energy, GE celebrate mechanical completion of $155 million supercritical CO2 pilot plant. Southwest Research Institute 2023. https://www.swri.org/press-release/swri-gti-energy-ge-celebrate-mechanical-completion-of-155-million-supercritical-co2 (accessed November 27, 2023).
[96] Concentrating Solar Power Projects | NREL n.d. https://solarpaces.nrel.gov/?utm_medium=domain-switch&utm_source=csp&utm_campaign=solarpaces (accessed July 21, 2023).
[97] Agromayor R, Nord LO. Preliminary Design and Optimization of Axial Turbines Accounting for Diffuser Performance. IJTPP 2019;4:32. https://doi.org/10.3390/ijtpp4030032.
[98] Invernizzi CM. The Binary Cycles. Closed Power Cycles, vol. 11, London: Springer London; 2013, p. 205–18. https://doi.org/10.1007/978-1-4471-5140-1_5.
[99] Gambini M, Vellini M. Turbomachinery: Fundamentals, Selection and Preliminary Design. Cham: Springer International Publishing; 2021. https://doi.org/10.1007/978-3-030-51299-6.
[100] Petr V, Kolovratnik M. Wet steam energy loss and related Baumann rule in low pressure steam turbines. Proceedings of the Institution of Mechanical Engineers, Part A: Journal of Power and Energy 2014;228:206–15. https://doi.org/10.1177/0957650913512314.
[101] Wesling G. Three-stage potassium turbine performance test summary. Cincinnati, USA: GE; 1969.
[102] Aspen Exchanger Design and Rating (EDR) | AspenTech n.d. https://www.aspentech.com/en/products/engineering/aspen-exchanger-design-and-rating (accessed July 25, 2023).
[103] Lemmon EW, Bell IH, Huber ML, McLinden MO. NIST Standard Reference Database 23: Reference Fluid Thermodynamic and Transport Properties-REFPROP, Version 10.0, National Institute of Standards and Technology 2018. https://doi.org/10.18434/T4/1502528.
[104] McMurtrey M. Alloy 709 Advanced Austenitic Stainless Steel. Idaho Falls USA: Idaho National Laboratory; 2021.
[105] Swindeman RW, Marriott DL. GENERATION IV/NGNP MATERIALS PROJECT TASK 11: NEW MATERIALS PART I- SELECTION OF CANDIDATE MATERIALS. Oak Ridge, USA: Cromtech Inc, Stress Engineering Services Inc; 2009.
[106] Sartor A. Condensing Heat Transfer Considerations Relevant to Rubidium and Other Alkali-metals. University of Michigan, 1968.
[107] Kroger DG. Heat transfer during film condensation of potassium vapor. MIT, 1966.
[108] Preferred supplier of INCONEL 740 Tube| Alloy 600 | INCONEL 740 Tubing| INCONEL 740 Pipe| INCONEL 740 coiled tubing - Aesteiron Steel Pipes n.d. http://aesteironsteelpipes.com/inconel-740-tube-tubing-pipe-272.html (accessed July 25, 2023).
[109] Incoloy 800 supplier, Alloy 800h material, Incoloy 800 price in India n.d. https://www.stindia.com/incoloy-alloy-800-800h-800ht-supplier.html (accessed July 25, 2023).
[110] Mori 2A. STAINLESS STEEL PRICE TREND. Mori 2A 2018. https://www.mori2a.com/en/dont-stop/news/in-depthprodotti/stainless-steel-price-trend/ (accessed July 26, 2023).
[111] Priminox. SA 199/ SA213 T91 Alloy Steel Seamless Tube Supplier in Mumbai, India n.d. https://www.priminox.com/alloy-steel-t91-seamless-tube-supplier/ (accessed July 26, 2023).
[112] AMERICAN ELEMENTS® | The Advanced Materials Manufacturer n.d. https://www.americanelements.com (accessed July 17, 2023).
[113] Maftoon-Azad L, Eslami H, Boushehri A. A perturbed hard-sphere equation of state for alkali metals. Fluid Ph Equilib 2008;263:1–5. https://doi.org/10.1016/j.fluid.2007.07.073.
[114] Yousefi F, Karimi H, Gandomkar Z. Equation of state and artificial neural network to predict the thermodynamic properties of pure and mixture of liquid alkali metals. Fluid Ph Equilib 2014;370:43–9. https://doi.org/10.1016/j.fluid.2014.02.011.
[115] Mousazadeh MH, Faramarzi E, Maleki Z. Equation of state for thermodynamic properties of pure and mixtures liquid alkali metals. Thermochimica Acta 2010;511:147–51. https://doi.org/10.1016/j.tca.2010.08.006.
[116] Shariyati R. The Saft-Vr Morse Equation of State for Liquid Alkali Metals. SSRN; 2023. https://doi.org/10.2139/ssrn.4363967.

10. Conclusions and future remarks

10.1. Conclusions

The next generation of CSP plants aims to reduce the electricity cost. They are planned to reach temperatures above 700°C and generate electricity with CO_2 Brayton power cycles. These cycles performance could be improved by utilizing power cycles with CO_2 mixtures using dopants with high critical temperatures. This thesis presents theoretical and experimental investigations into the CO_2 mixtures cycles and their equipment for CSP plants. The work is structured as a collection of scientific papers organized into four parts: part one focuses on the design and experimental characterization of equipment for sCO_2 and CO_2 mixture power cycles, part two investigates the novel dopants proposed in this work, part three evaluates the techno-economic performance of sCO_2 and CO_2 mixture power cycles in CSP plants and part four presents a high-temperature combined cycle configuration

The first part of the thesis is focused on equipment. The thermal and mechanical design of shell and tube heat exchangers for sCO_2 and CO_2+$SiCl_4$ cycles was carried out to determine the heat exchange area, number of shells, weight of components, and the amount of materials used. It was found that primary heat exchangers (PHE) have a similar product of overall heart transfer coefficient and surface (UA) and area for both sCO_2 and CO_2+$SiCl_4$ cycles. For recuperators, the main difference was the heat exchanger technology used, while the working fluids didn't show much influence.

Then, to experimentally characterize the performance of a novel heat exchanger technology with low finned tubes and two baffle spacings, the similarity of molten solar salt and water was explored. The design of the experiment was developed with water temperature ranges based on the Prandtl number similarity and flow rate based on the Reynolds number similarity. This allowed to test the heat transfer characteristics without the need of complex equipment to operate with solar salt. The finned tubes Fanning friction factor for bigger baffle spacing was found to align with literature data, while smaller baffle spacing results require further investigations. To characterize the technology heat transfer performance, the shell side Nusselt number was calculated and correlated with the average Reynolds number. The heat transfer performance for the first baffle spacing was found to be in accordance with the literature data, while for larger baffle spacings, the results need to be further investigated. The heat transfer performance results obtained cover the whole Reynolds number range of interest (5700-7800) and the average shell side temperature of 30-45°C, which translates to the solar salt temperature in the 400-480°C range.

Finally, the preliminary designs of equipment for the steam Rankine cycle and sCO_2 and CO_2 mixtures cycles were made and compared to correlations and data available in the literature. The comparison of the equipment for sCO_2 to CO_2 mixtures was done, with most pieces showing little dependence on the working fluid. The sCO_2 simple cycle was found to have the lowest equipment cost of 707 USD/kWe, which is between the average and the conservative steam Rankine power cycle values. Most of the cost was associated with the recuperative system and PHE. The masses and thicknesses of components for sCO_2, CO_2 mixture, and the steam Rankine cycles were also compared with implications for flexibility.

In the second part of the thesis, multiple novel CO_2 dopants were investigated both theoretically and experimentally. First, preliminary analysis showed that both CO_2+$GeCl_4$ and CO_2+Cl_3FSi mixture-based power cycles would offer a reduction in LCOE compared to conventional sCO_2 cycles for both Gen2 and Gen3 CSP plants. Second, the thermal stability of hexafluoropropylene (C_3F_6) and germanium tetrachloride ($GeCl_4$) was experimentally tested. Both dopants were found to have low thermal stability limits. A thermal stress test of hexafluoropropylene at 400°C led to the reduction of vapor pressure, which, according to literature, could happen due to the formation of i-C_4F_8. Vapor pressure of $GeCl_4$ after thermal stress at 450°C resembled that of the ideal gas, which would indicate that all fluid in the vessel has turned into solid and gas with very low critical pressure

In the third part of the thesis for techno-economic analysis, a CSP plant model was developed based on a combination of literature and custom models in Python. It was validated and showed a deviation of electricity production, total capital cost, and LCOE below 5% compared to SAM and SolarTherm for Gen2 and Gen3 CSP plants with liquid HTF. Using the CSP model, a comparison of steam, sCO_2, and CO_2+$SiCl_4$ mixture power cycles in Gen2 and Gen3 CSP plants was carried out, optimizing solar multiple (SM) and thermal energy storage (TES) size. The CO_2+$SiCl_4$ mixture in the simple or precompression cycle layout was found to have a lower LCOE than sCO_2 at 550 and 700°C TIT. The CO_2+$SiCl_4$ mixture cycle was even determined to be competitive with the steam Rankine cycle at 550°C TIT. Among the CO_2 mixture power cycle configurations, the simple and precompression cycles were identified to be the most promising. For sCO_2, the partial cooling layout achieves the lowest LCOE, followed by the simple and recompression layouts. In general, simpler power cycle layouts exhibit lower efficiencies and reduced PHE inlet temperatures, which increases solar receiver efficiency. Their overall solar-to-electric efficiency at the CSP plant level remains lower, but their primary advantage lies in reduced costs of both the power cycle and thermal energy storage. Therefore, the simple cycle consistently results in one of the lowest LCOEs for both sCO_2 and CO_2 mixtures, which is in accordance with findings reported in the literature. Then, the influence of cooler/condenser design on techno-economic parameters of the CSP plant was investigated using the simple recuperated cycles with sCO_2 and CO_2+$SiCl_4$ mixture. For design and off-design analysis of power cycles at different minimum cycle temperatures, detailed PCHE and cooler/condenser models were implemented to accurately describe the condensation of working fluid, while for the compressor, pump, turbine, and PHE, simplified models were adopted. The off-design power cycles curves were used in the CSP plant model to calculate the annual electricity production and techno-economic performance. It was found that the CO_2 mixture cycle has, on average, 3.9 and 4 percentage points higher thermal and electric efficiency than an sCO_2 one, with a higher difference at higher minimum cycle temperatures. For both CO_2 mixture and sCO_2 cycles, the minimum LCOE was reached at an air design temperature of 35°C (not exceeded 96.8% of hours in the location) and 12 hours of TES, while optimum SM was found to be 3 and 2.9, respectively. For all conditions and cycles, the reduction of cooler/condenser approach temperature (from 15 to 10 and 5°C) also led to the LCOE reduction. For both base and optimized SM and TES sizes, the CO_2 mixture cycle has 8.4% lower LCOE compared to the sCO_2 one and is less sensitive to changes in the ambient air design temperature.

In the fourth part of the thesis, a combined cycle is proposed to utilize high-temperature heat from the CSP using the alkali metal Rankine cycle as a topping one. A model is proposed for calculating the thermodynamic properties of Cs, K, and Na based on two standard, widespread equations with an efficiency difference of less than 1%. Cesium was chosen to keep the minimum pressure in the alkali metal cycle above the atmosphere. The alkali metal cycle was coupled with the sCO_2 cycle to reduce the risk of metal reactions. The proposed cycle is compared to the sCO_2 recompression cycle at different TIT and has higher thermal efficiency. Its feasibility is assessed by the preliminary selection of materials and equipment designs.

In summary, the most economically attractive are the cycles with low costs and primary heat exchanger inlet temperatures, allowing for lower TES and power plant costs without significant reduction of electricity production. This can be seen for both sCO_2 and different CO_2 mixture cycles investigated. Specifically, the most promising layouts using sCO_2 are partial cooling and simple recuperated cycles, while for CO_2 mixtures these are simple recuperated and precompression cycles. Therefore, the simple recuperated cycle would be the most promising option for industrial application since it has a simpler layout, is easier to control and operate reliably, and consistently ranks as one of the two most economically attractive options. Among the investigated CO_2 dopants, $SiCl_4$ was found to be the most promising, having both good thermal stability and material compatibility. Its use could reduce the cost of the power cycle, the power plant as a whole, and LCOE compared with both CO_2 and steam Rankine cycles.

Therefore, this thesis presents a theoretical and experimental investigation of equipment, CO_2 dopants, and the techno-economic performance of CSP plants using sCO_2 and CO_2 mixture power cycles, as well as high-temperature combined cycle configuration for CSP. This work is done to support the implementation of the next generation of CSP plants with better techno-economic performance for the generation of affordable, reliable, sustainable, clean energy.

10.2. Future remarks

The results of this study could be used as a starting point for the design of CSP plants with sCO_2 and CO_2 mixture power cycles. However, some uncertainty remains concerning the operation of CO_2 mixture power cycles, especially the composition shift due to the liquid phase hold-up in different parts of the cycle. These risks can be mitigated by the CFD modeling of equipment used, accounting for the phase transition and stagnant zones. The most promising approach is the experimental testing of the CO_2 mixture power cycle concept in university laboratories and pilot plants. Finally, for each CO_2 mixture of interest, extensive experimental test campaigns are needed to be certain of the thermal stability, accurate thermodynamic and transport property modeling, and chemical reactions with different materials present in the power cycle. The influence of uncertainties in thermodynamic and transport properties on the final plant design could also be evaluated by propagating these uncertainties through the power cycle model and, ultimately, to the techno-economic performance parameters of the CSP plant.

From the techno-economic perspective, substantial uncertainty remains in the cost assumptions for the primary heat exchanger and recuperators, which represent the largest contributions to total cycle cost. Moreover, the cost of recuperators is also subject to many variables that are not fully considered by the correlations in literature. Further research should therefore be done in collaboration with industrial partners to have a detailed design and better understanding of how the heat exchanger parameters (pressure drops, temperature levels, and approach temperature) influence the cost and the trade-off between the cost and efficiency of the system. However, even for the steam Rankine cycle, which is a mature technology, the major equipment cost estimates still vary significantly, even by a factor of 2 in the case of primary heat exchangers. Therefore, the detailed designs of equipment should be obtained for each specific case.

Depending on the dopant selected, additional material requirements may also arise from compatibility and corrosion tests, potentially increasing the cost of equipment. Furthermore, most dopants stable at high temperatures have negative health effects, so additional safety procedures will be needed, which would increase the cost of the plant.

Finally, the methodology adopted in this thesis could be further improved by incorporating dispatch optimization to match the local electricity price/demand profile, as well as by considering wet or hybrid cooling technologies to improve overall system efficiency in locations where water use is less constrained.